UNIVERSITY OF CALIFORNIA

Los Angeles

Polyelectrolyte Complex/Covalent Interpenetrating Polymer Network Hydrogels

A dissertation submitted in partial satisfaction of the requirements for the degree

Doctor of Philosophy in Chemical Engineering

by

Defu Li

2022

ABSTRACT OF THE DISSERTATION

Polyelectrolyte Complex/Covalent
Interpenetrating Polymer Network Hydrogels
by

Defu Li

Doctor of Philosophy in Chemical Engineering

University of California, Los Angeles, 2022

Professor Samanvaya Srivastava, Chair

The objectives of this dissertation are to gain a fundamental understanding of the assembly and properties of polyelectrolyte complex (PEC) hydrogels, harness the self-assembly of PEC hydrogels to mitigate the shortcomings of existing photocrosslinkable materials, and create PEC/covalent interpenetrating polymer network (IPN) hydrogels with precisely tuned microstructure and material properties.

PEC hydrogels self-assemble swiftly upon mixing oppositely charged triblock polyelectrolytes and feature tunable mechanical properties, microstructural diversity, as well as self-healing attributes and responsiveness to salt and pH changes in their environment. Moreover, the nanoscale PEC domains that constitute the three-dimensional (3D) network in PEC hydrogels spontaneously encapsulate charged macromolecules (e.g., protein, drug, and nucleic acids). However, a few drawbacks limit their widespread biomedical applications. The electrostatically assembled 3D network results in their moderate shear strength, poor tensile strength, and uncontrolled swelling. We demonstrate that interpenetration of the PEC network with a covalently-linked network not

only addressed the limitations of the PEC hydrogels but also contribute to synergistic improvements in the mechanical performance of the resulting IPN hydrogels.

The unique attributes of PEC hydrogels – swift self-assembly in aqueous surroundings, rapid moduli recovery upon cessation of flow, and interim insolubility in water – were further harnessed to employ them as scaffoldings for photocrosslinkable materials. PEC hydrogels were compatible with four representative precursors (linear and 4-arm poly(ethylene glycol) acrylate, acrylamide, and gelatin methacryloyl (GelMA)) and their corresponding networks, which featured different molecular weights, polymer origins, crosslinking mechanisms, and molecular structures. Mixing of oppositely charged bPEs with photocrosslinkable precursors resulted in precursor-encapsulating PEC hydrogels (PEC+precursor hydrogels) that exhibited significantly higher viscosity and shear strength as compared to precursors solutions. The PEC+precursor hydrogels did not suffer from issues such as dilution, precursor deactivation, and unwanted flows that affect *in situ* crosslinking of photocrosslinkable hydrogels in wet environments. Moreover, the PEC/precursor IPN hydrogels produced by *in situ* crosslinking of the PEC+precursor hydrogels exhibited improved shear and tensile properties. Consequently, PEC+GelMA hydrogels were demonstrated as robust bioinks for extrusion-based 3D bioprinting at physiological temperatures (37 °C). The PEC+GelMA inks avoided undesirable secondary flow and produced a higher printing resolution, enabling printing of intricate multilayered constructs.

The dissertation of Defu Li is approved.

Panagiotis D. Christofides

Timothy J. Deming

Nasim Annabi

Philippe Sautet

Samanvaya Srivastava, Committee Chair

University of California, Los Angeles

2022

ACKNOWLEDGMENT

First, I want to thank my advisor, Prof. Samanvaya Srivastava, for his support and guidance during my Ph.D. With his help, I have evolved to a higher level in research, technical writing, and public speaking.

I would like to thank all my committee members (Prof. Philippe Sautet, Prof. Nasim Annabi, Prof. Tim Deming, and Prof. Panagiotis D. Christofides) for feedback and guidance. Your suggestions helped me broaden my research horizon and helped me accomplish more in my research.

I want to thank all Srivastava lab members: Advait Holkar, Divya Jayaram Iyer, Holly Senebandith, and Fahed Albreiki. We helped each other in terms of experiments, data analysis, and revising manuscripts. It is a great time working with all of you! Besides, I also want to thank all of my collaborators, Tobias Göckler, Prof. Ute Schepers, and Prof. Nasim Annabi! I also want to thank Xiaobing Zuo and Suresh Narayanan at Argonne National Laboratory and Chenhui Zhu at Berkely National Laboratory, who helped me set up X-ray scattering experiments.

I want to thank all Chemical & Biomolecular Engineering (CBE) Graduate Student Committee (GSC) team members and Prof. Panagiotis D. Christofides for building this student organization. As a result, we have successfully built up the CBE community platform! Besides, I also want to thank Prof. Kenneth Kung for providing me TAship opportunities. It has been a great time working with you over the past three years.

In the end, I want to thank my parents for their love and support. Both of you are hardworking and kind people, which shaped my personality and diligent habits. Besides, I want to thank my younger brother for his support and help.

TABLE OF CONTENTS

LIST OF FIGURES

LIST OF TABLES

VITA

2013-2017	B.S. in Chemical and Biomolecular Engineering, University of California, Los Angeles
2017-	Ph.D. Candidate in Chemical Engineering, Advisor: Professor Samanvaya Srivastava University of California, Los Angeles

PUBLICATIONS

1. **Li, D. F.**; Gockler, T.; Schepers, U.; Srivastava, S. Polyelectrolyte Complex-Covalent Interpenetrating Polymer Network Hydrogels. *Macromolecules* **2022**, *55* (11), 4481-4491. DOI: 10.1021/acs.macromol.2c00590.

2. **Li, D. F.**; Ghovvati, M.; Annabi, N.; Srivastava, S. Polyelectrolyte Complex Scaffoldings for Photocrosslinked Hydrogels. *Molecular System Design & Engineering*, in review.

3**.** Göckler, T.; **Li, D. F.**; Grimm, A.; Mecklenburg F.; Grün, M.; Schepers U.; Srivastava, S. Hydrogel Scaffoldings Enable Extrusion-based 3D Bioprinting of Low Viscosity Bioinks. *Submitted*.

4. **Li, D. F**.; Narayanan, S.; Srivastava, S. Coupling Relationship between Relaxation Dynamics and Microstructures of Triblock Polyelectrolyte Complex Hydrogels by X-ray Photon Correlation Spectroscopy (XPCS). *Submitted.*

5. **Li, D. F.**; Srivastava, S. Polyelectrolyte Complex-Interpenetrating Polymer Network Hydrogels Comprising Poly (Ethylene Glycol) Diacrylate with Different Molecular Weights. *Manuscript in preparation.*

6. Göckler, T.*; **Li, D. F.***; Albreiki, F.*; Schepers U.; Srivastava, S. Macro- and microscopic study of complex fluids comprising GelMA and block polyelectrolytes for extrusion-based 3D printing. *Manuscript in preparation.*

SELECTED PRESENTATIONS

1. **Li, D. F.**; Göckler, T.; Srivastava, S. *Hybrid Electrostatic-Covalent Hydrogels*. American Institute of Chemical Engineers (AICHE) Annual Meeting, *November 2021*
2. **Li, D. F.**; Göckler, T.; Srivastava, S. Hybrid Electrostatic-Covalent Hydrogels. Annual Meeting of the American Physical Society, Online, March 2021
3. **Li, D. F.**; Göckler, T.; Srivastava, S. Hybrid Electrostatic-Covalent Hydrogels. 95th ACS Colloid and Surface Science Symposium (CSSS), Online, June 2021
4. **Li, D. F.**; Göckler, T.; Srivastava, S. Polyelectrolyte Complex-Interpenetrating Polymer Networks Hydrogels. Annual Meeting of the American Physical Society, March 2022 (Poster session)

    Received First Place Award for In-Person Presentation at the 2022 APS March Meeting Physics Poster Session.

Chapter 1

Introduction

1.1 Hydrogels

Hydrogels are three-dimensional hydrophilic polymer networks that can retain up to 95 wt% water.[1, 2] The water-rich nature of hydrogels provides similarity with living tissues, and thus their use as versatile materials in diverse biological and biomedical applications has gained significant research attention in recent decades.[1] Mechanical tunability, tailored functionalities, and versatile polymer chemistries have enabled fabrication of hydrogels with properties that match the requirements of diverse applications. Consequently, hydrogels have emerged as promising materials for cell scaffolds in tissue engineering, inks in extrusion-based 3D bioprinting, bioadhesives, carriers in drug delivery, ionic conductors, sensors, and versatile materials in consumer products and the food industry.[1, 3-16] The global market size of hydrogel products was around $22.1 billion in 2019 and is projected to reach $ 31.4 billion in 2027.[17]

Traditionally, hydrogels are composed of simple networks formed by a single constituent polymer or monomer. The properties of such hydrogels fail to satisfy the increasing demands for multifunctionality required in contemporary applications. For example, in applications wherein hydrogels are employed as scaffoldings to support cell growth, traditional hydrogels only mimic the static three-dimensional structure and the mechanical properties of the extracellular matrix (ECM) without considering microstructures and dynamics processes. However, recent studies have reported that dynamic processes stimulate cells to produce biological signals, accelerating cell proliferation, differentiation, and growth.[18, 19] Besides, it has also been reported that

microstructural complexity of the ECM contributes to multiple and complicated functions of human tissues.[20] Moreover, traditional hydrogels typically lack stimuli-responsiveness and self-healing characteristics, limiting their applications.[11] The shortcomings of traditional hydrogels to meet the requirements of contemporary and advanced applications have motivated research on hydrogels that have evolved from simple networks to complicated structures that often combine multiple crosslinking strategies or even multiple networks to achieve multifunctionality.[21] With our increasing interdisciplinary understanding and ever-improving synthetic chemistry approaches, hydrogels are evolving continually to feature desired properties for biomedical and industrial applications.

1.2 Chemically and Physically Crosslinked Hydrogels

1.2.1 Chemical Hydrogels

Chemical hydrogels form upon covalent crosslinking among polymer chains or monomers. Free radical polymerization, enzyme-catalyzed reaction, Diels-Alder reaction, Schiff base reaction, oxime formation, and Michael reaction are among the most common crosslinking reactions to synthesize chemical hydrogels.[22-24] Chemically crosslinked hydrogels typically possess strong mechanical strength and tunability, providing structural rigidity and stability.[25, 26] However, the covalent crosslinking process usually involves toxic crosslinking agents, such as initiators and catalysts, which lower material biocompatibility and even limit biomedical applications.[21] Besides, owing to permanent nature of the covalent crosslinking, they usually lack self-healing, injectability, stimuli-responsive, self-assembly, and anti-fatigue properties.[25, 27] To overcome these limitations, various approaches have been devised, but not without their respective shortcomings. For instance, *in-situ* polymerization is pursued following the injection of polymer precursors and cargos in

solution to overcome the lack of injectability of the hydrogels.[23] However, this method has strict requirements of optimized polymerization rate. Fast polymerization can result in gelation inside delivery devices or needles, and slow polymerization can cause a significant loss of unpolymerized precursor material at the target site. To acquire self-healing property, non-covalent interactions among the crosslinked chains have been introduced in the chemically crosslinked hydrogels, but provide only a limited range of responses.[27] Despite the advantages and modifications of chemical hydrogels, innovative strategies are needed to further develop these hydrogels with a broader set of functionalities to meet the contemporary requirements.

Photocrosslinkable hydrogels, a subset of chemical hydrogels, enable spatiotemporal control over the crosslinking owing to their photoreactive properties.[28] Their photocrosslinkable nature, injectability prior to crosslinking, mild crosslinking conditions, and tunable and strong mechanical properties make this class material a potential candidate for cell scaffolding, bioadhesives and 3D bioprinting inks. However, a few of their drawbacks limit their applications. For instance, before photocrosslinking, the low viscosity of precursors makes them easily diluted in a watery environment. Most bioadhesives applications involve wet environments due to blood and biological fluid. Thus, precursors undergo dilution and material loss at a wet target site, which eventually leads to failure of hydrogel functions. Similarly, the low viscosity and poor mechanical properties of precursors lead to undesirable secondary flow, low printing resolution, and an inability to print complicated structures in extrusion-based 3-D printing. Thus, a simple and versatile solution to address these issues and enable photocrosslinking of precursors in a protected environment is highly desired. At the same time, after photocrosslinking, most photocrosslinkable hydrogels lack microstructural complexity and stimuli-responsiveness, and also suffer from the strength-extensibility tradeoff. Thus, a strategy that can not only address the problems of

precursors but also enhance the mechanical properties of hydrogels after photocrosslinking is highly anticipated.

1.2.2 Physical Hydrogels

Noncovalent, reversible interactions, such as electrostatic interactions, π-π stacking, hydrogen bonding, crystallite formation, host-guest interactions, and hydrophobic interactions have been harnessed to create physical hydrogels.[22, 26] Physical hydrogels typically feature reversibility, self-healing, injectability, stimuli-responsiveness, hierarchical microstructures, and lower toxicity, which make them promising materials for diverse biomedical applications, such as tissue engineering, drug delivery, and bioadhesion. In recent years, stimuli-responsiveness become one of the key features of contemporary hydrogels – hydrogels that can undergo transitions in structure and/or mechanical properties in response to environmental changes, such as light, pH, chemicals, temperature, magnetic field, and electric field have been demonstrated,[7, 29] enabling control of drug encapsulation and release, *in situ* gelation for tissue engineering, biosensors, soft robotics, and 4D printing, etc.[7]

In recent years, hydrogels formed by electrostatic interactions have attracted research attention owing to their salt- and pH-sensitive properties. The electrostatically crosslinked hydrogels are typically categorized as either polyampholyte hydrogels or polyelectrolyte complex (PEC) hydrogels. Polyampholyte hydrogels consist of both covalent and ionic bonds. The covalent bonds provide structural support for the hydrogels, and ionic bonds serve as sacrificial bonds to enhance toughness and improve internal fraction.[16] These hydrogels are prepared by random copolymerization of cationic and anionic monomers.[16, 30] In comparison, PEC hydrogels are typically prepared by mixing oppositely charged polyelectrolytes and are crosslinked by

electrostatic interaction only. Before mixing, both cationic and anionic polyelectrolyte solutions exist as low viscosity liquids. Yet, upon mixing, the cationic and anionic polyelectrolytes self-assemble rapidly within a few seconds. Thus, the liquid-like cationic and anionic can be injected separately and initiate gelation at a target site without any additional requirements, such as ultraviolet (UV) light. The self-assembly and injectability are vital for applications requiring *in situ* gelation, such as cartilage engineering. Besides, the reversible dynamic electrostatic interaction can dissipate energy during stretching process, providing stress dissipation mechanisms.

1.3 Polyelectrolyte Complex (PEC) Hydrogels

Polyelectrolyte complex (PEC) hydrogels, a subset of electrostatically assembled hydrogels, are formed upon mixing oppositely charged homo-polyelectrolytes (hPE) or block polyelectrolytes (bPE).[31] In solutions, the oppositely charged chains, or parts of chains, complex with each other, and may also phase separate under appropriate circumstances. This complexation is typically driven by a combination of enthalpy gain from interchain electrostatic interactions, and the entropic gains acquired from the dissociation of small ions from PE chains.[32] The PEC networks, held by electrostatic interactions, feature tunable mechanical strength, self-assembly, versatile microstructures, stimuli responsiveness, and self-healing properties, which make PEC-based materials good candidates for cell scaffolds for tissue engineering, bioadhesives, and ionic conductors.[24, 33-37] Besides, their biocompatibility and electrostatic interactions render the ability to encapsulate and deliver charged therapeutic agents (drug, DNA, and protein) for biomedical applications.

As shown in Figure 1-1, hPEs polymers feature charged groups along the entire chain and while bPE chains only contain ionic groups on the charged blocks. Mixing oppositely charged hPEs

typically results in bulk phase separation or gelation (for stiff hPEs) owing to dense charged groups along the chains (Figure 1-1A). In comparison, complexation of bPEs typically results in formation of nanoscale PEC domains because their neutral blocks resist and restrict macrophase separation (Figure 1-1B). The properties of PEC hydrogels depend on pH, ionic strength, charge density, polymer chain length, salt concentration, and charge ratio.[38] Stronger charge density and ionic strength, and longer polymer chain length typically resulted in precipitates. In comparison, poor charge density and ionic strength can lead to uncontrollable swelling and even polyelectrolyte solutions.

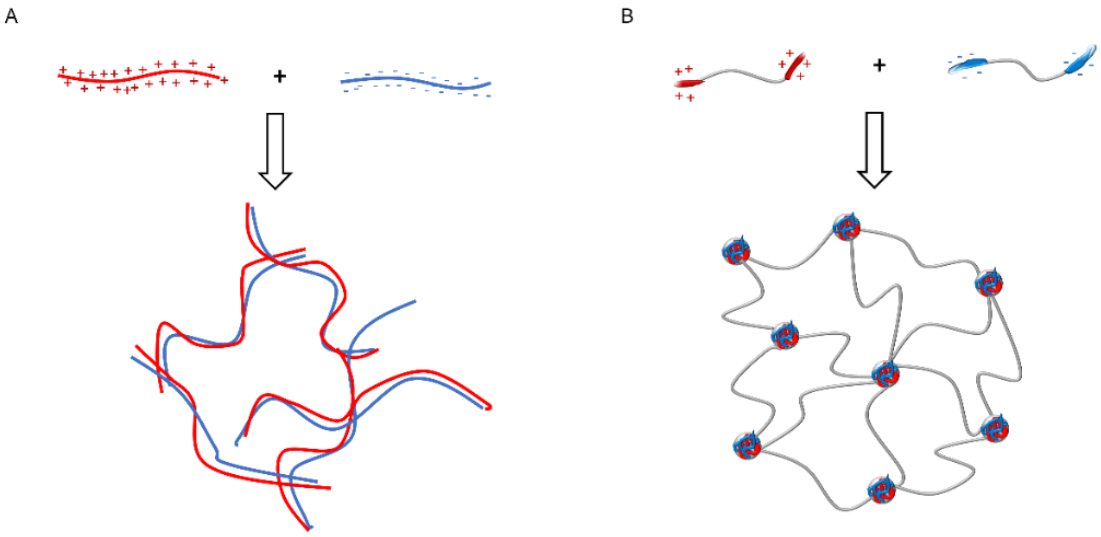

Figure 1-1. Representative schematics diagram of PEC hydrogels formed by (A) homogenous polyelectrolytes and (B) block polyelectrolytes.

PEC hydrogels formed by homo-polyelectrolytes have been used in many applications, such as drug delivery[32, 39, 40] and cell scaffolds for tissue engineering[41, 42]. One representative type of example is chitosan-based PEC hydrogels. Chitosan, derived from chitin, is a linear positively charged polysaccharide. Chitosan is one of the most popular natural-derived polyelectrolytes used in PEC hydrogels because of its low toxicity, high biocompatibility, biodegradability, and cheap material cost.[32] Chitosan has been employed to combine with negatively charged polyelectrolytes (e.g., alginate, hyaluronic acid, and sodium hyaluronate) to form PEC hydrogels. For instance, chitosan and hyaluronic acid can not only form hydrogels but also nanoparticles, sponges, film, and microspheres under different conditions.[38] Owing to their simple molecular structures, chitosan/hyaluronic acid PEC hydrogels have been used as a representative system to investigate the properties of PEC hydrogels influenced by different parameters, such as pH, ionic strength, charge density, polymer chain length, salt concentration, and charge ratio.[38]

In comparison to homo-PEs, when block-PEs form PEC hydrogels, the resulting hydrogels not only can avoid precipitation but also acquire nanoscale microstructure. One representative example is the PEC hydrogels formed by oppositely charged guanidinium (cationic) and sulfonate (anionic) functionalized poly(allyl glycidyl ether)$_n$-poly(ethylene oxide)$_m$- poly(allyl glycidyl ether)$_n$ (PAGE$_n$-PEO$_m$-PAGE$_n$) *ABA* triblock PEs, reported by Hunt *et al*.[24] Upon mixing, cationic and anionic *A*-block attract each other and form polyelectrolyte complex (PEC) domains, which are connected by the neutral PEO blocks and then establish three-dimensional electrostatically crosslinked networks, also known as PEC networks (Figure 1-1B). It is important to emphasize that, in this example, both cationic and anionic PEs are derived from the same unfunctionalized polymers via thiol-ene click reactions. Thus, both cationic and anionic PEs contain end *A*-block and middle *B*-block of exactly the same length, which provide precise stoichiometry and ensure

charge balance during hydrogel preparation.[24] These PEC hydrogels feature self-assembly, versatile microstructures, tunable mechanical properties, and stimuli-responsiveness. In recent years, their physical properties,[25, 35, 36, 43] mechanical properties,[25, 35] kinetics,[44-48] and mechanisms[25, 36] have been well studied, providing a well-understood platform to further develop their applications.

Rapid self-assembly of PEC hydrogels, driven by electrostatic interaction, provides innovative and tunable platforms for biomedical applications, such as drug delivery. Self-assembly is a spontaneous process and thus does not require any additives (e.g., photoinitiators, crosslinkers, and catalysts). For instance, Hunt *et al*. mentioned that the high shear moduli of PEC hydrogels were established within a few seconds, suggesting that self-assembly takes a few seconds.[24] In addition, Wu *et al*. investigated the spatiotemporal formation of PEC micelles by time-resolved SAXS and found that the initial micellization took around 100 ms and it took several seconds to reach equilibrium, in agreement with the previous observation.[44] Self-assembly and electrostatic feature of PEC hydrogels have been investigated and applied to encapsulate charged therapeutic agents (e.g., drugs, proteins, nucleic acid), and then their stimuli-responsive characteristics are used to release the therapeutic agents based on experimental cues.

Most PEC hydrogels feature pH- and salt-responsiveness owing to electrostatic interaction between oppositely charged PEs. This electrostatic interaction has two requirements. First, both cationic and anionic PEs need to be charged, which requires the pH value between the pKa values of anionic and cationic PEs. For instance, the pKa values of guanidinium and sulfonate groups are around 13.6 and 1.7. Thus, the hydrogels are expected to be stable in the pH range of 1.7 and 13.6 to ensure that guanidinium and sulfonate groups carry positive and negative charges, respectively. In a saline environment, salt ions interact with the charged functional groups along the PE chains

to form “external pairs”. Thus, sufficient salt ions can lead to screening of electrostatic interactions between oppositely charged PE chains, which reduce phase separation and even lead to a transformation from gel to a solution. These salt-responsive characteristics of PEC material have been harnessed to release therapeutic agents in drug delivery applications.

Diverse microstructures and anisotropic arrangement make PEC hydrogels a competitive platform for contemporary hydrogels in biomedical applications. Conventional hydrogels feature isotropic and amorphous structures, which fail to match the anisotropic ordered structures of human tissues, such as skin and muscle.[20] The anisotropic and ordered structures of human tissues allow them to perform complicated and multifunctional biological functions.[20] Conventional hydrogels have achieved mechanical properties well matching with human tissues but the matching dynamics and microstructures remain challenges. The PEC hydrogels prepared by block-PEs can form disordered spheres, body center cubic spheres, hexagonally close-packed cylinders, and lamellar PEC domains based on polymer concentration and their corresponding end-block charged fraction.[35] The tunable microstructure of PEC hydrogels provides an ideal platform to investigate and develop hydrogels with hierarchical microstructures.

Despite many advantages of PEC hydrogels, a few drawbacks limit their applications. For instance, compared to covalent bonding, the ionic interaction of PEC networks only can contribute to low shear moduli (typically less than 20 kPa) and negligible tensile properties. Biomedical applications, such as tissue engineering, require hydrogels to possess similar mechanical properties. Thus, PEC hydrogels confront difficulty to match the high shear properties of human tissues (e.g., muscle ~ 10 kPa, skin ~ 50 kPa, cartilage and bone > 100 kPa)[37, 49-51]. Besides, the physical crosslinks result in uncontrollable swelling in an aqueous environment over long times. The coupling relationship between microstructure and shear moduli restricts their mechanical and microstructural tunability,

and the dynamics of PEC hydrogels still remain poorly understood, adding uncertainty to systematic approaches for their design. Addressing these drawbacks can significantly improve the understanding of PEC hydrogels and provide a detailed guideline for their fabrication for diverse applications.

In this dissertation, we address some of these limitations of PEC hydrogels by combining the PEC network in covalently crosslinked networks to create PEC/covalent interpenetrating network (IPN) hydrogels.

1.4 Interpenetrating Polymer Network (IPN) Hydrogels

IPN hydrogels, comprising at least two partially or entirely interlaced polymer networks, have emerged as attractive hydrogel materials owing to their superior mechanical properties and unlimited combinations from different polymers. The first idea of IPNs was published as a patent by Aylsworth in 1914.[52] Over the last hundred years, IPN hydrogels have been employed as an effective method to break through the limitations of mechanical properties of simple hydrogels and produce gels or hydrogels with desired properties[3, 53].

Based on polymer network structure, IPN hydrogels can be classified as IPNs and semi-IPNs. IPNs consist of two ideally juxtaposed networks, in which polymer chains between them interpenetrate, entangle, and interact with each other. These two polymers cannot be separated without breaking bonds. Semi-IPNs formed by two polymer chain structures: one polymer is linear or branched, and the other polymers form networks. Theoretically, the polymers be can separated from semi-IPNs without breaking bonds.[54] If the IPNs or semi-IPNs are prepared by a procedure in which the first network is formed followed by the second network, the hydrogels are referred to as sequential IPNs or sequential semi-IPNs, respectively.

Many IPNs comprising both covalently and physically crosslinked have been reported. The covalently crosslinked networks provide excellent mechanical strength but lack dynamic restructurability. Physically crosslinked networks exhibit weak mechanical strength but provide stimuli-responsive property.[54] The combination of these networks usually can produce the IPNs with strong mechanical strength and stimuli-responsiveness.

In this dissertation, we have focused on IPN hydrogels comprising interlaced electrostatic and covalent networks. Termed polyelectrolyte complex/covalent interpenetrating polymer network (PEC/covalent IPN) hydrogels, they feature strong shear and tensile properties, versatile microstructures, and environmental responsiveness, and controllable swelling. It is important to highlight that interpenetration between PEC and covalent networks contributes to the synergistic effects in mechanical properties, which are difficult to achieve by either of the two networks.

1.5 Outline of this Dissertation

This dissertation presents our investigation on the fundamental properties of PEC hydrogels and our studies to employ PEC networks to create polyelectrolyte complex/covalent interpenetrating polymer network (PEC/covalent IPN) hydrogels.

In Chapter 2, we introduce the PEC/covalent IPN hydrogels comprising interpenetrated PEC and covalent networks. The PEC networks were prepared by mixing oppositely charged *ABA* triblock polyelectrolytes. The covalent networks were formed by photocrosslinked 4-arm poly(ethylene glycol) acrylate. The interpenetrated networks and the entanglements between them served as additional crosslinks and contributed to synergistic effects in both shear and tensile properties, which were inaccessible by either individual network.

In Chapter 3, we discuss the influence of PEGDA molecular weight on the microstructure, shear properties, and tensile properties of PEC/PEGDA IPN hydrogels. The longer PEGDA chains induced disorder-order transition and microstructural transformation in the PEC networks and a larger reduction in the shear moduli before phtotocrosslinking. After phtotocrosslinking, the shorter PEGDA chains lead to the highest shear moduli enhancements in the PEC/PEGDA IPN hydrogels as the shorter PEGDA chains could form covalent networks with higher crosslinking densities.

In Chapter 4, we report on the compatibility of the PEC networks with different types of photocrosslinked covalent networks, which were formed from 4-arm poly(ethylene glycol) acrylate, poly(ethylene glycol) diacrylate (PEGDA), acrylamide (AAm), and gelatin methacryloyl (GelMA). These four photocrosslinkable precursors were selected owing to different molecular structures, polymer origins, molecular weights, and crosslinking mechanisms. We discovered that PEC networks could encapsulate precursors and act as protective scaffolds to prevent precursors from dilution and meanwhile enhance viscosity and shear strength for extrusion-based 3D bioprinting application, which is discussed in Chapter 5. After photocrosslinking, all these four kinds of PEC-IPN hydrogels exhibited synergistic effects in shear moduli and tensile properties and demonstrate high compatibility for photocrosslinkable hydrogels regardless of their different molecular structures, polymer origin, and crosslinking mechanisms.

In Chapter 6, we explore the correlations between the microstructure, the nanoscale structural relaxation dynamics, and the shear relaxation dynamics of PEC hydrogels, ascertained by small angle X-ray scattering, X-ray photon correlation spectroscopy, and rheology. The microstructure of PEC hydrogels can be easily tuned by adjusting the polymer concentration. We discovered a coupling between microstructure and nanoscale dynamics, wherein the presence of ordered

microstructures correlated with a slow relaxation mode which is expected to arise from the relaxation of the microcrystalline grains of ordered PEC domains, in conjunction with a fast relaxation associated with the thermal relaxation of the spherical disordered PEC domains. Moreover, we found that the structural relaxation timescales were in agreement with the stress relaxation timescale windows.

Our research work not only introduced the methodology to create PEC/covalent IPN hydrogels with multi-functionalities, responsiveness, and versatile microstructures but also performed a systematic investigation of their fundamental properties to provide references for future application-based studies, such as wet bioadhesives and 3D bioprinting inks. In the future, this work can be extended to incorporate a higher degree of biocompatibility and biodegradability of the block polyelectrolytes, which will significantly broaden biomedical applications of PEC-based hydrogels.

1.6 Reference

(1) Ullah, F.; Othman, M. B. H.; Javed, F.; Ahmad, Z.; Akil, H. M. Classification, Processing and Application of Hydrogels: A Review. *Materials Science and Engineering: C* **2015**, *57*, 414-433. DOI: 10.1016/j.msec.2015.07.053.

(2) Zustiak, S. P.; Leach, J. B. Hydrolytically Degradable Poly(Ethylene Glycol) Hydrogel Scaffolds with Tunable Degradation and Mechanical Properties. *Biomacromolecules* **2010**, *11* (5), 1348-1357. DOI: 10.1021/bm100137q.

(3) Shivashankar, M.; Mandal, B. K. A review on interpenetrating polymer network. *International Journal of Pharmacy and Pharmaceutical Sciences* **2012**, *4* (5), 1-7.

(4) Schmaljohann, D. Thermo-and pH-responsive polymers in drug delivery. *Advanced drug delivery reviews* **2006**, *58* (15), 1655-1670.

(5) Peppas, N. A.; Hilt, J. Z.; Khademhosseini, A.; Langer, R. Hydrogels in biology and medicine: from molecular principles to bionanotechnology. *Advanced materials* **2006**, *18* (11), 1345-1360.

(6) Nonoyama, T.; Gong, J. P. Double-network Hydrogel and its Potential Biomedical Application: A Review. *Proceedings of the Institution of Mechanical Engineers, Part H: Journal of Engineering in Medicine* **2015**, *229* (12), 853-863. DOI: 10.1177/0954411915606935.

(7) Koetting, M. C.; Peters, J. T.; Steichen, S. D.; Peppas, N. A. Stimulus-responsive hydrogels: Theory, modern advances, and applications. *Materials Science and Engineering: R: Reports* **2015**, *93*, 1-49.

(8) Klouda, L.; Mikos, A. G. Thermoresponsive hydrogels in biomedical applications. *European journal of pharmaceutics and biopharmaceutics* **2008**, *68* (1), 34-45.

(9) Guiseppi-Elie, A. Electroconductive hydrogels: synthesis, characterization and biomedical applications. *Biomaterials* **2010**, *31* (10), 2701-2716.

(10) Ferreira, N.; Ferreira, L.; Cardoso, V.; Boni, F.; Souza, A.; Gremião, M. Recent advances in smart hydrogels for biomedical applications: From self-assembly to functional approaches. *European Polymer Journal* **2018**, *99*, 117-133.

(11) Zhang, Y. S.; Khademhosseini, A. Advances in Engineering Hydrogels. *Science* **2017**, *356* (6337), eaaf3627. DOI: 10.1126/science.aaf3627.

(12) Yu, J.; Xu, X.; Yao, F.; Luo, Z.; Jin, L.; Xie, B.; Shi, S.; Ma, H.; Li, X.; Chen, H. In situ covalently cross-linked PEG hydrogel for ocular drug delivery applications. *International journal of pharmaceutics* **2014**, *470* (1-2), 151-157.

(13) Xu, J.; Liu, X.; Ren, X.; Gao, G. The role of chemical and physical crosslinking in different deformation stages of hybrid hydrogels. *European Polymer Journal* **2018**, *100*, 86-95.

(14) Webber, R. E.; Creton, C.; Brown, H. R.; Gong, J. P. Large strain hysteresis and mullins effect of tough double-network hydrogels. *Macromolecules* **2007**, *40* (8), 2919-2927.

(15) Sun, J.-Y.; Zhao, X.; Illeperuma, W. R.; Chaudhuri, O.; Oh, K. H.; Mooney, D. J.; Vlassak, J. J.; Suo, Z. Highly stretchable and tough hydrogels. *Nature* **2012**, *489* (7414), 133.

(16) Sun, T. L.; Kurokawa, T.; Kuroda, S.; Ihsan, A. B.; Akasaki, T.; Sato, K.; Haque, M. A.; Nakajima, T.; Gong, J. P. Physical Hydrogels Composed of Polyampholytes Demonstrate High Toughness and Viscoelasticity. *Nature Materials* **2013**, *12* (10), 932. DOI: 10.1038/nmat3713.

(17) Snehal Mohite , E. P. **2020**.

(18) Darnell, M.; Young, S.; Gu, L.; Shah, N.; Lippens, E.; Weaver, J.; Duda, G.; Mooney, D. Substrate stress‐relaxation regulates scaffold remodeling and bone formation in vivo. *Advanced healthcare materials* **2017**, *6* (1), 1601185.

(19) Dey, K.; Agnelli, S.; Sartore, L. Dynamic freedom: substrate stress relaxation stimulates cell responses. *Biomaterials science* **2019**, *7* (3), 836-842.

(20) Yue, Y.; Gong, J. P. Structure and unique functions of anisotropic hydrogels comprising uniaxially aligned lamellar bilayers. *Bulletin of the Chemical Society of Japan* **2021**.

(21) Buwalda, S. J.; Boere, K. W. M.; Dijkstra, P. J.; Feijen, J.; Vermonden, T.; Hennink, W. E. Hydrogels in a Historical Perspective: From Simple Networks to Smart Materials. *Journal of Controlled Release* **2014**, *190*, 254-273. DOI: 10.1016/j.jconrel.2014.03.052.

(22) Hu, W.; Wang, Z.; Xiao, Y.; Zhang, S.; Wang, J. Advances in crosslinking strategies of biomedical hydrogels. *Biomaterials science* **2019**, *7* (3), 843-855.

(23) Guvendiren, M.; Lu, H. D.; Burdick, J. A. Shear-thinning hydrogels for biomedical applications. *Soft matter* **2012**, *8* (2), 260-272.

(24) Hunt, J. N.; Feldman, K. E.; Lynd, N. A.; Deek, J.; Campos, L. M.; Spruell, J. M.; Hernandez, B. M.; Kramer, E. J.; Hawker, C. J. Tunable, High Modulus Hydrogels Driven by Ionic Coacervation. *Advanced Materials* **2011**, *23* (20), 2327-2331. DOI: 10.1002/adma.201004230.

(25) Krogstad, D. V.; Lynd, N. A.; Choi, S.-H.; Spruell, J. M.; Hawker, C. J.; Kramer, E. J.; Tirrell, M. V. Effects of Polymer and Salt Concentration on the Structure and Properties of Triblock Copolymer Coacervate Hydrogels. *Macromolecules* **2013**, *46* (4), 1512-1518. DOI: 10.1021/ma302299r.

(26) Akhtar, M. F.; Hanif, M.; Ranjha, N. M. Methods of synthesis of hydrogels… A review. *Saudi Pharmaceutical Journal* **2016**, *24* (5), 554-559.

(27) Dong, R.; Pang, Y.; Su, Y.; Zhu, X. Supramolecular hydrogels: synthesis, properties and their biomedical applications. *Biomaterials science* **2015**, *3* (7), 937-954.

(28) Aubert, S.; Bezagu, M.; Spivey, A. C.; Arseniyadis, S. Spatial and temporal control of chemical processes. *Nature Reviews Chemistry* **2019**, *3* (12), 706-722. DOI: 10.1038/s41570-019-0139-6.

(29) Li, Z.; Zhou, Y.; Li, T.; Zhang, J.; Tian, H. Stimuli‐responsive hydrogels: Fabrication and biomedical applications. *View* **2022**, *3* (2), 20200112.

(30) Haag, S. L.; Bernards, M. T. Polyampholyte hydrogels in biomedical applications. *Gels* **2017**, *3* (4), 41.

(31) Shi, R.; Sun, T. L.; Luo, F.; Nakajima, T.; Kurokawa, T.; Bin, Y. Z.; Rubinstein, M.; Gong, J. P. Elastic–Plastic Transformation of Polyelectrolyte Complex Hydrogels from Chitosan and Sodium Hyaluronate. *Macromolecules* **2018**, *51* (21), 8887-8898. DOI: 10.1021/acs.macromol.8b01658.

(32) Luo, Y.; Wang, Q. Recent development of chitosan-based polyelectrolyte complexes with natural polysaccharides for drug delivery. *International journal of biological macromolecules* **2014**, *64*, 353-367.

(33) Zhang, Z.; Zhang, R.; Chen, L.; Tong, Q.; McClements, D. J. Designing hydrogel particles for controlled or targeted release of lipophilic bioactive agents in the gastrointestinal tract. *European Polymer Journal* **2015**, *72*, 698-716.

(34) Ortony, J. H.; Choi, S.-H.; Spruell, J. M.; Hunt, J. N.; Lynd, N. A.; Krogstad, D. V.; Urban, V. S.; Hawker, C. J.; Kramer, E. J.; Han, S. Fluidity and water in nanoscale domains define coacervate hydrogels. *Chemical Science* **2014**, *5* (1), 58-67.

(35) Srivastava, S.; Levi, A. E.; Goldfeld, D. J.; Tirrell, M. V. Structure, Morphology, and Rheology of Polyelectrolyte Complex Hydrogels Formed by Self-Assembly of Oppositely Charged Triblock Polyelectrolytes. *Macromolecules* **2020**, *53* (14), 5763-5774. DOI: 10.1021/acs.macromol.0c00847.

(36) Srivastava, S.; Andreev, M.; Levi, A. E.; Goldfeld, D. J.; Mao, J.; Heller, W. T.; Prabhu, V. M.; de Pablo, J. J.; Tirrell, M. V. Gel Phase Formation in Dilute Triblock Copolyelectrolyte Complexes. *Nature Communications* **2017**, *8* (1), 14131. DOI: 10.1038/ncomms14131.

(37) Li, D. F.; Gockler, T.; Schepers, U.; Srivastava, S. Polyelectrolyte Complex-Covalent Interpenetrating Polymer Network Hydrogels. *Macromolecules* **2022**, *55* (11), 4481-4491. DOI: 10.1021/acs.macromol.2c00590.

(38) Kayitmazer, A.; Koksal, A.; Iyilik, E. K. Complex coacervation of hyaluronic acid and chitosan: effects of pH, ionic strength, charge density, chain length and the charge ratio. *Soft Matter* **2015**, *11* (44), 8605-8612.

(39) Lin, W.-C.; Yu, D.-G.; Yang, M.-C. pH-sensitive polyelectrolyte complex gel microspheres composed of chitosan/sodium tripolyphosphate/dextran sulfate: swelling kinetics and drug delivery properties. *Colloids and surfaces B: Biointerfaces* **2005**, *44* (2-3), 143-151.

(40) Hamman, J. H. Chitosan based polyelectrolyte complexes as potential carrier materials in drug delivery systems. *Marine drugs* **2010**, *8* (4), 1305-1322.

(41) Coimbra, P.; Alves, P.; Valente, T. A. M.; Santos, R.; Correia, I.; Ferreira, P. Sodium hyaluronate/chitosan polyelectrolyte complex scaffolds for dental pulp regeneration: synthesis and characterization. *International journal of biological macromolecules* **2011**, *49* (4), 573-579.

(42) Florczyk, S. J.; Kim, D. J.; Wood, D. L.; Zhang, M. Influence of processing parameters on pore structure of 3D porous chitosan–alginate polyelectrolyte complex scaffolds. *Journal of Biomedical Materials Research Part A* **2011**, *98* (4), 614-620.

(43) Krogstad, D. V.; Choi, S.-H.; Lynd, N. A.; Audus, D. J.; Perry, S. L.; Gopez, J. D.; Hawker, C. J.; Kramer, E. J.; Tirrell, M. V. Small Angle Neutron Scattering Study of Complex Coacervate

Micelles and Hydrogels Formed from Ionic Diblock and Triblock Copolymers. *The Journal of Physical Chemistry B* **2014**, *118* (45), 13011-13018. DOI: 10.1021/jp509175a.

(44) Wu, H.; Ting, J. M.; Yu, B.; Jackson, N. E.; Meng, S.; de Pablo, J. J.; Tirrell, M. V. Spatiotemporal Formation and Growth Kinetics of Polyelectrolyte Complex Micelles with Millisecond Resolution. *ACS Macro Letters* **2020**, *9* (11), 1674-1680. DOI: 10.1021/acsmacrolett.0c00543.

(45) Takahashi, R.; Narayanan, T.; Yusa, S.; Sato, T. Formation Kinetics of Polymer Vesicles from Spherical and Cylindrical Micelles Bearing the Polyelectrolyte Complex Core Studied by Time-Resolved USAXS and SAXS. *Macromolecules* **2022**, *55* (2), 684-695. DOI: 10.1021/acs.macromol.1c02210.

(46) Amann, M.; Diget, J. S.; Lyngsø, J.; Pedersen, J. S.; Narayanan, T.; Lund, R. Kinetic Pathways for Polyelectrolyte Coacervate Micelle Formation Revealed by Time-Resolved Synchrotron SAXS. *Macromolecules* **2019**, *52* (21), 8227-8237. DOI: 10.1021/acs.macromol.9b01072.

(47) Liu, X.; Haddou, M.; Grillo, I.; Mana, Z.; Chapel, J.-P.; Schatz, C. Early Stage Kinetics of Polyelectrolyte Complex Coacervation Monitored through Stopped-Flow Light Scattering. *Soft Matter* **2016**, *12* (44), 9030-9038. DOI: 10.1039/c6sm01979j.

(48) Krogstad, D. V.; Lynd, N. A.; Miyajima, D.; Gopez, J.; Hawker, C. J.; Kramer, E. J.; Tirrell, M. V. Structural Evolution of Polyelectrolyte Complex Core Micelles and Ordered-Phase Bulk Materials. *Macromolecules* **2014**, *47* (22), 8026-8032. DOI: 10.1021/ma5017852.

(49) Discher, D. E.; Mooney, D. J.; Zandstra, P. W. Growth Factors, Matrices, and Forces Combine and Control Stem Cells. *Science* **2009**, *324* (5935), 1673-1677. DOI: 10.1126/science.1171643.

(50) Engler, A. J.; Sen, S.; Sweeney, H. L.; Discher, D. E. Matrix Elasticity Directs Stem Cell Lineage Specification. *Cell* **2006**, *126* (4), 677-689. DOI: 10.1016/j.cell.2006.06.044.

(51) Discher, D. E.; Janmey, P.; Wang, Y.-l. Tissue Cells Feel and Respond to the Stiffness of Their Substrate. *Science* **2005**, *310* (5751), 1139-1143. DOI: 10.1126/science.1116995.

(52) Sperling, L. H. History of Interpenetrating Polymer Networks Starting with Bakelite-Based Compositions. In *100+ Years of Plastics. <break></break>Leo Baekeland and Beyond*, ACS Symposium Series, Vol. 1080; American Chemical Society, 2011; pp 69-82.

(53) Myung, D.; Waters, D.; Wiseman, M.; Duhamel, P. E.; Noolandi, J.; Ta, C. N.; Frank, C. W. Progress in the Development of Interpenetrating Polymer Network Hydrogels. *Polymers for Advanced Technologies* **2008**, *19* (6), 647-657. DOI: 10.1002/pat.1134.

(54) Dragan, E. S. Design and Applications of Interpenetrating Polymer Network Hydrogels. A Review. *Chemical Engineering Journal* **2014**, *243*, 572-590. DOI: 10.1016/j.cej.2014.01.065.

Chapter 2

Polyelectrolyte Complex-Covalent Interpenetrating Polymer Network Hydrogels

Reproduced from "Polyelectrolyte Complex-Covalent Interpenetrating Polymer Network Hydrogels." Defu Li; Tobias Göckler; Ute Schepers; Samanvaya Srivastava. *Macromolecules* **2022**, *55* (11), 4481-4491

ABSTRACT

Polyelectrolyte complex (PEC) hydrogels possess a rich microstructural diversity and tunability of shear response, self-healing attributes, and pH- and salt-responsiveness. Yet, their utility in biotechnology and biomedicine has been limited, owing to their weak mechanical strength and uncontrolled swelling. Here, we introduce a strategy to overcome these drawbacks of PEC hydrogels by interlacing the electrostatically crosslinked PEC network with a covalently crosslinked polymer network, creating polyelectrolyte complex-covalent interpenetrating polymer network (PEC-IPN) hydrogels. Structural and material characterizations of model PEC-IPN hydrogels composed of oppositely charged *ABA* triblock copolymers and photocrosslinkable 4-arm poly(ethylene oxide) (PEO) highlight the key advantages of our approach. Upon initial mixing of the three constituents, the PEC network self-assembles swiftly in aqueous environs, providing structural rigidity and serving as protective scaffoldings for the covalently crosslinkable PEO precursors. Photocrosslinking of the PEO chains creates a covalent network, providing structural reinforcement to the PEC network. The resulting PEC-IPN hydrogels possess significantly improved shear and tensile strengths, swelling characteristics, and mechanical stability in saline

environments while preserving the intrinsic mesoscale structure of the PEC network and its salt-responsiveness. We envision that our approach to fabricating PEC-based IPN hydrogels will pave the way for the creation of self-assembled hybrid materials that harness the unique attributes of electrostatic self-assembly pathways, with broad applications in biomedicine.

2.1 Introduction

Polyelectrolyte complex (PEC) hydrogels[1-12] present an exciting platform for development of soft materials to cater to diverse applications in biomedicine[13, 14] as scaffolds for tissue engineering,[15-18] bioadhesives,[19-26] and drug delivery,[27-31] as well as ionic conductors[32, 33] and in food industries.[34, 35] These hydrogels self-assemble rapidly[1, 9] upon mixing of oppositely charged block polyelectrolytes and exhibit hierarchical microstructures,[4, 5, 36-39] comprising three-dimensional networks of PEC domains (composed of the oppositely charged blocks) connected to each other via the neutral blocks. This microstructure differentiates PEC hydrogels from ionically crosslinked hydrogels[40-47] (typically composed of homopolyelectrolytes) and contribute to their unique combination of attributes, including tunable shear properties,[2, 4-6, 9, 12, 48] stimuli (salt- and pH-) responsiveness,[1, 2, 4, 8, 9, 48] injectability,[12, 49] self-healing properties,[12, 49] and the ability to encapsulate charged macromolecules such as proteins and nucleic acids.[50-54]

Yet, broad applications of PEC hydrogels remain limited owing to their physical crosslinked structure contributing to low shear strength (typically less than 20 kPa), miniscule tensile strength, and an inherent coupling between the network microstructure and its shear response.[5] In contrast, applications such as tissue adhesion typically require hydrogel sealants to mimic shear properties of the tissue substrates (e.g., ~1 kPa for soft tissue, ~10 kPa for muscle, ~50 kPa for skin, > 100 kPa for cartilage and bone).[55-57] At the same time, PEC hydrogels swell indefinitely and eventually dissolve upon exposure to aqueous media, indicating degradation of hydrogel structure.[3, 58] Limited and tunable swelling can avoid material loss, preserve stability of structure and mechanical properties, and maintain the functions of PEC hydrogels which can broaden their utility. However, effective measures for controlling swelling of PEC hydrogels remain elusive.

Here, we introduce a strategy to address these shortcomings of PEC hydrogels while retaining their unique attributes by interlacing the PEC network with a covalent network. Interpenetration of polymer networks has been employed to imbue properties like toughness and stimuli-responsiveness in hydrogels.[59-64] In this work, we demonstrate synergic improvements in the material properties of PEC-covalent interpenetrating polymer network (IPN) hydrogels which are not accessible in hydrogels composed of either of the two networks, including substantial improvements in mechanical strength, toughness, and swelling performance while conserving the microstructure of the PEC network. Moreover, our approach offers a strategy to expand the utility of photocrosslinkable hydrogels by enabling *in situ* crosslinking of the photocrosslinkable precursor polymers. The self-assembled PEC hydrogels provide a protective environment for the photocrosslinkable precursors, mitigating dilution and deactivation prior to their crosslinking. We envision that the PEC-covalent IPN platform demonstrated here will constitute the first steps towards implementation of PEC-based IPN hydrogels in future biomedical applications.

2.2 Materials and Methods

Materials: Potassium (99.5% trace metals basis), naphthalene, poly(ethylene glycol) (M_n = 20,000 Da), 2,2-dimethoxy-2-phenylacetophenone, allyl glycidyl ether (AGE), calcium hydride, sodium 3-mercapto-1-propanesulfonate, technical grade (90%), 1H-pyrazole-1-carboxamidine hydrochloride (99%), cysteamine hydrochloride (≥ 98%), and Irgacure 2959 were obtained from Millipore Sigma. Tetrahydrofuran (THF) and dimethylformamide (DMF) were obtained from Fisher Scientific. 4-arm poly(ethylene oxide) acrylate (PEO, M_n = 20,000 Da, ≥ 95%) was obtained from JenKem Technology.

Block Polyelectrolyte Synthesis: Guanidinium, ammonium, and sulfonate functionalized poly(ally glycidyl ether)-*b*-poly(ethylene glycol)-*b*-poly(ally glycidyl ether) were synthesized following

previously published protocols.[1] Briefly, AGE was purified by stirring with calcium hydride overnight and then processed by three freeze-pump-thaw cycles and distillation. Poly(ethylene glycol) (M_n = 20,000 Da) was dissolved in anhydrous THF and titrated with potassium naphthalenide (0.4 M in anhydrous THF) until the solution acquired a light green color. AGE was added into the reaction mixture and stirred at 45 °C for 48 h. The polymerization reaction was terminated by addition of degassed methanol, and the final product poly(allyl glycidyl ether)-poly(ethylene glycol)-poly(allyl glycidyl ether) (PAGE-PEO-PAGE) was precipitated in hexane and filtered, followed by drying prior to further functionalization. The product was characterized by proton nuclear magnetic resonance (^{1}H NMR, 400 MHz), as shown in **Figure 2-S1**. The degree of polymerization of the PAGE blocks was calculated from the relative heights of peaks in the NMR spectra and was determined to be $PAGE_{98}$-PEO_{455}-$PAGE_{98}$.

The thiol-ene reactions were carried out by dissolving 2 g $PAGE_{98}$-PEO_{455}-$PAGE_{98}$ polymer and a functional thiol (5 equiv. per alkene) in a 30 mL DMF/water mixture with 1:1 volume ratio in a 100 mL round bottom flask. Cysteamine hydrochloride and sodium 3-mercapto-1-propanesulfonate were used to functionalize the block polymers with ammonium and sulfonate groups, respectively. After addition of the photoinitiator (2,2-dimethoxy-2-phenylacetophenone, 0.05 equiv. per alkene), the solution was irradiated with UV light (365 nm) for 6 hours under nitrogen atmosphere. Then, the final product solution was dialyzed against deionized water for 10 cycles of 8 hour each. The final ammonium or sulfonate functionalized polymers were obtained by lyophilization.[1, 5]

Guanidinium functionalized polymer was synthesized by dissolving ~ 2 g of ammonium functionalized $PAGE_{98}$-PEO_{455}-$PAGE_{98}$ in 200 mL phosphate-buffered saline (PBS) solution along with 1H-pyrazole-1-carboxamidine (4 equivalent per alkene). The pH of the solution was

adjusted to 10 by using 10 M NaOH solution. The reaction mixture was stirred for 3 days, followed by dialysis against deionized water for 10 cycles of 8 hours each. The final guanidinium functionalized polymers were obtained by lyophilization. All functionalized products were characterized by ^{1}H NMR (400 MHz) (**Figure 2-S1**).[1, 5]

Preparation of PEC, PEC+PEO, and PEC-IPN Hydrogels: 50 wt% stock solutions of the cationic and anionic block polyelectrolytes were prepared by mixing, for example, 500 mg of the polymers with 1 mL of deionized water. PEC hydrogels were prepared by the protocol: an appropriate amount of block polycation stock solution was mixed with deionized water. Then, an appropriate amount of the block polyanion stock solution was added to the solution. The polymers were mixed in proportions such that the molar charge ratio of cationic and anionic groups was 1:1.

PEC+PEO hydrogels were prepared by mixing the block polycation stock solution with an aqueous solution of PEO and photoinitiator Irgacure 2959. Subsequently, the block polyanion stock solution was added. Each addition step was followed by vortex mixing to homogenize the mixtures. The polymers were mixed in proportions such that the molar charge ratio of cationic and anionic groups was 1:1.

PEC-IPN hydrogels were prepared by exposing PEC+PEO hydrogels to UV radiation (302 nm, 8 W) for 5 minutes. The hydrogels were subjected to further characterization as is, without further purification or removal of unreacted PEO chains.

Small-angle X-ray scattering (SAXS) Measurement: Small-angle X-ray scattering measurements were performed at beamline 12-ID-B at the Advanced Photon Source, Argonne National Laboratory with 13 keV X-rays. The sample-to-detector distance was set at 4 meters, corresponding to a wave vector (q) range of 0.0002 Å^{-1} to 0.5 Å^{-1}. PEC and PEC+PEO hydrogels were loaded into holes (3 mm diameter) in 4 mm thick aluminum strips using a positive

displacement pipette and sealed on both side with Kapton tape to avoid water evaporation. PEC-IPN hydrogels were prepared by loading PEC+PEO hydrogels in the aluminum strips and followed by 5 minutes UV light exposure and then sealed by Kapton tape. All the samples were prepared and loaded onto the sample holders at least 24 hours before the SAXS measurements. All experiments were performed at room temperature. The X-ray exposure time was set at 0.1 second. The two-dimensional scattering data were converted into one-dimensional data (I_{sample}) by using the matSAXS package. Sample scattering intensity was acquired by subtracting the appropriately scaled background (solvent) scattering intensity ($I_{solvent}$) from the measured scattering intensity, $I(q) = I_{sample} - \alpha I_{solvent}$, with α being the scaling parameter.[5] $P(q)$ and $S(q)$ fits to the $I(q)$ data were carried out using the Irena package[65] in Igor Pro.

Rheological Measurements: Oscillatory rheological measurements were performed on an Anton Paar MCR 302 rheometer using a parallel plate (diameter: 8 mm, gap size: 0.7 mm) fixture for PEC-IPN hydrogels and a cone and plate (diameter: 10 mm, cone angle: 2°) fixture for PEC and PEC+PEO hydrogels. An appropriate amount of PEC or PEC+PEO hydrogel samples was placed on the lower plate, and excess sample volume was trimmed after reaching the appropriate gap between the cone and the plate. PEC-IPN hydrogel samples were prepared by pipetting 70 μL of PEC+PEO hydrogels into a cylindrical polydimethylsiloxane (PDMS) mold (diameter: 8 mm, height: 1.5 mm) and irradiating the hydrogels with UV radiation for 5 minutes. The crosslinked hydrogel samples thus obtained were placed between the parallel plates of the rheometer fixture. The hydrogels samples were subjected to small-amplitude oscillatory strain ($\omega = 1$ Hz, $\gamma = 0.3\%$) for an extended period (1800 s) to equilibrate the samples. Amplitude sweeps, with strain amplitude γ ranging from 0.01 - 100% (**Figure 2-S2**) were carried out at frequency $\omega = 1$ rad/s to assess the linear viscoelastic (LVE) regime. Frequency sweeps ($\omega =$ 0.01-100 Hz) were

performed at $\gamma = 0.3\%$, staying within the LVE regime. A solvent trap was employed to minimize water evaporation. All rheology data were acquired at 25 °C.

*Tensile Tests***:** All tensile measurements were conducted on an Instron 5542 mechanical tester. PEO and PEC-IPN hydrogels were prepared by pipetting 80 microliters of the precursor solution into a rectangular PDMS mold (12 mm × 5 mm × 1.5 mm) and exposed to UV radiation for photocrosslinking. The crosslinked hydrogels were affixed to the machine tension grips with double-sided tape. The extension rate was set to 1 mm/min, and the stress-strain data were continuously collected until the fracture of samples. The tensile properties were estimated by averaging data obtained from at least 3 hydrogel samples.

*Swelling Ratio***:** PEO and PEC-IPN hydrogel samples were prepared by pipetting 60 microliter of precursor solution (PEO solution or PEC+PEO hydrogels) into a cylindrical PDMS mold (diameter: 5 mm, height: 3 mm) and irradiating with UV radiation for 5 minutes. After UV exposure, the hydrogel samples were transferred into a 24-well culture plate filled with deionized water. After 0, 1, 4, 9, 24, and 48 h, the hydrogel samples were weighed after carefully removing residual water from the surface. The swelling ratio of hydrogels was calculated as

$$Swelling\ Ratio = \frac{m_t}{m_0} \times 100\%$$

Here m_t is the weight of the hydrogel at time t (hour), m_0 is the initial weight. The swelling ratio was calculated by averaging the data of at least 3 samples.

2.3 Results and Discussion

2.3.1 Self-Assembled PEC Networks as Protective Scaffoldings for Covalent Crosslinkable Polymers

PEC hydrogels self-assemble swiftly ($\lesssim 500$ ms)[66-69] upon mixing of aqueous solutions of oppositely charged block polyelectrolytes (bPEs) based on poly(ally glycidyl ether)$_{98}$-poly(ethylene oxide)$_{455}$-poly(ally glycidyl ether)$_{98}$ (PAGE-PEO-PAGE). The PAGE blocks were functionalized with ionic (guanidinium and sulfonate) moieties[1] (**Figure 2-1A**, row 1). These hydrogels are injectable and remain insoluble in water, even upon shaking, over a few minutes (**Figure 2-1B**, row 1, see also **Supplementary Movie 2-SM1**).

Introduction of hydrophilic chemically crosslinkable 4-arm poly(ethylene oxide)$_{455}$ acrylate (PEO) did not impede with the PEC gel formation, resulting in injectable PEC+PEO hydrogels (**Figure 2-1A**, row 3). The electrostatically self-assembled PEC networks provide structural stability and insolubility in aqueous environments to the PEC+PEO hydrogels (**Figure 2-1B**, row 3, see also **Supplementary Movie 2-SM2**). Moreover, the PEC networks serve as scaffoldings to protect the PEO precursors against uncontrolled dilution (**Figure** 2-**1B**, row 3). Ultraviolet (UV) irradiation of the PEC+PEO hydrogels for 5 minutes resulted in the formation of polyelectrolyte complex-interpenetrating polymer networks (PEC-IPN) hydrogels composed of water-laden interlaced PEC and chemically crosslinked PEO networks (**Figure 2-1A**, row 3). In stark contrast, exposure of the solution of crosslinkable polymer precursors to aqueous environments prior to UV-induced crosslinking resulted in rapid dilution of the precursors, limiting their ability to form chemically crosslinked hydrogels (**Figures 2-1A and 2-1B**, row 2, see also **Supplementary Movie 2-SM3**).

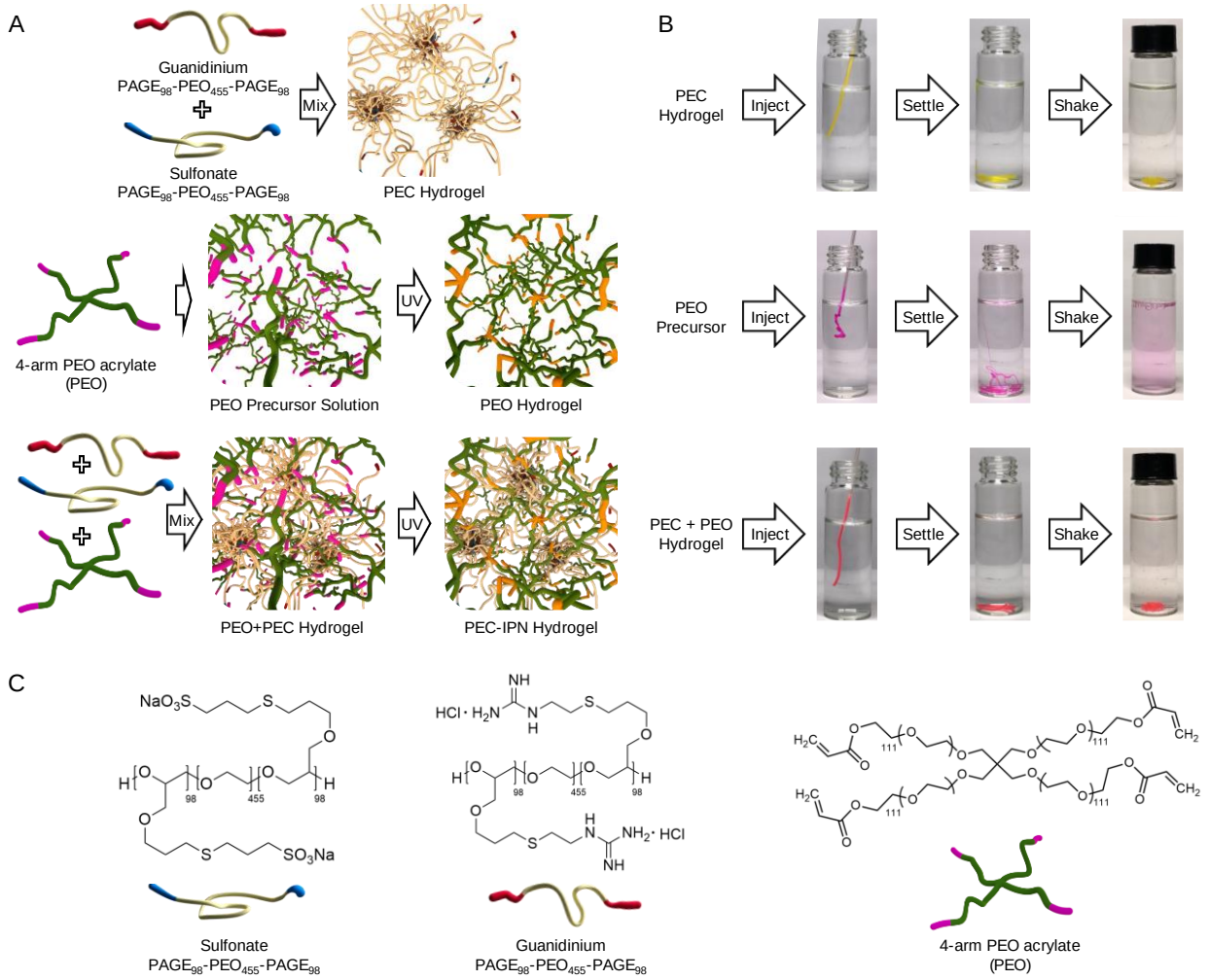

Figure 2-1. Schematic depiction of PEC, PEC+PEO and PEC-IPN hydrogels. **(A)** Schematics representing PEC (*row 1*), PEO (*row 2*), and PEC+PEO and PEC-IPN hydrogels (*row 3*). **(B)** Photographs demonstrating injectability and insolubility of PEC (*row 1*) and PEC+PEO (*row 3*) hydrogels in water. In contrast, the PEO precursor (*row 2*) dissolves in water readily. Dyes (Acid Yellow 73, Rhodamine B, and a combination of Acid Yellow 73 and Rhodamine B in rows 1, 2, and 3, respectively) were added in the hydrogels to aid visualization. (**C**) The chemical structures of the block polyelectrolytes and the 4-arm PEO acrylate.

2.3.2 Structural Resilience of PEC Domains Against Inclusion of Polymers and Covalent Networks

Small angle X-ray scattering (SAXS) reveal the structural attributes of the PEC network comprising PEC domains interlinked with the neutral blocks of the bPEs. The PEC domains are composed of the charged blocks of the bPEs possess higher polymer concentration than the surroundings and include higher atomic number elements including nitrogen and sulfur, providing sufficient electron density contrast.[1, 4, 5] **Figure 2-2A** shows representative one-dimensional SAXS intensity $I(q)$ as a function of wave vector q obtained from PEC hydrogels with increasing bPE concentrations (C_{bPE}, grey traces, see also **Figure 2-S3A**). These SAXS spectra exhibit a broad primary peak near q = 0.02 Å^{-1} followed by secondary peaks at higher q values. The primary and the secondary peaks became more prominent with increasing C_{bPE}, indicating strengthening spatial correlations among the PEC domains. Yet, an absence of Bragg reflection peaks denote that the PEC domains remained in a disordered arrangement even in PEC hydrogels with C_{bPE} = 40 wt%.[1, 4, 5]

Modeling $I(q)$ as a combination of a form factor $P(q)$ for polydisperse spheres and a hard sphere structure factor $S(q)$ as $I(q) \sim P(q)S(q)$, as shown in **Figure 2-S4**, enabled estimation of the domain radius (R_{PEC}) and the characteristic inter-domain distance (d_{PEC}).[70, 71] The position of the primary $S(q)$ peak, q^*, represents the inverse inter-domain distance d_{PEC} as $d_{PEC} \sim 2\pi/q^*$.[70] R_{PEC} and d_{PEC} for the PEC hydrogels are shown in **Figure 2-2C** with grey symbols. Consistent with previous observations[5] that PEC domain size depends on the length of the charged block only while inter-domain correlation and distances are dictated by lengths of both the charged and the neutral blocks as well as C_{bPE}, R_{PEC} was found to be independent of C_{bPE} while d_{PEC} decreased progressively with increasing C_{bPE}.

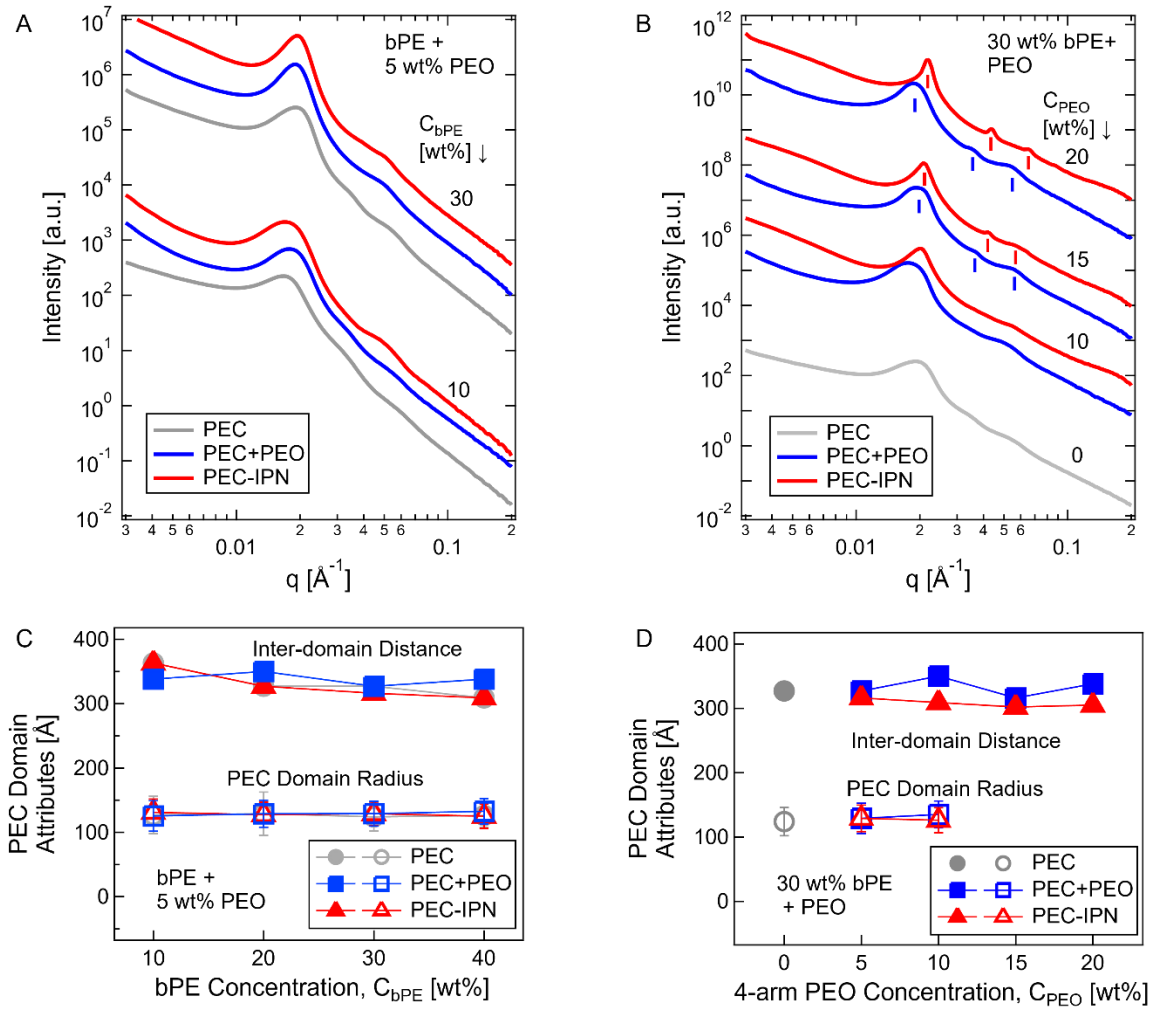

Figure 2-2.Representative SAXS scattering spectra and PEC domain attributes in PEC, PEC+PEO, and PEC-IPN hydrogels. **(A)** One-dimensional scattering intensity $I(q)$ as a function of wave vector q for PEC (grey), PEC+PEO (blue), and PEC-IPN (red) hydrogels with varying C_{bPE} from 10 wt% to 30 wt%. PEC+PEO, and PEC-IPN hydrogels also contained a constant C_{PEO} (= 5 wt%). **(B)** $I(q)$ spectra for PEC hydrogels with $C_{bPE} = 30$ wt%, and PEC+PEO, and PEC-IPN hydrogels with varying C_{PEO} (between 10 and 20 wt%) and constant $C_{bPE} = 30$ wt%. In the SAXS spectra for PEC+PEO, and PEC-IPN hydrogels with $C_{PEO} = 15$ wt% and 20 wt%, the small vertical bars indicate the positions of the Bragg scattering peaks. The secondary and the tertiary peaks appear at $2q^*$ and $3q^*$ with respect to the primary peak at q^*, denoting lamellar microstructure of the PEC domains. In both (A) and (B), $I(q)$ spectra are shifted vertically for clarity. **(C, D)** Inter-domain

distance (d_{PEC}) and domain radius (R_{PEC}) as a function of C_{bPE} (C) and C_{PEO} (D) for PEC, PEC+PEO, and PEC-IPN hydrogels. In (C), $C_{PEO} = 5$ wt% while in (D), $C_{bPE} = 30$ wt%. The filled and open symbols referred to inter-domain distance and PEC domain radius, respectively. See Supplementary Information Table S1 for peak assignments in (B).

Scattering from the PEC network persisted upon the inclusion of polymeric additives (PEO) and their subsequent crosslinking. **Figure 2-2A** highlights the similarity of the $I(q)$ spectra obtained from PEC hydrogels (grey traces) with PEC+PEO and PEC-IPN hydrogels containing 5 wt% PEO content (C_{PEO}), depicted by blue and red traces, respectively (see also **Figure 2-S3A and 2-S3B**). Correspondingly, both R_{PEC} and d_{PEC} for PEC hydrogels (grey symbols), PEC+PEO hydrogels (blue symbols) and PEC-IPN hydrogels (red symbols) evolved near identically with increasing C_{bPE} (**Figure 2-2C**).

Tuning the PEO content in the PEC+PEO or the PEC-IPN hydrogels enabled modulation of the PEC network nanostructure. Morphological transition and ordering of the PEC domains, signified by the appearance of sharp Bragg reflection peaks in the SAXS spectra in **Figure 2-2B** accompanied with a subtle decrease of d_{PEC} (**Figure 2-2D**) were observed with increasing C_{PEO} in both PEC+PEO and PEC-IPN hydrogels comprising C_{bPE} = 30 wt%. The relative positions of the primary (q_1), secondary (q_2) and tertiary (q_3) Bragg peaks as $q_1 : q_2 : q_3 \cong 1 : 2 : 3$ denote the presence of parallelly stacked lamellar PEC domains in the PEC network with $C_{PEO} \geq 15$ wt%.

Such morphological and ordering transitions, as well as reduction in domain spacing have been previously observed in PEC hydrogels with increasing bPE concentration[1, 4, 5, 37] and have been hypothesized to arise from the compression of the neutral middle blocks beyond their equilibrium conformations.[5] Here, we expect macromolecular crowding by the 4-arm PEO chains or the covalent network to result in compression and loss of conformational entropy of the PEO midblocks, which in turn induces morphological and ordering transitions in PEC domains. It should be noted that the SAXS spectra shown here are representative of the nearly identical spectra obtained from multiple spots in each of the hydrogel samples, denoting the spatial homogeneity of the hydrogels. Moreover, we note that the PEC domains contain substantial amounts of water,[8, 37]

and hence morphological transitions in PEC networks can be induced even in assemblies comprising asymmetric bPE, as opposed to amphiphilic block copolymer assemblies wherein lamellar morphologies are expected in polymers with symmetric blocks.

PEC networks comprising weaker ammonium groups instead of strong guanidinium groups in the block polycations exhibit similar behaviors. Guanidinium groups have a higher degree of protonation due to their high pKa value (~ 13.6) compared to the ammonium groups (pKa ~ 9.25), owing to a combination of proton delocalization assisted by resonance stabilization and two binding sites on adjacent nitrogen atoms. The stability of the ionized state of the ionizable groups contributes to the strength of the electrostatic interaction between the oppositely charged blocks and the network properties. Thus, weaker electrostatic interactions between ammonium and sulfonate groups resulted in larger PEC domains and faster equilibration of the PEC network. The resulting PEC hydrogels contained ordered PEC domains at $C_{bPE} \geq 30$ wt%. Addition of 5 wt% PEO did not disrupt either the disordered or the ordered PEC networks (**Figures 2-S5A and 2-S6**). Both disordered and ordered PEC networks, although, required smaller C_{PEO} to undergo ordering and morphological transition in PEC+PEO and PEC-IPN hydrogels (**Figure 2-S5B**). Notwithstanding, the trends in d_{PEC} and R_{PEC} with varying C_{bPE} and C_{PEO} (**Figures 2-S5C and 2-S5D**) remained consistent with the trends shown in Figure 2.

2.3.3 Modulation of Shear Properties of PEC Hydrogels by Polymer Diluents and Interpenetrating Covalent Networks

PEC hydrogels exhibited frequency-independent storage and loss moduli (G' and G'', respectively) with $G' > G''$, for $C_{bPE} \geq 10$ wt%, indicating solid-like gels with an absence of terminal relaxation within the time of experiments (grey symbols in **Figures 2-3A-C**).[4, 5] With increasing C_{bPE}, G' and G'' both increased before G' plateauing around 10 kPa, typical for PEC hydrogels (**Figure 2-**

3D).[4, 5] Inclusion of PEO chains in the PEC hydrogels led to a decrease of both G' and G'' while conserving their frequency-independent behavior (blue symbols in **Figures 2-3A-C**). Subsequent crosslinking of the PEO chains led to a marked increase in the shear moduli of the resulting PEC-IPN hydrogels, even higher than the corresponding moduli for PEC hydrogels (red symbols in **Figures 2-3A-C**).

Figure 2-3F summarizes the evolution of shear response of PEC-IPN hydrogels with increasing C_{bPE} for a constant C_{PEO}. The influence of the covalent network on the shear moduli of PEC-IPN hydrogels was more pronounced when the covalent network served as the primary load-bearing network. When the shear moduli of PEC hydrogels with $C_{bPE} \leq 20$ wt% (**Figure 2-3D**) were smaller than of the 5 wt% covalent hydrogels (**Figure 2-3E** and **Figure 2-S7**), the corresponding PEC-IPN hydrogels exhibited more than two-fold improvements in both G' and G'' as compared to the PEC hydrogels (**Figures 2-3D and 2-3F**, see also **Figures 2-3A and 2-3B**). In contrast, only modest enhancements in moduli were achieved in PEC-IPN hydrogels with $C_{bPE} > 20$ wt%. At high bPE concentrations, loop formation as well as hindrance of the photocrosslinking of the PEO chains by the PEC network can reduce the shear moduli contributions from the PEO network to the IPN hydrogels. Importantly, since the moduli of the covalent PEO network is directly proportional to the C_{PEO} (**Figure 2-3E**), PEO content in the PEC-IPN hydrogels can be harnessed as a facile route to tune their moduli. As an illustration, steady improvements in G' and G'' of PEC-IPN hydrogels with $C_{bPE} = 30$ wt% were observed upon increasing C_{PEO} (**Figure 2-3C, 2-3D, 2-3G**, see also **Figure 2-S8**).

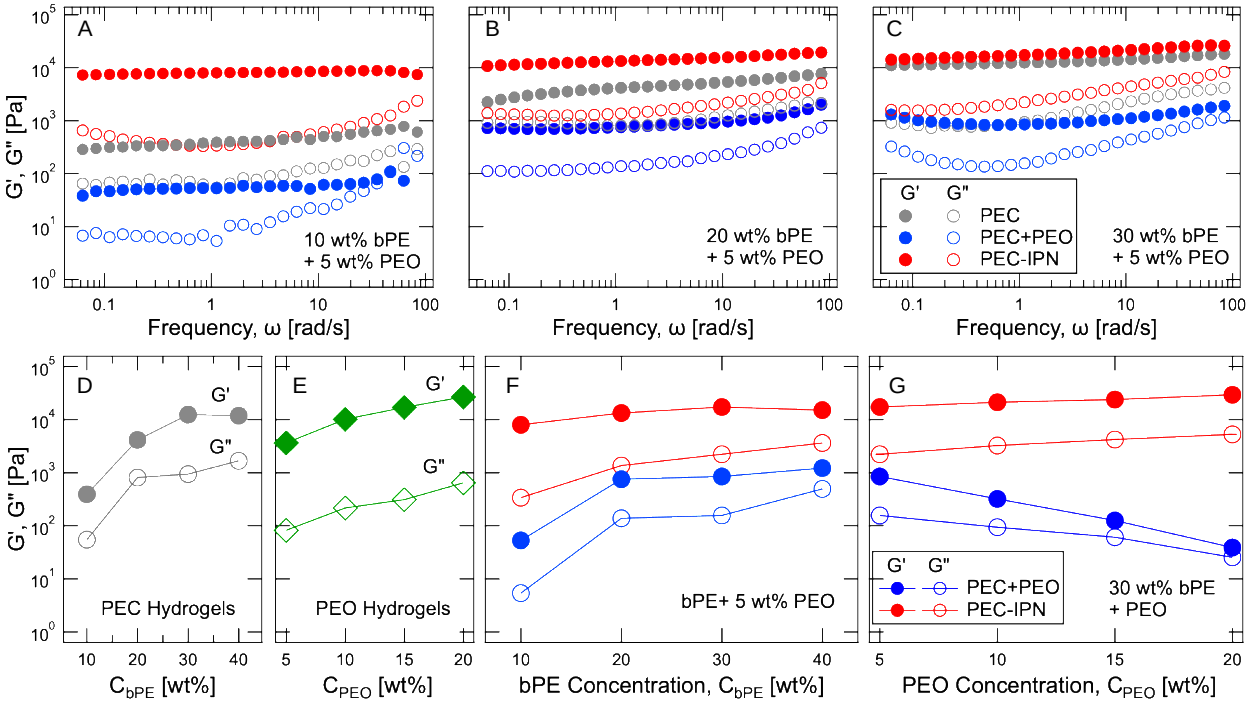

Figure 2-3. Modulations of shear strength of PEC+PEO and PEC-IPN hydrogels. **(A-C)** Storage (G') and loss (G'') moduli as a function of frequency (ω), measured by imposing oscillatory strain (strain amplitude γ = 0.3%) on PEC hydrogels (grey), PEC+PEO hydrogels (blue), and PEC-IPN hydrogels (red) with varying C_{bPE} and a constant C_{PEO}. **(D-G)** G' and G'' (at $\omega = 1.12$ rad/s and γ = 0.3%) for PEC hydrogels with increasing C_{bPE} (D), PEO hydrogels with increasing C_{PEO} (E); and PEC+PEO hydrogels (blue) and PEC-IPN hydrogels (red) with increasing C_{bPE} and constant $C_{PEO} = 5$ wt% (F) and with increasing C_{PEO} and constant $C_{bPE} = 30$ wt% (G).

These moduli enhancements serve as an indicator of the interpenetrating nature of the PEC and the covalent networks and their synergistic contribution to shear strength of the resulting hybrid hydrogel. Interlacing of the two networks is hypothesized to introduce further entanglements between them, in effect acting as additional crosslinks, leading to higher moduli of the IPN hydrogels as compared to hydrogels comprising either of the components. The synergy between the two networks is further illustrated through a comparison of the moduli of the PEC-IPN hydrogels with the sum of the moduli of the constituent networks (**Figure 2-S9**). Both G' and G" for the PEC-IPN hydrogels were found to be larger than the linear combination of the respective moduli of the constituent networks in most cases, except for the PEC-IPN hydrogels with high C_{bPE} (= 30 wt%) and C_{PEO} (> 15 wt%). In these hydrogels, the high polymer concentration can be expected to hinder the crosslinking of the PEO network, resulting in loop formation or unreacted PEO ends, or both. Overall, PEC-IPN hydrogels exhibit superior shear strength which either PEC hydrogels or covalent hydrogels cannot achieve either individually, or, in most cases, in a linear combination with each other.

In contrast, PEC+PEO hydrogels exhibit a marked decrease in shear strength as compared to the PEC hydrogels (blue symbols in **Figures 2-3A-C and 2-3F**). Increasing PEO content in PEC+PEO hydrogels led to continuing reduction of G' and G'' (**Figure 2-3G**). We hypothesize that this reduction can be attributed to a reconfiguration of the PEC network by the 4-arm PEO chains.

Previously, it has been shown that self-assembly of symmetric, oppositely charged *ABA* triblock polyelectrolytes results in networks with a higher-than-expected fraction of *B* blocks forming bridges instead of loops, manifesting as gel formation at surprisingly low polymer concentrations.[3] Here, we argue that inclusion of 4-arm PEO chains induces macromolecular crowding, hindering

bridge formation and promoting loop formation, reducing the network connectivity and reducing its shear moduli. Furthermore, the injectability of the PEC network containing precursor solutions can also be tuned precisely. The PEC+PEO hydrogels exhibit strong shear thinning characteristics (**Figure 2-S10A-D**) and the microstructure of the PEC networks recover quickly after strong shearing (**Figure 2-S10E**),[72] resulting in facile injection and swift recovery of hydrogel elasticity post injection (**Figure 2-1B**, row 3).

We note that the PEC+PEO and the PEC-IPN hydrogels are both expected to be spatially uniform, and therefore, spatial inhomogeneities and phase separation are not expected to play a role in contributing to the observed decay of the PEC+PEO hydrogel moduli. The mixing protocols, comprising mixing of the 4-arm PEO and the block polyanions before the addition of the block polycations ensured uniform mixing of the polymers. Additionally, SAXS spectra collected from various locations in the hydrogel samples were identical, pointing towards spatially homogenous distribution of the PEC domains. We also note that the drop in the moduli with increasing ω in the low ω ($\lesssim 0.5$ rad/s) range in frequency sweeps for PEC+PEO hydrogels in **Figures 2-3C and 2-S8D** indicates that the hydrogel was equilibrating while the initial low ω moduli measurements were made. We attribute this trend to the specific measurement protocol we followed where the shearing frequency of the sample jumped from $\omega = 1$ Hz to $\omega = 0.01$ Hz nearly instantaneously upon transition from the pre-shearing step to the frequency sweep measurements. For the other PEC+PEO, PEC and PEC-IPN hydrogels, the moduli are ω independent and therefore did not show any effect of this change in the shearing frequency. However, for the PEC+PEO hydrogels with $C_{bPE} \geq 30$ wt% and 5 wt% PEO, the moduli are frequency dependent, and the recovery and equilibration of the samples is evident in the first few points in the frequency sweep.

Similar trends were observed in PEC, PEC+PEO and PEC-IPN hydrogels comprising ammonium and sulfonated bPEs (**Figure 2-S11**). These PEC hydrogels exhibited G' and G'' that were lower than the corresponding guanidinilated bPE-containing PEC hydrogels, and both moduli exhibited a maximum with increasing C_{bPE} owing to the morphological transitions of the PEC domains.[5] G' and G'' of these PEC hydrogels were lower even than that of 5 wt% 4-arm PEO hydrogels across C_{bPE} varying from 10 wt% to 40 wt%. Thus, distinct improvements in the moduli were achieved in PEC-IPN hydrogels compared to the PEC hydrogels upon introduction of 5 wt% PEO (**Figure 2-S11H**). And, similar to variations depicted in **Figure 2-3G**, PEC-IPN and PEC+PEO hydrogel moduli varied continually with increasing C_{PEO} (**Figure 2-S11I**).

2.3.4 Imparting Tensile Strength to PEC Hydrogels by Interpenetration with Covalent Networks

Combining PEC networks with covalent networks also rendered tensile strength and extensibility to PEC-IPN hydrogels, characteristics that are inaccessible to PEC hydrogels, as illustrated in the representative stress-strain curves obtained from uniaxial tensile testing in **Figure 2-4**. The physically crosslinked PEC hydrogels do not possess tensile strength as the block polyelectrolyte chains can rearrange readily when subjected to tensile strain. In contrast, covalently crosslinked PEO hydrogels exhibit elasticity emerging from the finite extensibility of the polymer chains between the crosslinks. In PEC-IPN hydrogels, the covalent network is hypothesized to provide the tension points while the self-assembled domains that comprise the PEC network serve as energy-dissipating physical multi-linkages. The ultimate strength of the PEC-IPN hydrogels (C_{PEO} = 5 or 15 wt% + C_{bPE} = 30 wt%) was found to remain comparable to the corresponding covalent hydrogels, with minor loss of strength (**Figure 2-S12A**). At the same time, as compared to

corresponding PEO hydrogels, PEC-IPN hydrogels exhibit improvements in both extensibility and toughness (**Figure 2-S12B and 2-S12C**).

These improvements can be attributed to the reconfigurable nature of the PEC network, that enable network restructuring and promote stress dissipation. Network restructuring is further evident in the distinct two-step stress growth during uniaxial stretching of the PEC-IPN hydrogels (**Figure 2-4**, see also **Figure 2-S13**). At the same time, formation of the covalent network may be hindered partially by the PEC network, resulting in lower ultimate strength but contributing to higher extensibility. Similar enhancements in tensile performance were also noted upon replacing the guanidinium moieties with ammonium moieties in the bPEs comprising the PEC-IPN hydrogels (**Figures 2-S14 and 2-S15**).

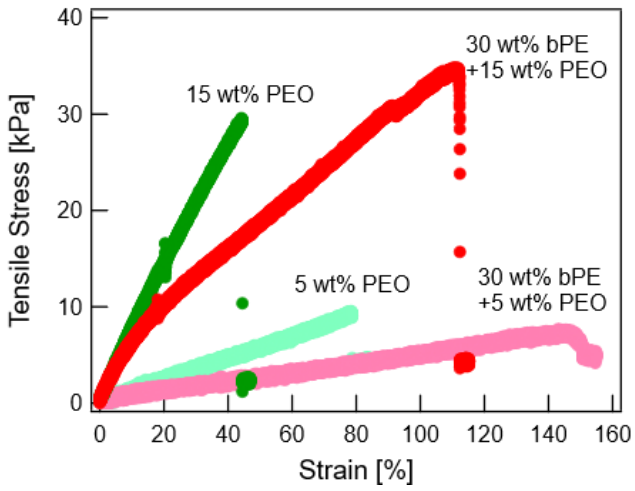

Figure 2-4. Imparting tensile strength to PEC network *via* PEC-IPN hydrogels. Representative stress curves as a function of strain for PEO and PEC-IPN hydrogels with C_{bPE} = 30 wt% and C_{PEO} = 5 or 15 wt%.

2.3.5 Modulating the Response of PEC Hydrogels to Aqueous or Saline Environments

Figure 5 presents representative data highlighting the swelling characteristics of the PEC-IPN hydrogels. PEC-IPN hydrogels swelled more than their corresponding PEO hydrogels yet reached equilibrium within a few hours. Swelling in all hydrogels were found to plateau within 24 hours. The larger swelling of the PEC-IPN hydrogels could be attributed to the hydrophilic bPEs absorbing larger amounts of water, providing an excess osmotic pressure to further expand the interpenetrating polymer networks and partially hindered formation of the covalent network in the PEC-IPN hydrogels enabling its larger expansion and resulting in loss of uncrosslinked chains into the surrounding solution. At the same time, some of the bPE chains can also be expected to leave the PEC network and dissolve in the surrounding solution, although their fraction is expected to be very small owing to the extremely small fraction of uncomplexed bPE chains in the PEC networks.[3] The swelling of PEC-IPN hydrogels could be tuned by varying C_{PEO}; the swelling ratio of PEC-IPN hydrogels increased by 18% upon increasing C_{PEO} from 5 wt% to 15 wt%. This is commensurate with the larger swelling of the 15 wt% PEO hydrogels as compared to the 5 wt% PEO hydrogels (**Figure 2-5**). Again, these are distinct improvements over the indefinite swelling of PEC hydrogels, ascribable to their physically crosslinked structure.

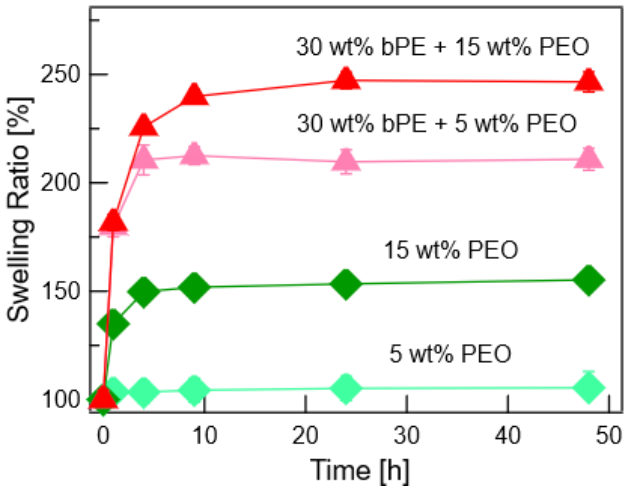

Figure 2-5. Controlling the swelling behavior of PEC network by interpenetration with covalent networks. The swelling of PEO and PEC-IPN hydrogels with C_{bPE} = 30 wt% and C_{PEO} = 5 or 15 wt%, as denoted by their weight gain with time.

PEC-IPN hydrogels also retained their mechanical strength upon exposure to salt. Introduction of salt resulted in progressive breakdown of the PEC network, evident from the broadening peaks in the SAXS spectra obtained from PEC-IPN hydrogels (C_{bPE} = 30 wt%, C_{PEO} = 5 wt%) with increasing salt concentrations (**Figures 2-6A and 2-6C**, see also **Figures 2-S16A and 2-S16D**). The influence of salt on the network microstructure was more evident in PEC networks containing ammonium functionalized bPEs (**Figure 2-6C**) as compared to guanidinilated bPEs (**Figure 2-6A**). Correspondingly, shear moduli of PEC hydrogels with guanidinium moieties decreased by ~2 orders of magnitude upon increasing C_{salt} up till 600 mM (grey symbols in **Figure 2-6B**, see also **Figures 2-S16B and 2-S16C**) while the moduli of the PEC hydrogels with ammonium moieties decreased precipitously with increasing C_{salt}. In contrast, the corresponding PEC-IPN hydrogels exhibited far superior shear strength even when PEC network was disrupted, ascribable to the presence of the covalent network that sustains the shear response of the hydrogels in salty environments (red symbols in **Figures 2-6B and 2-6D**, see also **Figures 2-S16E and 2-S16F**). Thus, the PEC-IPN hydrogels present a possibility of hydrogel design wherein ionic strength or pH can be varied to induce changes in network microstructure while retaining controlled moduli and swelling responses.

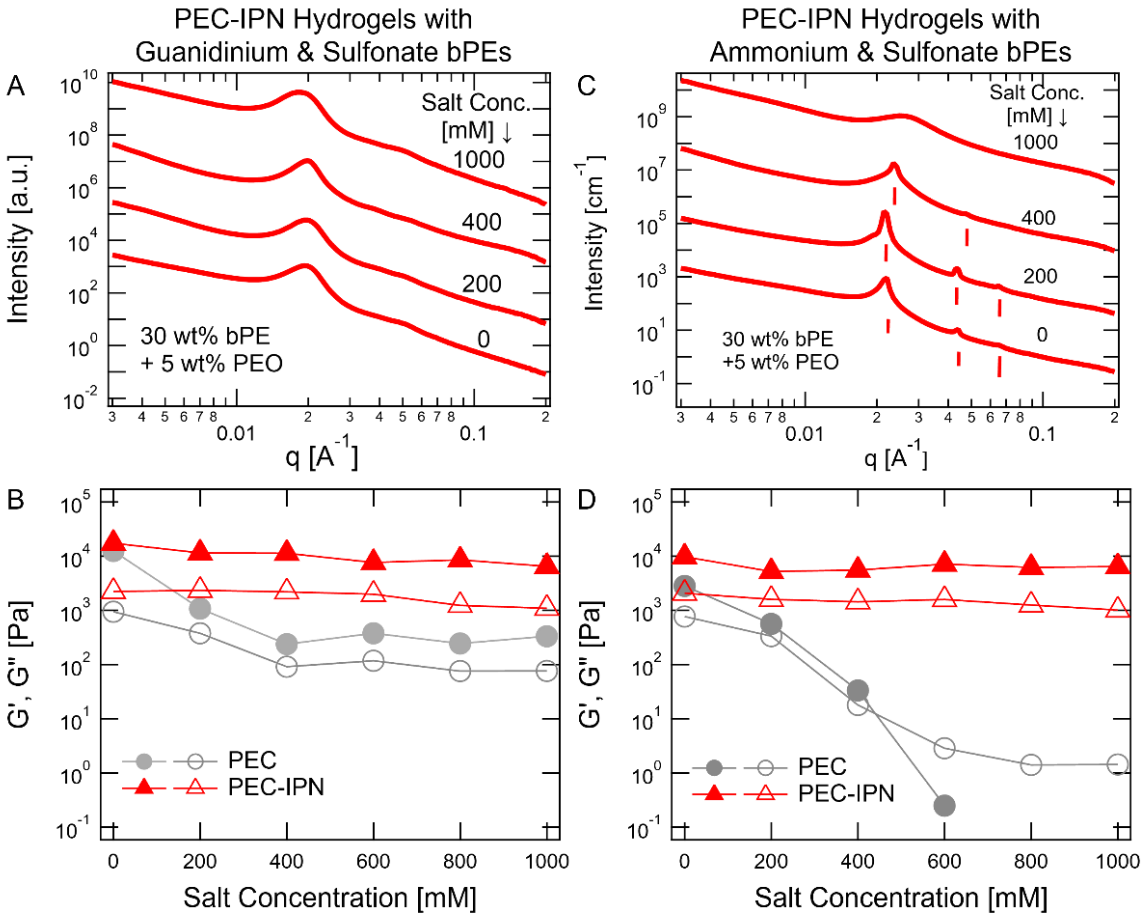

Figure 2-6. Evolution of microstructure and shear strength of PEC-IPN hydrogels in saline environments. (**A**) One-dimensional SAXS intensities $I(q)$ versus wave vector q and (**B**) the shear moduli (G' and G"), measured at $\omega = 1.12$ rad/s and $\gamma = 0.3\%$, as a function of salt concentration C_{salt} for PEC-IPN hydrogels ($C_{bPE} = 30$ wt% + $C_{PEO} = 5$ wt%) composed of bPEs functionalized with guanidinium and sulfonate moieties. In (B), corresponding G' and G" data are also shown for PEC hydrogels ($C_{bPE} = 30$ wt%). (**C**) and (**D**) show data corresponding to (A) and (B), respectively for PEC-IPN hydrogels ($C_{bPE} = 30$ wt% + $C_{PEO} = 5$ wt%) and PEC hydrogels ($C_{bPE} = 30$ wt%) composed of bPEs functionalized with ammonium and sulfonate moieties. In (A) and (C), the $I(q)$ spectra were shifted vertically for clarity. See Supplementary Information Table S2 for peak assignments in (C).

2.4 Conclusion and Implications in Biomaterials Development

In summary, we have demonstrated, for the first time, a facile approach to create PEC-IPN hydrogels composed of interpenetrating PEC networks (composed of oppositely charged block polyelectrolytes) and covalent networks (composed of photocrosslinked 4-arm PEO chains). PEC-IPN hydrogels are shown to possess superior shear and tensile properties which cannot be achieved by either of the individual networks. Moreover, the PEC-IPN hydrogels exhibit enhanced mechanical stability in salt environments and tunable swelling response.

The PEO chains and networks, at sufficiently high loadings, induce morphological and ordering transitions in the PEC domains, providing a handle to tune the PEC domain morphologies and arrangements. At the same time, interpenetration of the PEC network with the covalent network enables an independent modulation of the shear properties of the PEC network. PEC-IPN hydrogels with interpenetrating covalent and PEC networks featured $G' > 10$ kPa, a regime rarely accessible by PEC hydrogels but is important for design of strong hydrogels and adhesives.

These improved features of the PEC-IPN hydrogels, as compared to PEC hydrogels, are highly desirable in numerous biomedical applications. For instance, the PEC-IPN hydrogels demonstrated here can serve as a model platform to establish routes for use of materials based on block polyelectrolyte self-assembly in biomedical applications as adhesives and scaffolding wherein a control over gel microstructure (and drug loading capacity), shear and tensile strength, and extensibility are sought.

In parallel, the platform can act as a facile method to address current challenges associated with the use of photocrosslinkable polymers in advanced materials and biomedicine. PEC hydrogels can serve as a protective scaffolding, preventing uncontrolled dilution of the precursor solution and avoiding material loss and functional deactivation in wet environments. Moreover, the

crosslinked gels can achieve higher moduli owing to the interpenetrating PEC network. Thus, combination of existing photocrosslinkable polymers and PEC hydrogels represents a promising one-pot solution that could be employed directly on application site without additional processing steps. These improvements can prove very beneficial for various applications where photocrosslinked hydrogels are employed, and especially applications wherein *in situ* crosslinking of the precursor polymers is sought.[73, 74] For instance, light-based biofabrication processes like extrusion-based 3D printing that face issues of low viscosity and weak structural integrity of the hydrogel precursor solution prior to photocrosslinking can benefit from inclusion of PEC networks into the 3-D printing inks. Such a combination can achieve initial shear strength, minimize loss of precursor from secondary flows, and promote inter-layer bonding, paving the way for high-resolution printing.[74] Similarly, drug-loaded hydrogels patches or adhesive tissue sealants that rely on chemical crosslinking of precursors *in situ* can also benefit from introduction of PEC networks in the precursor solution. The injectable precursor solutions in these applications typically possess a low viscosity and tend to perfuse from the site of injection into the surrounding tissue, leading to premature release of their drug cargo or weak and ineffective adhesion, respectively.[73] Incorporation of PEC networks can reinforce the mechanical properties of the injected hydrogel precursors, and thus mitigate the loss of precursor molecules and reduce their dosage.

2.5 Supplementary Information

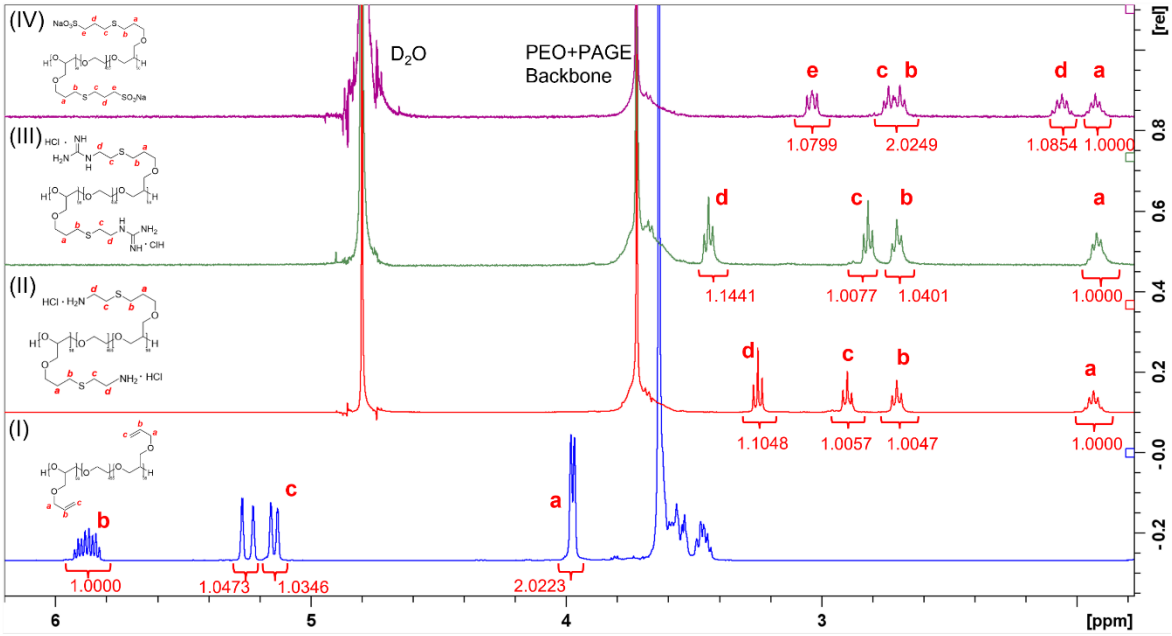

Figure 2-S1. ^{1}H NMR spectra of **(I)** $PAGE_{98}$-PEO_{455}-$PAGE_{98}$, **(II)** ammonium-functionalized $PAGE_{98}$-PEO_{455}-$PAGE_{98}$, **(III)** guanidinium functionalized $PAGE_{98}$-PEO_{455}-$PAGE_{98}$, **(IV)** sulfonate-functionalized $PAGE_{98}$-PEO_{455}-$PAGE_{98}$.

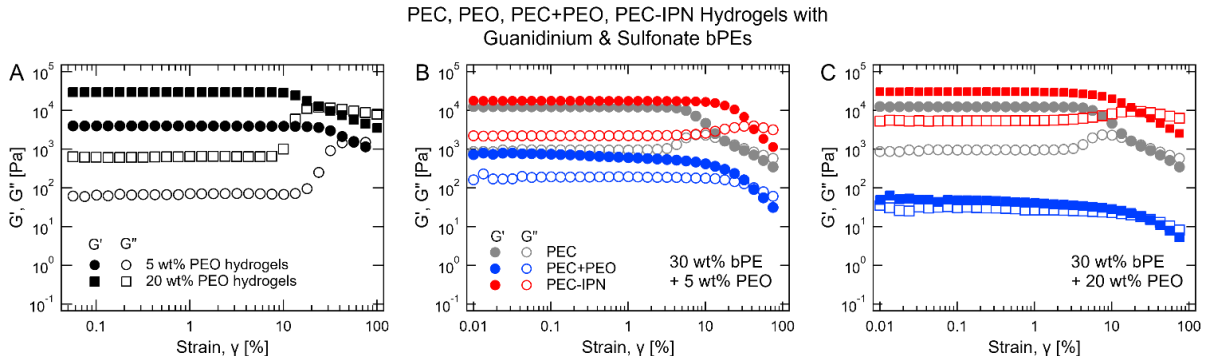

Figure 2-S2. Representative amplitude sweeps showing the shear moduli (G' and G") as a function of strain for PEO, PEC, PEC+PEO, and PEC-IPN hydrogels. **(A)** PEO hydrogels with C_{PEO} (= 5 wt% and 20 wt%), **(B)** PEC hydrogels (grey) with C_{bPE} (= 30 wt%), PEC+PEO hydrogels (blue) and PEC-IPN hydrogels (red) with C_{bPE} (= 30 wt%) and C_{PEO} (= 5 wt%), **(C)** PEC hydrogels (grey) with C_{bPE} (= 30 wt%), PEC+PEO hydrogels (blue) and PEC-IPN hydrogels (red) with C_{bPE} (= 30 wt%) and C_{PEO} (= 20 wt%).

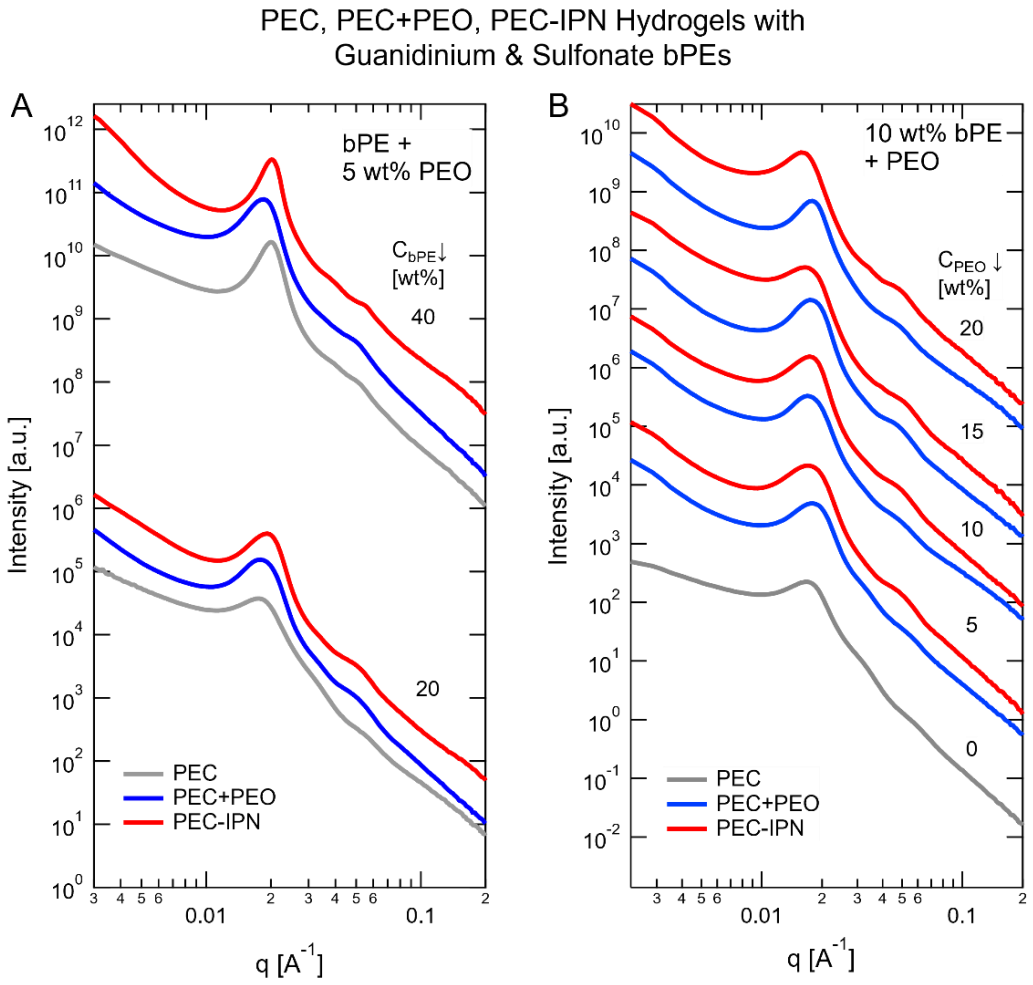

Figure 2-S3. Representative SAXS scattering spectra in PEC, PEC+PEO, PEC-IPN hydrogels consisting of guanidinium and sulfonate functionalized polyelectrolytes. **(A)** 1-D scattering intensity $I(q)$ as a function of wave factor q for PEC (grey), PEC+PEO (blue), and PEC-IPN (red) hydrogels with a fixed C_{PEO} (= 5 wt%) and varying C_{bPE} from 20 wt% to 40 wt%. **(B)** $I(q)$ spectra for PEC hydrogels (with C_{bPE}= 10 wt%), PEC+PEO, and PEC-IPN hydrogels with varying C_{PEO} from 5 wt% to 20 wt%. $I(q)$ spectra are shifted vertically for clarity.

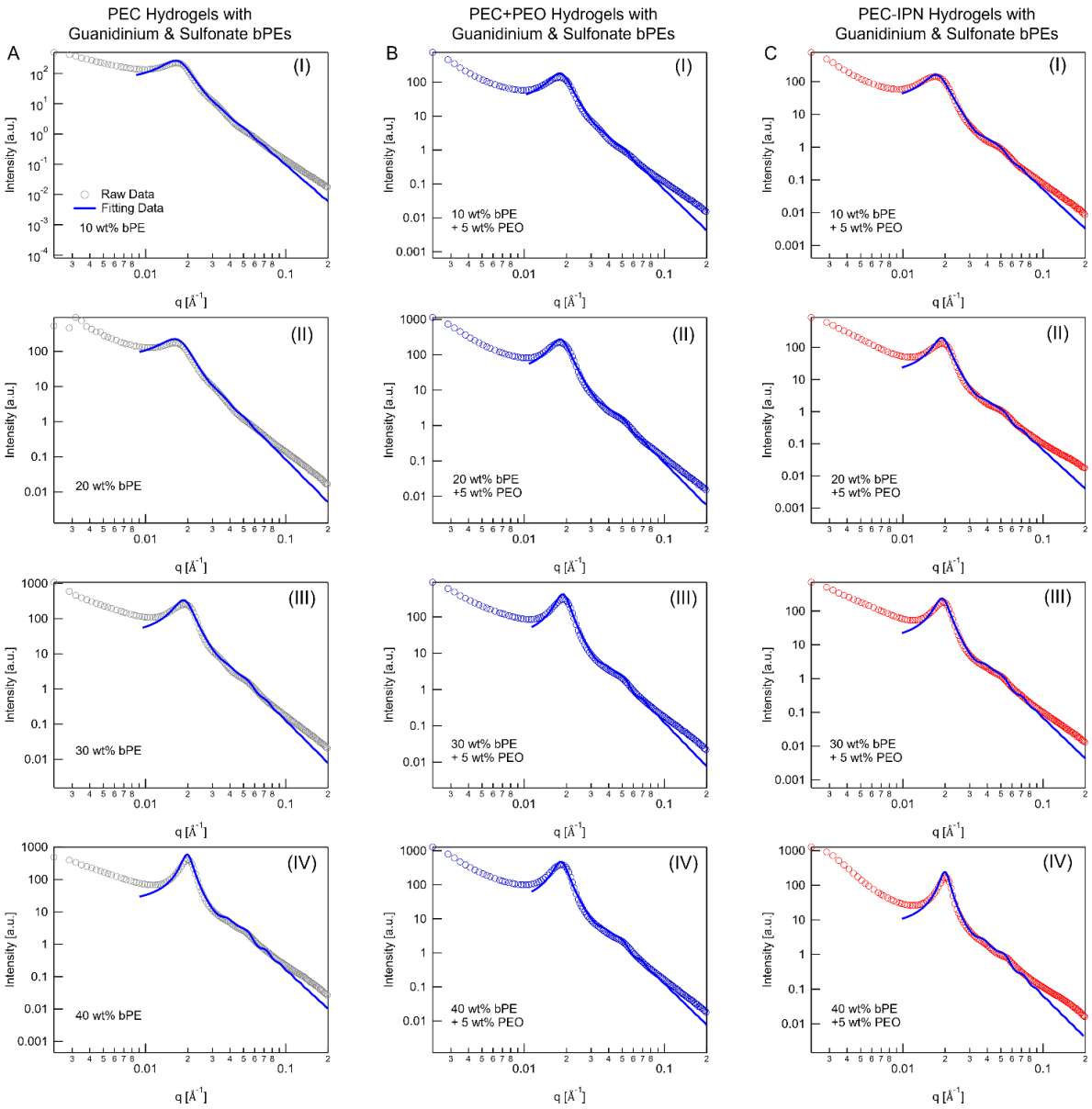

Figure 2-S4. Representative fitting curves of PEC domain core radius of **(A, I-IV)** PEC hydrogels with varying C_{bPE} from 10 wt% to 40 wt%, **(B, I-IV)** PEC+PEO hydrogels and **(C, I-IV)** PEC-IPN hydrogels with a fixed C_{PEO} (= 5 wt%) and varying C_{bPE} from 10 wt% to 40 wt%. The fitting curves were modeled by polydisperse spheroid form factor and hard-sphere structure factor.

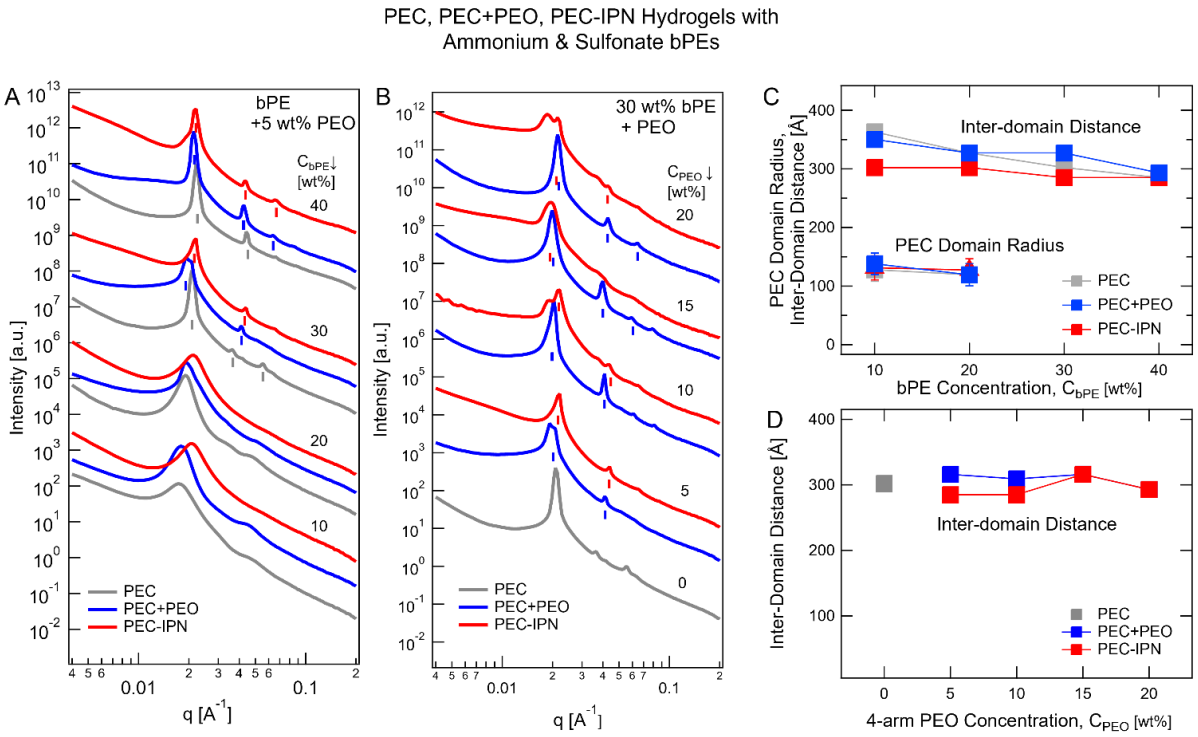

Figure 2-S5. SAXS scattering spectra and PEC domain attributes in PEC, PEC+PEO, PEC-IPN hydrogels with polyelectrolytes functionalized with ammonium and sulfonate groups. **(A)** 1-D scattering intensity $I(q)$ as a function of wave vector q for PEC (grey), PEC+PEO (blue), and PEC-IPN (red) hydrogels with varying C_{bPE} from 10 wt% to 40 wt%. PEC+PEO and PEC-IPN hydrogels also contained a fixed C_{PEO} (= 5 wt%). **(B)** $I(q)$ spectra for PEC hydrogels with C_{bPE} = 30 wt%, and PEC+PEO, and PEC-IPN hydrogels with varying C_{PEO} (between 5 wt% and 20 wt%) and constant C_{bPE} = 30 wt%. The small vertical bars indicate the positions of the Bragg scattering peaks. With respect to the primary peak (at q^*), the secondary and the tertiary peaks appear at $2q^*$ and $3q^*$, denoting lamellar microstructure of the PEC domains. In (A) and (B), $I(q)$ spectra are shifted vertically for clarity. **(C, D)** Inter-domain distance (d_{PEC}) and domain radius (R_{PEC}) as a function of C_{bPE} (C) and C_{PEO} (D) for PEC, PEC+PEO, and PEC-IPN hydrogels. In (C), C_{PEO} =

5 wt%, while in (D), $C_{bPE} = 30$ wt%. See Supplementary Information Tables S3 and S4 for peak assignments in (C) and (D).

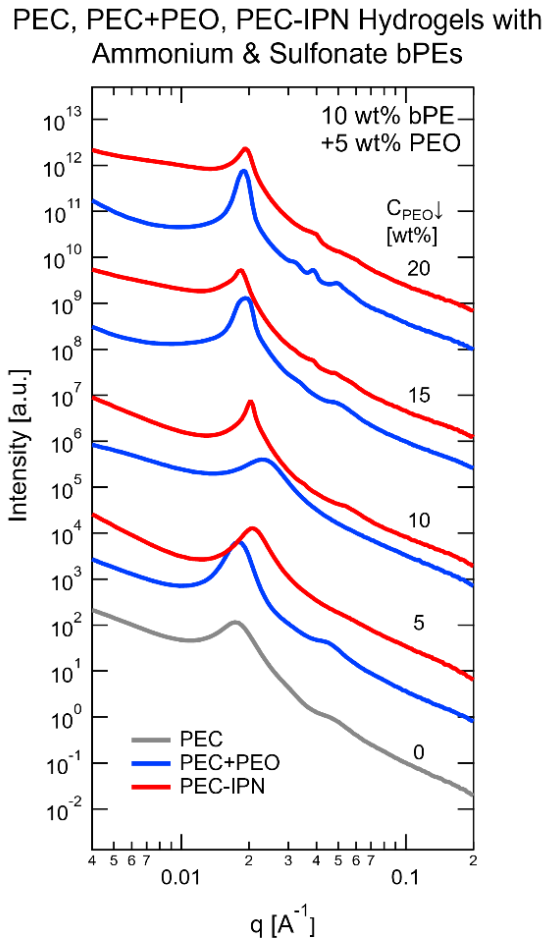

Figure 2-S6. SAXS scattering spectra in PEC, PEC+PEO, and PEC-IPN hydrogels. 1-D scattering intensity $I(q)$ as a function of wave vector q for PEC (grey), PEC+PEO (blue), and PEC-IPN (red) hydrogels with a fixed C_{bPE} (= 10 wt%) and varying C_{PEO} from 5 wt% to 20 wt%. $I(q)$ spectra are shifted vertically for clarity.

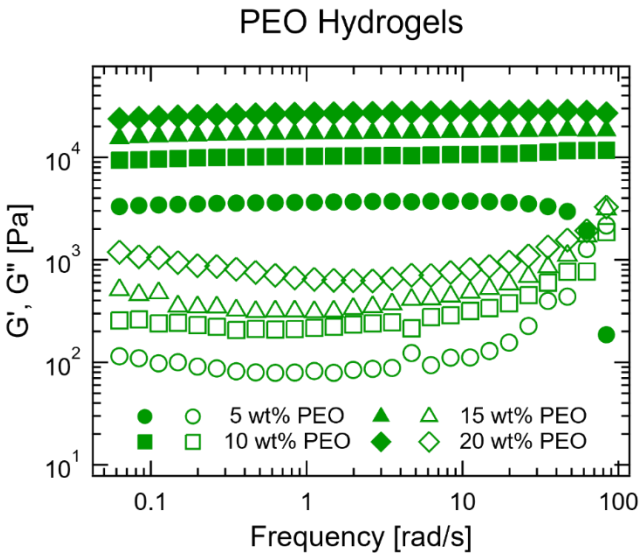

Figure 2-S7. Shear strength of PEO hydrogels. Storage (G') and loss (G'') moduli as a function of frequency (ω) for PEO hydrogels with varying C_{PEO} from 5 wt% to 20 wt%.

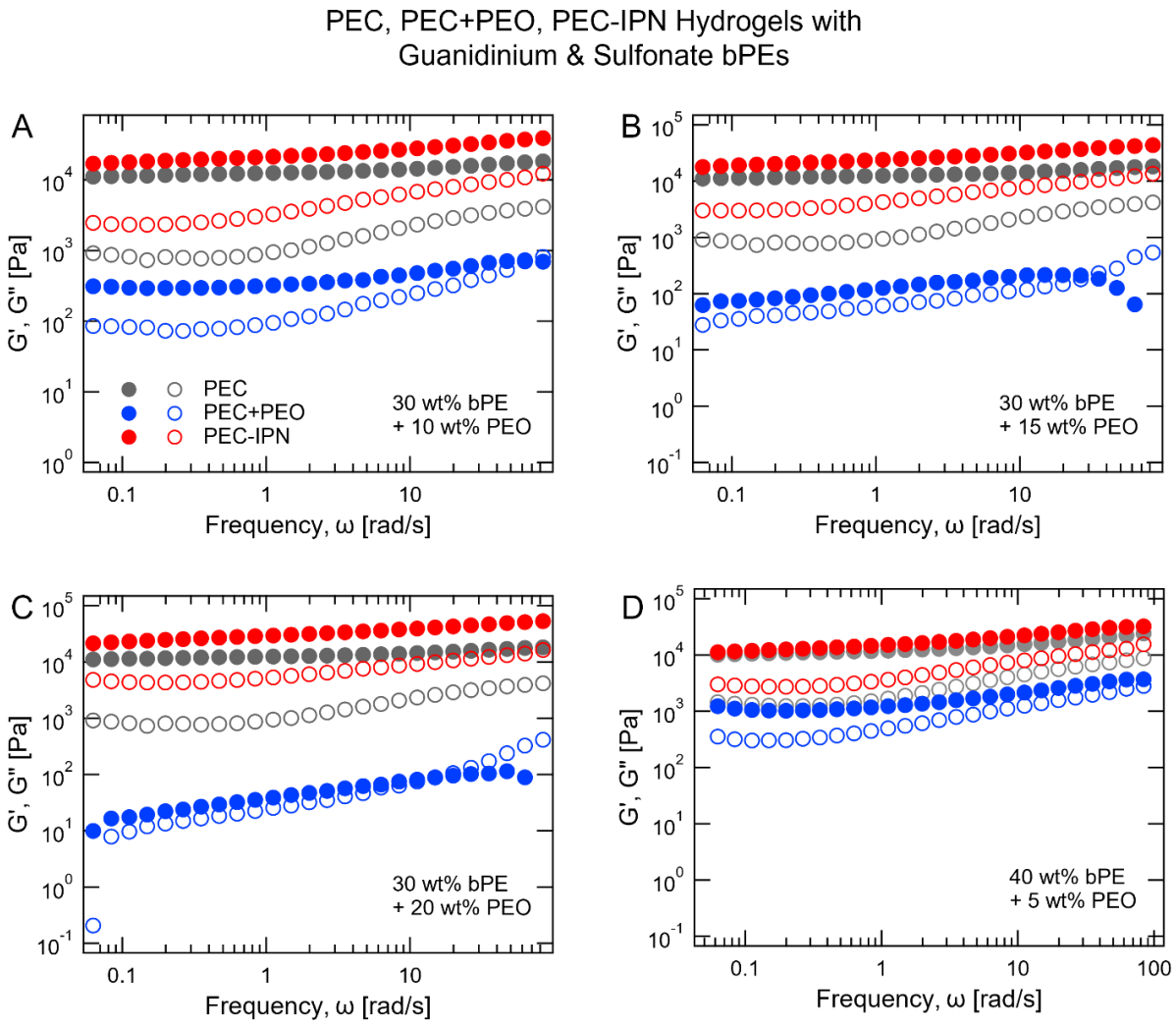

Figure 2-S8. Shear strength of PEC, PEC+PEO, PEC-IPN hydrogels. **(A-C)** Storage (G') and loss (G'') moduli as a function of frequency (ω) for PEC hydrogels (grey), PEC+PEO hydrogels (blue), and PEC-IPN hydrogels (red) with varying C_{PEO} from 10 wt% to 20 wt% and a constant C_{bPE} (= 30 wt%). **(D)** $G'$and (G") as a function of ω for PEC (with C_{bPE} = 40 wt%), PEC+PEO, and PEC-IPN hydrogels with C_{bPE} = 40 wt% and C_{PEO} = 5 wt%.

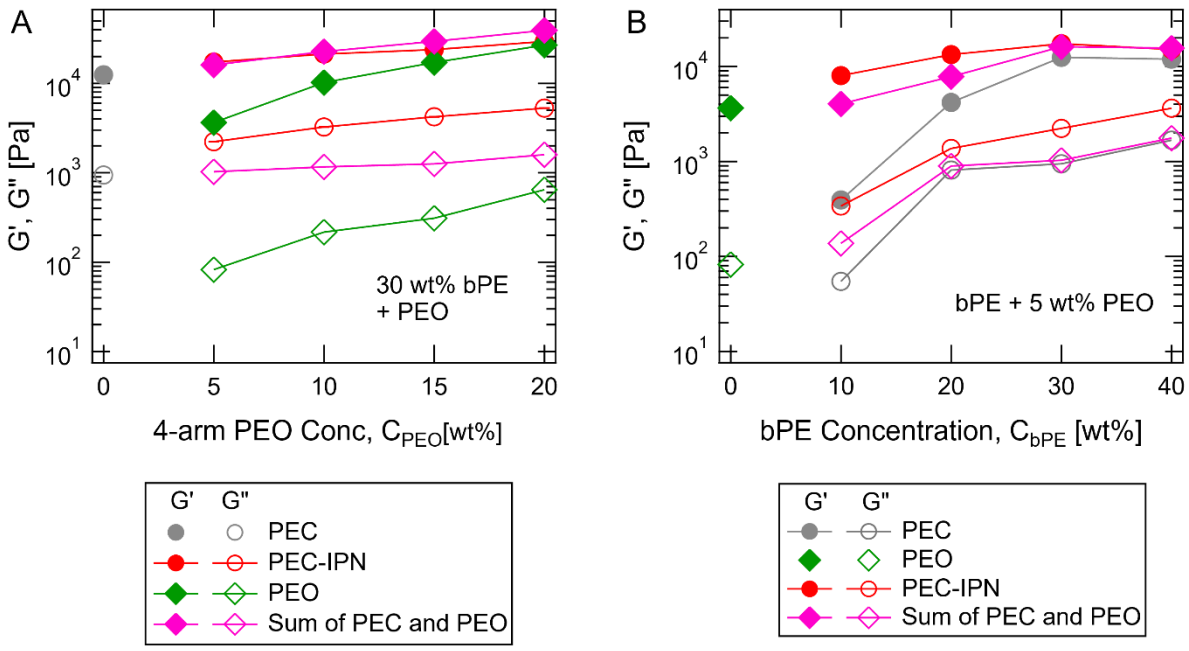

Figure 2-S9. Synergistic Shear Response of Guanidinium & Sulfonate PEC-IPN Hydrogels. Storage (G') and loss ($G"$) moduli of PEC-IPN hydrogels with **(A)** a constant C_{bPE} = 30 wt% and increasing C_{PEO}, and **(B)** a constant C_{PEO} = 5 wt% and increasing C_{bPE}. The shear moduli of the corresponding the PEC hydrogels and the PEO hydrogels, and the sum of the moduli of PEC and PEO hydrogels are also shown.

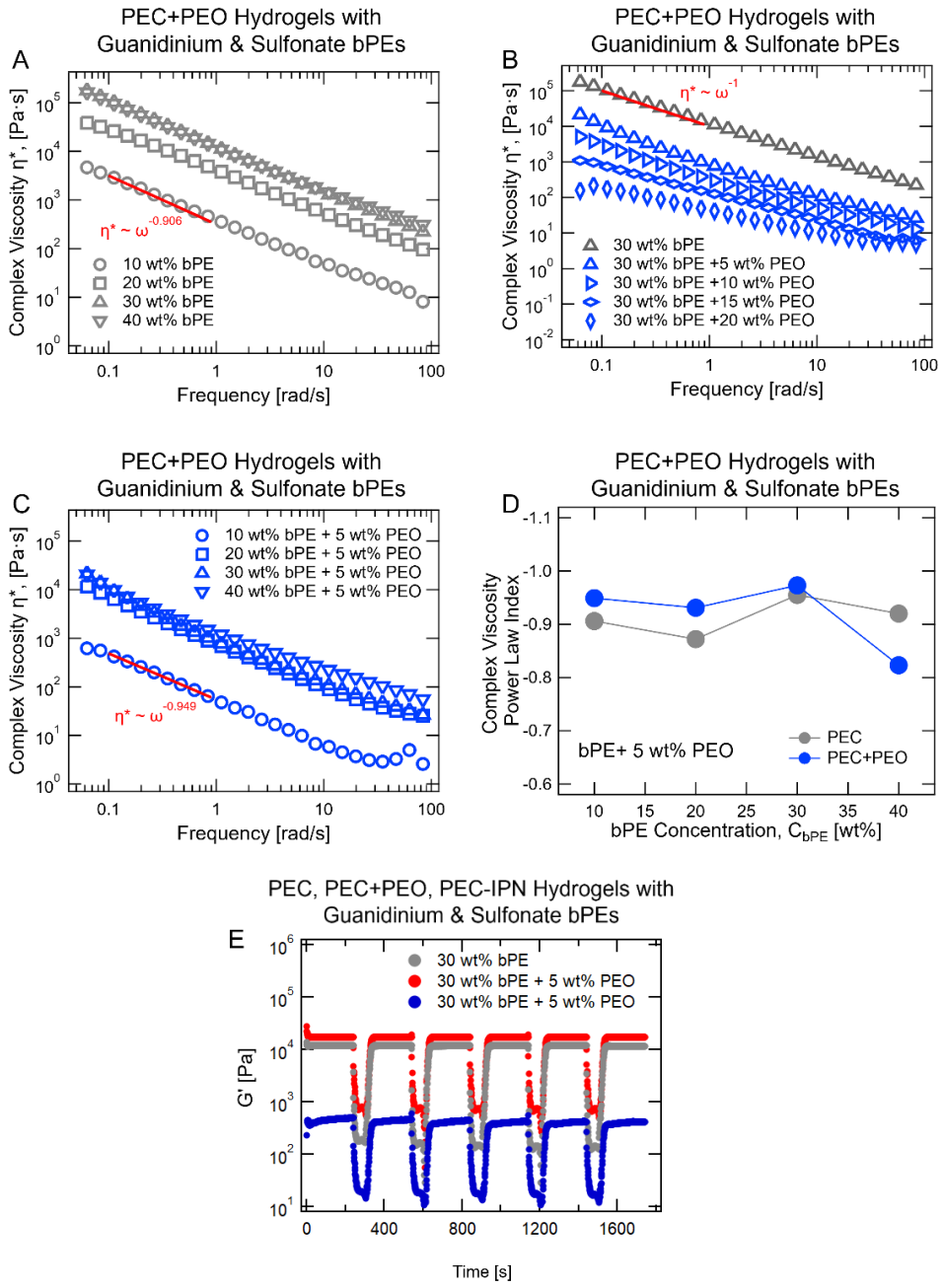

Figure 2-S10. Representative complex viscosity and cyclic strain performance of PEC and PEC+PEO hydrogels comprising polyelectrolytes with guanidinium and sulfonate moieties. Complex viscosity (η^*) as a function of frequency (ω) for **(A)** PEC hydrogels with varying C_{bPE} from 10 wt% to 40 wt%, **(B)** PEC hydrogels (grey) with C_{bPE} (= 30 wt%) and PEC+PEO hydrogels with a constant C_{bPE} (= 30 wt%) and increasing C_{PEO} from 5 wt% to 20 wt%, and **(C)**

PEC+PEO hydrogels with a fixed C_{PEO}(= 5 wt%) and increasing C_{bPE} from 10 wt% to 40 wt%. **(D)** Complex viscosity power law index (n, where $\eta^* \sim \omega^n$) for PEC and PEC+PEO hydrogels with C_{bPE} from 10 wt% to 40 wt%. PEC+PEO hydrogels contained a fixed C_{PEO} (= 5 wt%). **(E)** Cyclic strain performance of PEC hydrogels (grey) with C_{bPE} = 30 wt% and PEC+PEO (blue) and PEC-IPN hydrogels (red) with C_{bPE} = 30 wt% and C_{PEO} = 5 wt% in the cyclic strains between 0.3% and 100%.

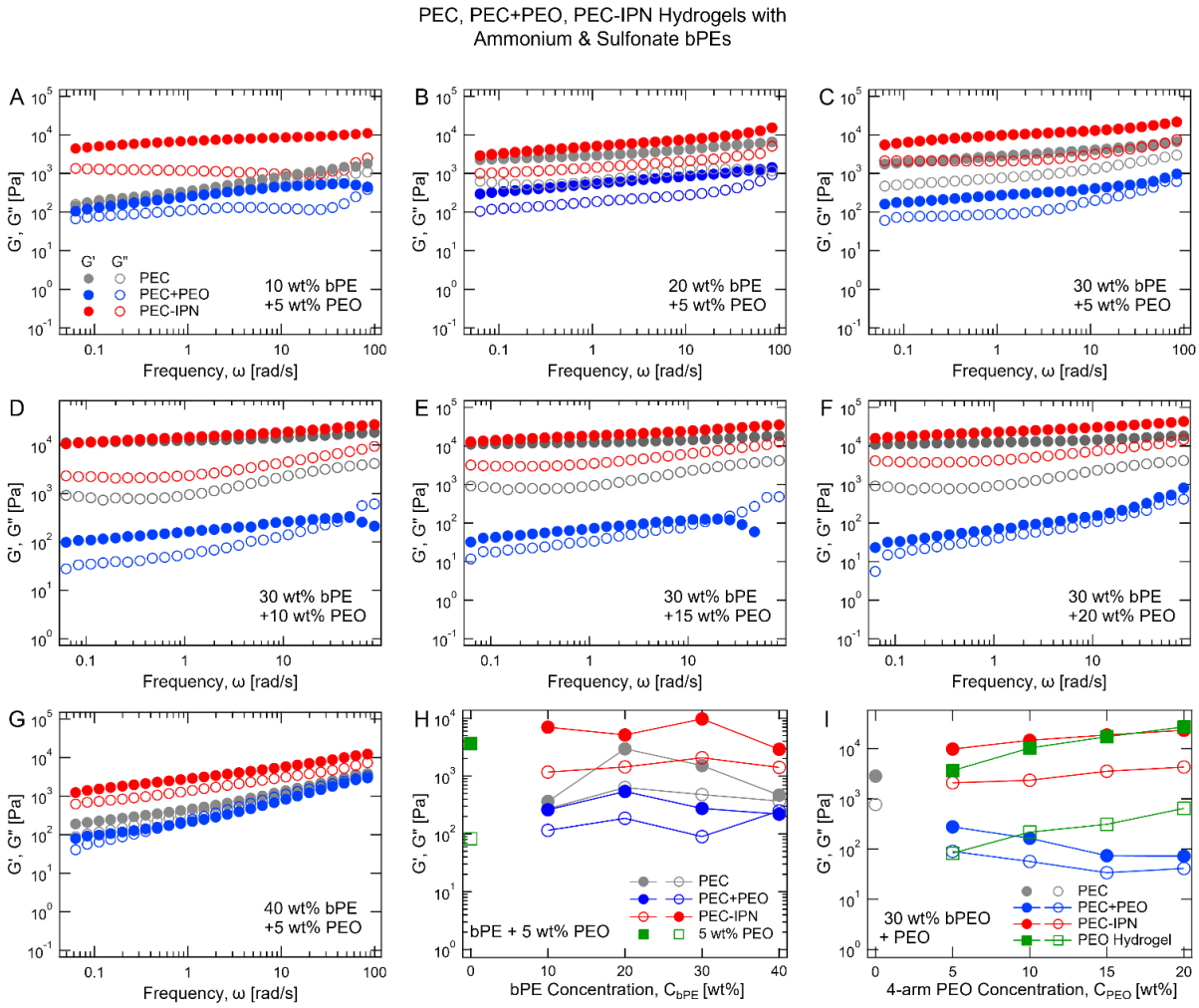

Figure 2-S11. Modulations of shear strengths of PEC, PEO, PEC+PEO, and PEC-IPN hydrogels. **(A-G)** Storage (G') and loss (G'') moduli as a function of frequency (ω) for PEC hydrogels (grey), PEC+PEO hydrogels (blue), and PEC-IPN hydrogels (red) with varying C_{bPE} and C_{PEO}. **(H)** G' and G'' (at $\omega = 1.12$ rad/s) for PEO hydrogels (black) with C_{PEO}(= 5 wt%), PEC hydrogels (grey) with increasing C_{bPE} from 10 wt% to 40 wt%, PEC+PEO (blue) and PEC-IPN (red) hydrogels with a constant C_{PEO} (= 5 wt%) and increasing C_{bPE} from 10 wt% to 40 wt%. **(I)** G' and G'' (at $\omega = 1.12$ rad/s) for PEC hydrogels with C_{bPE} (= 30 wt%), PEO hydrogels with C_{PEO} from 5 wt% to 20 wt%, PEC+PEO hydrogels and PEC-IPN hydrogels with a constant C_{bPE} (= 30 wt%) and increasing C_{PEO} from 5 wt% to 20 wt%.

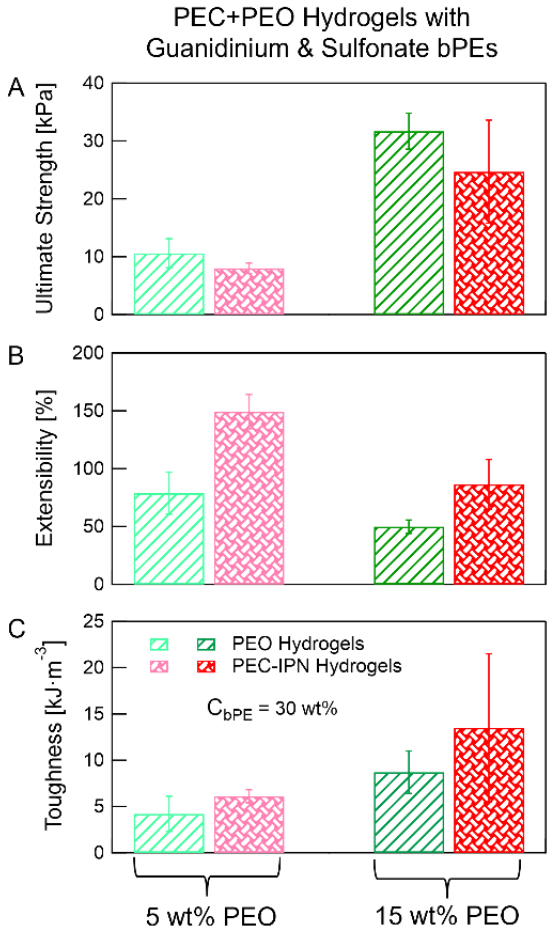

Figure 2-S12. Tensile characterization for PEO hydrogels and PEC-IPN hydrogels comprising polyelectrolytes functionalized with guanidinium and sulfonate groups. (A) Ultimate strength, (B) extensibility, and (C) toughness. Data in (A–C) are averages obtained from measurements on three distinct samples.

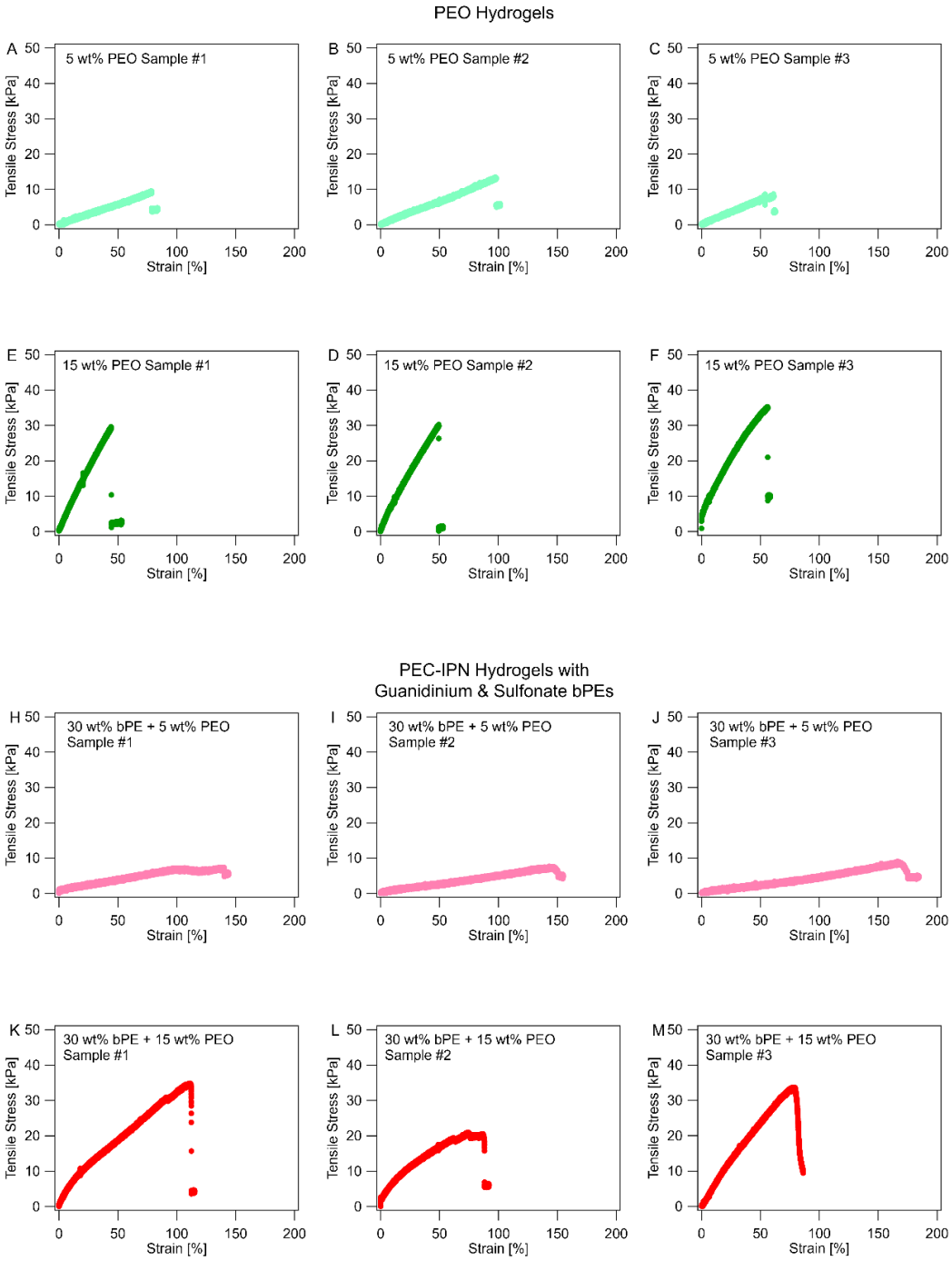

Figure 2-S13. Representative stress vs. strain curves for PEO and PEC-IPN hydrogels. **(A-C)** PEO hydrogels with C_{PEO} (= 5 wt%), **(E-F)** PEO hydrogels with C_{PEO} (= 15 wt%), **(H-J)** PEC-IPN hydrogels with C_{bPE} (= 30 wt%) and C_{PEO} (= 5 wt%), **(K-M)** PEC-IPN hydrogels with C_{bPE} (= 30 wt%) and C_{PEO} (= 15 wt%).

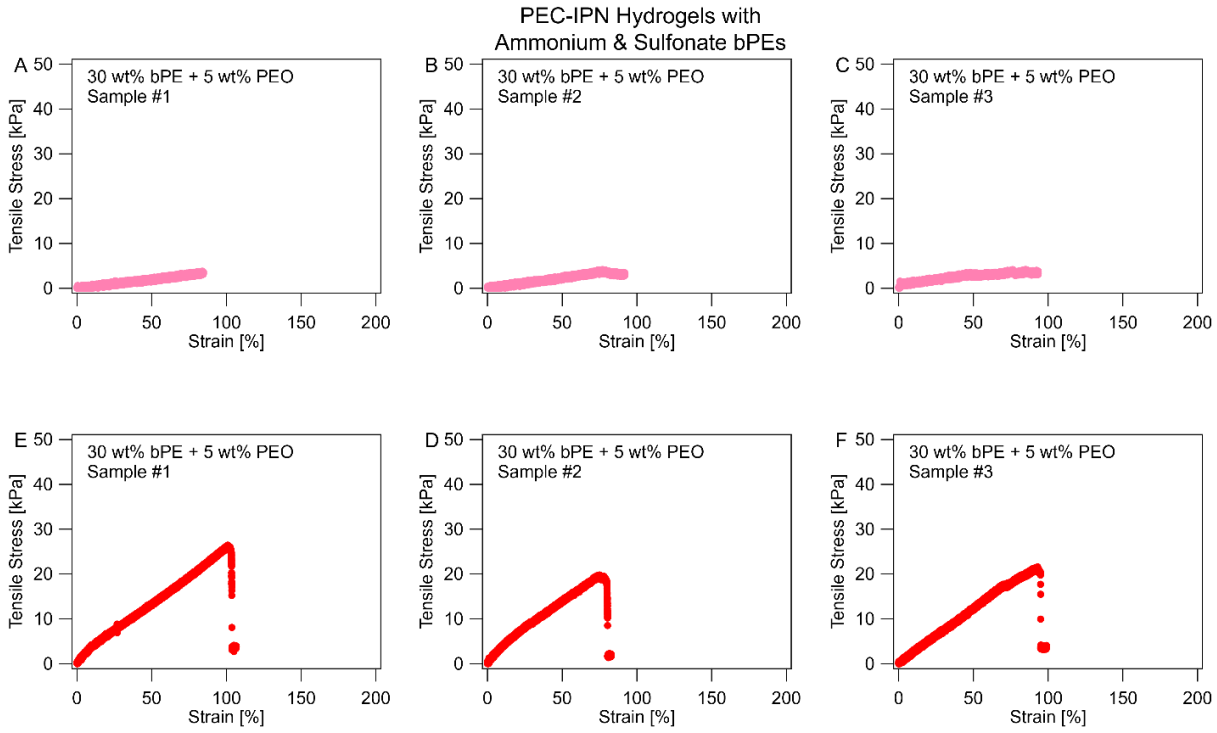

Figure 2-S14. Representative Stress vs. strain curves for PEC-IPN hydrogels consisting of polyelectrolytes functionalized with ammonium and sulfonate groups. **(A-C)** PEC-IPN hydrogels with C_{bPE} (= 30 wt%) and C_{PEO} (= 5 wt%), **(E-F)** PEC-IPN hydrogels with C_{bPE} (= 30 wt%) and C_{PEO} (= 15 wt%).

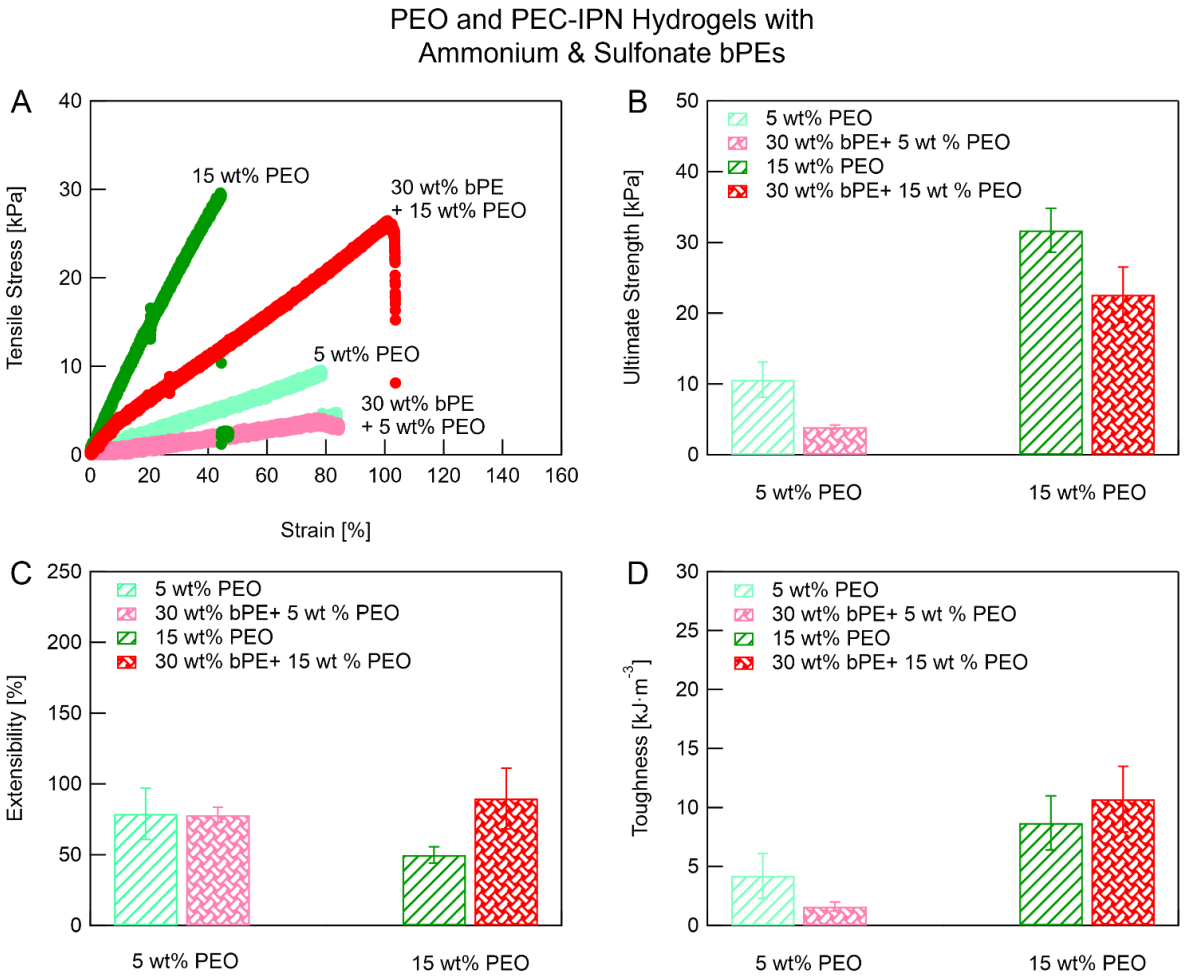

Figure 2-S15. Tensile characterization for PEO hydrogels and PEC-IPN hydrogels comprising polyelectrolytes functionalized with ammonium and sulfonate groups. **(A)** Representative stress-strain curves, **(B)** ultimate stress, **(C)** extensibility, and **(E)** toughness for PEO and PEC-IPN hydrogels with C_{bPE} = 30 wt% and C_{PEO} = 5 wt% or 15 wt%. Data in (B–D) are averages obtained from measurements on three distinct samples.

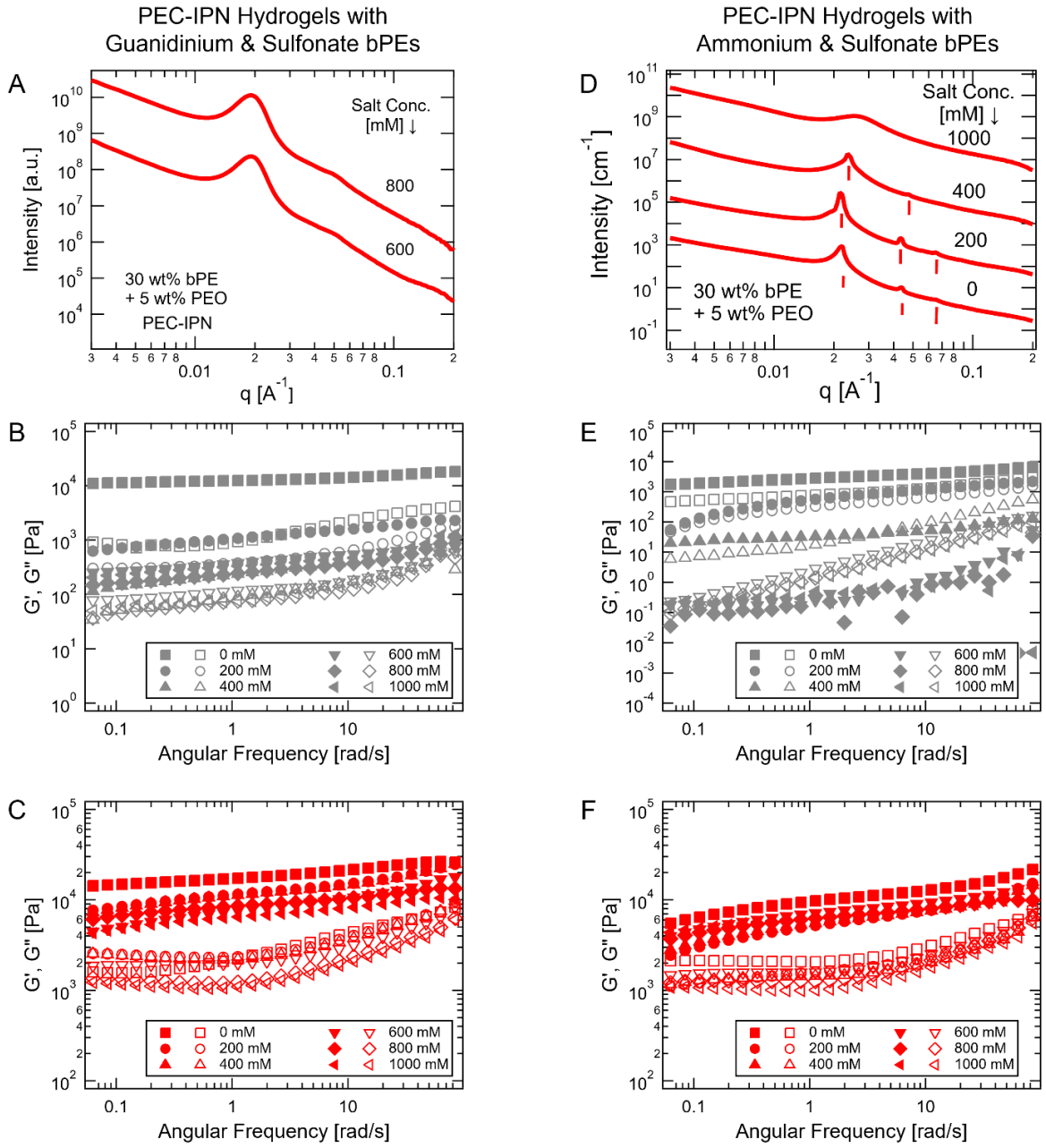

Figure 2-S16. Evolution of microstructure and shear strength of PEC-IPN hydrogels in saline environments. **(A)** 1-D $I(q)$ versus wave vector q for PEC-IPN hydrogels (C_{bPE} = 30 wt% + C_{PEO} = 5 wt%) composed of block polyelectrolytes functionalized with guanidinium and sulfonate moieties and **(B-C)** the shear moduli (G' and G'') as a function of ω for PEC hydrogels (grey, C_{bPE} = 30 wt%) and PEC-IPN hydrogels (red, C_{bPE} = 30 wt% + C_{PEO} = 5 wt%) in saline

environments with a variation of C_{salt}. **(D)**, **(E)**, and **(F)** show the data corresponding to (A), (B), and (C), respectively, for PEC-IPN hydrogels ($C_{bPE} = 30$ wt% + $C_{PEO} = 5$ wt%) and PEC hydrogels ($C_{bPE} = 30$ wt%) composed of block polyelectrolytes functionalized with ammonium and sulfonate moieties. In (A) and (D), the $I(q)$ spectra were shifted vertically for clarity.

Supplementary Tables

Table 2-S1. Bragg peak locations and microstructure information for PEC+PEO and PEC-IPN hydrogels with a constant $C_{bPE} = 30$ wt% and varying C_{PEO}. The PEC+PEO and PEC-IPN hydrogels consisted of polyelectrolytes functionalized with guanidinium and sulfonate groups.

Hydrogel Description	q [Å^{-1}]	q/q^*	Expected q/q^*	**Microstructure**
PEC+PEO hydrogels with $C_{bPE} = 30$ wt% and $C_{PEO} = 15$ wt%	0.020	1.000	1.000	Lam
	0.038	1.928	2.000	
	0.057	2.888	3.000	
PEC-IPN hydrogels with $C_{bPE} = 30$ wt% and $C_{PEO} = 15$ wt%	0.021	1.000	1.000	Lam
	0.042	2.015	2.000	
	0.060	2.863	3.000	
PEC+PEO hydrogels with $C_{bPE} = 30$ wt% and $C_{PEO} = 20$ wt%	0.019	1.000	1.000	Lam
	0.036	1.914	2.000	
	0.054	2.889	3.000	
PEC-IPN hydrogels with $C_{bPE} = 30$ wt% and $C_{PEO} = 15$ wt%	0.021	1.000	1.000	Lam
	0.042	2.015	2.000	
	0.060	2.863	3.000	

Table 2-S2. Bragg peak locations and microstructure information for PEC+PEO and PEC-IPN hydrogels with a constant C_{PEO} = 5 wt% and C_{bPE} = 30 wt% in the saline environments with different C_{salt} . The PEC+PEO and PEC-IPN hydrogels consisted of polyelectrolytes functionalized with ammonium and sulfonate groups.

Hydrogel Description	q [Å^{-1}]	q/q^*	Expected q/q^*	**Microstructure**
PEC+PEO hydrogels with C_{salt} = 0 mM	0.020	1.000	1.000	Lam
	0.041	2.064	2.000	
PEC-IPN hydrogels with C_{salt} = 0 mM	0.022	1.000	1.000	Lam
	0.044	1.993	2.000	
	0.064	2.885	3.000	
PEC+PEO hydrogels with C_{salt} = 200 mM	0.022	1.000	1.000	Lam
	0.044	1.993	2.000	
PEC-IPN hydrogels with C_{salt} = 200 mM	0.021	1.000	1.000	Lam
	0.044	2.052	2.000	
	0.065	3.017	3.000	
PEC+PEO hydrogels with C_{salt} = 400 mM	0.022	1.000	1.000	Lam
	0.044	1.993	2.000	
PEC-IPN hydrogels with C_{salt} = 400 mM	0.024	1.000	1.000	Lam
	0.047	2.000	2.000	

Table 2-S3. Bragg peak locations and microstructure information for PEC+PEO and PEC-IPN hydrogels with a constant C_{PEO} = 5 wt% and varying C_{bPE}. The PEC+PEO and PEC-IPN hydrogels consisted of polyelectrolytes functionalized with ammonium and sulfonate groups.

Hydrogel Description	q [Å^{-1}]	q/q^*	Expected q/q^*	**Microstructure**
PEC hydrogels with C_{bPE} = 30 wt%	0.021	1.000	1.000	HCP Cylinder
	0.037	1.756	1.732	
	0.055	2.634	2.000	
PEC+PEO hydrogels with C_{bPE} = 30 wt% and C_{PEO} = 5 wt%	0.020	1.000	1.000	Lam
	0.041	2.064	2.000	
PEC-IPN hydrogels with C_{bPE} = 30 wt% and C_{PEO} = 5 wt%	0.022	1.000	1.000	Lam
	0.044	1.993	2.000	
PEC hydrogels with C_{bPE} = 40 wt%	0.022	1.000	1.000	Lam
	0.044	1.993	2.000	
	0.066	3.000	3.000	
PEC+PEO hydrogels with C_{bPE} = 40 wt% and C_{PEO} = 5 wt%	0.021	1.000	1.000	Lam
	0.043	2.000	2.000	
	0.064	2.970	3.000	
PEC-IPN hydrogels with C_{bPE} = 40 wt% and C_{PEO} = 5 wt%	0.022	1.000	1.000	Lam
	0.044	1.993	2.000	
	0.066	3.000	3.000	

Table 2-S4. Bragg peak locations and microstructure information for PEC+PEO and PEC-IPN hydrogels with a constant $C_{bPE} = 30$ wt% and varying C_{PEO}. The PEC+PEO and PEC-IPN hydrogels consisted of polyelectrolytes functionalized with ammonium and sulfonate groups.

Hydrogel Description	q [Å^{-1}]	q/q^*	Expected q/q^*	**Microstructure**
PEC hydrogels with $C_{bPE} = 30$ wt%	0.021	1.000	1.000	HCP Cylinder
	0.037	1.756	1.732	
	0.055	2.634	2.000	
PEC+PEO hydrogels with $C_{bPE} = 30$ wt% and $C_{PEO} = 5$ wt%	0.020	1.000	1.000	Lam
	0.041	2.064	2.000	
PEC-IPN hydrogels with $C_{bPE} = 30$ wt% and $C_{PEO} = 5$ wt%	0.022	1.000	1.000	Lam
	0.044	1.993	2.000	
PEC+PEO hydrogels with $C_{bPE} = 30$ wt% and $C_{PEO} = 10$ wt%	0.020	1.000	1.000	Lam
	0.041	2.016	2.000	
	0.061	2.992	3.000	
PEC-IPN hydrogels with $C_{bPE} = 30$ wt% and $C_{PEO} = 10$ wt%	0.022	1.000	1.000	Lam
	0.043	1.942	2.000	
PEC+PEO hydrogels with $C_{bPE} = 30$ wt% and $C_{PEO} = 15$ wt%	0.020	1.000	1.000	Lam
	0.040	2.016	2.000	
	0.060	3.000	3.000	

PEC-IPN hydrogels with $C_{bPE} = 30$ wt% and $C_{PEO} = 15$ wt%	0.020	1.000	1.000	Lam
	0.039	1.968	2.000	
PEC+PEO hydrogels with $C_{bPE} = 30$ wt% and $C_{PEO} = 20$ wt%	0.021	1.000	1.000	Lam
	0.043	2.000	2.000	
	0.065	3.030	3.000	
PEC-IPN hydrogels with $C_{bPE} = 30$ wt% and $C_{PEO} = 20$ wt%	0.021	1.000	1.000	Lam
	0.043	2.000	2.000	

Supplementary Movies

Movie 2-SM1. Movie depicting the injection, settling, and insolubility upon shaking of PEC hydrogels with $C_{bPE} = 10$ wt%. The PEC hydrogels consisted of bPEs functionalized with guanidinium and sulfonate groups.

Movie 2-SM2. Movie depicting the injection, settling, and insolubility upon shaking of PEC+PEO hydrogels with $C_{bPE} = 10$ wt% and $C_{PEO} = 5$ wt%. The PEC+PEO hydrogels consisted of bPEs functionalized with guanidinium and sulfonate groups.

Movie 2-SM3. Movie depicting the injection, settling, and solubility upon shaking of PEO precursor polymers with $C_{PEO} = 5$ wt%.

2.6 Reference

(1) Hunt, J. N.; Feldman, K. E.; Lynd, N. A.; Deek, J.; Campos, L. M.; Spruell, J. M.; Hernandez, B. M.; Kramer, E. J.; Hawker, C. J. Tunable, High Modulus Hydrogels Driven by Ionic Coacervation. *Advanced Materials* **2011**, *23* (20), 2327-2331. DOI: 10.1002/adma.201004230.

(2) Lemmers, M.; Sprakel, J.; Voets, I. K.; van der Gucht, J.; Cohen Stuart, M. A. Multiresponsive Reversible Gels Based on Charge-Driven Assembly. *Angewandte Chemie* **2010**, *122* (4), 720-723. DOI: 10.1002/anie.200905515.

(3) Srivastava, S.; Andreev, M.; Levi, A. E.; Goldfeld, D. J.; Mao, J.; Heller, W. T.; Prabhu, V. M.; de Pablo, J. J.; Tirrell, M. V. Gel Phase Formation in Dilute Triblock Copolyelectrolyte Complexes. *Nature Communications* **2017**, *8* (1), 14131. DOI: 10.1038/ncomms14131.

(4) Krogstad, D. V.; Lynd, N. A.; Choi, S.-H.; Spruell, J. M.; Hawker, C. J.; Kramer, E. J.; Tirrell, M. V. Effects of Polymer and Salt Concentration on the Structure and Properties of Triblock Copolymer Coacervate Hydrogels. *Macromolecules* **2013**, *46* (4), 1512-1518. DOI: 10.1021/ma302299r.

(5) Srivastava, S.; Levi, A. E.; Goldfeld, D. J.; Tirrell, M. V. Structure, Morphology, and Rheology of Polyelectrolyte Complex Hydrogels Formed by Self-Assembly of Oppositely Charged Triblock Polyelectrolytes. *Macromolecules* **2020**, *53* (14), 5763-5774. DOI: 10.1021/acs.macromol.0c00847.

(6) Lemmers, M.; Spruijt, E.; Beun, L.; Fokkink, R.; Leermakers, F.; Portale, G.; Stuart, M. A. C.; van der Gucht, J. The Influence of Charge Ratio on Transient Networks of Polyelectrolyte Complex Micelles. *Soft Matter* **2012**, *8* (1), 104-117. DOI: 10.1039/c1sm06281f.

(7) Lemmers, M.; Spruijt, E.; Akerboom, S.; Voets, I. K.; van Aelst, A. C.; Cohen Stuart, M. A.; van der Gucht, J. Physical Gels Based on Charge-Driven Bridging of Nanoparticles by Triblock Copolymers. *Langmuir* **2012**, *28* (33), 12311-12318. DOI: 10.1021/la301917e.

(8) Krogstad, D. V.; Choi, S.-H.; Lynd, N. A.; Audus, D. J.; Perry, S. L.; Gopez, J. D.; Hawker, C. J.; Kramer, E. J.; Tirrell, M. V. Small Angle Neutron Scattering Study of Complex Coacervate Micelles and Hydrogels Formed from Ionic Diblock and Triblock Copolymers. *The Journal of Physical Chemistry B* **2014**, *118* (45), 13011-13018. DOI: 10.1021/jp509175a.

(9) Krogstad, D. V.; Lynd, N. A.; Miyajima, D.; Gopez, J.; Hawker, C. J.; Kramer, E. J.; Tirrell, M. V. Structural Evolution of Polyelectrolyte Complex Core Micelles and Ordered-Phase Bulk Materials. *Macromolecules* **2014**, *47* (22), 8026-8032. DOI: 10.1021/ma5017852.

(10) Cui, H.; Zhuang, X.; He, C.; Wei, Y.; Chen, X. High Performance and Reversible Ionic Polypeptide Hydrogel Based on Charge-Driven Assembly for Biomedical Applications. *Acta Biomaterialia* **2015**, *11*, 183-190. DOI: 10.1016/j.actbio.2014.09.017.

(11) Papadakis, C. M.; Tsitsilianis, C. Responsive Hydrogels from Associative Block Copolymers: Physical Gelling Through Polyion Complexation. *Gels* **2017**, *3* (1), 3. DOI: 10.3390/gels3010003.

(12) Kim, J.-M.; Heo, T.-Y.; Choi, S.-H. Structure and Relaxation Dynamics for Complex Coacervate Hydrogels Formed by ABA Triblock Copolymers. *Macromolecules* **2020**, *53* (21), 9234-9243. DOI: 10.1021/acs.macromol.0c01600.

(13) Seliktar, D. Designing Cell-Compatible Hydrogels for Biomedical Applications. *Science* **2012**, *336* (6085), 1124-1128. DOI: 10.1126/science.1214804.

(14) Zhang, Y. S.; Khademhosseini, A. Advances in Engineering Hydrogels. *Science* **2017**, *356* (6337), eaaf3627. DOI: 10.1126/science.aaf3627.

(15) Lee, K. Y.; Mooney, D. J. Hydrogels for Tissue Engineering. *Chemical Reviews* **2001**, *101* (7), 1869-1880. DOI: 10.1021/cr000108x.

(16) Nguyen, K. T.; West, J. L. Photopolymerizable Hydrogels for Tissue Engineering Applications. *Biomaterials* **2002**, *23* (22), 4307-4314. DOI: 10.1016/s0142-9612(02)00175-8.

(17) Khademhosseini, A.; Langer, R. Microengineered Hydrogels for Tissue Engineering. *Biomaterials* **2007**, *28* (34), 5087-5092. DOI: 10.1016/j.biomaterials.2007.07.021.

(18) Wang, H.; Heilshorn, S. C. Adaptable Hydrogel Networks with Reversible Linkages for Tissue Engineering. *Advanced Materials* **2015**, *27* (25), 3717-3736. DOI: 10.1002/adma.201501558.

(19) Mehdizadeh, M.; Yang, J. Design Strategies and Applications of Tissue Bioadhesives. *Macromolecular Bioscience* **2013**, *13* (3), 271-288. DOI: 10.1002/mabi.201200332.

(20) Peak, C. W.; Wilker, J. J.; Schmidt, G. A Review on Tough and Sticky Hydrogels. *Colloid and Polymer Science* **2013**, *291* (9), 2031-2047. DOI: 10.1007/s00396-013-3021-y.

(21) Scognamiglio, F.; Travan, A.; Rustighi, I.; Tarchi, P.; Palmisano, S.; Marsich, E.; Borgogna, M.; Donati, I.; de Manzini, N.; Paoletti, S. Adhesive and Sealant Interfaces for General Surgery Applications. *Journal of Biomedical Materials Research Part B: Applied Biomaterials* **2016**, *104* (3), 626-639. DOI: 10.1002/jbm.b.33409.

(22) Kord Forooshani, P.; Lee, B. P. Recent Approaches in Designing Bioadhesive Materials Inspired by Mussel Adhesive Protein. *Journal of Polymer Science Part A: Polymer Chemistry* **2017**, *55* (1), 9-33. DOI: 10.1002/pola.28368.

(23) Bhagat, V.; Becker, M. L. Degradable Adhesives for Surgery and Tissue Engineering. *Biomacromolecules* **2017**, *18* (10), 3009-3039. DOI: 10.1021/acs.biomac.7b00969.

(24) Li, J.; Celiz, A.; Yang, J.; Yang, Q.; Wamala, I.; Whyte, W.; Seo, B.; Vasilyev, N.; Vlassak, J.; Suo, Z. Tough Adhesives for Diverse Wet Surfaces. *Science* **2017**, *357* (6349), 378-381. DOI: 10.1126/science.aah6362.

(25) Chen, X.; Yuk, H.; Wu, J.; Nabzdyk, C. S.; Zhao, X. Instant Tough Bioadhesive with Triggerable Benign Detachment. *Proceedings of the National Academy of Sciences* **2020**, *117* (27), 15497-15503. DOI: 10.1073/pnas.2006389117.

(26) Gao, Y.; Han, X.; Chen, J.; Pan, Y.; Yang, M.; Lu, L.; Yang, J.; Suo, Z.; Lu, T. Hydrogel-Mesh Composite for Wound Closure. *Proceedings of the National Academy of Sciences* **2021**, *118* (28). DOI: 10.1073/pnas.2103457118.

(27) Hoare, T. R.; Kohane, D. S. Hydrogels in Drug Delivery: Progress and Challenges. *Polymer* **2008**, *49* (8), 1993-2007. DOI: 10.1016/j.polymer.2008.01.027.

(28) Kesharwani, P.; Bisht, A.; Alexander, A.; Dave, V.; Sharma, S. Biomedical Applications of Hydrogels in Drug Delivery System: An Update. *Journal of Drug Delivery Science and Technology* **2021**, *66*, 102914. DOI: 10.1016/j.jddst.2021.102914.

(29) Li, J.; Mooney, D. J. Designing Hydrogels for Controlled Drug Delivery. *Nature Reviews Materials* **2016**, *1* (12), 1-17. DOI: 10.1038/natrevmats.2016.71.

(30) Dimatteo, R.; Darling, N. J.; Segura, T. In situ Forming Injectable Hydrogels for Drug Delivery and Wound Repair. *Advanced Drug Delivery Reviews* **2018**, *127*, 167-184. DOI: 10.1016/j.addr.2018.03.007.

(31) Pakulska, M. M.; Vulic, K.; Tam, R. Y.; Shoichet, M. S. Hybrid Crosslinked Methylcellulose Hydrogel: A Predictable and Tunable Platform for Local Drug Delivery. *Advanced Materials* **2015**, *27* (34), 5002-5008. DOI: 10.1002/adma.201502767.

(32) Yang, C.; Suo, Z. Hydrogel Ionotronics. *Nature Reviews Materials* **2018**, *3* (6), 125-142. DOI: 10.1038/s41578-018-0018-7.

(33) Deng, J.; Yuk, H.; Wu, J.; Varela, C. E.; Chen, X.; Roche, E. T.; Guo, C. F.; Zhao, X. Electrical Bioadhesive Interface for Bioelectronics. *Nature Materials* **2020**, 1-8. DOI: 10.1038/s41563-020-00814-2.

(34) Cao, Y.; Mezzenga, R. Design Principles of Food Gels. *Nature Food* **2020**, *1* (2), 106-118. DOI: 10.1038/s43016-019-0009-x.

(35) Li, J.; Jia, X.; Yin, L. Hydrogel: Diversity of Structures and Applications in Food Science. *Food Reviews International* **2021**, *37* (3), 313-372. DOI: 10.1080/87559129.2020.1858313.

(36) Jiang, J.; Chen, E.-Q.; Yang, S. The Effect of Ion Pairs on Coacervate-Driven Self-Assembly of Block Polyelectrolytes. *Journal of Chemical Physics* **2021**, *154* (14), 144903. DOI: 10.1063/5.0044845.

(37) Audus, D. J.; Gopez, J. D.; Krogstad, D. V.; Lynd, N. A.; Kramer, E. J.; Hawker, C. J.; Fredrickson, G. H. Phase Behavior of Electrostatically Complexed Polyelectrolyte Gels Using an Embedded Fluctuation Model. *Soft Matter* **2015**, *11* (6), 1214-1225. DOI: 10.1039/c4sm02299h.

(38) Audus, D. J.; Fredrickson, G. H. Field-Based Simulations of Nanostructured Polyelectrolyte Gels. In *Materials for Energy Infrastructure*, Springer, 2016; pp 1-9.

(39) Staňo, R.; Košovan, P.; Tagliabue, A.; Holm, C. Electrostatically Cross-Linked Reversible Gels—Effects of pH and Ionic Strength. *Macromolecules* **2021**, *54* (10), 4769-4781. DOI: 10.1021/acs.macromol.1c00470.

(40) Sun, T. L.; Kurokawa, T.; Kuroda, S.; Ihsan, A. B.; Akasaki, T.; Sato, K.; Haque, M. A.; Nakajima, T.; Gong, J. P. Physical Hydrogels Composed of Polyampholytes Demonstrate High Toughness and Viscoelasticity. *Nature Materials* **2013**, *12* (10), 932. DOI: 10.1038/nmat3713.

(41) Shi, R.; Sun, T. L.; Luo, F.; Nakajima, T.; Kurokawa, T.; Bin, Y. Z.; Rubinstein, M.; Gong, J. P. Elastic–Plastic Transformation of Polyelectrolyte Complex Hydrogels from Chitosan and Sodium Hyaluronate. *Macromolecules* **2018**, *51* (21), 8887-8898. DOI: 10.1021/acs.macromol.8b01658.

(42) Sun, T. L.; Cui, K.; Gong, J. P. Tough, Self-Recovery and Self-Healing Polyampholyte Hydrogels. *Polymer Science, Series C* **2017**, *59* (1), 11-17. DOI: 10.1134/S1811238217010118.

(43) Fan, H.; Wang, J.; Gong, J. P. Barnacle Cement Proteins-Inspired Tough Hydrogels with Robust, Long-Lasting, and Repeatable Underwater Adhesion. *Advanced Functional Materials* **2020**, *31* (11). DOI: 10.1002/adfm.202009334.

(44) Li, S. H.; Pan, H. Y.; Wang, Y. T.; Sun, J. Q. Polyelectrolyte Complex-Based Self-Healing, Fatigue-Resistant and Anti-Freezing Hydrogels as Highly Sensitive Ionic Skins. *Journal of Materials Chemistry A* **2020**, *8* (7), 3667-3675. DOI: 10.1039/c9ta13213a.

(45) Luo, F.; Sun, T. L.; Nakajima, T.; Kurokawa, T.; Zhao, Y.; Sato, K.; Ihsan, A. B.; Li, X.; Guo, H.; Gong, J. P. Oppositely Charged Polyelectrolytes Form Tough, Self-Healing, and Rebuildable Hydrogels. *Advanced Materials* **2015**, *27* (17), 2722-2727. DOI: 10.1002/adma.201500140.

(46) Li, G.; Zhang, G.; Sun, R.; Wong, C.-P. Dually pH-Responsive Polyelectrolyte Complex Hydrogel Composed of Polyacrylic Acid and Poly (2-(Dimthylamino) Ethyl Methacrylate). *Polymer* **2016**, *107*, 332-340. DOI: 10.1016/j.polymer.2016.11.037.

(47) Liu, Q.; Dong, Z.; Ding, Z.; Hu, Z.; Yu, D.; Hu, Y.; Abidi, N.; Li, W. Electroresponsive Homogeneous Polyelectrolyte Complex Hydrogels from Naturally Derived Polysaccharides. *ACS Sustainable Chemistry & Engineering* **2018**, *6* (5), 7052-7063. DOI: 10.1021/acssuschemeng.8b00921.

(48) Lemmers, M.; Voets, I. K.; Stuart, M. A. C.; van der Gucht, J. Transient Network Topology of Interconnected Polyelectrolyte Complex Micelles. *Soft Matter* **2011**, *7* (4), 1378-1389. DOI: 10.1039/c0sm00767f.

(49) Lee, A. L. Z.; Voo, Z. X.; Chin, W.; Ono, R. J.; Yang, C.; Gao, S.; Hedrick, J. L.; Yang, Y. Y. Injectable Coacervate Hydrogel for Delivery of Anticancer Drug-Loaded Nanoparticles in vivo. *ACS Applied Materials & Interfaces* **2018**, *10* (16), 13274-13282. DOI: 10.1021/acsami.7b14319.

(50) Gao, S.; Holkar, A.; Srivastava, S. Protein-Polyelectrolyte Complexes and Micellar Assemblies. *Polymers* **2019**, *11* (7), 1097. DOI: 10.3390/polym11071097.

(51) Magana, J. R.; Sproncken, C. C. M.; Voets, I. K. On Complex Coacervate Core Micelles: Structure-Function Perspectives. *Polymers* **2020**, *12* (9), 1953. DOI: 10.3390/polym12091953.

(52) Chen, F.; Stenzel, M. H. Polyion Complex Micelles for Protein Delivery. *Australian Journal of Chemistry* **2018**, *71* (10), 768-780. DOI: 10.1071/Ch18219.

(53) Horn, J. M.; Kapelner, R. A.; Obermeyer, A. C. Macro-and Microphase Separated Protein-Polyelectrolyte Complexes: Design Parameters and Current Progress. *Polymers* **2019**, *11* (4), 578. DOI: 10.3390/polym11040578.

(54) Shah, S.; Leon, L. Structural Dynamics, Phase behavior, and Applications of Polyelectrolyte Complex Micelles. *Current Opinion in Colloid & Interface Science* **2021**, *53*, 101424. DOI: 10.1016/j.cocis.2021.101424.

(55) Discher, D. E.; Mooney, D. J.; Zandstra, P. W. Growth Factors, Matrices, and Forces Combine and Control Stem Cells. *Science* **2009**, *324* (5935), 1673-1677. DOI: 10.1126/science.1171643.

(56) Engler, A. J.; Sen, S.; Sweeney, H. L.; Discher, D. E. Matrix Elasticity Directs Stem Cell Lineage Specification. *Cell* **2006**, *126* (4), 677-689. DOI: 10.1016/j.cell.2006.06.044.

(57) Discher, D. E.; Janmey, P.; Wang, Y.-l. Tissue Cells Feel and Respond to the Stiffness of Their Substrate. *Science* **2005**, *310* (5751), 1139-1143. DOI: 10.1126/science.1116995.

(58) Kamata, H.; Li, X.; Chung, U.-i.; Sakai, T. Design of Hydrogels for Biomedical Applications. *Advanced Healthcare Materials* **2015**, *4* (16), 2360-2374. DOI: 10.1002/adhm.201500076.

(59) Yang, H.; Ghiassinejad, S.; van Ruymbeke, E.; Fustin, C.-A. Tunable Interpenetrating Polymer Network Hydrogels Based on Dynamic Covalent Bonds and Metal–Ligand Bonds. *Macromolecules* **2020**, *53* (16), 6956-6967. DOI: 10.1021/acs.macromol.0c00494.

(60) Dhand, A. P.; Galarraga, J. H.; Burdick, J. A. Enhancing Biopolymer Hydrogel Functionality through Interpenetrating Networks. *Trends in Biotechnology* **2021**, *39* (5), 519-538. DOI: 10.1016/j.tibtech.2020.08.007.

(61) Waters, D. J.; Engberg, K.; Parke-Houben, R.; Ta, C. N.; Jackson, A. J.; Toney, M. F.; Frank, C. W. Structure and Mechanism of Strength Enhancement in Interpenetrating Polymer Network Hydrogels. *Macromolecules* **2011**, *44* (14), 5776-5787. DOI: 10.1021/ma200693e.

(62) Dragan, E. S. Design and Applications of Interpenetrating Polymer Network Hydrogels. A Review. *Chemical Engineering Journal* **2014**, *243*, 572-590. DOI: 10.1016/j.cej.2014.01.065.

(63) Myung, D.; Waters, D.; Wiseman, M.; Duhamel, P. E.; Noolandi, J.; Ta, C. N.; Frank, C. W. Progress in the Development of Interpenetrating Polymer Network Hydrogels. *Polymers for Advanced Technologies* **2008**, *19* (6), 647-657. DOI: 10.1002/pat.1134.

(64) Silverstein, M. S. Interpenetrating Polymer Networks: So Happy Together? *Polymer* **2020**, *207*, 122929. DOI: 10.1016/j.polymer.2020.122929.

(65) Ilavsky, J.; Jemian, P. R. Irena: Tool Suite for Modeling and Analysis of Small-Angle Scattering. *Journal of Applied Crystallography* **2009**, *42* (2), 347-353. DOI: 10.1107/S0021889809002222.

(66) Wu, H.; Ting, J. M.; Yu, B.; Jackson, N. E.; Meng, S.; de Pablo, J. J.; Tirrell, M. V. Spatiotemporal Formation and Growth Kinetics of Polyelectrolyte Complex Micelles with Millisecond Resolution. *ACS Macro Letters* **2020**, *9* (11), 1674-1680. DOI: 10.1021/acsmacrolett.0c00543.

(67) Takahashi, R.; Narayanan, T.; Yusa, S.; Sato, T. Formation Kinetics of Polymer Vesicles from Spherical and Cylindrical Micelles Bearing the Polyelectrolyte Complex Core Studied by Time-Resolved USAXS and SAXS. *Macromolecules* **2022**, *55* (2), 684-695. DOI: 10.1021/acs.macromol.1c02210.

(68) Amann, M.; Diget, J. S.; Lyngsø, J.; Pedersen, J. S.; Narayanan, T.; Lund, R. Kinetic Pathways for Polyelectrolyte Coacervate Micelle Formation Revealed by Time-Resolved Synchrotron SAXS. *Macromolecules* **2019**, *52* (21), 8227-8237. DOI: 10.1021/acs.macromol.9b01072.

(69) Liu, X.; Haddou, M.; Grillo, I.; Mana, Z.; Chapel, J.-P.; Schatz, C. Early Stage Kinetics of Polyelectrolyte Complex Coacervation Monitored through Stopped-Flow Light Scattering. *Soft Matter* **2016**, *12* (44), 9030-9038. DOI: 10.1039/c6sm01979j.

(70) Guinier, A.; Fournet, G. *Small-angle Scattering of X-rays*; John Wiley and Sons, New York, NY 1955.

(71) Kratky, O.; Porod, G. *Small angle X-ray Scattering*; Academic Press, New York, NY 1982.

(72) Krogstad, D. V. Investigating the Structure-Property Relationships of Aqueous Self-Assembled Materials. University of California, Santa Barbara, 2012.

(73) Bian, S.; Zheng, Z.; Liu, Y.; Ruan, C.; Pan, H.; Zhao, X. A Shear-Thinning Adhesive Hydrogel Reinforced by Photo-Initiated Crosslinking as a Fit-to-Shape Tissue Sealant. *Journal of Materials Chemistry B* **2019**, *7* (42), 6488-6499. DOI: 10.1039/C9TB01521C.

(74) Townsend, J. M.; Beck, E. C.; Gehrke, S. H.; Berkland, C. J.; Detamore, M. S. Flow Behavior Prior to Crosslinking: The Need for Precursor Rheology for Placement of Hydrogels in Medical Applications and for 3D Bioprinting. *Progress in Polymer Science* **2019**, *91*, 126-140. DOI: 10.1016/j.progpolymsci.2019.01.003.

Chapter 3

PEC/PEGDA IPN Hydrogels: Influence of PEGDA Molecular Weight

Abstract

Polyelectrolyte complexes (PEC) hydrogels, formed by mixing oppositely charged block polyelectrolytes, feature versatile microstructures, rapid self-assembly, self-healing properties, and environmental responsiveness. Recently, interpenetration of PEC and covalent networks has emerged as an effective strategy to create polyelectrolyte complex/covalent interpenetrating polymer networks (IPN) hydrogels, which combined advantages and minimize drawbacks from each single network. However, it remains poorly understood how precursor chain length or covalent network mesh size affects PEC IPN hydrogel properties. In this work, we employed photo-crosslinkable poly(ethylene glycol) diacrylate (PEGDA) with five different molecular weights (0.7, 1.5, 6, 10, and 20 kg/mol) to individually interpenetrate with PEC networks to investigate the influence of PEGDA precursor molecular weight and network mesh size on the microstructures, shear moduli, and tensile properties of resulting hydrogels. We found that longer PEGDA chains had a higher ability to induce microstructural and disorder-order transition. Before photocrosslinkinig, adding PEGDA with large MWs (6, 10, and 20 kg/mol) resulted in lower shear moduli of PEC+PEGDA hydrogels because longer PEGDA chains caused macromolecular crowding, perturbed PEC domain formation, and reduced partial connectivity of PEC networks. After photo-crosslinking, PEGDA networks were interpenetrated with PEC networks and formed PEC IPN hydrogels, which possessed synergistic effects on both shear and tensile performance

regardless of different PEGDA network mesh sizes. As PEGDA MW was decreased, the shear moduli of PEC/PEGDA IPN hydrogels were increased due to higher crosslinking density, demonstrating an approach to achieve mechanical tunability without changing polymer concentration. Upon decreasing PEGDA MW, the extensibility and toughness of PEC/PEGDA IPN hydrogels were reduced while their Young's moduli were reinforced, suggesting an important role of PEGDA network mesh size on the tensile properties. It is important to highlight that the interpenetration strategy overcame the stiffness-toughness and stiffness-extensibility tradeoffs in all PEC/PEGDA IPN hydrogels despite different PEGDA MWs. We envision that a clear relationship between precursor polymer MW and hydrogel properties will provide a reference to design PEC-based hydrogels with the physical and mechanical properties required by biomedical applications.

3.1 Introduction

Hydrogels, comprising of three-dimensional polymer networks, have received ever-increasing attraction as scaffolds for tissue engineering,[1-4] drug delivery,[5-9] biomedicine,[10, 11] and bioadhesives.[12-19] Polyelectrolyte complexes (PEC) hydrogels,[20-32] whose formation by electrostatic interaction is driven between oppositely charged polyelectrolytes,[20, 24, 25, 31] present an exciting approach to combine or interpenetrate with covalent network hydrogels to further develop their properties.[31] The PEC hydrogels rapidly assemble within seconds[20, 28, 33-36] upon mixing oppositely charged block-polyelectrolytes and featured versatile microstructures,[24, 27, 37-40] which differentiate ionically crosslinked hydrogels formed by oppositely charged homo-polyelectrolytes.[41-48] The oppositely charged blocks of polyelectrolytes attract each other and form PEC domains acting as network joints while the neutral blocks connected them to form networks. The electrostatic interaction nature of PEC hydrogels attribute to stimuli-responsiveness (pH and salt),[20, 21, 26-28, 49] controllable shear properties,[21, 23, 24, 27, 28, 30, 49] injectability,[30, 50] self-healing properties,[30, 50] and encapsulate and delivery charged macromolecules, such as nucleic acid and proteins.[51-55]

However, weak ionic interactions and reconfigurable nature of PEC networks typically contribute to their weak shear moduli (typically < 20 kPa) and negligible strength,[24] restricting applications. In comparison, covalent hydrogels typically feature strong mechanical strength and Young's moduli but confront long-standing challenges in stiffness-extensibility and stiffness-toughness tradeoff issues, meaning these properties cannot be improved simultaneously by changing polymer concentration. Interpenetration between two polymer networks has been employed previously to acquire mechanical strength, toughness, and stimuli-responsive properties.[31, 56-64] Our previous works had demonstrated that a combination of PEC and photocrosslinkable covalent networks

integrated advantages and unique features from each network and meanwhile mitigate their disadvantages.[31] Before formation of covalent networks, PEC networks act as protective structures to provide tunable viscosity and shear strength for PEC+precursor hydrogels, enhancing interlayer bonding and avoiding secondary flow issues in wound dressing and extrusion-based 3D bioprinting applications. After photocrosslinking, interpenetration between PEC and covalent networks experience remarkable improvements in terms of mechanical strength, stiffness, and toughness owing to polymer entanglements between two interpenetrated networks and energy-dissipative structure of PEC networks. The interpenetration strategy overcomes the tradeoffs limiting covalent hydrogels and contributes to synergistic effects in mechanical properties, inaccessible by either network. We have demonstrated the compatibility of PEC networks with four different kinds of representative covalent networks formed by 4-arm poly(ethylene glycol) acrylate (4-arm PEGA), poly(ethylene glycol) diacrylate (PEGDA), acrylamide (AAm), and gelatin methacryloyl (GelMA), which contain different molecular structures, crosslinking mechanisms, and polymer origin (Chapter 4). An interesting feature was that an increase of 4-arm PEGA concentration progressively lowered shear moduli of resulting PEC+precursor hydrogels (Chapter 2); the corresponding mechanism behind this decay remain poorly understood. Moreover, it remains unclear whether the interpenetration strategy still produces synergistic effects when covalent networks with different mesh sizes are used. To the best of our knowledge, no prior scientific report has systematically studied the influence of covalent polymer chain length or mesh size on disorder-order transition and mechanical properties of hydrogels comprising interpenetrated PEC and covalent networks.

Herein, we employed poly(ethylene glycol) diacrylate (PEGDA) with five different MWs (0.7, 1.5, 6, 10, and 20 kg/mol) to fabricate the covalent networks with different mesh sizes, which were

interpenetrated with PEC networks to form polyelectrolyte complex-interpenetrating polymer networks (PEC/PEGDA IPN) hydrogels as a model system to systematically study the influence of precursor MW on the properties of resulting hydrogel properties. Owing to the same linear polymer structure, the mesh size of PEGDA networks varies monotonically with PEGDA MW. The nanoscale physical attributes, shear moduli, and tensile properties of hydrogels were characterized by small-angle X-ray scattering (SAXS), rheology, and tensile testing, respectively. The microstructures of hydrogels were summarized and compared in the morphological maps with parameters of block polyelectrolyte concentration (C_{bPE}), PEGDA concentration (C_P), and PEGDA MW. The PEGDA with larger MWs possessed a higher ability to induce microstructural and disorder-order transition. Before photo-crosslinking, addition of the PEGDA with larger MWs (6, 10, and 20 kg/mol) led to more decline in shear moduli of PEC+PEGDA hydrogels and while the PEGDA with smaller MWs (0.7 and 1.5 kg/mol) had limited influence. After photo-crosslinking, all PEC/PEGDA IPN hydrogels achieved remarkable improvements and synergistic effects in both shear moduli and tensile properties, which were unreachable by either PEC or covalent networks. PEGDA with a smaller MW led to higher shear moduli owing to a higher crosslinking density of PEGDA networks. In terms of tensile performance, despite different PEGDA MWs, the PEC/PEGDA IPN hydrogels still broke the stiffness-toughness tradeoff and enhanced tensile strength, Young's moduli, and toughness while remaining similar extensibility. Upon decreasing PEGDA MW, the extensibility and toughness of PEC/PEGDA IPN hydrogels were reduced while their Young's moduli were increased, suggesting PEGDA mesh size played an important role in PEC/PEGDA IPN hydrogel properties. Overall, the PEC network platform exhibited high compatibility with covalent networks with different mesh sizes. We envision that a comprehensive understanding of the relationship between covalent networks and physical and

mechanical properties of resultant hydrogels provides a guideline to design controllable and predictable properties of PEC-based hydrogels, another step toward biomedical applications.

3.2 Experimental methods

Materials: Poly(ethylene oxide) (PEO) with molecular weights of 1.5 kg/mol, 6 kg/mol, 10 kg/mol, and 20 kg/mol, Celite, naphthalene, calcium hydride, allyl glycidyl ether (AGE), potassium chunk, sodium 3-mercapto-1-propanesulfonate, 2,2-dimethoxy-2-phenylacetophenone, cysteamine hydrochloride, 1-H-pyrazole-1-carboxamidine hydrochloride, poly(ethylene glycol) diacrylate (MW = 0.7 kg/mol), and Irgacure 2959 were purchased from Sigma-Aldrich.

Polyelectrolytes Synthesis: *ABA* triblock poly(ally glycidyl ether)$_{65}$-*b*-poly(ethylene oxide)$_{455}$-*b*-poly(ally glycidyl ether)$_{65}$ (PAGE$_{65}$-PEO$_{455}$-PAGE$_{65}$) was synthesized via anionic polymerization.[20] Allyl glycidyl ether (AGE) was dried with calcium hydride overnight, degassed by three cycles of freeze-pump-thaw, and then purified by distillation. 20 grams of polyethylene glycol (PEG, MW 20 kg/mol) were dried in a vacuum for 12 hours and then dissolved in ~60 ml anhydrous tetrahydrofuran (THF) at 45 °C in a 250 ml round bottom flask in a glove box full of Argon gas. The PEO solution was slowly added with 0.4 M potassium naphthalenide in anhydrous THF solvent until it became light green. An appropriate volume of AGE was injected into the PEG solution. The reaction was continued for 48 hours at 45 °C and then was stopped by adding 10 mL degassed methanol. The final product was precipitated in hexane solvent, filtered, and dried in a vacuum for the following thiol-ene click reactions.

The PAGE$_{65}$-PEO$_{455}$-PAGE$_{65}$ was functionalized with either ammonium or sulfonate groups via thiol-ene click reactions. Ammonium functionalization was performed by dissolving 2 g PAGE$_{65}$-PEO$_{455}$-PAGE$_{65}$ in a mixture solvent (15 ml DMF and 15 ml water) in a 100 mL round bottom

flask. Cysteamine hydrochloride, in a 5-fold molar amount of alkene group of $PAGE_{65}$-PEO_{455}-$PAGE_{65}$, was added to functionalize $PAGE_{65}$-PEO_{455}-$PAGE_{65}$ with ammonium moieties with the aid of photoinitiator, 2,2-dimethoxy-2-phenylacetophenone, 0.05 Equiv. per alkene, under ultraviolet light (8 watts and 365 nm) for at least 6 hours. The same method was applied to synthesize sulfonate-functionalized $PAGE_{65}$-PEO_{455}-$PAGE_{65}$ by replacing cysteamine hydrochloride with sodium 3-mercapto-1-propanesulfonate. 2 grams of ammonium-functionalized $PAGE_{65}$-PEO_{455}-$PAGE_{65}$ was further reacted with 1H-Pyrazole-1-1-carboxamidine hydrochloride in phosphate-buffered saline (PBS) buffer solution with pH =10 to convert ammonium groups to guanidinium groups.[20] All product solutions were first purified by 14 cycles of dialysis in deionized water and then followed by lyophilized to obtain dry final products, which were characterized by ^{1}H NMR (**Figure 3-S1**).

Poly(ethylene glycol) Diacrylate (PEGDA) Synthesis and Characterization: Polyethylene glycol (PEG) with molecular weight (1.5, 6, 10, and 20 kg/mol) was dried in a vacuum oven at room temperature for at least 12 hours. 30 grams of PEG was dissolved in 160 mL anhydrous toluene with stirring, and then the solution was heated up to ~125 °C to distill 40 ml toluene to evaporate any trace amount of water. Afterward, the solution temperature was adjusted to 40 °C and maintained at this temperature for reaction, and meanwhile, the solution was continuously degassed by nitrogen gas. Triethylamine (TEA), in a 4-fold molar amount of -OH group of PEG, was added to the PEG solution. After 10 minutes of adding TEA, acryloyl chloride, with a 4-fold molar amount of -OH group of PEG, was injected slowly into the PEG solution. After 90 minutes, the product solution was filtered twice by a Buchner funnel half full of Celite to remove insoluble salts. The resultant solution was precipitated in 4 °C hexane to precipitate the product PEG, which was dried under vacuum and then characterized by ^{1}H NMR (**Figure 3-S2**, **Figure 3-S3**). The

substitution efficiency of PEG terminal -OH for acrylate was calculated based on comparing the integral areas under PEG backbone peak (around 3.5 ppm) and two-ended acrylate peaks (approximately 5.8 -6.4 ppm).[65, 66]

$$\text{Acrylation}\% = \frac{PEG\ \text{MW}}{\left(\frac{\text{Area under PEG Backbone} \times 6}{\text{Area under Acrylate} \times 4} \times 44\right)} \times 100\%$$

Hydrogel Preparation: The PEGDA, guanidinium- and sulfonate-functionalized bPEs were separately dissolved in deionized water to prepare 50 wt% stock solutions. An appropriate amount of photoinitiator Irgacure 2959 was dissolved in deionized water to prepare 5 wt% stock solutions, which were preheated to dissolve before each use. The PEC hydrogels were prepared by mixing a designed amount of oppositely charged bPEs stock solution in deionized water to reach a targeted bPEs concentration (C_{bPE}) and meanwhile maintaining the equimolar charge ratio. The PEC+PEG hydrogels were first prepared by vortex-mixing appropriate amounts of the sulfonate bPEs, PEGDA, and photoinitiator in deionized water to produce a homogeneous solution, which was followed by adding an appropriate amount of guanidinium bPEs stock solution to reach the equimolar charge ratio between oppositely charged bPEs. PEC/PEGDA IPN hydrogels were formed by exposing the corresponding PEC+PEGDA hydrogels under ultraviolet light (wavelength: 302 nm; 8 watts) for 10 minutes.

Rheology: All rheological measurements were performed by an Anton Paar (MCR 203) rheometer with a solvent cap at 25 °C. PEC hydrogels and PEC+PEGDA hydrogels were transferred by a positive displacement pipette to a rheometer plate and then measured by a cone plate with a diameter of 10 mm and cone angle of 2°. The PEC/PEGDA IPN hydrogels were prepared by first loading the PEC+PEGDA material into a polydimethylsiloxane (PDMS) with the dimensions (diameter: 8 mm and height: 8 mm), and then followed by 10 minutes of UV light irradiation.

Before each measurement, an oscillatory pre-shear at strain (γ) of 0.8% and frequency (ω) of 1 rad/s were performed to reach a steady state. The linear viscoelastic (LVE) regime was determined by running amplitude sweeps at frequency ω = 1 rad/s and with the strain ranging from 0.01% to 100% (**Figure 3-S4**). Frequency sweeps were measured at the γ = 0.8 %, which reflected the viscoelastic properties of hydrogels within the LEV regime.

Tensile Characterization: All tensile measurements were carried out with a stretching rate of 9 mm/min on an Instron 5542 mechanical tester. Tensile samples were prepared by loading PEGDA precursor or PEC+PEGDA hydrogels into a PDMS mode with a geometric feature (18 mm × 4.5 mm × 1 mm) and followed by UV light exposure. The two ends of hydrogel samples were fixed on a double-sized tape via a small amount of superglue, and the double size tapes were clipped by the machine tension grips. During the tests, the stress and corresponding strain data were continuously collected until the hydrogel rupture. The tensile properties were averaged by at least four samples.

Small-angle X-ray scattering (SAXS): SAXS characterization experiments were carried out at beamline 12-ID-B in the Advanced Photon Source, Argonne National Laboratory with a detector distance of 2 meters and the X-ray power of 13.3 keV. All PEC, PEC+PEGDA, and PEC/PEGDA IPN hydrogels were loaded in the solid sample holders provided by the beamline and then sealed by Kapton tape on both sides to avoid water evaporation. The solid sample holders, made from clear resin, contained 10 × 10 cells with 8 mm spacing. The X-ray scattering exposure time was set to 0.1 s. The two-dimensional SAXS data were converted to one-dimensional intensity I(q) by employing the matSAXS package. The final sample scattering data was acquired by removing the background data from the raw intensity data.

Radius of Gyration of PEGDA chains and Mesh Size of PEGDA Networks: Radius of gyration R_g is typically used to estimate the size of random polymer coil chains in solution. The R_g of PEGDA were calculated by using $R_g = \sqrt{Nb^2/6}$, where N is the number of PEO Kuhn block and b is the PEO Kuhn block length (1.1 nm). An overlap concentration (C^*) of each PEGDA with different MWs is necessary to compute the mesh size of covalently crosslinked PEGDA networks. The overlap concentration reflects the polymer concentration, where the polymer chains started to overlap and interact with each other. The overlap concentration can be $C^* = M/(4/3\pi R_g^3 N_A)$, where M is molecular weight, and N_A is Avogadro's number. The correlation block (ξ_c) can be employed to compute covalent network size depending on polymer concentration. Equation (1) is applied in a dilute polymer concentration, and Equation (2) suits a semidilute polymer solution.

$$\xi_c \cong R_g \quad (C < C^*) \qquad (1)$$

$$\xi_c \cong R_g \left(\frac{C}{C^*}\right)^{-\frac{\nu}{3\nu-1}} \quad (C \geq C^*) \qquad (2)$$

where C is polymer concentration, and ν is the Flory exponent (ν = 3/5 for good solvent).

3.3 Results and Discussion

Combination of PEC networks and PEGDA chains with different molecular weights is an effective method to systematically investigate the influence induced by PEGDA MWs and crosslinking density owing to the controllable synthetic nature of PEGDA and bPE chains. Owing to the same linear polymer structure, PEGDA with a larger MW possesses a longer chain. Upon increasing MW, the R_g of PEGDA chains and the mesh size of PEGDA networks are progressively increased, as shown in **Figure 3-S5A**. The complexation-induced PEC networks are assembled by mixing

oppositely charged bPE chains. Oppositely two-end charged blocks of bPEs chains assemble spontaneously and form PEC domains driven by electrostatic interaction, and meanwhile the middle block PEO chains act as bridges connecting the PEC domains to form 3-D physical networks (**Figure 3-1A**). PEC+PEGDA hydrogels are prepared by homogeneously mixing PEGDA and bPEs chains, in which the bPEs self-assemble to form PEC networks with the presence of PEGDA chains (**Figure 3-1B**). Upon ultraviolet light (302 nm) irradiation, the PEGDA chains crosslink with each other via covalent bonding in the two-end acrylate groups. The interpenetration between PEGDA and PEC networks leads to PEC/PEGDA IPN hydrogels (**Figure 3-1C**).

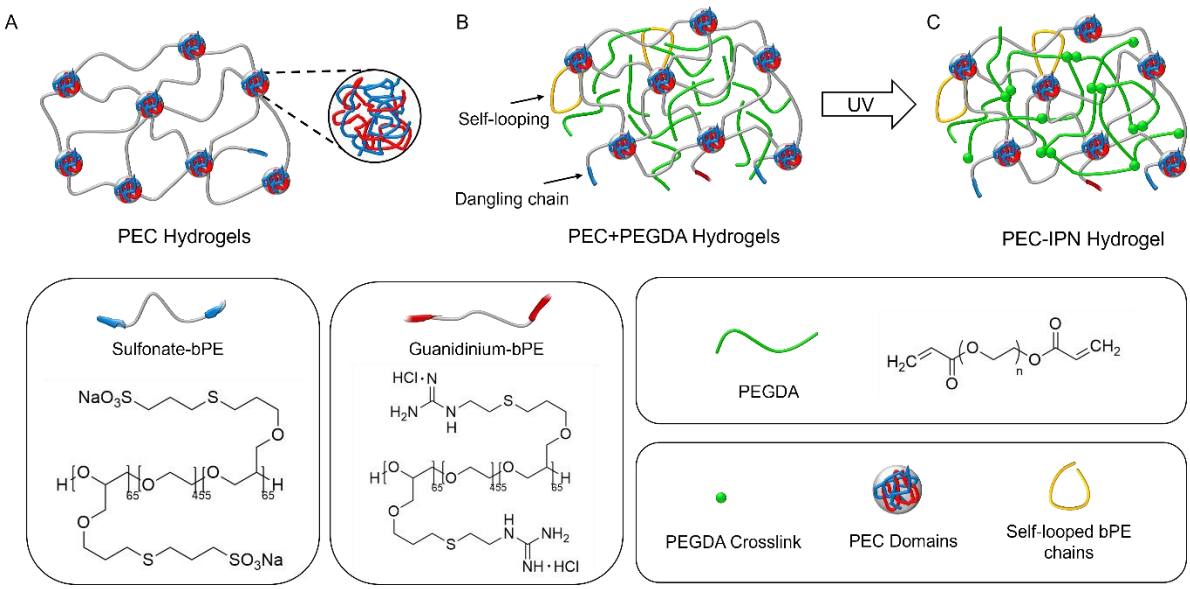

Figure 3-1. Schematic illustration of **(A)** Polyelectrolyte complex (PEC) hydrogels, **(B)** PEC+PEGDA hydrogels, and **(C)** Polyelectrolyte complex-interpenetrating polymer network (PEC/PEGDA IPN) hydrogels.

3.3.1 Nanoscale Microstructure of PEC+PEGDA and PEC/PEGDA IPN Hydrogels

Small-angle X-ray scattering (SAXS) is a highly effective and fast technique to capture the nanoscale physical properties (e.g., size, shape, and spatial distance) of soft materials, such as micelles, proteins, and hydrogels. In this work, the PEC domains contained highly dense charged blocks of bPE chain and relatively high atomic number of elements (e.g., sulfur and nitrogen atoms), which provided higher electron contrast than surrounding environments to examine PEC domain arrangement and size distribution via synchrotron X-ray scattering. The one-dimensional SAXS intensity profiles $I(q)$ were acquired by averaging the two-dimensional scatterings information across all azimuthal angles and then followed by removing water background scattering patterns. SAXS scattering intensity $I(q)$ generally are characterized as the product of form factor $P(q)$ and structure factor $S(q)$, wherein the former captures scattering information of an individual scatter and the latter describes the spatial correlation among scatters.[67, 68]

Representative 1-D SAXS patterns of $I(q)$ as a function of wave factor q are shown in **Figure 3-2A** for PEC hydrogel (grey) with C_{bPE} = 10 wt%, and the PEC+PEGDA (blue) and PEC/PEGDA IPN (red) hydrogels with a constant C_{bPE} = 10 wt% and C_P = 10 wt%. The SAXS profiles of PEC+PEGDA and PEC/PEGDA IPN hydrogels were organized with varying PEGDA MW from 0.7 kg/mol to 20 kg/mol to distinguish the differences. All scattering figures in **Figure 3-2A** featured only a broad peak and lacked additional Bragg peaks in higher q region ($q > 0.02$ Å), suggested the disordered sphere (DIS) lattice microstructure of PEC domains. The broad peaks near $q = 0.02$ Å^{-1} not only denoted the formation of PEC domains and PEC networks but also reflected that the presence of PEGDA chains with different MWs had a negligible influence on self-assembly of PEC networks (**Figure 3-2A**). Besides, with C_{bPE} = 10 wt% and C_P = 10 wt%,

PEGDA with MWs from 0.7 kg/mol to 20 kg/mol had little impact on the microstructure. To analyze the morphological evolution of microstructures, the PEC+PEGDA and PEC/PEGDA IPN hydrogels with C_{bPE} = 30 wt% and C_P = 20 wt% were selected to demonstrate the influence of PEGDA MW (**Figure 3-2C**). Upon increasing PEGDA MW from 0.7 kg/mol to 20 kg/mol, the PEC+PEGDA and PEC/PEGDA IPN hydrogels started to feature the Bragg peaks at the PEGDA MW of 10 kg/mol and 20 kg/mol (**Figure 3-2C**), indicating the disorder-order morphological transition. Moreover, the PEC+PEGDA and PEC/PEGDA IPN hydrogels containing PEGDA with possessed sharper Bragg peaks than that of the hydrogels consisting of PEGDA-10, suggesting a higher-ordered PEC domain arrangement. This signified that PEGDA-20 chains demonstrated a stronger capability to construct a higher-ordered system than PEGDA-10. As shown in **Figure 3-2C**, the primary, secondary, tertiary, and quaternary peaks of PEC+PEGDA and PEC/PEGDA IPN hydrogels with PEGDA MW of 20 kg/mol had the relative positions of q^*, $2q^*$, $3q^*$, and $4q^*$, respectively, in which q^* referred to broad peak position. The relative Bragg peak positions of $q_1 : q_2 : q_3 : q_4 = 1 : 2 : 3 : 4$ matched with the unique features of lamellar (LAM) microstructure, denoting a large PEGDA MW was capable to rearrange the PEC domains from DIS to LAM morphology.

The PEC domains and inter-domain distance exhibited resilience and compatibility with addition of PEGDA chains and networks. A hard-sphere structure factor and polydisperse form factors were employed to estimate the PEC domain radius of the PEC, PEC+PEGDA, and PEC/PEGDA IPN hydrogels with DIS microstructure (**Figure 3-S6**) by Irena package[69] in Igor Pro. As shown in **Figures 3-2B and 3-2C**, both PEC+PEGDA and PEC/PEGDA IPN hydrogels had similar R_{PEC} as that of PEC hydrogels, around 10-12 nm. This reflected that PEGDA molecular weights had minimal influence on the R_{PEC}. Further, at a constant C_{bPE} (=10 wt% or 30 wt%) and PEGDA

MW (0.7, 1.5, 6, 10, or 20 kg/mol) (**Figure 3-S7** and **Figure 3-S8**), upon increasing C_P from 0 wt % to 20 wt%, the R_{PEC} remained nearly constant. This suggests that different loadings of PEGDA content had a negligible impact on the R_{PEC} because it mostly depended on the charged block length of bPEs chain. In **Figure 3-2D**, there were no available R_{PEC} on the PEGDA MW of 10 kg/mol and 20 kg/mol because the corresponding PEC+PEGDA and PEC/PEGDA IPN hydrogels possessed LAM microstructures, which feature parallelly stacked lamellar domains instead of spherical domains. The inter-domain distance (d_{PEC}) was estimated by $2\pi/q^*$,[68] majorly depended on the neutral block PEO length of the bPE chains. Thus, with a constant C_{bPE} and C_P, a progressive increase of PEGDA MWs from 0.7, to 20 kg/mol had an insignificant impact on the inter-domain distances in their corresponding PEC+PEGDA and PEC/PEGDA IPN hydrogels (**Figure 3-2B**, **3-2D**, see also in **Figure 3-S7**, and **Figure 3-S8**).

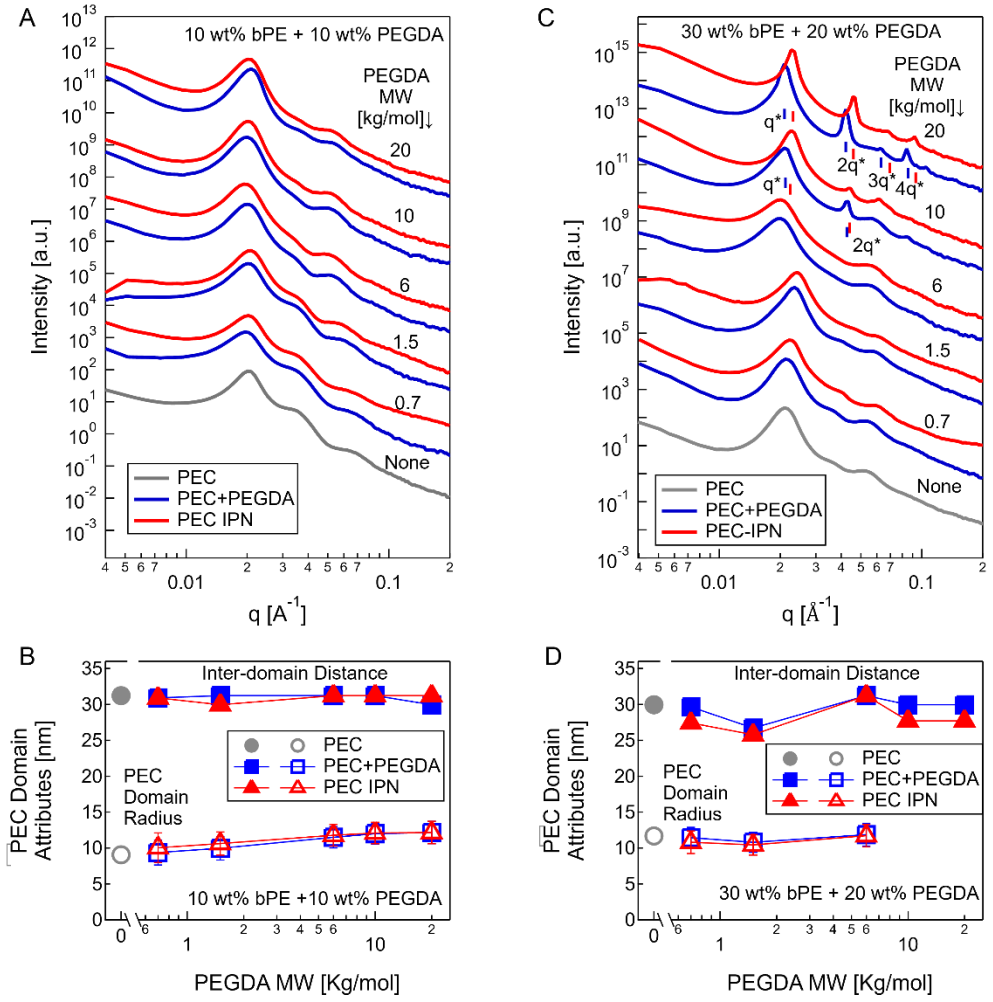

Figure 3-2. One-dimensional synchrotron X-ray scatterings profiles for PEC, PEC+PEGDA, and PEC/PEGDA IPN hydrogels. **(A)** The PEC hydrogel (grey) with C_{bPE} = 10 wt%, and PEC+PEGDA (blue) and PEC/PEGDA IPN (red) hydrogels with a constant C_{bPE} = 10 wt% and C_P = 10 wt% but varying PEGDA MW from 0.7 kg/mol to 20 kg/mol. **(B)** Inter-domain distance and PEC domain radius as a function of PEGDA MW for the hydrogels showed in (A). **(C)** The PEC hydrogel (grey) with C_{bPE} = 30 wt%, and PEC+PEGDA (blue) and PEC/PEGDA IPN (red) hydrogels with a constant C_{bPE} = 30 wt% and C_P = 20 wt% but with varying PEGDA MWs. **(D)** PEC domain radius and inter-domain distance were plotted against PEGDA MWs for the hydrogels demonstrated in (B). SAXS scattering curves were shifted up vertically for clarity.

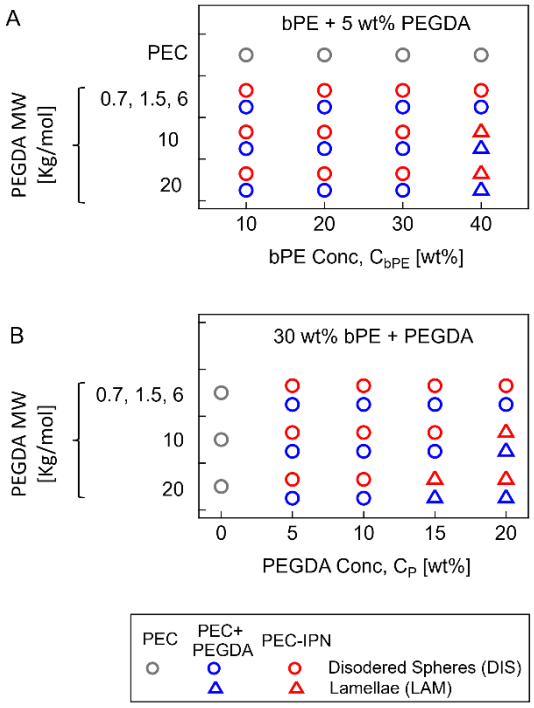

Figure 3-3. Morphological evolution and disorder-order transition of PEC domains for PEC (grey), PEC+PEGDA (blue), and PEC/PEGDA IPN (red) hydrogels. (A) PEC hydrogels with C_{bPE} from 10 wt% to 40 wt%. PEC+PEGDA and PEC/PEGDA IPN hydrogels with a constant C_P = 5 wt% and varying C_{bPE} and PEGDA MW. (B) PEC hydrogels with C_{bPE} = 30 wt%, PEC+PEGDA and PEC/PEGDA IPN hydrogels with a constant C_{bPE} = 30 wt% and varying C_P and PEGDA MW. The symbols of circles: spheres (DIS) and triangles: lamellae (LAM).

Three morphological maps were presented with a function of PEGDA MW, C_p, and C_{bPE} to investigate the mechanisms driving morphological transformation. As shown in **Figure 3-3A** and **Figure 3-S9**, the PEC hydrogels possessed DIS microstructure upon increasing C_{bPE} from 10 wt% to 40 wt%. At C_P = 5 wt%, an increase of C_{bPE} from 10 wt% to 40 wt% demonstrated that combination of high bPE content and a large PEGDA MW could initiate a microstructural transformation. At C_{bPE} = 40 wt% and C_P = 5 wt%, the PEC+PEGDA and PEC/PEGDA IPN hydrogels comprising PEGDA MWs of 10 kg/mol and 20 kg/mol featured LAM microstructure but the remaining hydrogels with smaller PEGDA MWs (0.7, 1.5, and 6 kg/mol) only had DIS microstructures (**Figure 3-3A**). These phenomena reflected that PEGDA MWs played an important role in the microstructural transformation. To further confirm this hypothesis, two morphological maps were made with varying PEGDA MW and C_P at a constant C_{bPE}. As shown in **Figure 3-S10** and **Figure 3-S11**, with C_{bPE} = 10 wt%, all PEC+PEGDA and PEC/PEGDA IPN hydrogels possessed DIS microstructure and did not experience any disorder-order transition, suggesting that a variation in PEGDA MWs and C_P has no influence on the microstructures at a low C_{bPE}. In comparison, a microstructural evolution was observed in PEC+PEGDA and PEC/PEGDA IPN hydrogels at a higher C_{bPE}. At C_{bPE} = 30 wt%, the PEC+PEGDA and PEC/PEGDA IPN hydrogels with PEGDA MWs of 0.7, 1.5, and 6 kg/mol possessed DIS microstructure but the hydrogels with PEGDA MW of 10 and 20 kg/mol started to feature LAM microstructure at C_P = 20 wt% and C_P = 15 wt%, respectively (**Figure 3-3B** and **Figure 3-S12**). These results suggested that PEGDA with a larger MW possessed a strong ability to rearrange PEC domains and induced morphological transition.

To explore the relationship between PEGDA MWs and microstructures, we computed the radius of gyration (R_g) of PEGDA chains and mesh size (ξ) of PEGDA networks, as shown in **Figure 3-S5A**. An increase of PEGDA MWs from 0.7 kg/mol to 20 kg/mol resulted in a continuous increase of R_g. The R_g of PEGDA-20 and PEGDA-10 chains are 5.3 and 3.8 times larger than that of PEGDA-0.7. A larger MW contributed to a longer PEGDA chain and a larger R_g, which are the major factors directly induced the microstructural transformation. A PEGDA polymer with a long chain and large R_g occupied more space and were more difficult to diffuse through the PEC networks without perturbation and interaction. In comparison, the PEGDA chains with smaller MWs had shorter polymer chains length and smaller R_g,which occupied less space and diffused more easily through the PEC networks with less disruption. As shown in **Figure 3-S5**, with increasing PEGDA MWs, the overlap concentration (C^*), where polymer chains started to overlap and interact with each other, was progressively reduced. This reflected that the PEGDA chains with a larger MW have a smaller overlap concentration, denoting it requires a smaller polymer concentration to occupy entire system. As a comparison, the overlap concentrations of PEGDA-0.7 and PEGDA-20 were 26.5 wt% and 5 wt%, respectively, suggesting that PEGDA-0.7 required an additional 430% polymer concentration to reach the similar influence caused by PEGDA-20.

During photo-crosslinking process, the two-end acrylate groups of PEGDA chains covalently crosslinked with each other and formed network joints, where the average distance between the network joints is typically referred to as mesh size, ξ. Two mesh size calculation methods were employed depending on the C_P and corresponding overlap concentration. With $C_P < C^*$, the PEGDA polymer chains were relaxed and uncompressed, and thus the mesh size was the same as its R_g, as shown in Equation (1). With $C_P \geq C^*$, the PEGDA polymer chains were overlapped and

compressed, leading to the mesh size smaller than its R_g. Thus, Equation (2) was applied to estimate the mesh size at a compressed state. For example, with 10 wt% PEGDA, the concentration of the PEGDA with MWs of 0.7 and 1.5 kg/mol were below their C^* (**Figure 3-S5**), resulting in the same values of mesh size and their corresponding R_g (**Figure 3-S5**). In comparison, the concentration of the PEGDA with MWs of 6, 10, and 20 kg/mol were above their corresponding C^*, leading to the mesh sizes smaller than R_g (**Figure 3-S5**). Although their mesh sizes were smaller than corresponding R_g, their microstructures were same before and after photo-crosslinking. This suggested the formation of PEGDA covalent networks imposed an insignificant influence on the microstructural transformation. In other words, the major microstructural transition has been completed before light activation.

3.3.2 Tunability of Shear Moduli of PEC+PEGDA and PEC/PEGDA IPN Hydrogels

Bulk rheology of hydrogels was examined by oscillatory tests within the linear viscosity regime (LVE). Representative frequency sweeps are summarized in **Figure 3-4**, also seen in **Figure 3-S13**, **Figure 3-S14**, and **Figure 3-S15** with the frequency range of 0.1 rad/s to 20 rad/s. All PEC hydrogels with C_{bPE} ranging from 10 wt% to 40 wt% featured DIS microstructure. Thus, with a constant DIS microstructure, an increasing C_{bPE} led to progressive improvement of G' and G'' of PEC hydrogels across the entire frequency (**Figure 3-S16**), in agreement with the previous works.[24] The shear properties of PEC hydrogels exhibited solid-like properties ($G' > G''$) and an independent relationship on frequency. Before photo-crosslinking, addition of the PEGDA with a larger MW resulted in a lower G' and G'' of PEC+PEGDA hydrogels. After photo-crosslinking, opposite phenomena were observed, in which PEGDA with a smaller MW contributed to higher shear moduli of PEC/PEGDA IPN hydrogels because of denser crosslinking density. After photo-

crosslinking, the formation of PEGDA networks significantly enhanced the shear strength of PEC/PEGDA IPN hydrogels, which were higher than that of either individual PEC or PEGDA networks, and even their summation (**Figure 3-S17**).

Before photo-crosslinking, PEC networks majorly contributed to the shear strength of PEC+PEGDA hydrogels because the PEC networks served as scaffolds to supply structural support. As shown in **Figure 3-4A**, addition of PEGDA-0.7 had an insignificant influence or slight improvement on shear moduli of PEC+PEGDA-0.7 hydrogels. Similar to the PEC hydrogel, the frequency sweeps of PEC+PEGDA-0.7 hydrogels exhibited an independent relationship against frequency, maintaining solid behavior. On the contrary, incorporation of PEGDA-20 attenuated the G′ and G" of PEC+PEGDA-20 hydrogels, up to 80% lower than that of the PEC hydrogels. Interestingly, similar phenomena were observed in other PEC+PEGDA hydrogels. From 0.7 kg/mol to 20 kg/mol, PEGDA with a larger MW resulted in lower shear moduli of PEC+PEGDA hydrogels. The PEGDA with larger MWs featured larger R_g and longer chain lengths. Thus, they possessed a stronger ability to induce macromolecular crowding, cause more perturbation of PEC networks, and reduce the connectivity between PEC domains. Thus, incorporation of the PEGDA with a longer chain length resulted in lower G′ and G" of PEC+PEGDA hydrogels before light irradiation.

In addition, the PEGDA MWs also influenced the slope behavior of loss moduli G" of PEC+PEGDA hydrogels. Addition of the PEGDA with small MWs (e.g., 0.7 and 1.5 kg/mol) had insignificant influence on the slope of shear moduli (**Figure 3-4A** and **Figure 3-S14C,E**), but incorporation of the PEGDA with larger MWs (6, 10, and 20 kg/mol) promoted a noticeable change in the slope and ω-dependence behavior (**Figure 3-4B** and **Figure 3-S13A**,**B**,**C**, **Figure 3-**

S14A). PEC hydrogels with C_{bPE} = 30 wt% featured a nearly flat slope, suggesting a weak ω-dependence. In comparison, adding 20 wt% PEGDA-20 changed the slope from nearly flat to approximate 0.5. With a constant C_P, PEGDA with a larger MW caused this phenomenon clearer. Interestingly, at C_P= 20 wt% and C_{bPE}=30 wt%, the PEC+PEGDA hydrogels containing PEGDA with MWs of 10 kg/mol and 20 kg/mol featured LAM structure, which had been previously observed in block copolymer hydrogels with LAM structures.[24] The hydrogels with LAM structures possessed approximate $\omega^{0.5}$ dependence, ascribed to either the presence of defects (e.g, dislocation) in LAM structure[70] or second-sound modes in a logical region of LAM structure.[71]

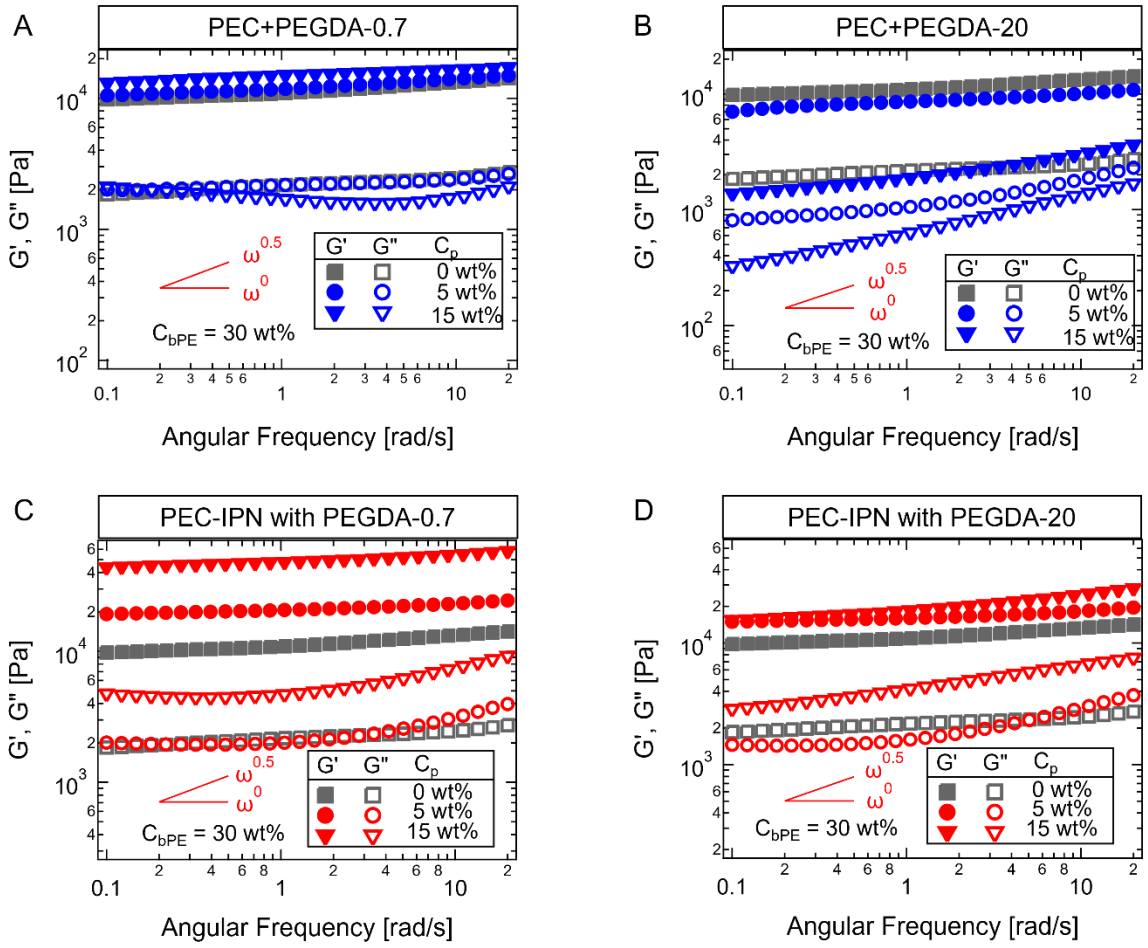

Figure 3-4. Representative shear moduli of PEC, PEC+PEGDA, and PEC/PEGDA IPN hydrogels. All four figures include a PEC hydrogel (grey) with C_{bPE} = 30 wt% for a reference. (A-B) Frequency sweeps for (A) PEC+PEGDA-0.7 hydrogels (blue, C_{bPE} = 30 wt% and C_P=5 and 15 wt%) and (B) their corresponding PEC/PEGDA IPN hydrogels (red, C_{bPE} = 30 wt% and C_P=5 and 15 wt%). (C-D) Frequency sweeps for PEC+PEGDA-20 hydrogels (blue, C_{bPE} = 30 wt% and C_P=5 and 15 wt%) and their corresponding PEC/PEGDA IPN hydrogels (red, C_{bPE} = 30 wt% and C_P=5 and 15 wt%).

After photo-crosslinking, PEGDA chains covalently crosslinked with each other and formed stress-bearing PEGDA networks in the PEC/PEGDA IPN hydrogels, which significantly enhanced shear properties across entire frequency (**Figure 3-4C**,**D**). During photo-crosslinking progress, the PEGDA chains crosslinked with each other with the presence of PEC networks. This implied that some PEGDA chains remained unreacted and become self-looped or dangling chains. However, these did not contribute to lower shear moduli of PEC/PEGDA IPN hydrogels. Instead, the shear moduli of PEC/PEGDA IPN were only higher than either sub-network but also their summation, demonstrating the synergic effects (**Figure 3-S17** and **Figure 3-S18**). The shear moduli of PEC/PEGDA IPN hydrogels were not only contributed from PEC networks and PEGDA networks but also the polymer entanglement between two interpenetrated sub-networks. Therefore, this compromised the loss caused by unreacted PEGDA chains. As shown in **Figures 3-4C**,**D**, **Figure 3-5**, and **Figure 3-S13**, **Figure 3-S14**, decreasing PEGDA MWs progressively strengthened the G' and G'' of PEC/PEGDA IPN hydrogels because smaller PEGDA MWs led to higher crosslinking density and smaller mesh size of PEGDA network. Each PEGDA chain possessed two acrylate groups. Under the same weight, the PEGDA with a shorter chain has a more molar amount, indicating more acrylate groups. For instance, under the same weight, PEGDA-10 and PEGDA-6 had 2-fold and 3.33-fold acrylate groups as that PEGDA-20. Thus, upon decreasing PEGDA MWs from 20 kg/mol to 6 kg/mol, the G' and G'' of PEC/PEGDA IPN hydrogels were progressively enhanced (**Figure 3-5**). Although PEGDA-0.7 and PEGDA-1.5 also featured small MWs, the shear moduli of their PEC/PEGDA IPN were similar or only slightly higher than those of the PEC/PEGDA IPN hydrogels containing PEGDA-6 because PEGDA-6 had a relatively much lower overlap concentration (**Figure 3-S5B**). It can ensure more completed PEGDA networks as C_P is much higher than C^*. More completed PEGDA networks indicated higher shear moduli. In

addition, With C_{bPE} = 30 wt%, increasing C_P resulted in progressive improvement in G' and G" owing to denser PEGDA networks (**Figure 3-5**). Overall, in an attempt to meet the shear moduli required in applications, the mechanical tunability can be achieved by adjusting PEGDA MW, C_P, or C_{bPE} (**Figure 3-5**, see also in **Figure 3-S15**).

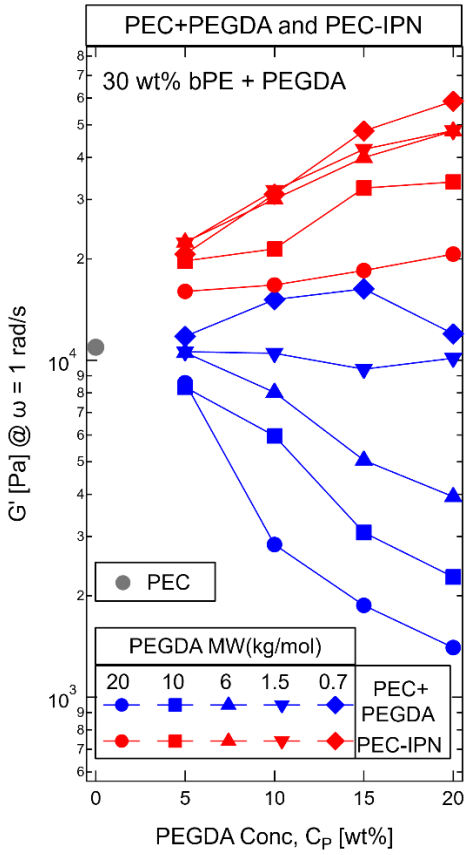

Figure 3-5. Storage moduli (G′) of PEC hydrogels with C_{bPE} = 30 wt%, and the PEC+PEGDA and PEC/PEGDA IPN hydrogels , comprising of PEGDA with different MWs, with a constant C_{bPE} = 30 wt% and varying C_P at frequency ω = 1 rad/s.

3.3.3 Tensile Properties PEC/PEGDA IPN Hydrogels Influenced by PEGDA Mesh Size

The PEGDA with five different chain lengths were employed to fabricate PEGDA hydrogels with C_P = 10 wt% and PEC/PEGDA IPN hydrogels with C_P = 10 wt% and C_{bPE} = 10wt% for tensile properties studies. **Figure 3-6A**,**B** and **Figure 3-S19**, **Figure 3-S20**, **Figure 3-S21** showed the representative stress-strain curves for PEGDA (grey) hydrogels and PEC/PEGDA IPN (red) hydrogels. The PEC/PEGDA IPN hydrogels featured two-step stress curves and plastic deformation, reflecting the strong electrostatic interaction inside the PEC networks. At room temperature, the ionic dissociation energy of an ionic pair is around 1 k_BT,[72] which was much lower than a common covalent bond dissociation energy, 140 k_BT (~347 kJ/mol).[41, 73] The strong ionic interactions typically contained tens to hundreds of ion pairs.[41] Each charged block of bPEs carried around 65 either guanidinium or sulfonate moieties, and the PEC domains contained several to tens of dense charged blocks of bPE chains. Thus, several hundred pairs of ionic interaction between guanidinium and sulfonate groups ensured strong ionic interaction inside PEC domains.

Compared to PEGDA hydrogels, their corresponding PEC/PEGDA IPN hydrogels exhibited remarkable enhancement in ultimate strength, Young's moduli, and toughness and meanwhile preserved similar or slightly improved extensibility, as showed in **Figure 3-6C**,**D**. A completed covalent network played a significant role in the overall tensile properties. The completed and incomplete PEGDA networks were determined by $C_P \geq C^*$ and $C_P < C^*$, respectively. In a dilute system with $C_P < C^*$, the PEGDA chains did not fully occupy the system and failed to form a completed crosslinked covalent network. Thus, 10 wt% of PEGDA-0.7 and PEGDA-1.5 were below their corresponding C^* (**Figure 3-S5B**), indicating their incomplete covalent networks in

the PEGDA hydrogels and corresponding PEC/PEGDA IPN hydrogels. Thus, they featured poor ultimate strength, Young's moduli, and toughness in comparison with the remaining PEGDA and PEC/PEGDA IPN hydrogels containing PEGDA with MWs of 6, 10, and 20 kg/mol, whose concentrations were above their C^*.

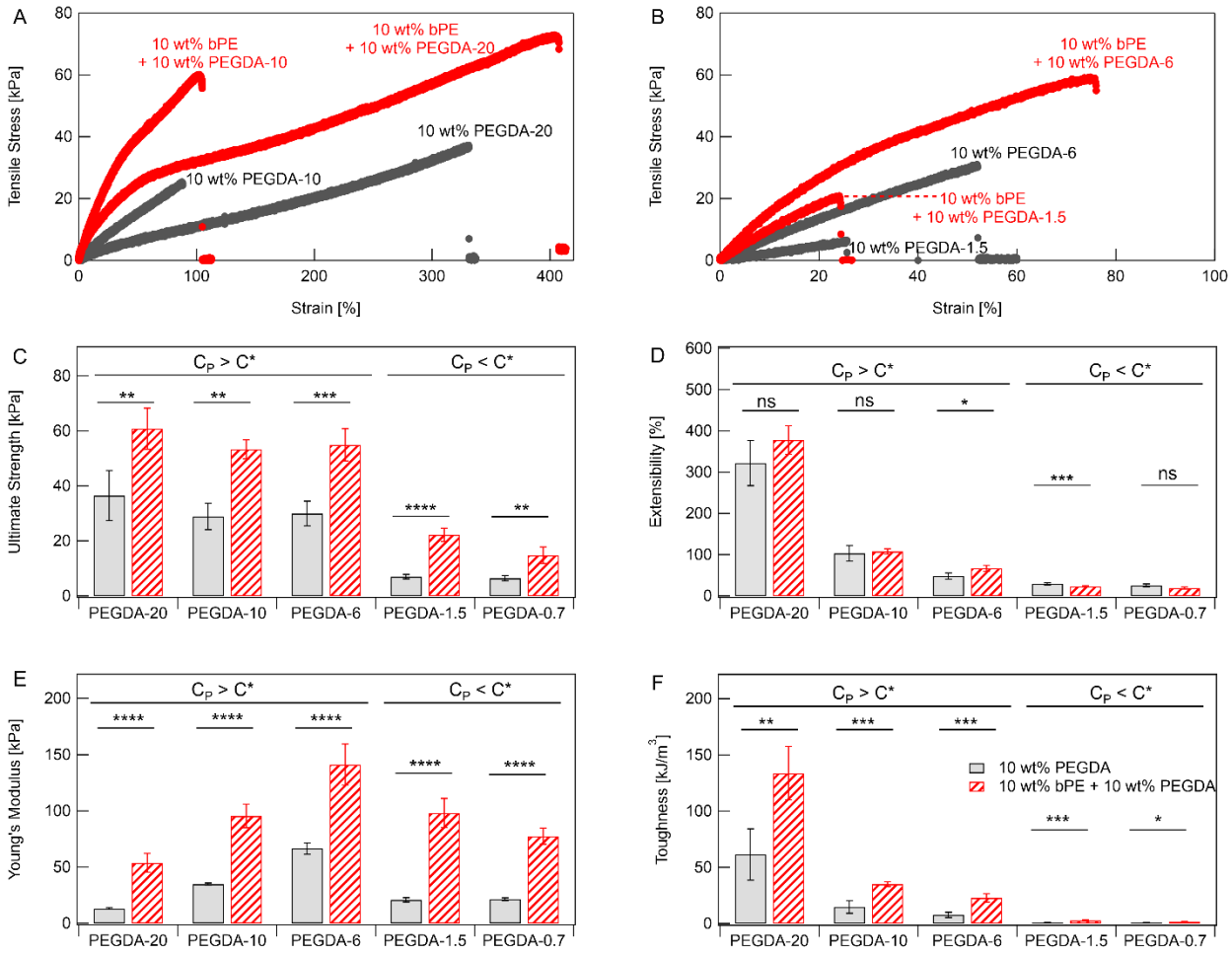

Figure 3-6. Tensile performance of PEGDA hydrogels with C_P = 10 wt% and PEC/PEGDA IPN hydrogels with C_P = 10 wt% and C_{bPE} = 10 wt%. (A) Representative stress-strain curves for PEGDA and PEC/PEGDA IPN hydrogels consisting of PEGDA-10 and PEGDA-20. (B) Representative stress-strain curves for PEGDA and PEC/PEGDA IPN hydrogels containing PEGDA-6 and PEGDA-1.5. (C) Ultimate Stress, (D) Extensibility, (E) Young's modulus, and (F) Toughness. (Sample number $n \geq 4$)

The PEGDA hydrogels formed by PEGDA-6, PEGDA-10, and PEGDA-20 featured comparable ultimate strength owing to the similar polymer backbone, polymer structure, and crosslink (**Figure 3-6C**). The PEGDA hydrogels with MWs of 0.7 kg/mol and 1.5 kg/mol had poor ultimate strength due to incomplete covalent networks. With the assistance of PEC networks, the PEC/PEGDA IPN hydrogels achieved higher ultimate strength because of the additional contribution of PEC networks and polymer entanglements between two interpenetrated sub-networks. Young's modulus of PEGDA hydrogels featured a positive relationship with crosslinking density or a negative relationship with the mesh size of PEGDA networks. A smaller mesh size suggested a higher crosslinking density. Thus, we observed a progressive increase in Young's modulus of PEGDA hydrogels with decreasing PEGDA MWs from 20 to 6 kg/mol (**Figure 3-6E**) and mesh size (**Figure 3-S5B**). Compared to pure PEGDA hydrogels, all PEC/PEGDA IPN hydrogels possessed one- to two-fold improvement in Young's modulus because the strong ionic interactions inside the PEC domains and polymer entanglements between two sub-networks required more stress to stretch the same displacement.

Extensibility, referring to the maximum displacement a hydrogel can withstand before rupture, reflected the ductility and rigidness of polymer networks. A larger mesh size meant a more ductile network and larger extensibility. Upon decreasing PEGDA MW, the PEGDA network was transferred from a ductile network to a less ductile or more rigid network. Thus, the extensibility of PEGDA and PEC/PEGDA IPN hydrogels was continuously decreased. We noticed that incorporation of PEC networks did not render extra extensibility because extensibility majorly depended on the mesh size of covalent networks. The d_{PEC} and R_{PEC} were approximately 30 nm and 10 nm, respectively. The surface distance between two PEC domains (d_S) was estimated by $d_S = d_{PEC} - R_{PEC}$, around 10 nm. The neutral block PEO of bPEs featured the MW of 20 kg/mol.

Thus, the mesh sizes of PEGDA networks were smaller than 10 nm. Due to the smaller mesh size of PEGDA networks and the reconfigurable nature of PEC networks, the PEGDA network was the major factor limiting the extensibility. Thus, incorporation of PEC networks had negligible influence on the extensibility of PEC/PEGDA IPN hydrogels. However, it is important to highlight that Young's modulus was increased without sacrificing extensibility. This demonstrated that PEC/PEGDA IPN hydrogels were not limited by stiffness-extensibility tradeoff.

Reversible ionic interactions inside PEC domains promoted energy dissipation during the stretching process. Therefore, the toughness of PEC/PEGDA IPN hydrogels was approximately one-fold higher than that of the corresponding PEGDA hydrogels. Traditional chemical hydrogels confront the limitation of stiffness-toughness tradeoff, suggesting the inverse relationship between them. As shown in **Figure 3-6C**,**F**, combing PEC networks and PEGDA networks could enhance Young's modulus and toughness significantly at the same time, breaking the Young's modulus-toughness tradeoff. The PEGDA hydrogels were not capable of reaching the similar effects by simply changing C_P. Many chemical hydrogels, such as PEGDA hydrogels, have been extensively investigated as potential materials for cartilage tissue engineering.[74, 75] Yet, their limited toughness has been known as a typical factor restricting their applications. Incorporation of PEC network is a promising approach to enhance the stiffness and toughness of hydrogels without attenuating extensibility. The relationship between PEGDA MWs and hydrogel properties provided guidelines for designing PEC/PEGDA IPN hydrogels with anticipated properties that match the requirements of applications.

3.4 Conclusion

In conclusion, we have demonstrated that (1) PEC/PEGDA IPN hydrogels preserved the synergistic effects in both shear and tensile properties regardless of different covalent network mesh sizes, and (2) PEGDA MWs as well as C_{bPE} and C_P played important roles in rearranging PEC domains and induced morphological transition. At sufficient high C_P and C_{bPE}, longer PEGDA chains possessed a stronger ability to cause a microstructural transition because longer chains could form polymer coils and lead to more macromolecular crowding. In comparison, shorter PEGDA chains had better mobility and were easier diffuse through the PEC networks with less perturbation. In this system, no difference in microstructures of PEC/PEGDA IPN hydrogels was observed before and after photo-crosslinking. This suggested that the microstructural transition process had been completed before photo-crosslinking. Besides, the inter-domain distance and PEC domain radius were independent of PEGDA MW and PEGDA network mesh size because the former depended on bPE concentration and middle PEO block length of bPEs, and the latter depended on the charged block length of bPEs.

Before crosslinking, the PEC networks served as scaffolds to provide major shear strength. Thus, the continuous addition of PEGDA with a larger MW (e.g., 10 and 20 kg/mol) progressively lowered shear moduli of PEC+PEGDA hydrogels since the long PEGDA chain caused macromolecular crowding, perturbed formation of PEC domains, and reduced connectivity of PEC networks. In addition, when the PEC+PEGDA featured LAM microstructure, the G" had a close $\omega^{0.5}$-dependence, in agreement with observations of block polymers with LAM structures.[24] After photo-crosslinking, the additional polymer entanglements between interpenetrated PEGDA and PEC networks led to high shear moduli, which were even higher than the summation of the PEC

hydrogels and covalent networks. Under the condition of $C_P > C^*$, the PEC/PEGDA IPN hydrogels with smaller PEGDA MWs featured higher G' and G'' because of higher crosslinking density, demonstrating an approach to tune shear moduli without changing polymer concentration.

Traditional chemical hydrogels typically face a stiffness-toughness tradeoff, limiting their tensile performance. Interpenetration between PEC and PEGDA networks broke through this tradeoff. Thus, PEC/PEGDA IPN hydrogels possessed remarkably improved ultimate strength, Young's moduli, and toughness and meanwhile maintaining similar extensibility. With $C_P > C^*$, decreasing PEGDA MW resulted in higher crosslinking density. This led to higher Young's moduli, lower toughness, and lower extensibility of PEC/PEGDA IPN hydrogels, suggesting that PEGDA network mesh size played an important role in the tensile properties of PEC/PEGDA IPN hydrogels. Our previous works have provided the first step to demonstrating the compatibility of PEC-based materials and their potential extrusion-based 3D bioprinting, cartilage tissue engineering, and drug-loaded bioadhesives applications. In this work, the influence of precursor chain length on the microscale properties and mechanical properties of resultant hydrogels further demonstrated the compatibility of PEC network platform with covalent networks comprising different mesh sizes and provided a design reference to engineer PEC/PEGDA IPN hydrogels for biomedical applications.

3.5 Supplementary Information

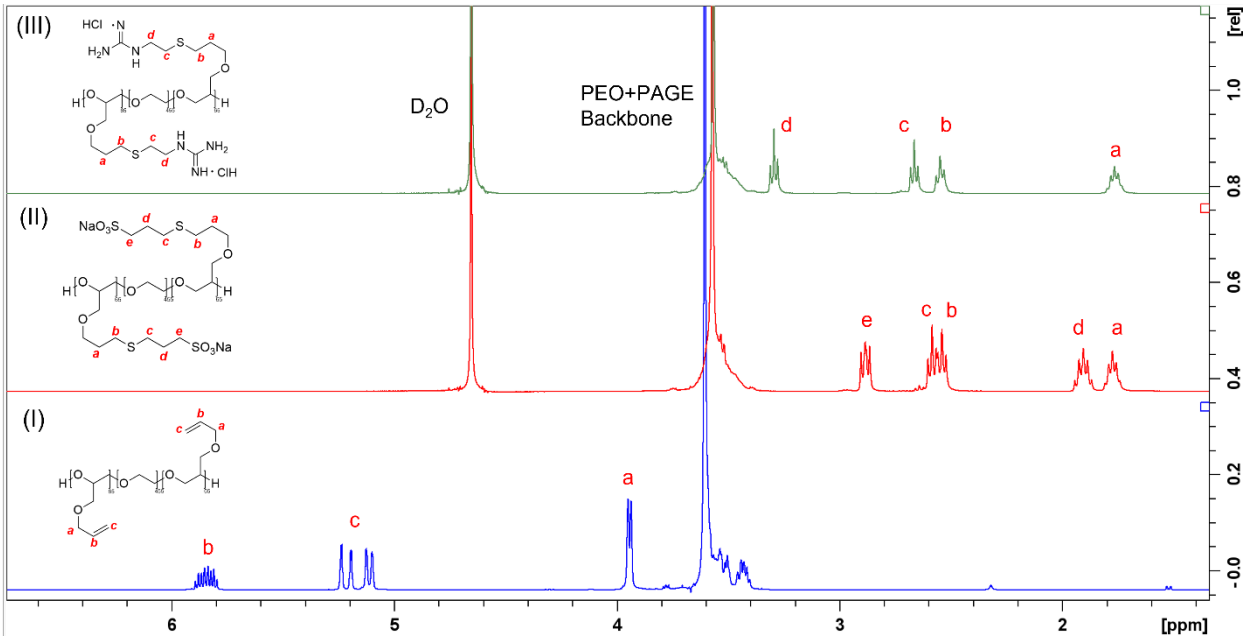

Figure 3-S1. ^{1}H NMR spectraof (I) $PAGE_{65}$-PEO_{455}-$PAGE_{65}$, (II) sulfonate-functionalized $PAGE_{65}$-PEO_{455}-$PAGE_{65}$, and (III) guanidinium-functionalized $PAGE_{65}$-PEO_{455}-$PAGE_{65}$.

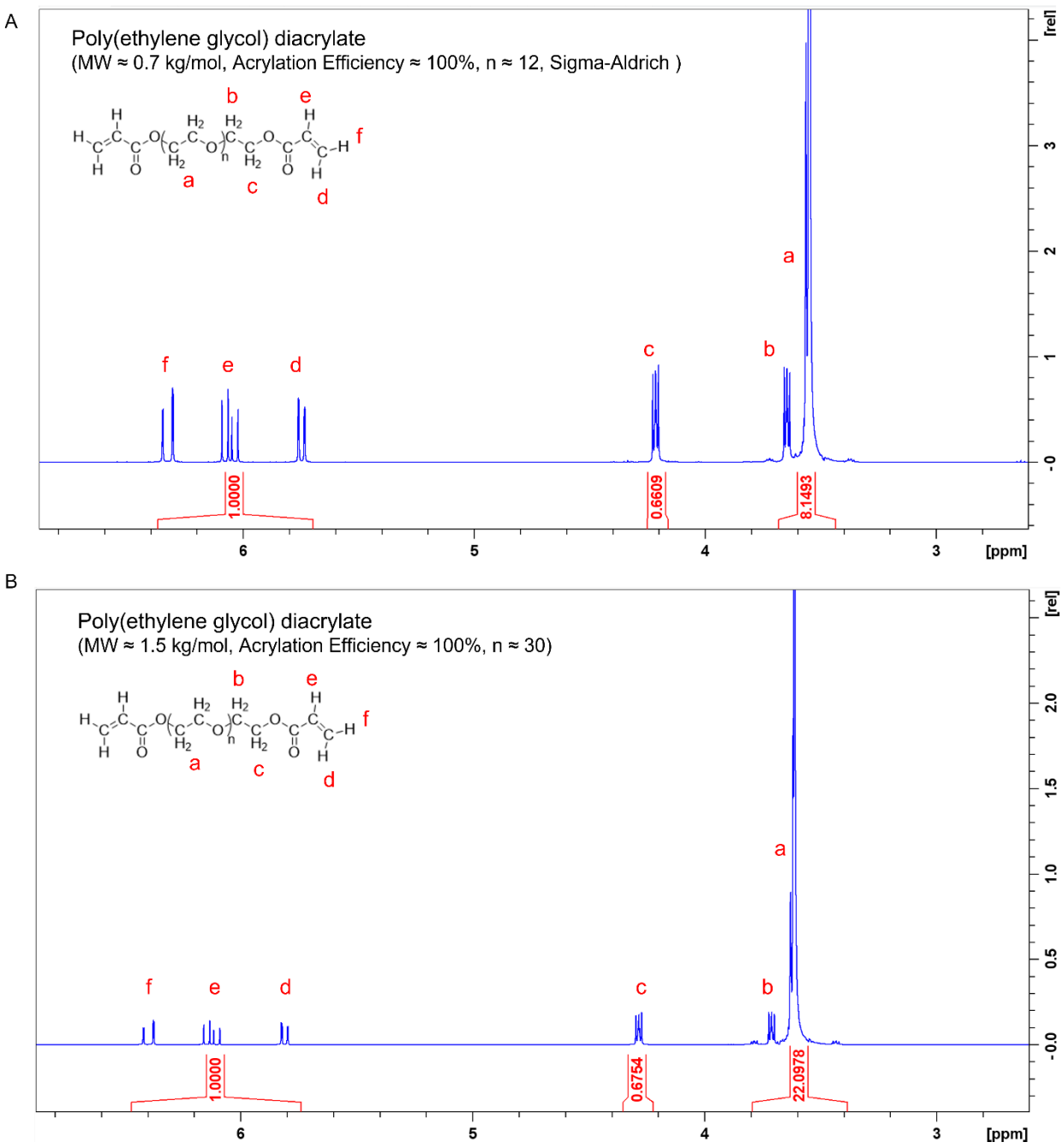

Figure 3-S2. ^{1}H NMR spectra of (A) Poly(ethylene glycol) diacrylate (MW ≈ 0.7 kg/mol) and (B) Poly(ethylene glycol) diacrylate (MW ≈ 1.5 kg/mol).

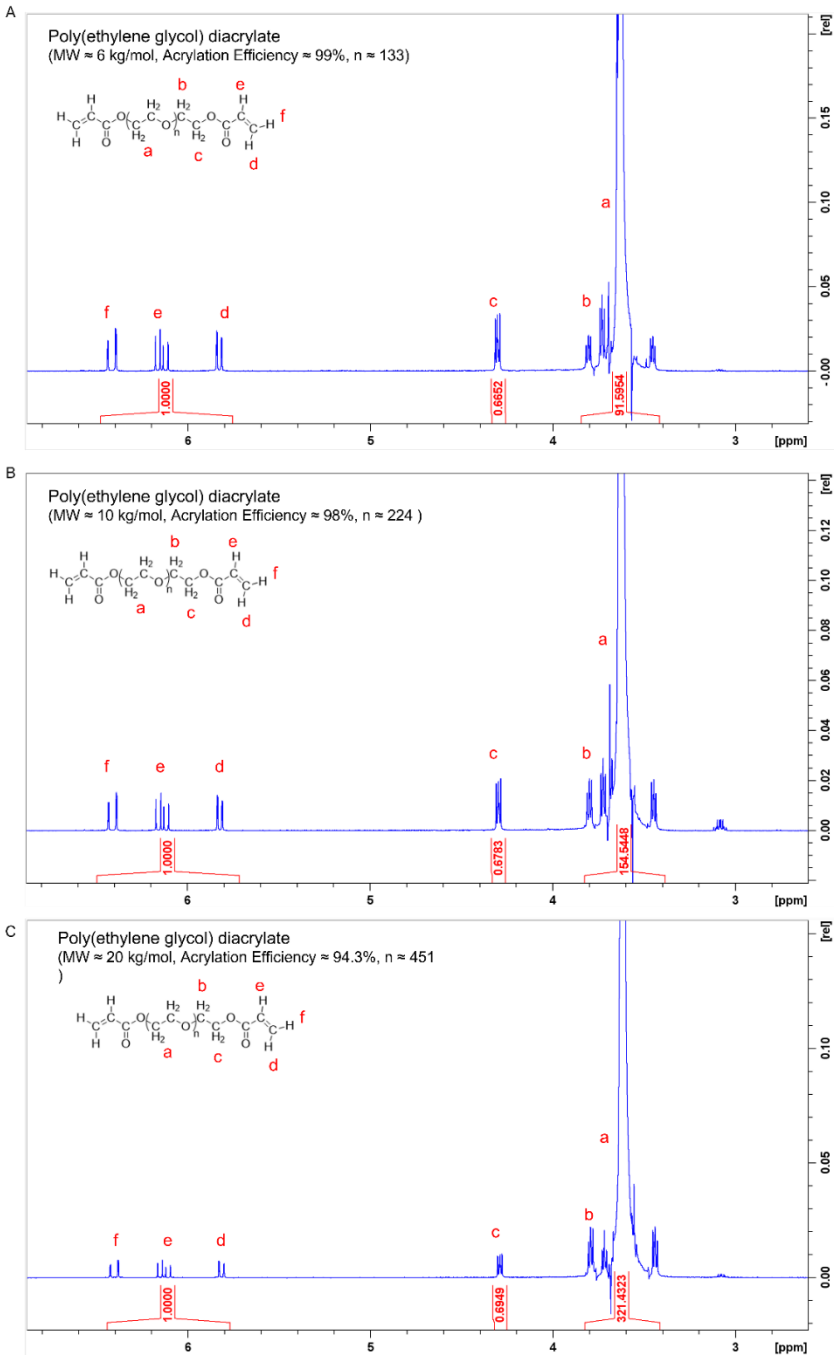

Figure 3-S3. ^{1}H NMR spectra of (A) Poly(ethylene glycol) diacrylate (MW ≈ 6 kg/mol), (B) Poly(ethylene glycol) diacrylate (MW ≈ 10 kg/mol), and (C) Poly(ethylene glycol) diacrylate (MW ≈ 20 kg/mol).

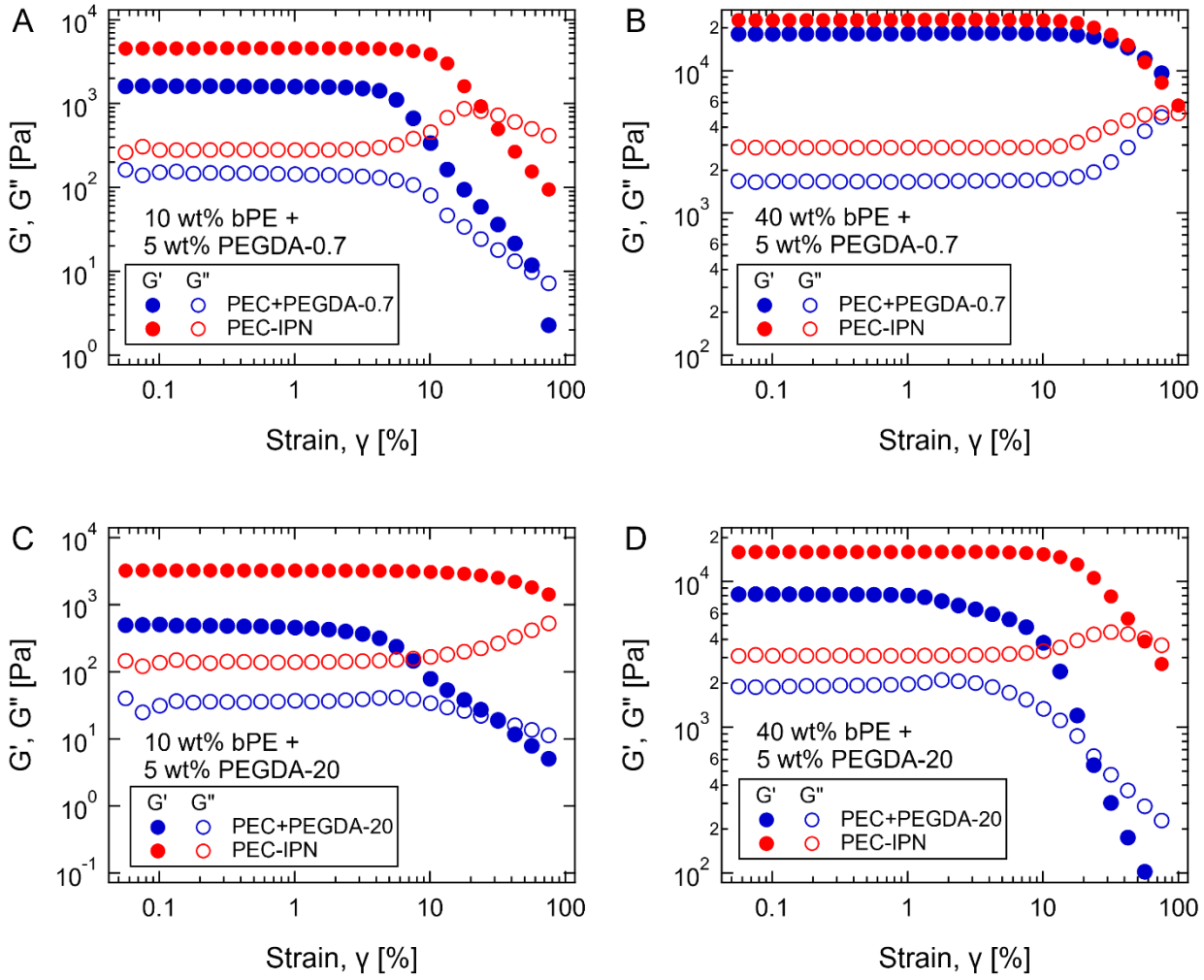

Figure 3-S4. Representative amplitude sweeps for PEC+PEGDA and PEC/PEGDA IPN hydrogels. (A) PEC+PEGDA-0.7 and PEC/PEGDA-0.7 IPN hydrogels with C_{bPE} = 10 wt% and C_P= 5 wt%. (B) PEC+PEGDA-0.7 and PEC/PEGDA-0.7 IPN hydrogels with C_{bPE} = 40 wt% and C_P= 5 wt%. (C) PEC+PEGDA-20 and PEC/PEGDA-20 IPN hydrogels with C_{bPE} = 10 wt% and C_P= 5 wt%. (D) PEC+PEGDA-20 and PEC/PEGDA-20 IPN hydrogels with C_{bPE} = 40 wt% and C_P= 5 wt%.

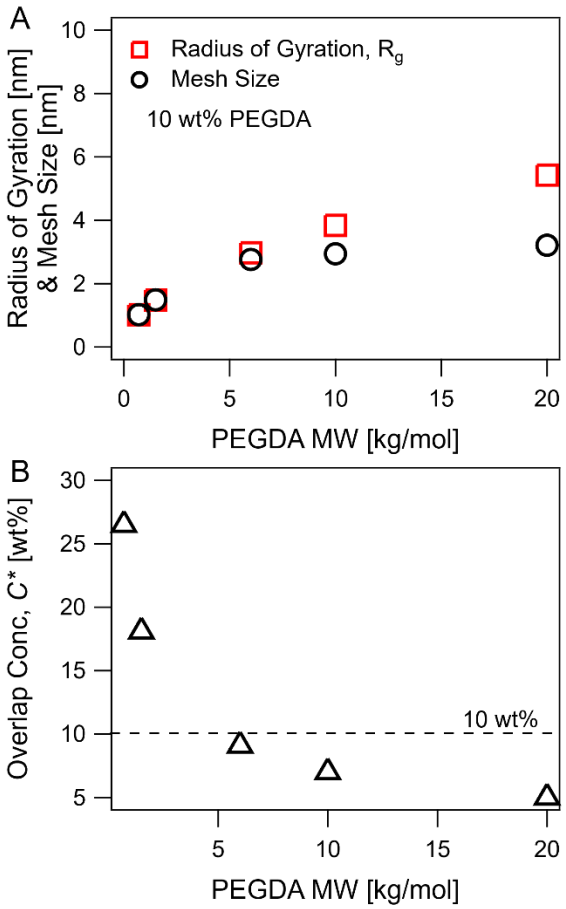

Figure 3-S5. Radius of gyration and overlap concentration. (A) Radius of gyration (R_g) of PEGDA chains and mesh size of PEGDA hydrogels with different MWs. (B) Overlap concentration for the PEGDA with different molecular weights.

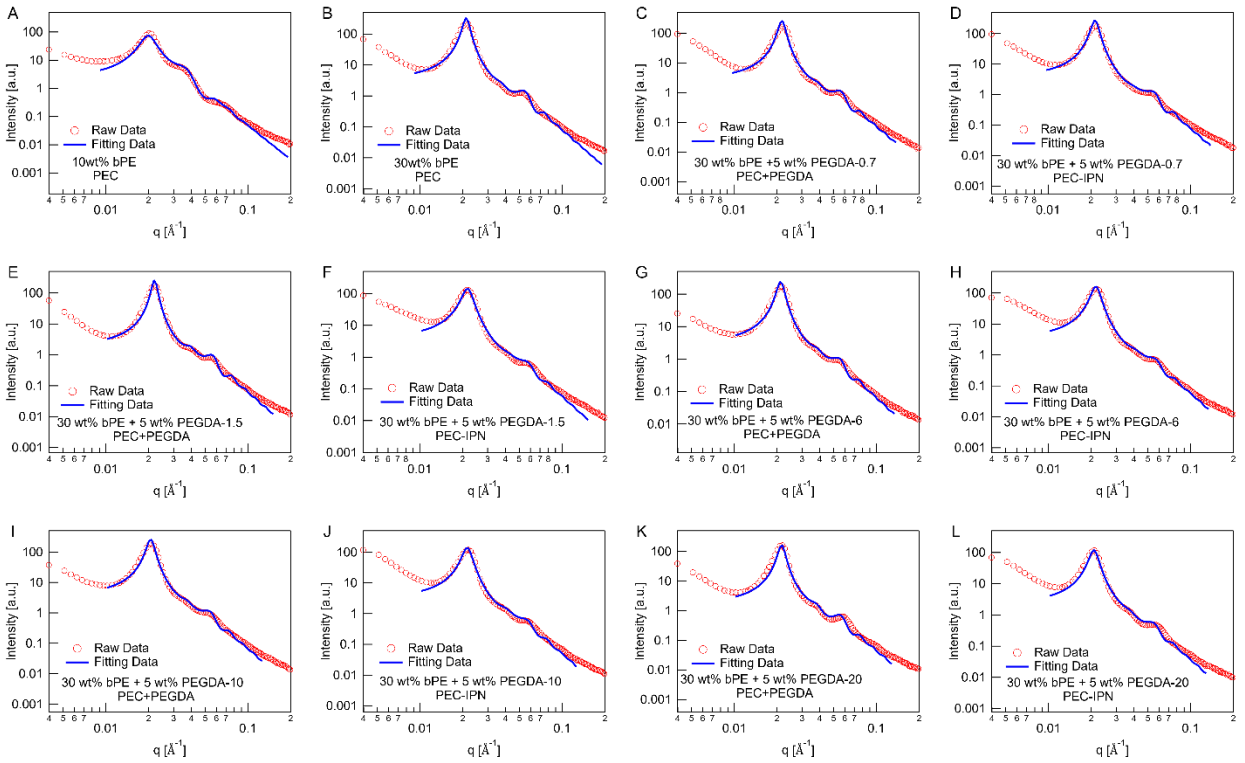

Figure 3-S6. Representative SAXS curves fittings for PEC domain size estimation for PEC hydrogels, PEC+PEGDA hydrogels, and PEC/PEGDA IPN hydrogels. (A-B) PEC hydrogels with C_{bPE} = 10 wt% and 30 wt%. (C-L) PEC+PEGDA and PEC/PEGDA IPN hydrogels, which contained C_{bPE} = 30 wt% and C_P = 5 wt%, consisted of (C-D) PEGDA-0.7, (E-F) PEGDA-1.5, (G-H) PEGDA-6, (I-J) PEGDA-10, (K-L) PEGDA-20. The structure factor with hard-sphere feature and polydisperse-spheroid form factor were harnessed to produce fitting data (blue) with a well fit for the raw data (red).

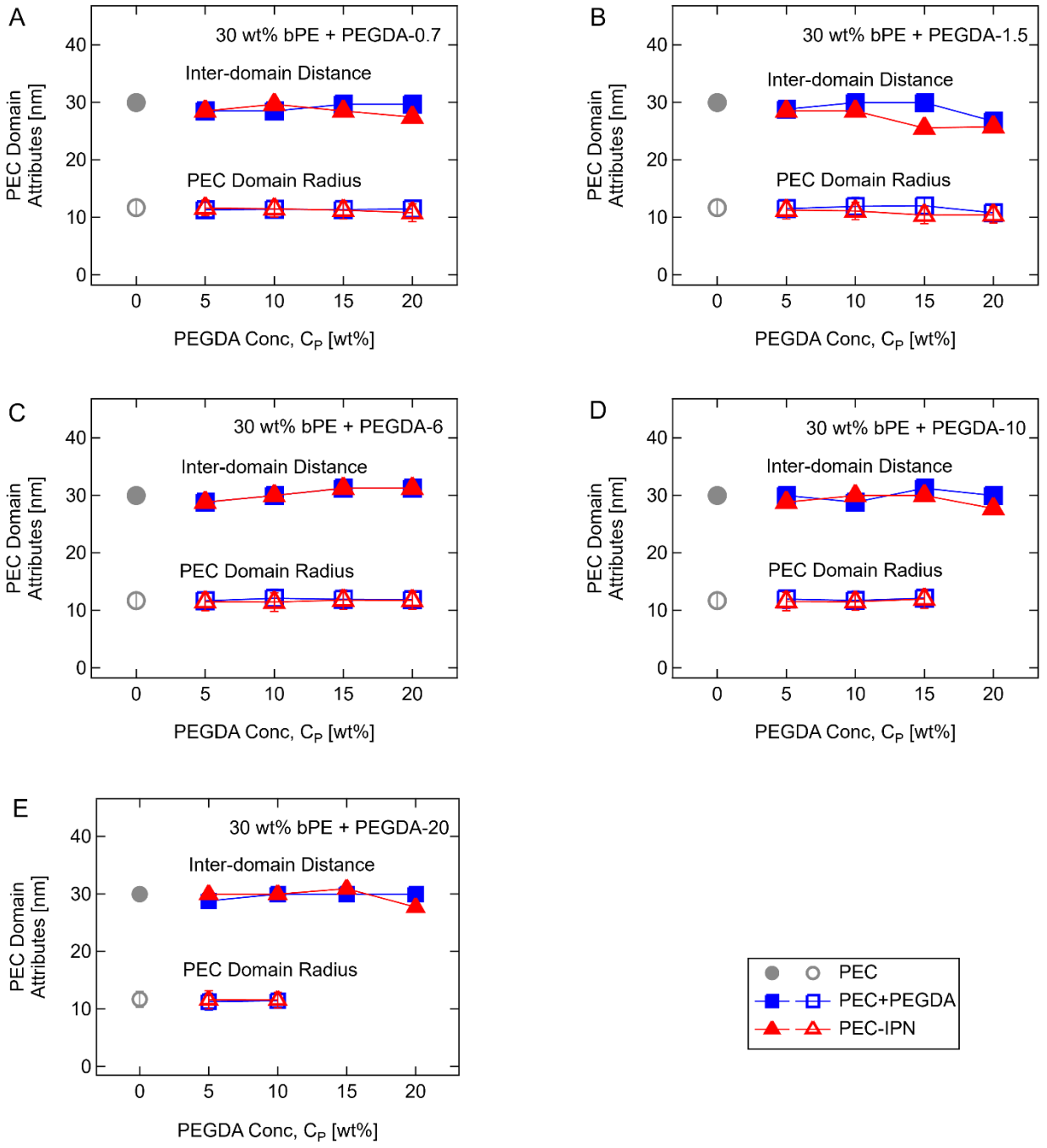

Figure 3-S7. Inter-domain distance and PEC domain radius as a function of PEGDA concentration (C_P) for PEC (grey), PEC+PEGDA (blue), and PEC/PEGDA IPN (red) hydrogels with different PEGDA MWs. The PEC hydrogels with C_{bPE} = 30 wt% while PEC+PEGDA and PEC/PEGDA IPN hydrogels with C_{bPE} = 30 wt% and varying C_P from 5 wt% to 20 wt%. The PEC+PEGDA

and PEC/PEGDA IPN hydrogels consisted of (A) PEGDA-0.7, (B) PEGDA-1.5, (C) PEGDA-6, (D) PEGDA-10, and PEGDA-20.

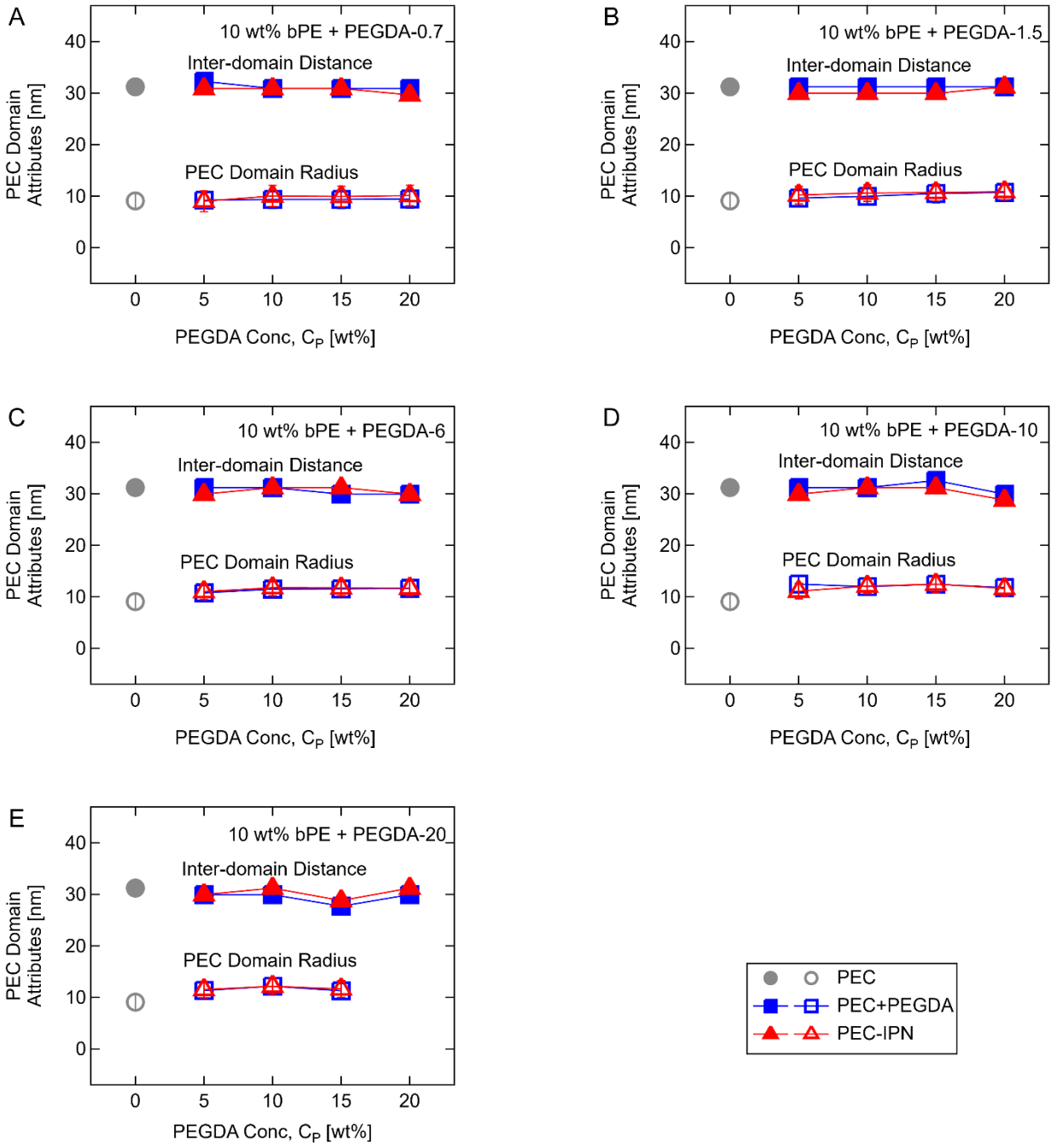

Figure 3-S8. Inter-domain distance and PEC domain radius as a function of C_P for PEC (grey), PEC+PEGDA (blue), and PEC/PEGDA IPN (red) hydrogels with different PEGDA MWs. The PEC hydrogels contained 10 wt% PE while PEC+PEGDA and PEC/PEGDA IPN hydrogels consisted of a constant 10 wt% bPE and PEGDA content with C_P ranging from 5 wt% to 20 wt%.

The PEC+PEGDA and PEC/PEGDA IPN hydrogels consisted of (A) PEGDA-0.7, (B) PEGDA-1.5, (C) PEGDA-6, (D) PEGDA-10, and (E) PEGDA-20.

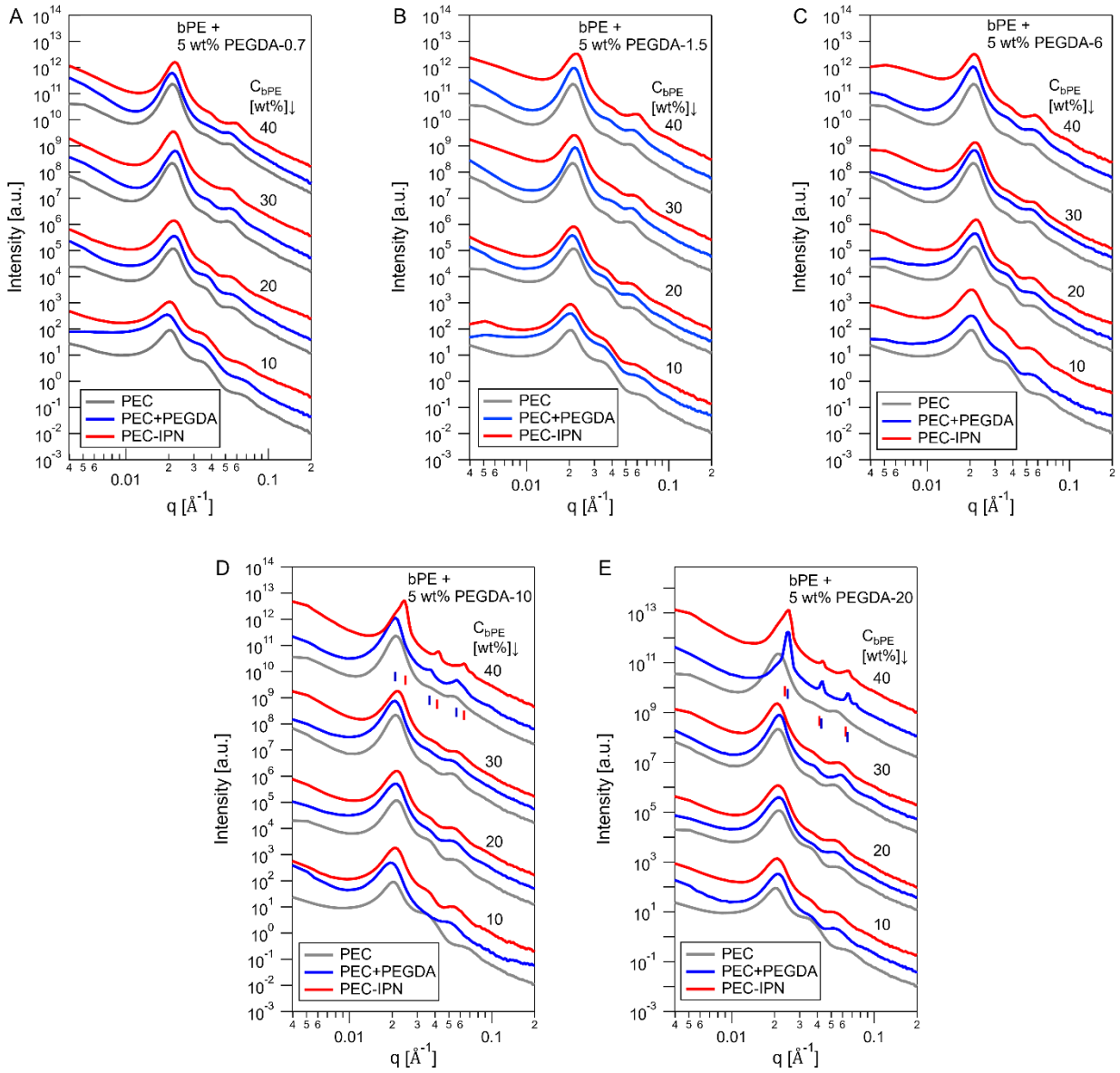

Figure 3-S 9. SAXS scattering patterns for PEC (grey), PEC+PEGDA (blue), and PEC/PEGDA IPN (red) hydrogels with different PEGDA MWs. One-dimensional intensity *I(q)* as a function of wave factor *q* for PEC hydrogels with polyelectrolyte concentration (C_{bPE}) varying from 10 wt% to 40 wt% and for PEC+PEGDA and PEC/PEGDA IPN hydrogels with a constant C_P = 5 wt% and varying C_{bPE} from 10 wt% to 40 wt%. PEC+PEGDA and PEC/PEGDA IPN hydrogels

comprised (A) PEGDA-0.7, (B) PEGDA-1.5, (C) PEGDA-6, (D) PEGDA-10, and (E) PEGDA-20. The X-ray scattering curves were shifted vertically for clarity. Peak positions were summarized in Tables 3-S1 and 3-S2.

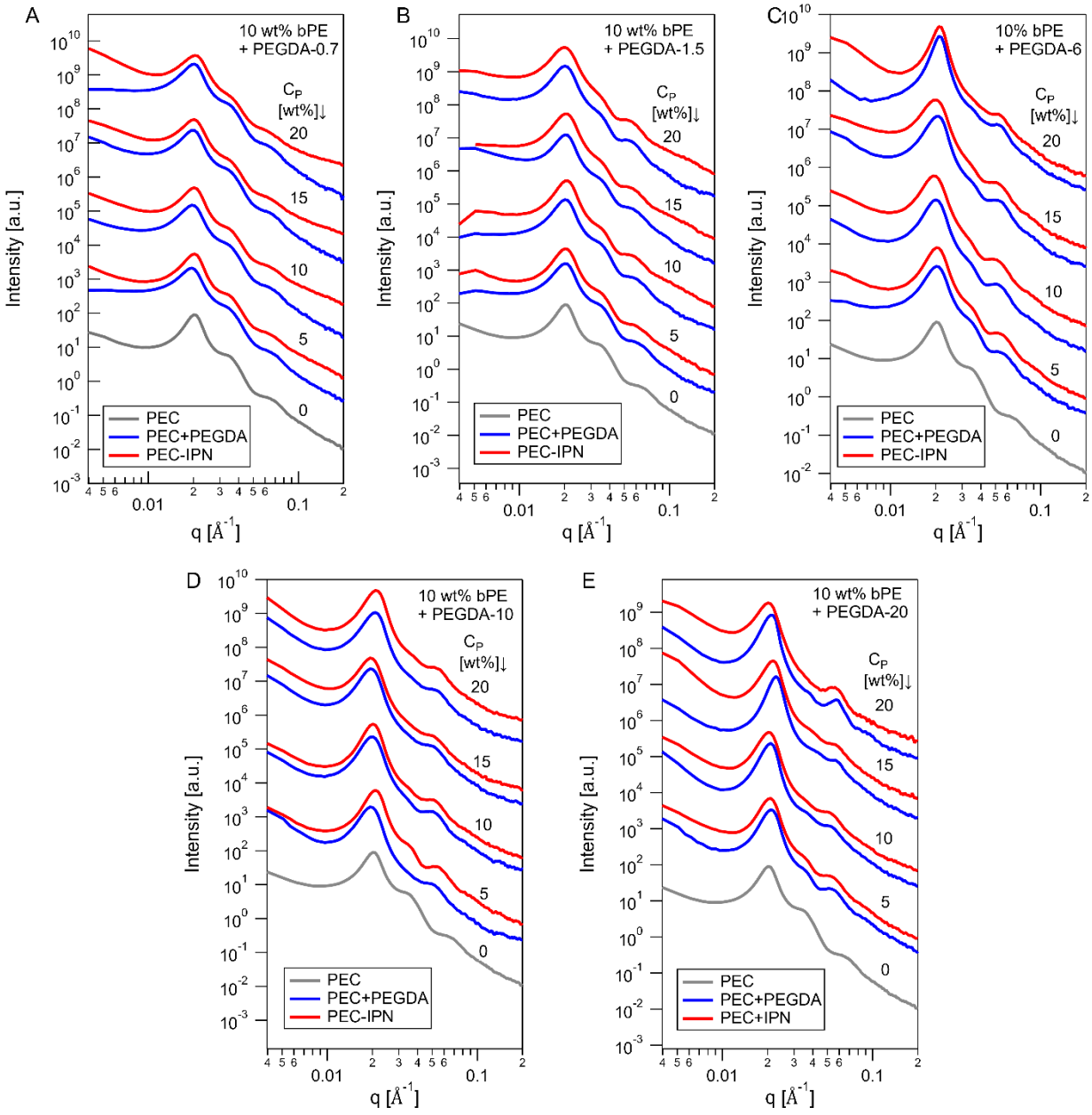

Figure 3-S10. SAXS scattering patterns for PEC (grey), PEC+PEGDA (blue), and PEC/PEGDA IPN (red) hydrogels with different PEGDA MWs. The PEC hydrogels with a constant C_{bPE} = 10 wt%, and PEC+PEGDA and PEC/PEGDA IPN hydrogel with C_{bPE} = 10 wt% and varying C_P from 5 wt% to 20 wt%. The PEC+PEGDA and PEC/PEGDA IPN hydrogels consisted of (A) PEGDA-

0.7, (B) PEGDA-1.5, (C) PEGDA-6, (D) PEGDA-10, and (E) PEGDA 20K. The SAXS scattering curves were shifted vertically for clarity.

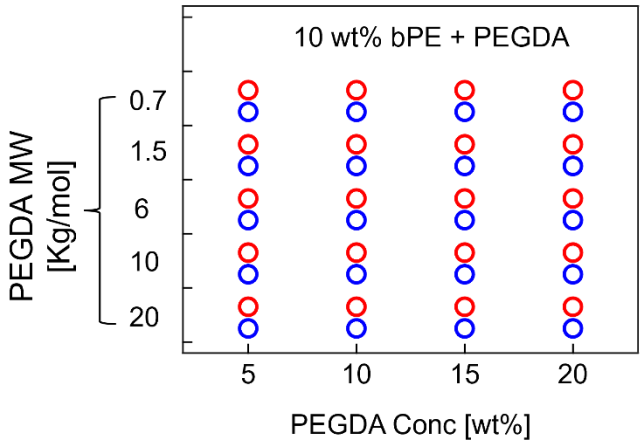

Figure 3-S11. Microstructures summary for PEC+PEGDA (blue) and PEC/PEGDA IPN (red) hydrogels with a constant C_{bPE} = 10 wt% and varying PEGDA concentration on x-axis and varying PEGDA molecular weight on y-axis.

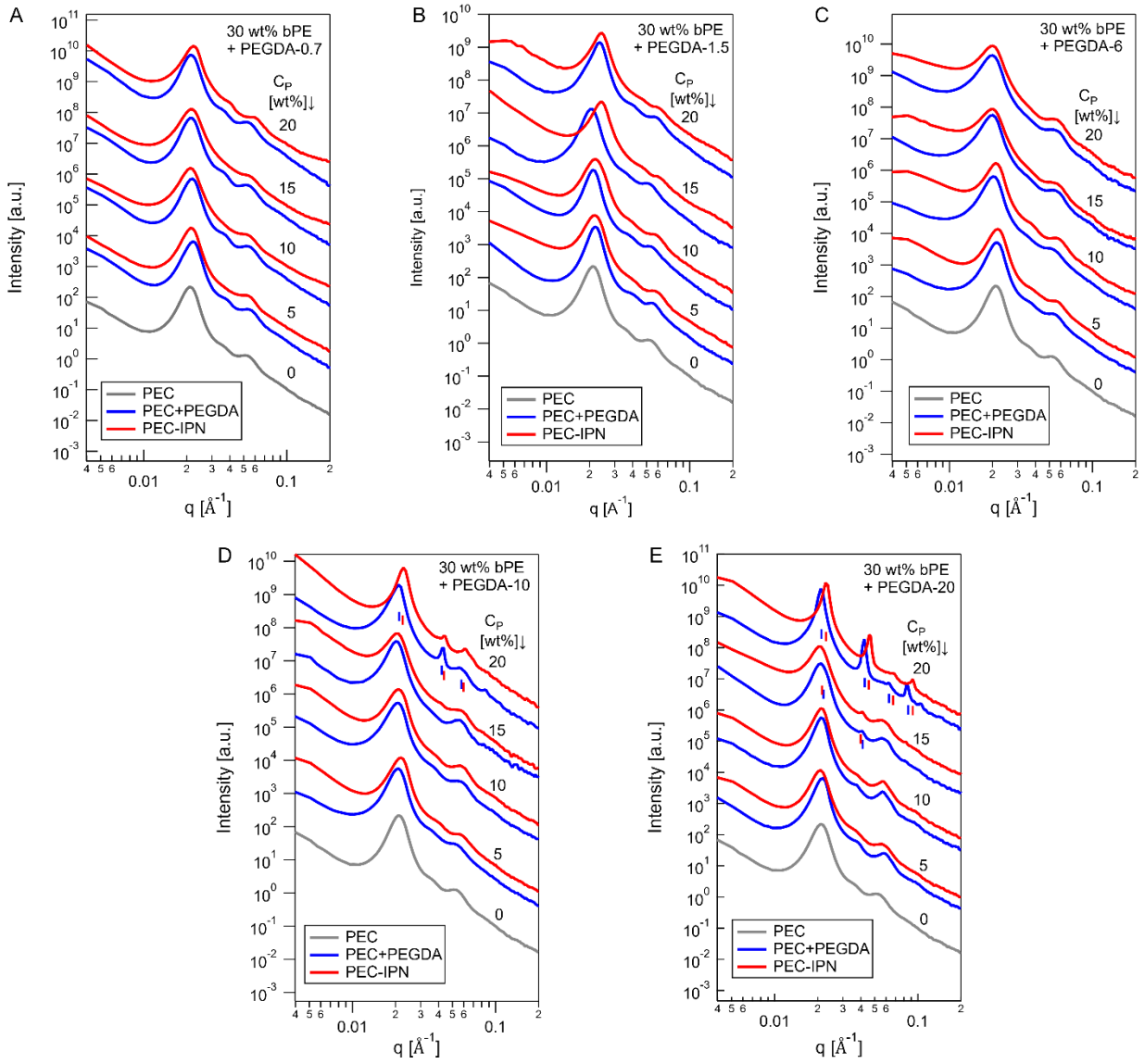

Figure 3-S12. Experimental X-ray scatterings for PEC (grey), PEC+PEGDA (blue), and PEC/PEGDA IPN (red) hydrogels with different PEGDA MWs. The PEC hydrogels with C_{bPE} = 30 wt%, and PEC+PEGDA and PEC/PEGDA IPN hydrogels with C_{bPE} = 30 wt% and varying C_P from 5 wt% to 20 wt%. The PEC+PEGDA and PEC/PEGDA IPN hydrogels consisted of (A) PEGDA-0.7, (B) PEGDA-1.5, (C) PEGDA-6, (D) PEGDA-10, and (E) PEGDA-20. The X-ray scattering curves were shifted vertically for clarity. Peak positions were summarized in Tables 3-S1 and 3-S2.

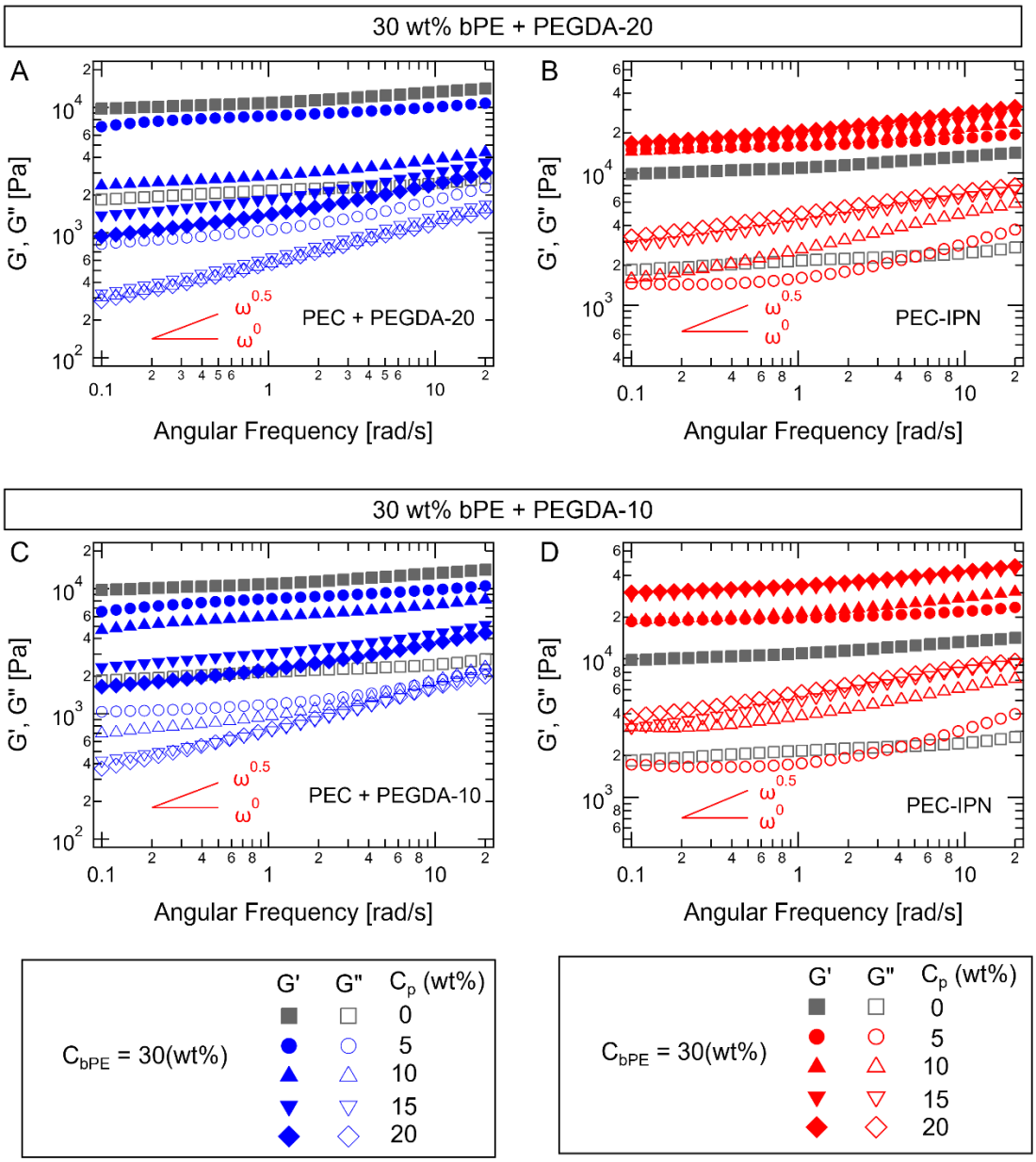

Figure 3-S13. Frequency sweeps exhibiting storage and loss moduli (G′and G") as a function of angular frequency (ω) for PEC (grey), PEC+PEGDA (blue), and PEC/PEGDA IPN (red) hydrogels with different PEGDA MWs. The PEC hydrogels with C_{bPE} = 30 wt% were included in every figure for comparison. (A-B) PEC+PEGDA-20 (blue) and PEC/PEGDA-20 IPN (red)

hydrogels with C_{bPE} = 30 wt% and varying C_P. (C-D) PEC+PEGDA-10 (blue) and PEC/PEGDA-10 IPN (red) hydrogels with C_{bPE} = 30 wt% and varying C_p.

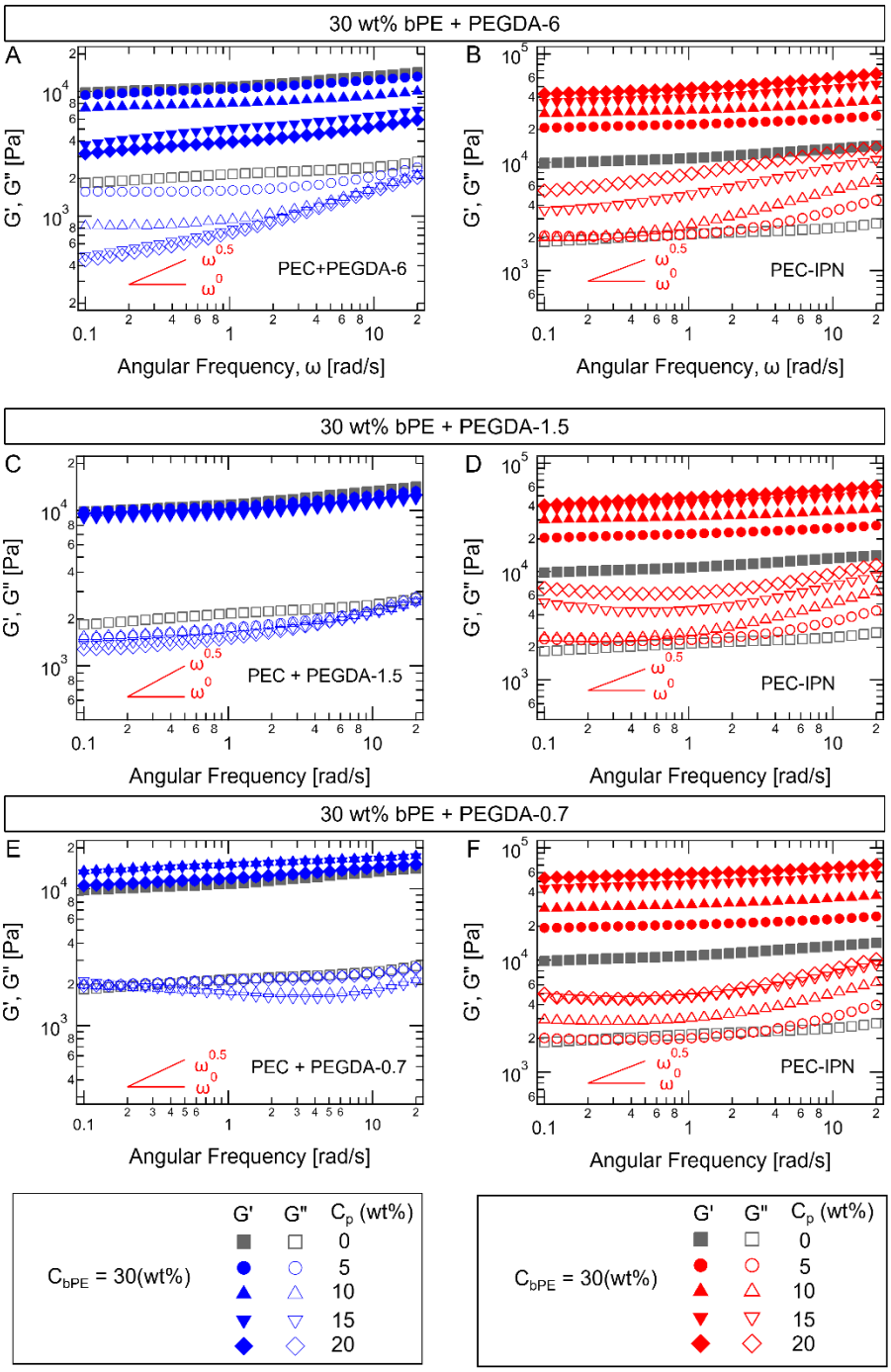

Figure 3-S14. Frequency sweeps exhibiting storage and loss moduli (G′and G") as a function of angular frequency (ω) for PEC (grey), PEC+PEGDA (blue), and PEC/PEGDA IPN (red) hydrogels with different PEGDA MWs. The PEC hydrogels with C_{bPE} = 30 wt% were included

in every figure for comparison. (A-B) PEC+PEGDA-6 (blue) and PEC/PEGDA-6 IPN (red) hydrogels with a constant C_{bPE} = 30 wt% and varying C_P. (C-D) PEC+PEGDA-1.5 (blue) and PEC/PEGDA-1.5 IPN (red) hydrogels with a constant C_{bPE} = 30 wt% and varying C_P. (E-F) PEC+PEGDA-0.7 (blue) and PEC/PEGDA-0.7 IPN (red) hydrogels with a constant C_{bPE} = 30 wt% and varying C_P.

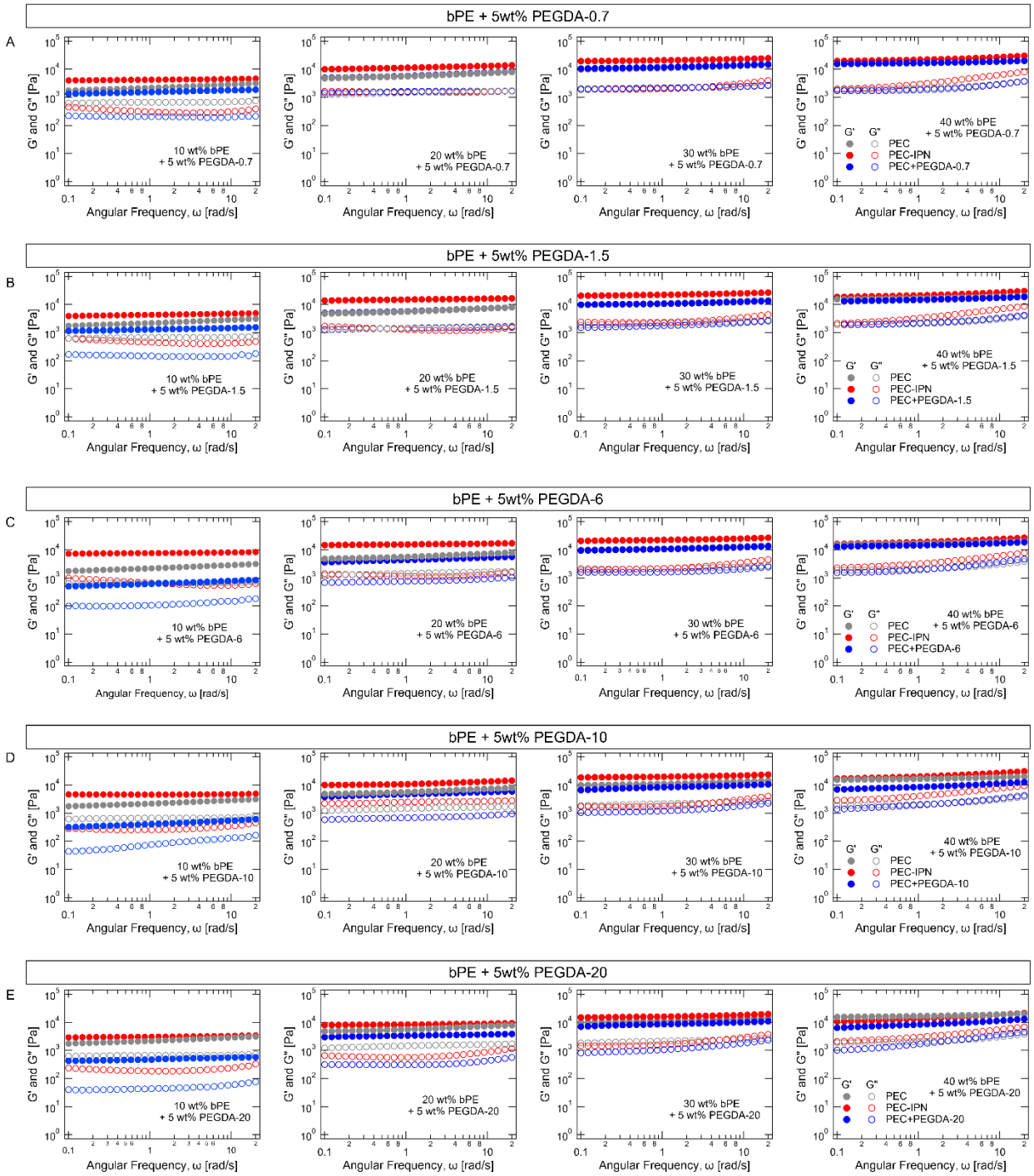

Figure 3-S15. Frequency sweeps exhibiting storage and loss moduli (G′ and G") as a function of angular frequency (ω) for PEC (grey), PEC+PEGDA (blue), and PEC/PEGDA IPN (red) hydrogels. The C_{bPE} of PEC hydrogels was varied from 10 wt% to 40 wt%. The PEC+PEGDA

and PEC/PEGDA IPN hydrogels contained PEGDA content with C_P = 5 wt% and polyelectrolytes with C_{bPE} ranging from 10 wt% to 40 wt%. The PEC+PEGDA and PEC/PEGDA IPN hydrogels consisted of (A) PEGDA-0.7, (B) PEGDA-1.5, (C) PEGDA-6, (D) PEGDA-10, and (E) PEGDA-20.

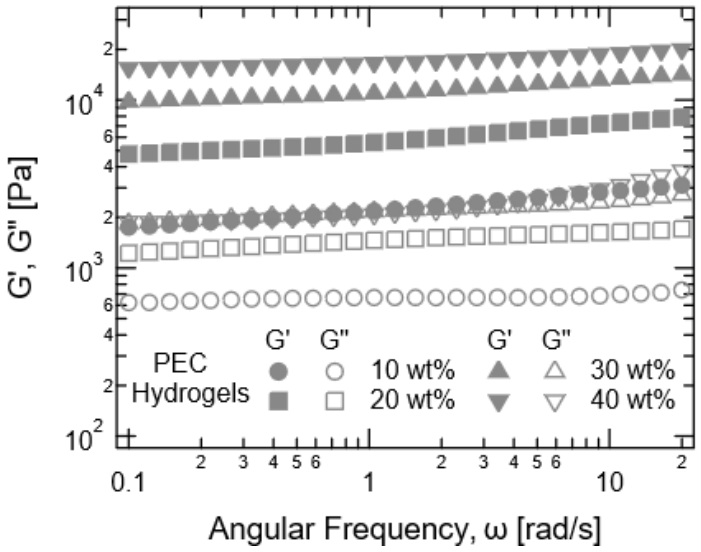

Figure 3-S16. Frequency sweeps showing storage and loss moduli (G′ and G") as a function of angular frequency (ω) for PEC hydrogels with bPE concentration varying from 10 wt% to 40 wt%.

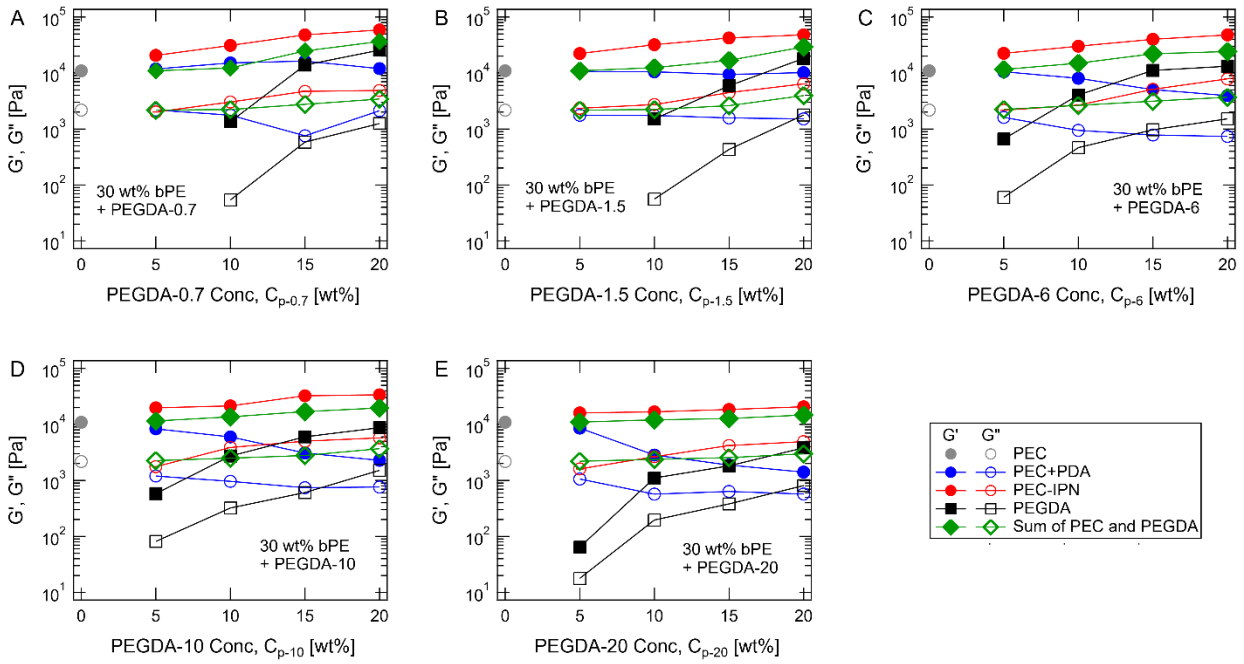

Figure 3-S17. Storage (G′) and loss (G") moduli as a function of C_P for PEC (grey), PEC+PEGDA (blue), PEC/PEGDA IPN (red), pure PEGDA (black) hydrogels , and sum of PEC hydrogel and PEGDA hydrogel (green). PEC hydrogels with C_{bPE} = 30 wt% were included in every figure for reference. Pure PEGDA, PEC+PEGDA, and PEC/PEGDA IPN hydrogels comprising of (A) PEGDA-0.7, (B) PEGDA-1.5, (C) PEGDA-6, (D) PEGDA-10, and (E) PEGDA-20.

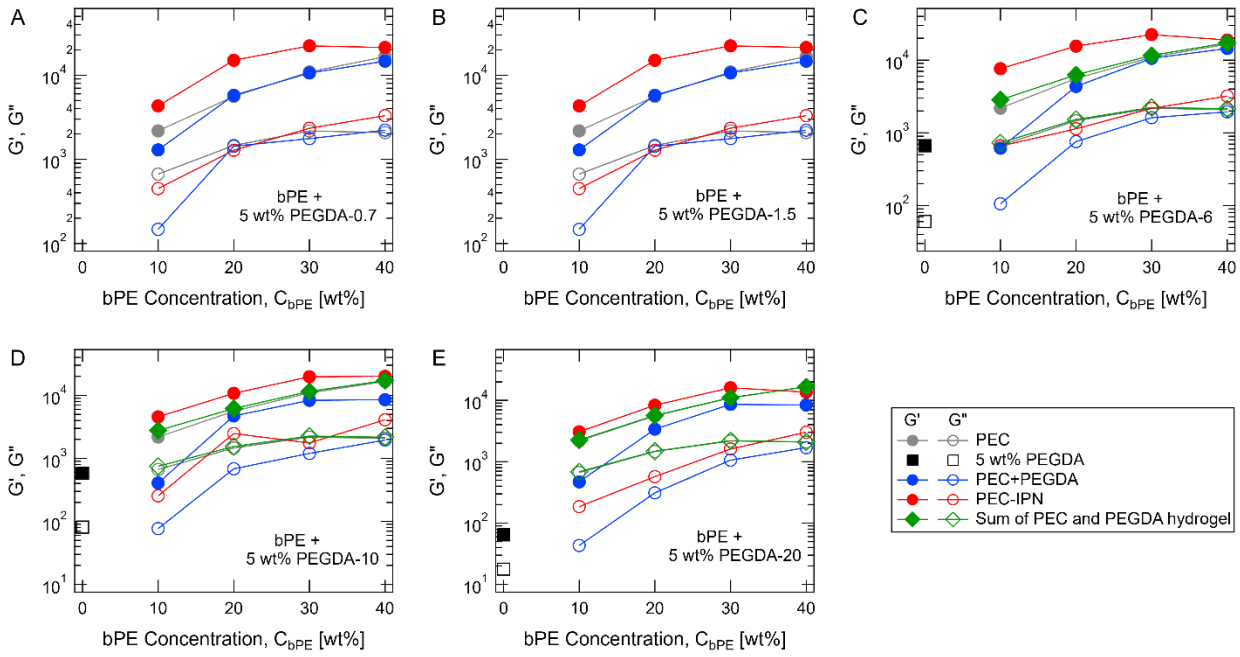

Figure 3-S18. Storage (G') and loss (G'') moduli as a function of C_{bPE} for PEC (grey), PEC+PEGDA (blue), PEC/PEGDA IPN (red), pure PEGDA (black) hydrogels , and sum of PEC hydrogel and PEGDA hydrogel (green). For each PEGDA molecular weight, PEGDA hydrogels with C_P = 5 wt% were included in every figure as a reference. Pure PEGDA, PEC+PEGDA, and PEC/PEGDA IPN hydrogels comprising of (A) PEGDA-0.7, (B) PEGDA-1.5, (C) PEGDA-6, (D) PEGDA-10, and (E) PEGDA-20.

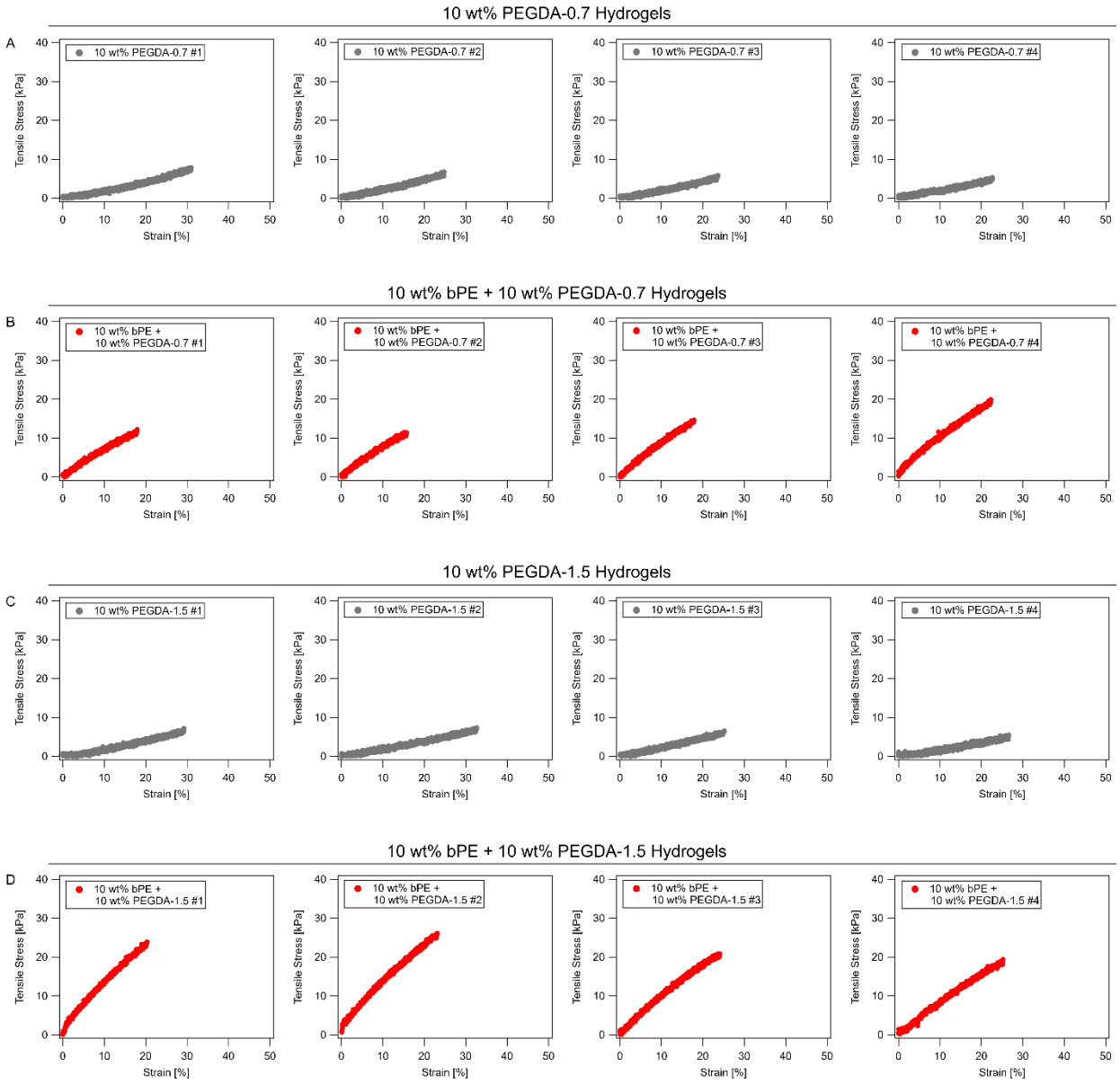

Figure 3-S19. Representative tensile stress curves as a function of strain for PEGDA hydrogels and PEC/PEGDA IPN hydrogels. (A) PEGDA-0.7 hydrogels with C_P (= 10 wt%), (B) PEC/PEGDA IPN hydrogels with 10 wt% PEGDA-0.7 and C_{bPE} (= 10 wt%), (C) PEGDA-1.5 hydrogels with C_P = 10 wt%, (D) PEC/PEGDA IPN hydrogels with 10 wt% PEGDA-1.5 and C_{bPE} = 10 wt%.

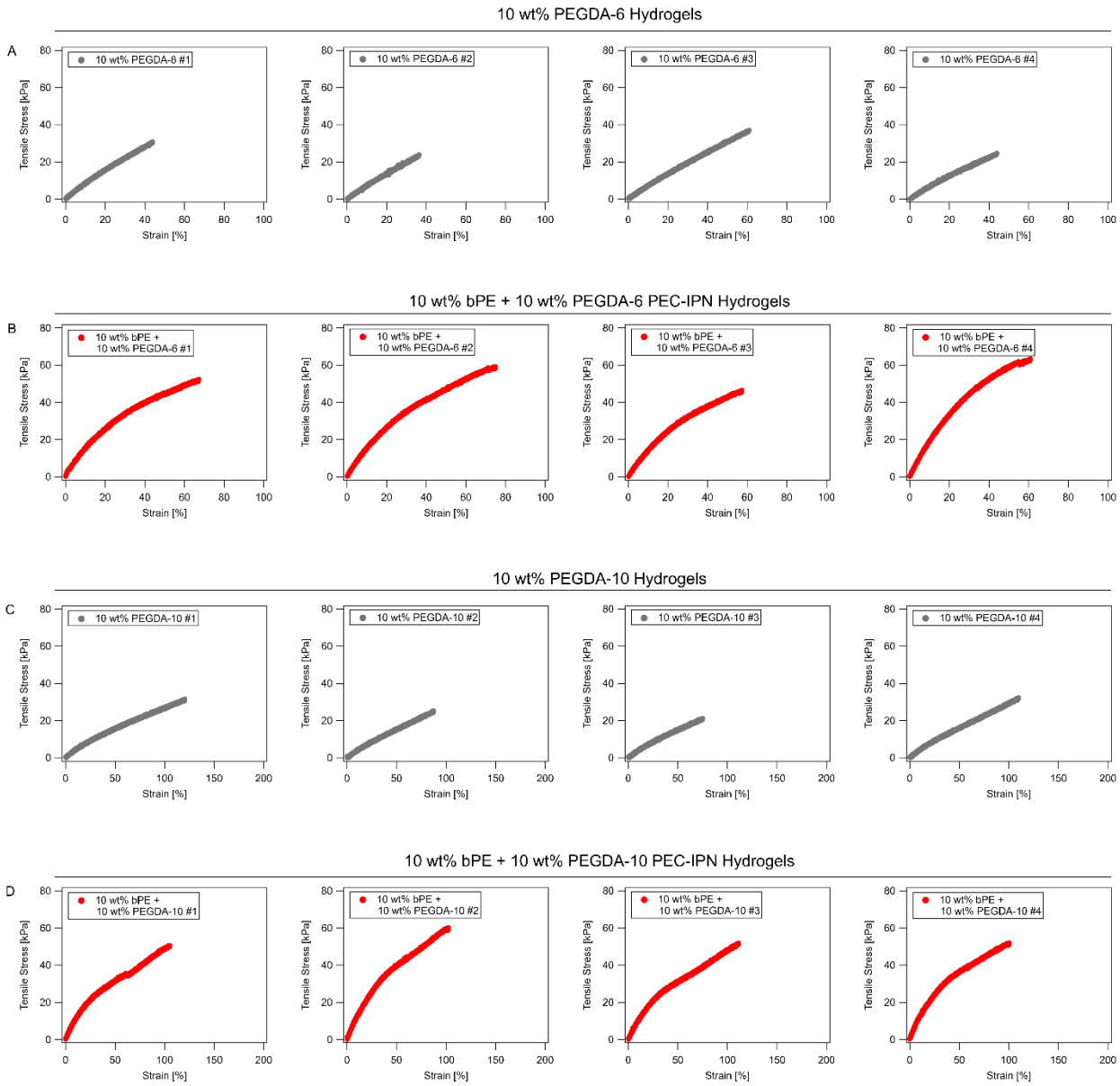

Figure 3-S20. Representative tensile stress curves as a function of strain for PEO hydrogels and PEC/PEGDA IPN hydrogels. (A) PEGDA-6 hydrogels with C_p (= 10 wt%), (B) PEC/PEGDA IPN hydrogels with 10 wt% PEGDA-6 and C_{bPE} (= 10 wt%), (C) PEGDA-10 hydrogels with C_p (= 10 wt%), (D) PEC/PEGDA IPN hydrogels with 10 wt% PEGDA-10 and C_{bPE} (= 10 wt%).

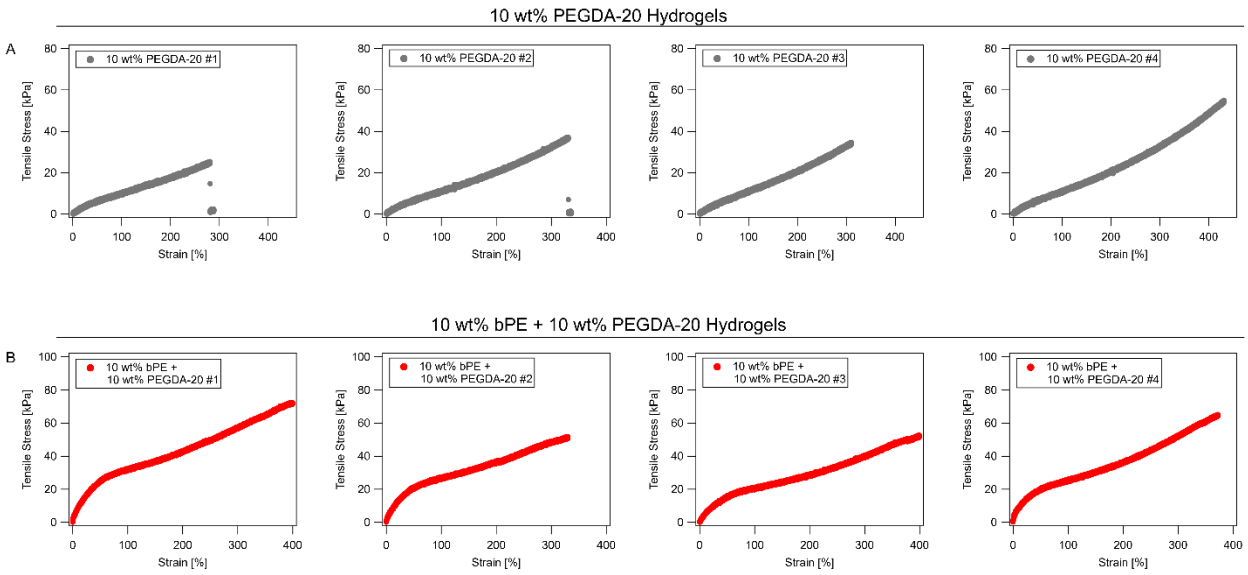

Figure 3-S21. Representative tensile stress curves as a function of strain for PEGDA hydrogels and PEC/PEGDA IPN hydrogels. (A) PEGDA-20 hydrogels with C_P = 10 wt%, (B) PEC/PEGDA-20 IPN hydrogels with C_P= 10 wt% and C_{bPE} = 10 wt%.

Table 3-S1. Bragg's peak information of PEC+PEGDA and PEC/PEGDA IPN hydrogels containing PEGDA-20.

Hydrogel Description	**q [Å^{-1}]**	$\frac{q}{q^*}$	**Expected** $\frac{q}{q^*}$	**Microstructure**
PEC+ PEGDA-20 with C_{bPE} = 30 wt% and C_P = 15 wt%, q^*= 0.0203 Å^{-1}	0.0409	2.01	2	Lam
PEC/PEGDA-20 IPN with C_{bPE} = 30 wt% and C_P = 15 wt%, q^*= 0.0203 Å^{-1}	0.0409	2.01	2	Lam
PEC+ PEGDA-20 with C_{bPE} = 30 wt% and C_P = 20 wt%, q^*= 0.0210 Å^{-1}	0.0422	2.01	2	Lam
	0.0624	2.97	3	
	0.0842	4.01	4	
PEC+ PEGDA-20 with C_{bPE} = 30 wt% and C_P = 20 wt%, q^*= 0.0227 Å^{-1}	0.0456	2.01	2	Lam
	0.0686	3.02	3	
	0.0921	4.06	4	
	0.0434	1.78	1.73	HCP

PEC+ PEGDA-20 with C_{bPE} =40 wt% and C_P = 5 wt%, q^*= 0.0244 Å^{-1}	0.0652	2.67	2.65	
PEC+ PEGDA-20 with C_{bPE} =40 wt% and C_P = 5 wt%, q^*= 0.0252 Å^{-1}	0.0434	1.72	1.73	HCP
	0.0669	2.65	2.65	

Table 3-S2. Bragg's peak information of PEC+PEGDA and PEC/PEGDA IPN hydrogels containing PEGDA-10.

Hydrogel Description	**q [Å^{-1}]**	$\frac{q}{q^*}$	**Expected** $\frac{q}{q^*}$	**Microstructure**
PEC+ PEGDA-10 with C_{bPE} = 30 wt% and C_P = 20 wt%, q^*= 0.0210 Å^{-1}	0.0434	2.07	2	HCP
	0.0564	2.69	2.65	
PEC/PEGDA-10 IPN with C_{bPE} = 30 wt% and C_P = 20 wt%, q^*= 0.0227 Å^{-1}	0.0445	1.96	2	HCP
	0.0623	2.74	2.65	
PEC+ PEGDA-10 with C_{bPE} = 40 wt% and C_P = 5 wt%, q^*= 0.0210 Å^{-1}	0.0366	1.74	1.73	HCP
	0.0564	2.69	2.65	
PEC/PEGDA-10 IPN with C_{bPE} = 40 wt% and C_P = 5 wt%, q^*= 0.0244 Å	0.0422	1.73	1.73	HCP
	0.0638	2.62	2.65	

3.6 Reference

(1) Lee, K. Y.; Mooney, D. J. Hydrogels for Tissue Engineering. *Chemical Reviews* **2001**, *101* (7), 1869-1880. DOI: 10.1021/cr000108x.

(2) Nguyen, K. T.; West, J. L. Photopolymerizable Hydrogels for Tissue Engineering Applications. *Biomaterials* **2002**, *23* (22), 4307-4314. DOI: 10.1016/s0142-9612(02)00175-8.

(3) Khademhosseini, A.; Langer, R. Microengineered Hydrogels for Tissue Engineering. *Biomaterials* **2007**, *28* (34), 5087-5092. DOI: 10.1016/j.biomaterials.2007.07.021.

(4) Wang, H.; Heilshorn, S. C. Adaptable Hydrogel Networks with Reversible Linkages for Tissue Engineering. *Advanced Materials* **2015**, *27* (25), 3717-3736. DOI: 10.1002/adma.201501558.

(5) Hoare, T. R.; Kohane, D. S. Hydrogels in Drug Delivery: Progress and Challenges. *Polymer* **2008**, *49* (8), 1993-2007. DOI: 10.1016/j.polymer.2008.01.027.

(6) Kesharwani, P.; Bisht, A.; Alexander, A.; Dave, V.; Sharma, S. Biomedical Applications of Hydrogels in Drug Delivery System: An Update. *Journal of Drug Delivery Science and Technology* **2021**, *66*, 102914. DOI: 10.1016/j.jddst.2021.102914.

(7) Li, J.; Mooney, D. J. Designing Hydrogels for Controlled Drug Delivery. *Nature Reviews Materials* **2016**, *1* (12), 1-17. DOI: 10.1038/natrevmats.2016.71.

(8) Dimatteo, R.; Darling, N. J.; Segura, T. In situ Forming Injectable Hydrogels for Drug Delivery and Wound Repair. *Advanced Drug Delivery Reviews* **2018**, *127*, 167-184. DOI: 10.1016/j.addr.2018.03.007.

(9) Pakulska, M. M.; Vulic, K.; Tam, R. Y.; Shoichet, M. S. Hybrid Crosslinked Methylcellulose Hydrogel: A Predictable and Tunable Platform for Local Drug Delivery. *Advanced Materials* **2015**, *27* (34), 5002-5008. DOI: 10.1002/adma.201502767.

(10) Seliktar, D. Designing Cell-Compatible Hydrogels for Biomedical Applications. *Science* **2012**, *336* (6085), 1124-1128. DOI: 10.1126/science.1214804.

(11) Zhang, Y. S.; Khademhosseini, A. Advances in Engineering Hydrogels. *Science* **2017**, *356* (6337), eaaf3627. DOI: 10.1126/science.aaf3627.

(12) Mehdizadeh, M.; Yang, J. Design Strategies and Applications of Tissue Bioadhesives. *Macromolecular Bioscience* **2013**, *13* (3), 271-288. DOI: 10.1002/mabi.201200332.

(13) Peak, C. W.; Wilker, J. J.; Schmidt, G. A Review on Tough and Sticky Hydrogels. *Colloid and Polymer Science* **2013**, *291* (9), 2031-2047. DOI: 10.1007/s00396-013-3021-y.

(14) Scognamiglio, F.; Travan, A.; Rustighi, I.; Tarchi, P.; Palmisano, S.; Marsich, E.; Borgogna, M.; Donati, I.; de Manzini, N.; Paoletti, S. Adhesive and Sealant Interfaces for General Surgery Applications. *Journal of Biomedical Materials Research Part B: Applied Biomaterials* **2016**, *104* (3), 626-639. DOI: 10.1002/jbm.b.33409.

(15) Kord Forooshani, P.; Lee, B. P. Recent Approaches in Designing Bioadhesive Materials Inspired by Mussel Adhesive Protein. *Journal of Polymer Science Part A: Polymer Chemistry* **2017**, *55* (1), 9-33. DOI: 10.1002/pola.28368.

(16) Bhagat, V.; Becker, M. L. Degradable Adhesives for Surgery and Tissue Engineering. *Biomacromolecules* **2017**, *18* (10), 3009-3039. DOI: 10.1021/acs.biomac.7b00969.

(17) Li, J.; Celiz, A.; Yang, J.; Yang, Q.; Wamala, I.; Whyte, W.; Seo, B.; Vasilyev, N.; Vlassak, J.; Suo, Z. Tough Adhesives for Diverse Wet Surfaces. *Science* **2017**, *357* (6349), 378-381. DOI: 10.1126/science.aah6362.

(18) Chen, X.; Yuk, H.; Wu, J.; Nabzdyk, C. S.; Zhao, X. Instant Tough Bioadhesive with Triggerable Benign Detachment. *Proceedings of the National Academy of Sciences* **2020**, *117* (27), 15497-15503. DOI: 10.1073/pnas.2006389117.

(19) Gao, Y.; Han, X.; Chen, J.; Pan, Y.; Yang, M.; Lu, L.; Yang, J.; Suo, Z.; Lu, T. Hydrogel-Mesh Composite for Wound Closure. *Proceedings of the National Academy of Sciences* **2021**, *118* (28). DOI: 10.1073/pnas.2103457118.

(20) Hunt, J. N.; Feldman, K. E.; Lynd, N. A.; Deek, J.; Campos, L. M.; Spruell, J. M.; Hernandez, B. M.; Kramer, E. J.; Hawker, C. J. Tunable, High Modulus Hydrogels Driven by Ionic Coacervation. *Advanced Materials* **2011**, *23* (20), 2327-2331. DOI: 10.1002/adma.201004230.

(21) Lemmers, M.; Sprakel, J.; Voets, I. K.; van der Gucht, J.; Cohen Stuart, M. A. Multiresponsive Reversible Gels Based on Charge-Driven Assembly. *Angewandte Chemie* **2010**, *122* (4), 720-723. DOI: 10.1002/anie.200905515.

(22) Lemmers, M.; Spruijt, E.; Akerboom, S.; Voets, I. K.; van Aelst, A. C.; Cohen Stuart, M. A.; van der Gucht, J. Physical Gels Based on Charge-Driven Bridging of Nanoparticles by Triblock Copolymers. *Langmuir* **2012**, *28* (33), 12311-12318. DOI: 10.1021/la301917e.

(23) Lemmers, M.; Spruijt, E.; Beun, L.; Fokkink, R.; Leermakers, F.; Portale, G.; Stuart, M. A. C.; van der Gucht, J. The Influence of Charge Ratio on Transient Networks of Polyelectrolyte Complex Micelles. *Soft Matter* **2012**, *8* (1), 104-117. DOI: 10.1039/c1sm06281f.

(24) Srivastava, S.; Levi, A. E.; Goldfeld, D. J.; Tirrell, M. V. Structure, Morphology, and Rheology of Polyelectrolyte Complex Hydrogels Formed by Self-Assembly of Oppositely Charged Triblock Polyelectrolytes. *Macromolecules* **2020**, *53* (14), 5763-5774. DOI: 10.1021/acs.macromol.0c00847.

(25) Srivastava, S.; Andreev, M.; Levi, A. E.; Goldfeld, D. J.; Mao, J.; Heller, W. T.; Prabhu, V. M.; de Pablo, J. J.; Tirrell, M. V. Gel Phase Formation in Dilute Triblock Copolyelectrolyte Complexes. *Nature Communications* **2017**, *8* (1), 14131. DOI: 10.1038/ncomms14131.

(26) Krogstad, D. V.; Choi, S.-H.; Lynd, N. A.; Audus, D. J.; Perry, S. L.; Gopez, J. D.; Hawker, C. J.; Kramer, E. J.; Tirrell, M. V. Small Angle Neutron Scattering Study of Complex Coacervate Micelles and Hydrogels Formed from Ionic Diblock and Triblock Copolymers. *The Journal of Physical Chemistry B* **2014**, *118* (45), 13011-13018. DOI: 10.1021/jp509175a.

(27) Krogstad, D. V.; Lynd, N. A.; Choi, S.-H.; Spruell, J. M.; Hawker, C. J.; Kramer, E. J.; Tirrell, M. V. Effects of Polymer and Salt Concentration on the Structure and Properties of Triblock Copolymer Coacervate Hydrogels. *Macromolecules* **2013**, *46* (4), 1512-1518. DOI: 10.1021/ma302299r.

(28) Krogstad, D. V.; Lynd, N. A.; Miyajima, D.; Gopez, J.; Hawker, C. J.; Kramer, E. J.; Tirrell, M. V. Structural Evolution of Polyelectrolyte Complex Core Micelles and Ordered-Phase Bulk Materials. *Macromolecules* **2014**, *47* (22), 8026-8032. DOI: 10.1021/ma5017852.

(29) Papadakis, C. M.; Tsitsilianis, C. Responsive Hydrogels from Associative Block Copolymers: Physical Gelling Through Polyion Complexation. *Gels* **2017**, *3* (1), 3. DOI: 10.3390/gels3010003.

(30) Kim, J.-M.; Heo, T.-Y.; Choi, S.-H. Structure and Relaxation Dynamics for Complex Coacervate Hydrogels Formed by ABA Triblock Copolymers. *Macromolecules* **2020**, *53* (21), 9234-9243. DOI: 10.1021/acs.macromol.0c01600.

(31) Li, D. F.; Gockler, T.; Schepers, U.; Srivastava, S. Polyelectrolyte Complex-Covalent Interpenetrating Polymer Network Hydrogels. *Macromolecules* **2022**, *55* (11), 4481-4491. DOI: 10.1021/acs.macromol.2c00590.

(32) Cui, H.; Zhuang, X.; He, C.; Wei, Y.; Chen, X. High Performance and Reversible Ionic Polypeptide Hydrogel Based on Charge-Driven Assembly for Biomedical Applications. *Acta Biomaterialia* **2015**, *11*, 183-190. DOI: 10.1016/j.actbio.2014.09.017.

(33) Wu, H.; Ting, J. M.; Yu, B.; Jackson, N. E.; Meng, S.; de Pablo, J. J.; Tirrell, M. V. Spatiotemporal Formation and Growth Kinetics of Polyelectrolyte Complex Micelles with Millisecond Resolution. *ACS Macro Letters* **2020**, *9* (11), 1674-1680. DOI: 10.1021/acsmacrolett.0c00543.

(34) Takahashi, R.; Narayanan, T.; Yusa, S.; Sato, T. Formation Kinetics of Polymer Vesicles from Spherical and Cylindrical Micelles Bearing the Polyelectrolyte Complex Core Studied by Time-Resolved USAXS and SAXS. *Macromolecules* **2022**, *55* (2), 684-695. DOI: 10.1021/acs.macromol.1c02210.

(35) Amann, M.; Diget, J. S.; Lyngsø, J.; Pedersen, J. S.; Narayanan, T.; Lund, R. Kinetic Pathways for Polyelectrolyte Coacervate Micelle Formation Revealed by Time-Resolved Synchrotron SAXS. *Macromolecules* **2019**, *52* (21), 8227-8237. DOI: 10.1021/acs.macromol.9b01072.

(36) Liu, X.; Haddou, M.; Grillo, I.; Mana, Z.; Chapel, J.-P.; Schatz, C. Early Stage Kinetics of Polyelectrolyte Complex Coacervation Monitored through Stopped-Flow Light Scattering. *Soft Matter* **2016**, *12* (44), 9030-9038. DOI: 10.1039/c6sm01979j.

(37) Jiang, J.; Chen, E.-Q.; Yang, S. The Effect of Ion Pairs on Coacervate-Driven Self-Assembly of Block Polyelectrolytes. *Journal of Chemical Physics* **2021**, *154* (14), 144903. DOI: 10.1063/5.0044845.

(38) Audus, D. J.; Gopez, J. D.; Krogstad, D. V.; Lynd, N. A.; Kramer, E. J.; Hawker, C. J.; Fredrickson, G. H. Phase Behavior of Electrostatically Complexed Polyelectrolyte Gels Using an Embedded Fluctuation Model. *Soft Matter* **2015**, *11* (6), 1214-1225. DOI: 10.1039/c4sm02299h.

(39) Audus, D. J.; Fredrickson, G. H. Field-Based Simulations of Nanostructured Polyelectrolyte Gels. In *Materials for Energy Infrastructure*, Springer, 2016; pp 1-9.

(40) Staňo, R.; Košovan, P.; Tagliabue, A.; Holm, C. Electrostatically Cross-Linked Reversible Gels—Effects of pH and Ionic Strength. *Macromolecules* **2021**, *54* (10), 4769-4781. DOI: 10.1021/acs.macromol.1c00470.

(41) Sun, T. L.; Kurokawa, T.; Kuroda, S.; Ihsan, A. B.; Akasaki, T.; Sato, K.; Haque, M. A.; Nakajima, T.; Gong, J. P. Physical Hydrogels Composed of Polyampholytes Demonstrate High Toughness and Viscoelasticity. *Nature Materials* **2013**, *12* (10), 932. DOI: 10.1038/nmat3713.

(42) Shi, R.; Sun, T. L.; Luo, F.; Nakajima, T.; Kurokawa, T.; Bin, Y. Z.; Rubinstein, M.; Gong, J. P. Elastic–Plastic Transformation of Polyelectrolyte Complex Hydrogels from Chitosan and Sodium Hyaluronate. *Macromolecules* **2018**, *51* (21), 8887-8898. DOI: 10.1021/acs.macromol.8b01658.

(43) Sun, T. L.; Cui, K.; Gong, J. P. Tough, Self-Recovery and Self-Healing Polyampholyte Hydrogels. *Polymer Science, Series C* **2017**, *59* (1), 11-17. DOI: 10.1134/S1811238217010118.

(44) Fan, H.; Wang, J.; Gong, J. P. Barnacle Cement Proteins-Inspired Tough Hydrogels with Robust, Long-Lasting, and Repeatable Underwater Adhesion. *Advanced Functional Materials* **2020**, *31* (11). DOI: 10.1002/adfm.202009334.

(45) Li, S. H.; Pan, H. Y.; Wang, Y. T.; Sun, J. Q. Polyelectrolyte Complex-Based Self-Healing, Fatigue-Resistant and Anti-Freezing Hydrogels as Highly Sensitive Ionic Skins. *Journal of Materials Chemistry A* **2020**, *8* (7), 3667-3675. DOI: 10.1039/c9ta13213a.

(46) Luo, F.; Sun, T. L.; Nakajima, T.; Kurokawa, T.; Zhao, Y.; Sato, K.; Ihsan, A. B.; Li, X.; Guo, H.; Gong, J. P. Oppositely Charged Polyelectrolytes Form Tough, Self-Healing, and Rebuildable Hydrogels. *Advanced Materials* **2015**, *27* (17), 2722-2727. DOI: 10.1002/adma.201500140.

(47) Li, G.; Zhang, G.; Sun, R.; Wong, C.-P. Dually pH-Responsive Polyelectrolyte Complex Hydrogel Composed of Polyacrylic Acid and Poly (2-(Dimthylamino) Ethyl Methacrylate). *Polymer* **2016**, *107*, 332-340. DOI: 10.1016/j.polymer.2016.11.037.

(48) Liu, Q.; Dong, Z.; Ding, Z.; Hu, Z.; Yu, D.; Hu, Y.; Abidi, N.; Li, W. Electroresponsive Homogeneous Polyelectrolyte Complex Hydrogels from Naturally Derived Polysaccharides. *ACS Sustainable Chemistry & Engineering* **2018**, *6* (5), 7052-7063. DOI: 10.1021/acssuschemeng.8b00921.

(49) Lemmers, M.; Voets, I. K.; Stuart, M. A. C.; van der Gucht, J. Transient Network Topology of Interconnected Polyelectrolyte Complex Micelles. *Soft Matter* **2011**, *7* (4), 1378-1389. DOI: 10.1039/c0sm00767f.

(50) Lee, A. L. Z.; Voo, Z. X.; Chin, W.; Ono, R. J.; Yang, C.; Gao, S.; Hedrick, J. L.; Yang, Y. Y. Injectable Coacervate Hydrogel for Delivery of Anticancer Drug-Loaded Nanoparticles in vivo. *ACS Applied Materials & Interfaces* **2018**, *10* (16), 13274-13282. DOI: 10.1021/acsami.7b14319.

(51) Gao, S.; Holkar, A.; Srivastava, S. Protein-Polyelectrolyte Complexes and Micellar Assemblies. *Polymers* **2019**, *11* (7), 1097. DOI: 10.3390/polym11071097.

(52) Magana, J. R.; Sproncken, C. C. M.; Voets, I. K. On Complex Coacervate Core Micelles: Structure-Function Perspectives. *Polymers* **2020**, *12* (9), 1953. DOI: 10.3390/polym12091953.

(53) Chen, F.; Stenzel, M. H. Polyion Complex Micelles for Protein Delivery. *Australian Journal of Chemistry* **2018**, *71* (10), 768-780. DOI: 10.1071/Ch18219.

(54) Horn, J. M.; Kapelner, R. A.; Obermeyer, A. C. Macro-and Microphase Separated Protein-Polyelectrolyte Complexes: Design Parameters and Current Progress. *Polymers* **2019**, *11* (4), 578. DOI: 10.3390/polym11040578.

(55) Shah, S.; Leon, L. Structural Dynamics, Phase behavior, and Applications of Polyelectrolyte Complex Micelles. *Current Opinion in Colloid & Interface Science* **2021**, *53*, 101424. DOI: 10.1016/j.cocis.2021.101424.

(56) Engler, A. J.; Sen, S.; Sweeney, H. L.; Discher, D. E. Matrix Elasticity Directs Stem Cell Lineage Specification. *Cell* **2006**, *126* (4), 677-689. DOI: 10.1016/j.cell.2006.06.044.

(57) Discher, D. E.; Janmey, P.; Wang, Y.-l. Tissue Cells Feel and Respond to the Stiffness of Their Substrate. *Science* **2005**, *310* (5751), 1139-1143. DOI: 10.1126/science.1116995.

(58) Kamata, H.; Li, X.; Chung, U.-i.; Sakai, T. Design of Hydrogels for Biomedical Applications. *Advanced Healthcare Materials* **2015**, *4* (16), 2360-2374. DOI: 10.1002/adhm.201500076.

(59) Yang, H.; Ghiassinejad, S.; van Ruymbeke, E.; Fustin, C.-A. Tunable Interpenetrating Polymer Network Hydrogels Based on Dynamic Covalent Bonds and Metal–Ligand Bonds. *Macromolecules* **2020**, *53* (16), 6956-6967. DOI: 10.1021/acs.macromol.0c00494.

(60) Dhand, A. P.; Galarraga, J. H.; Burdick, J. A. Enhancing Biopolymer Hydrogel Functionality through Interpenetrating Networks. *Trends in Biotechnology* **2021**, *39* (5), 519-538. DOI: 10.1016/j.tibtech.2020.08.007.

(61) Waters, D. J.; Engberg, K.; Parke-Houben, R.; Ta, C. N.; Jackson, A. J.; Toney, M. F.; Frank, C. W. Structure and Mechanism of Strength Enhancement in Interpenetrating Polymer Network Hydrogels. *Macromolecules* **2011**, *44* (14), 5776-5787. DOI: 10.1021/ma200693e.

(62) Dragan, E. S. Design and Applications of Interpenetrating Polymer Network Hydrogels. A Review. *Chemical Engineering Journal* **2014**, *243*, 572-590. DOI: 10.1016/j.cej.2014.01.065.

(63) Myung, D.; Waters, D.; Wiseman, M.; Duhamel, P. E.; Noolandi, J.; Ta, C. N.; Frank, C. W. Progress in the Development of Interpenetrating Polymer Network Hydrogels. *Polymers for Advanced Technologies* **2008**, *19* (6), 647-657. DOI: 10.1002/pat.1134.

(64) Silverstein, M. S. Interpenetrating Polymer Networks: So Happy Together? *Polymer* **2020**, *207*, 122929. DOI: 10.1016/j.polymer.2020.122929.

(65) Dust, J. M.; Fang, Z. H.; Harris, J. M. Proton NMR characterization of poly (ethylene glycols) and derivatives. *Macromolecules* **1990**, *23* (16), 3742-3746.

(66) Cruise, G. M.; Scharp, D. S.; Hubbell, J. A. Characterization of permeability and network structure of interfacially photopolymerized poly (ethylene glycol) diacrylate hydrogels. *Biomaterials* **1998**, *19* (14), 1287-1294. DOI: 10.1016/s0142-9612(98)00025-8.

(67) Kratky, O.; Porod, G. *Small angle X-ray Scattering*; Academic Press, New York, NY 1982.

(68) Guinier, A.; Fournet, G. *Small-angle Scattering of X-rays*; John Wiley and Sons, New York, NY 1955.

(69) Ilavsky, J.; Jemian, P. R. Irena: Tool Suite for Modeling and Analysis of Small-Angle Scattering. *Journal of Applied Crystallography* **2009**, *42* (2), 347-353. DOI: 10.1107/S0021889809002222.

(70) Rubinstein, M.; Obukhov, S. Power-law-like stress relaxation of block copolymers: disentanglement regimes. *Macromolecules* **1993**, *26* (7), 1740-1750.

(71) Kawasaki, K.; Onuki, A. Dynamics and rheology of diblock copolymers quenched into microphase-separated states. *Physical Review A* **1990**, *42* (6), 3664.

(72) Hołyst, R. Some Features of Soft Matter Systems. *Soft Matter* **2005**, *1* (5), 329-333.

(73) Zavitsas, A. A. Quantitative relationship between bond dissociation energies, infrared stretching frequencies, and force constants in polyatomic molecules. *Journal of Physical Chemistry* **1987**, *91* (22), 5573-5577.

(74) Haque, M. A.; Kurokawa, T.; Gong, J. P. Super tough double network hydrogels and their application as biomaterials. *Polymer* **2012**, *53* (9), 1805-1822. DOI: https://doi.org/10.1016/j.polymer.2012.03.013.

(75) Nguyen, Q. T.; Hwang, Y.; Chen, A. C.; Varghese, S.; Sah, R. L. Cartilage-like mechanical properties of poly (ethylene glycol)-diacrylate hydrogels. *Biomaterials* **2012**, *33* (28), 6682-6690. DOI: 10.1016/j.biomaterials.2012.06.005.

Chapter 4

Polyelectrolyte Complex Scaffoldings for Photocrosslinked Hydrogels

Reproduced from a manuscript in preparation. "Polyelectrolyte Complex Scaffoldings for Photocrosslinked Hydrogels". Defu Li, Mahsa Ghovvati, Nasim Annabi, Samanvaya Srivastava. *Manuscript Submitted*.

Abstract

Photocrosslinkable precursors (small molecules or polymers) undergo rapid crosslinking upon photoirradiation, forming covalently crosslinked hydrogels. The spatiotemporally controlled crosslinking, which can be achieved *in situ*, encourages the utility of photocrosslinked hydrogels in biomedicine as bioadhesives, bioprinting inks, and extracellular matrix mimics. However, the low viscosity of the precursor solutions results in handling difficulties owing to unwanted flows and dilution and compromises the strength of the photocrosslinked hydrogels. Here, we introduce oppositely charged triblock polyelectrolytes as additives for precursor solutions that transform the precursor solution into a self-assembled polyelectrolyte complex (PEC) hydrogel with enhanced shear strength and viscosity, providing interim protection against precursor dilution and mitigating secondary flows. The PEC network also augments the properties of the photocrosslinked hydrogels. Crosslinking of the precursors upon photoirradiation results in the formation of interpenetrating polymer network hydrogels with PEC and covalently-linked networks that exhibit shear moduli exceeding the linear combination of the moduli of the constituent networks and

overcome the tensile strength–extensibility tradeoff that restricts the performance of covalently-linked hydrogels. The reinforcement approach is shown to be compatible with four types of photocrosslinkable precursors, does not require any modification of the precursors, and introduces minimal processing steps, paving the way for broader translation of photocrosslinkable materials for biomedical applications.

4.1 Design, System, and Application

Photocrosslinked hydrogels have attracted extensive research and clinical interest as bioadhesives, extrusion-based 3D bioprinting, drug delivery, and tissue engineering. Although these hydrogels typically possess rigid structures after crosslinking, the low viscosity and shear strength of their precursors limit their application in situations involving uneven surfaces or excess fluids. We present self-assembled networks of oppositely charged block polyelectrolytes as scaffoldings to address these limitations and concomitantly enrich the microstructure and the mechanical properties of hydrogels. We establish broad compatibility of our approach by demonstrating improvements in precursor and hydrogel properties for four distinct photocrosslinkable materials. Moreover, we present systematic approaches to enhance the viscosity and shear strength of the precursor solutions and the shear and tensile strength as well as the hierarchical microstructure of the photocrosslinked hydrogels by varying the concentration of and interactions between the block polyelectrolytes and photocrosslinkable precursors. We envision that the design rules for block polyelectrolyte reinforced photocrosslinkable precursors and hydrogels we present will facilitate their adoption in biomedicine.

4.2 Introduction

Photocrosslinked hydrogels are employed widely in biomedicine as bioadhesives,[1-6] inks for three-dimensional (3D) bioprinting,[7-20] carriers for drug delivery,[21-33] and scaffoldings for bone and cartilage tissue engineering.[7, 21, 22, 34-45] Upon (ultraviolet) light activation, the photocrosslinkable precursors (small molecules or polymers) in aqueous solutions covalently crosslink to form three-dimensional water-laden networks.[7, 22, 34, 46, 47] Thus, precise spatiotemporal control of crosslink density, mechanical properties, and functionality is achieved by regulating light dosage.[21, 47] The

irreversible covalent linkages contribute to their mechanical strength and structural stability in diverse environments regardless of pH and salt variations. In addition, the facile injectability of low-viscosity hydrogel precursor solutions into confined spaces makes them suitable for minimally invasive surgery applications.[34, 47-49]

However, even with these desirable attributes and their use in myriad biomedical applications, photocrosslinked hydrogels still suffer from several shortcomings, before and after photocrosslinking, that limit their utility. Before light activation, the uncrosslinked precursor solutions typically have low viscosity and weak mechanical strength. When employed as bioadhesives, this results in unwanted secondary flows and a minimal capacity to mold to conform to complex geometries of irregular, non-horizontal wound sites.[50] Moreover, wet environments created by blood and biological fluids at the wound site lead to dilution and deactivation of the precursors, resulting in potential adhesive failure.[50] Similar challenges emerge in extrusion-based 3D bioprinting applications, wherein the viscosity and the structural strength of the precursor solution are too poor to print a construct with adequate printing resolution, shape fidelity, and height.[51] Therefore, appropriate reinforcements of shear strength and viscosity of precursors are essential for expanding the utility of photocrosslinkable hydrogels.

Similarly, effective solutions to improve hydrogel's shear and tensile properties after photocrosslinking are highly anticipated. Typical covalently linked hydrogels (including photo-crosslinked hydrogels) suffer from a strength-extensibility tradeoff wherein their tensile strength, extensibility, and toughness cannot be all simultaneously enhanced by increasing polymer concentration.[52-56] Moreover, such hydrogels lack self-healing characteristics and stimuli responsiveness (pH and salt), owing to the *permanent* netpoints comprising the network.[57, 58] They also do not typically feature hierarchical microstructures, resulting in poor stress dissipation

characteristics and an inability to encapsulate and release small molecule or macromolecular cargo (therapeutics, etc.).[59-61] Such features are highly sought to meet the demands of sophisticated structure-property-function relations in advanced biomaterials.

Here, we introduce a simple strategy to ameliorate the shortcomings of photocrosslinked hydrogels, both in the uncrosslinked and the crosslinked states, by harnessing polyelectrolyte complexation-driven self-assembly pathways. Oppositely charged triblock polyelectrolytes (bPEs), when introduced into the precursor solutions, self-assemble into 3D polyelectrolyte complex (PEC) networks swiftly, providing a near-instant enhancement in viscosity and preventing dilution and flow of precursors.[58, 62-64] Photocrosslinking of the precursors containing PEC gels results in hydrogels with interpenetrating covalent and bPE networks exhibiting improved shear and tensile performance.[64] We demonstrate the generality of our approach by combining bPEs with four photocrosslinkable materials, poly(ethylene glycol) diacrylate (PEGDA), 4-arm poly(ethylene glycol) acrylate (4-arm PEGA), acrylamide (AAm), and gelatin methacryloyl (GelMA), representing the diversity of precursor type (polymer vs. small molecule), structure (linear vs. star), and origin (synthetic vs. bioderived) (**Figure 4-1A**). Starting with proof-of-concept demonstrations of the viability of our proposed approach, we discuss the improvements in shear properties of the uncrosslinked precursor solutions and shear and tensile properties of photocrosslinked hydrogels. Scattering measurements are employed to argue that these improvements emerge from the self-assembled PEC network that forms when bPEs are introduced in the precursor solutions and persists in the photocrosslinked hydrogels. We conclude by discussing the design principles for improved bPE-containing photocrosslinked hydrogels. We envision that the PEC hydrogel scaffoldings proposed here will facilitate a broader transition of existing photocrosslinkable materials from research products to clinical applications.

4.3 Materials and Methods

Materials: Poly(ethylene oxide) (PEO, MW = 20,000 g/mol), potassium (99.5%), ally glycidyl ether (AGE), naphthalene, calcium hydride, N,N,N',N'- tetramethylethylenediamine (TEMED), acrylamide, gelatin (from cold-water fish skin, MW ≈ 60,000 g/mol), triethyamine, acryloyl chloride, Celite, methacrylic anhydride, 2,2-dimethoxy-2-phenylacetophenone (DMPA), sodium 3-mercapto-1-propanesulfonate (90 %), N,N′-Methylenebisacrylamide (MBAA), 1H-pyrazole-1-carboxamidine hydrochloride (99%), cysteamine hydrochloride (98%), and Irgacure 2959 were bought from Sigma-Aldrich. 4-arm poly(ethylene glycol) acrylate (MW = 20,000 g/mol) was purchased from JenKem Technology. All reagents were used as received.

Synthesis of Triblock Polyelectrolytes (bPEs): Triblock polyelectrolytes (bPEs) were synthesized following previously published methods.[58, 62-64] PEO was dried under vacuum for 12 hours. AGE was dried by stirring with calcium hydride, degassed by three cycles of freeze-pump-thaw, and purified by distillation. 20 grams of PEO were dissolved at 40 °C in anhydrous tetrahydrofuran (THF) in a glove box full of Argon gas. Potassium naphthalenide (0.4M in THF) solution was added to the PEO solution until it turned light green. Approximate of 28 mL AGE was transferred into the PEO solution and allowed to react for 48 hours. The product poly(ally glycidyl ether)$_{96}$-*b*-poly(ethylene oxide)$_{455}$-*b*-poly(ally glycidyl ether)$_{96}$ (PAGE$_{96}$-PEO$_{455}$-PAGE$_{96}$) was precipitated in hexane. Afterward, 2 g of PAGE$_{96}$-PEO$_{455}$-PAGE$_{96}$, cysteamine hydrochloride (5 equivalents per alkene), and DMPA (0.05 equivalents per alkene) was dissolved in 30 mL equal volume water/DMF mixture.[58] The solution was degassed for 30 minutes by bubbling with N_2 and then exposed under UV light (365 nm, 8 watts) for at least 6 hours to produce ammonium functionalized PAGE$_{96}$-PEO$_{455}$-PAGE$_{96}$. Sulfonate functionalized PAGE$_{96}$-PEO$_{455}$-PAGE$_{96}$ was synthesized with the same procedure except replacing cysteamine hydrochloride with sodium 3-

mercapto-1-propanesulfonate. Guanidinium functionalized $PAGE_{96}$-PEO_{455}-$PAGE_{96}$ was synthesized by dissolving 2 grams of ammonium-functionalized $PAGE_{96}$-PEO_{455}-$PAGE_{96}$ and 1H-Pyrazole-1-1-carboxamidine hydrochloride (5 equivalent per amine) in 200 ml phosphate-buffered saline (PBS) buffer. The pH of the solution was adjusted to 10, and the reaction mixture was stirred at room temperature for 3 days. All reaction mixtures were dialyzed against deionized water for 10 cycles of 12 hours each using regenerated-cellulose dialysis tubing (MWCO 3.5K, Fisher Scientific) to remove excess reagents and lyophilized to collect dry final products, which were characterized by ^{1}H NMR (**Figure 4-S1**).

Synthesis of Gelatin Methacryloyl (GelMA): Gelatin was dissolved in Dulbecco's phosphate-buffered saline (DPBS) (HyClone) to prepare 10% (W/V) solution, which was added dropwise by 8% (v/v) methacrylic anhydride under stirring.[65] The reaction was performed at around 60 °C and terminated after 2.5-3 hours by 2-3 fold dilution with preheated DPBS (~60°C). The reaction mixture was dialyzed against deionized water in dialysis tubes (Spectrum Laboratories, MWCO 12-14 kDa) for 7 days with 2 cycles per day to remove unreacted reactants and solvents.[65] The purified solution was lyophilized to collect white spongy final product, which was characterized by ^{1}H NMR (**Figure 4-S2A**).

Synthesis of poly(ethylene glycol) dimethacrylate (PEGDA): 30 grams of PEG was dissolved in 160 ml anhydrous toluene under stirring. The solution was heated to 125 ℃ to distill out approximately 40 mL of toluene to remove any trace amount of water.[66] The solution was cooled to 40 °C and sparged with N_2 gas. Triethylamine (8 equivalent per PEG chain) was added to the solution.[67] After 10 minutes, acryloyl chloride (8 equivalent per PEG chain, diluted with anhydrous toluene) was added dropwise into the solution. After 90 minutes, the product solution was filtered twice through fritted funnel filled with Celite®545.[66] The product solution was precipitated in 4 °C

hexane, and the PEGDA product was dried in a vacuum and characterized by ^{1}H NMR (**Figure 4-S2B**).

Hydrogel Preparation: PEC hydrogels were prepared by mixing oppositely charged bPEs with a molar charge ratio of 1:1 in deionized water. PEC+precursor hydrogels were prepared by mixing sulfonate functionalized bPEs with the precursor, at concentrations C_{tbPE} and C_{PC}, respectively, and 0.5 wt% photoinitiator 2959 in deionized water, followed by the addition of guanidinium functionalized bPEs. The mixtures were mixed on a vortex mixer for 60 seconds to obtain homogenous hydrogels. The PEC + precursor hydrogels were placed in polydimethylsiloxane (PDMS) molds and irradiated with ultraviolet (UV) light (302 nm, 8 W) for 10 mins to obtain the corresponding PEC/covalent hydrogels. The PEC/AAm IPN hydrogels required an additional MBAA crosslinker with a molar ratio of AAm:MBAA=1:54, TEMED catalyst (0.5 wt%), and 30 minutes of UV light exposure to form the polyacrylamide network. A micro cover glass (VWR) with a thickness of 0.16 mm was placed on the top of PDMS mold to minimize water evaporation during UV light irradiation process.

Rheology: Rheology measurements with steady and oscillatory strains were carried out on an Anton Paar MCR 302 rheometer. The viscosity of precursor solutions as a function of shear rate were measured by using a cone and plate fixture (diameter: 50 mm, core angle: 1°). The precursor solutions were placed on the bottom plate and trimmed before initiating the measurements. The shear moduli were measured using a parallel plate (diameter: 8 mm, gap height: 0.7 mm) for covalent or IPN hydrogels and a cone and plate fixture (diameter: 10 mm, cone angle: 2°) for PEC or PEC+precursor hydrogels. The PEC or PEC+precursor hydrogel samples were placed on the bottom plate and trimmed before initiating the measurements. Covalent or IPN hydrogels were prepared for rheology measurements by placing 70 µL of precursor solution or PEC+precursor

hydrogels solution using a positive displacement pipet into a cylindrical PDMS mold (diameter 8 mm, height 1.5 mm) and photocrosslinked by UV irradiation. The crosslinked samples were placed in between the parallel plates of the measurements fixture. Water evaporation was minimized during testing by using a solvent trap. All samples were pre-sheared for 195 s at strain γ = 0.8% and frequency ω = 1 rad/s to achieve a stabilization of the shear moduli. Amplitude sweeps with γ ranging from 0.01% to 100% and ω = 1 rad/s were employed to determine the linear viscoelastic regime (**Figure 4-S3)**. Frequency sweeps were carried out with ω ranging from 0.1 to 20 rad/s and γ = 0.8% (within the LVE region). All measurements were carried out at 25 °C.

Tensile Testing: Tensile measurements were performed by employing an Instron 5943 tensile system. 120 µL of precursor solutions or PEC+precursor hydrogels were placed into a cuboid PDMS mold (length: 18 mm, height: 4.5 mm, width: 1.5 mm), followed by UV irradiation. The two ends of crosslinked hydrogel samples were affixed on two pieces of rigid plastic film (ARcare 90445Q) using super glue. The plastic films were mounted on the machine tension grips. The uniaxial stretch rate was set to 6 mm/min to stretch the hydrogel samples until hydrogel rupture. The ultimate stress was collected by locating the maximum stress that a tensile sample could withstand before rupture, and the corresponding strain was defined as extensibility. Young's modulus was calculated by the slope of stress-strain curves in the linear elastic region. Toughness, quantifying the ability of hydrogels to absorb energy before fracture, was determined by integrating the area under a stress vs unitless strain curve. The statistical analysis was performed by ANOVA two-way without replication. (Alpha value = 0.05, Excel). All data of ultimate strength, extensibility, Young's modulus, and toughness are reported as mean ± standard deviation.

Small-Angle X-ray Scattering (SAXS): SAXS characterizations were performed in beamline 12-ID-B at Advanced Photon Sources, Argonne National Laboratory. Samples were loaded into the

gel sample holders provided and sealed with Kapton tape to minimize water evaporation. Wave factor q covered a range from 0.004 $Å^{-1}$ to 0.8 $Å^{-1}$ by setting the sample-to-detector distance to 2.0 m. All samples were exposed to X-rays for 0.1 s at room temperature. One-dimensional intensity $I(q)$ was converted from 2-D scattering data by the matSAXS package. The background-removed intensity $I(q)$ was acquired by subtracting the background data from sample raw data by employing Irena package in Igor Pro.

4.4 Results and Discussion

PEC hydrogels self-assemble nearly instantly upon mixing aqueous solutions of the oppositely charged bPEs. The hydrogelation is driven by electrostatic interactions between the oppositely charged bPEs and the entropy gains from counterion release, resulting in their associative phase separation.[68-70] The neutral middle blocks of the bPEs, however, restrict macroscale phase separation, resulting in the formation of a three-dimensional, physically crosslinked polymer network comprising nanoscale polymer-rich PEC domains (composed of the oppositely charged end-blocks) interconnected via the neutral blocks.[62] These PEC hydrogels are injectable, extrudable, and maintain interim resistance against dissolution and swelling upon injection in water, even upon shaking (**Figure 4-S4** and **Movie 4-SM1)**.

PEC hydrogels serve as supportive matrices for photocrosslinkable precursors, offering protection against dilution, materials loss, and deactivation, enabling their application and curing in aqueous surroundings. To ensure adequate mixing, the precursors were mixed with the negatively charged bPEs, followed by the addition of the positively charged bPEs. Charge-driven self-assembly of the bPEs resulted in PEC hydrogels with homogeneously distributed precursor materials, denoted as PEC+precursor hydrogels (**Figure 4-1B** shows a representative schematic of PEC+PEGDA

hydrogel). When injected onto underwater glass substrates, the PEC+precursor hydrogels conserve the precursors in aqueous surroundings without any apparent dilution (**Figure 4-1C**; see also **Figures 4-S5, 4-S6, 4-S7, 4-S8** and **Movies 4-SM2, 4-SM3, 4-SM4, 4-SM5**). The PEC hydrogel scaffolding retained the precursor materials, providing sufficient time for photocrosslinking of the precursors. Upon UV irradiation, crosslinking of the precursor formed a covalent network, transforming the PEC+precursor hydrogels into PEC/covalent interpenetrating polymer network (IPN) hydrogels (**Figure 4-1C**). In contrast, dilution of uncrosslinked precursors occurred immediately when exposed to aqueous media, making them incapable of forming crosslinked hydrogels (**Figure 4-S9, 4-S10, 4-S11, 4-S12** and **Movies 4-SM6, 4-SM7, 4-SM8, 4-SM9**). We note that no modification of the precursors was required to make them amenable with our reinforcement strategy; they were mixed as received or synthesized with the bPEs to create the PEC+precursor hydrogels.

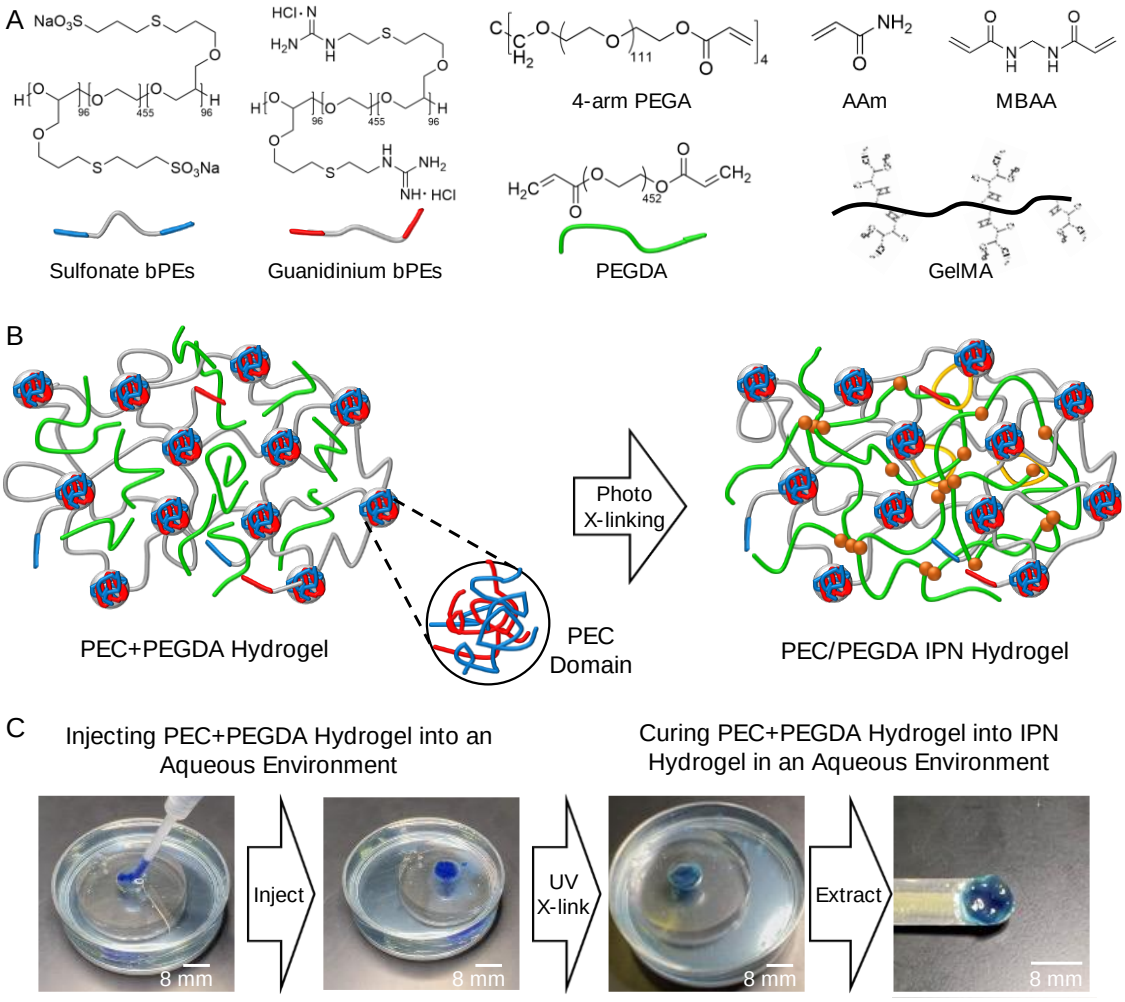

Figure 4-1. PEC scaffoldings for photocrosslinked hydrogels . **(A)** Chemical structures of sulfonate functionalized bPEs, guanidinium functionalized bPEs, 4-arm poly(ethylene glycol) acrylate (4-arm PEGA), poly(ethylene glycol) diacrylate (PEGDA), acrylamide (AAm), N,N′-Methylenebisacrylamide (MBAA), and gelatin methacryloyl (GelMA). **(B)** Schematic illustration of PEC+PEGDA hydrogels and PEC/PEGDA IPN hydrogels. **(C)** Photos demonstrating injectability and photocrosslinking of PEC+PEGDA hydrogels in an aqueous environment. Water and PEC+PEGDA hydrogels were both dyed with blue color to enhance visibility.

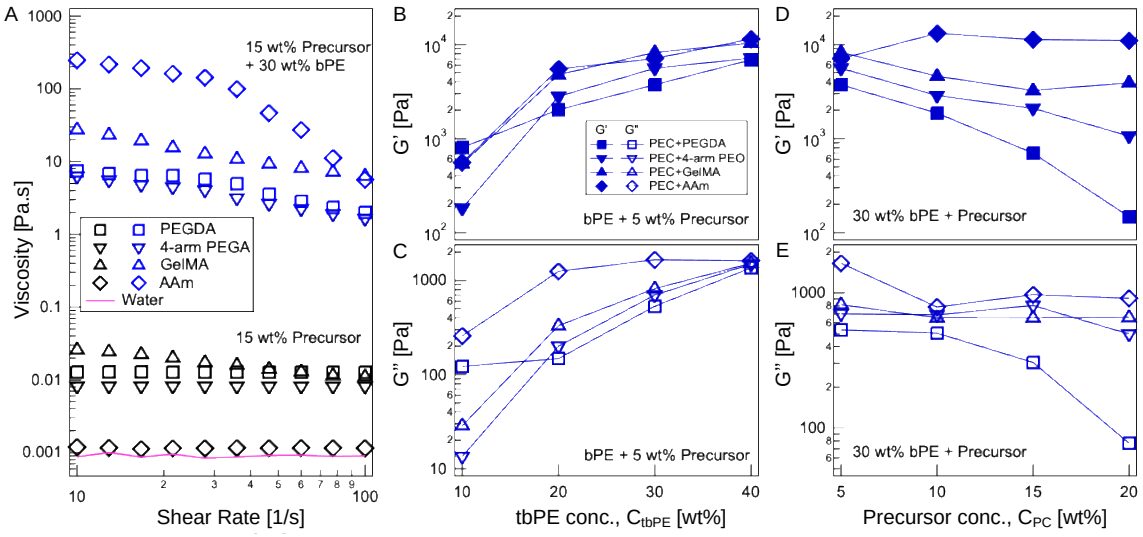

Figure 4-2. Enhancing shear properties of precursor solution with PEC hydrogel scaffoldings. (A) Viscosity of precursor solutions and PEC+precursor hydrogels versus shear rate profiles demonstrating that incorporation of bPEs in precursor solutions enhanced their viscosity significantly. Data shown for 15 wt% precursor solutions (black symbols) and PEC+precursor hydrogels (blue symbols) with 30 w% bPEs and 15 wt% precursors. (B,D) Storage (G') and (C,E) loss (G'') moduli of PEC+precursor hydrogels with a constant C_{PC} = 5 wt% and varying C_{bPE} (B,C), and with a constant C_{bPE} = 30 wt% and varying C_{PC} (D,E).

4.4.1 Modulating the Viscosity and Shear Response of Photocrosslinkable Precursors

PEC hydrogels serve as a scaffolding supporting photocrosslinkable precursors by forming a precursor-encapsulating hydrogel. These PEC+precursor hydrogels possess viscoelastic attributes that are significant improvements over the corresponding properties of the precursor solutions. The viscosity of 15 wt% solutions of PEGDA, 4-arm PEGA, and GelMA are all ~0.01 Pa·s, and of 15 wt% solution of AAm was even lower (~0.001 Pa·s), similar to water (**Figure 4-2A**). The incorporation of 30 wt% bPEs enhanced the viscosity of resultant PEC+precursor hydrogels by three to four orders of magnitude (**Figure 4-2A**), enabling easier handling of precursors.

PEC networks also imbue shear strength to resulting PEC+precursor hydrogels. Varying the content of the precursors (C_{PC}) and the bPEs (C_{bPE}) allowed for facile tuning of the shear properties of the PEC+precursor hydrogels. **Figure 4-2B, 4-2C, 4-2D, 4-2E** highlights the tunability of the shear moduli of PEC+precursor hydrogels, depicting the evolution of storage (G') and loss (G'') moduli of PEC+precursor hydrogels with increasing C_{bPE} (at constant C_{PC}) (**Figure 4-2B, 4-2C**) and with increasing C_{PC} (at constant C_{bPE}) (**Figure 4-2D, 4-2E**). Increasing C_{bPE} from 10 to 40 wt% while keeping $C_{PC} = 5$ wt% improved both G' and G'' of PEC+precursor hydrogels progressively (**Figures 4-2B, 4-2C**, see also **Figures 4-S13 and 4-S14**), ascribable to the concomitantly increasing density of the PEC domains and shear strength of the PEC network. At the same time, increasing C_{PC} from 5 to 20 wt% while maintaining a constant C_{bPE} = 30 wt% led to a progressive lowering of the shear moduli of the resulting PEC+precursor hydrogels (**Figures 4-2D, 4-2E**, see also **Figures 4-S15 and 4-S16**). We posit that the photocrosslinkable precursors encapsulated within the PEC network crowd the interstitial spaces between the PEC domains. This resulted in steric hindering of the bridging among the PEC domains by the neutral midblocks and promoting loop formation, reduced the PEC network connectivity, and thus reduced the shear moduli of the

PEC+precursor hydrogels.[64] This steric hindrance by the precursors and the accompanying reduction in moduli with increasing C_{PC} is expected to be dictated by the size of the precursor molecules (PEGDA > 4-arm PEGA > AAm), and thus is most prominent for PEC+PEGDA hydrogels, followed by PEC+4-arm PEGA hydrogels, and least prominent for PEC+AAm hydrogels (**Figures 4-2D, 4-2E**). Interactions of the precursors with the charged blocks of the bPEs are also expected to influence PEC network formation and the shear moduli of the resulting hydrogels. For example, GelMA chains comprise charged functional groups (e.g., guanidinium and carboxylic acid groups),[71, 72] which could interact with the sulfonate and the guanidinium moieties on the bPEs, and influence PEC network connectivity and shear moduli. Both these factors can be combined to precisely tune the viscoelastic behavior of the PEC+precursor hydrogels to meet the varying requirements of diverse biomedical applications requiring *in situ* polymerization, such as extrusion-based 3D bioprinting and bioadhesion.

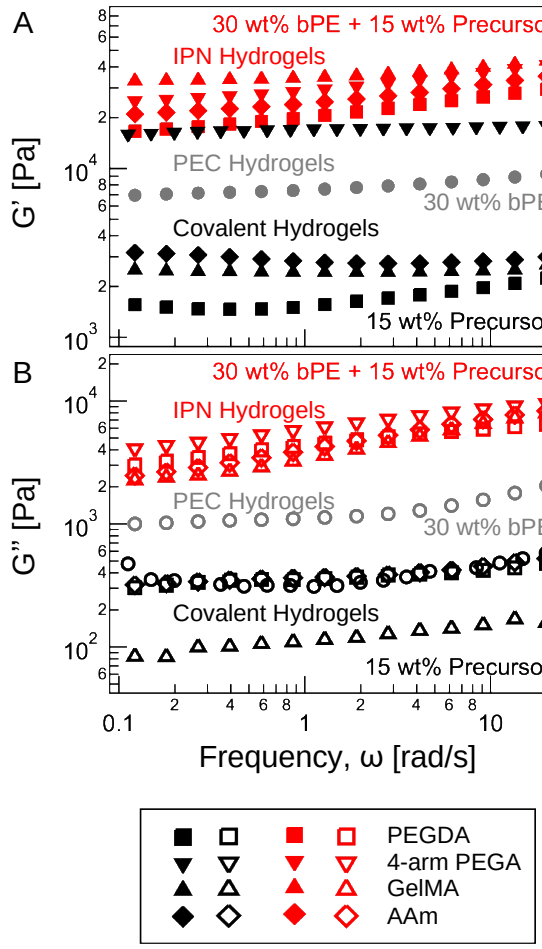

Figure 4-3. Frequency response of covalent, PEC, and IPN hydrogels. (A) Storage (G') and (B) loss (G'') moduli of PEC (grey symbols), covalent (black symbols), and IPN (red symbols) hydrogels as a function of frequency (ω) of oscillatory strain with strain amplitude γ = 0.8%.

4.4.2 Enhancing the Shear Strength of Photocrosslinked Hydrogels

The PEC network not only serves as a scaffolding for the crosslinkable precursors but also enhances the shear moduli of the crosslinked hydrogels. Upon photoirradiation, the precursors encapsulated in the PEC+precursor hydrogels crosslinked to form covalent networks, which interpenetrated with PEC networks to form IPN hydrogels. The interpenetration of the two networks is evident from the marked improvements in shear strengths of the IPN hydrogels compared to the corresponding PEC hydrogels or covalently crosslinked hydrogels. **Figure 4-3** shows the ω dependence of G' and G'', subjected to oscillatory shear strain with $\gamma = 0.8\%$, for PEC hydrogels (grey circles), covalent hydrogels (black symbols), and the corresponding IPN hydrogels (red symbols) comprising $C_{PC} = 15$ wt% and $C_{bPE} = 30$ wt% (see also **Figures 4-S17 and 4-S18**). All the hydrogels exhibit ω-independent moduli indicating robust PEC, covalent, and interpenetrating PEC/covalent networks. Notably, the shear moduli of the IPN hydrogels were higher than those of either of the constituent networks across the investigated ω range.

Figure 4-4 shows the comparison of G' and G'' (measured at ω =1.12 rad/s and $\gamma = 0.8\%$) for PEC hydrogels (grey circles), covalently crosslinked hydrogels (black squares), and the corresponding IPN hydrogels (red circles) comprising C_{PC} varying between 5 and 20 wt% and a constant $C_{bPE} = 30$ wt%. We note that all the PEC, covalent, and IPN hydrogels, except the 5 wt% covalent hydrogels, exhibited ω −independent moduli (**Figures 4-S14, 4-S17, and 4-S18**). The trend of IPN hydrogels possessing higher shear moduli than either the PEC network or the covalently crosslinked network persisted across the range of C_{PC}; for all the four kinds of photocrosslinked networks investigated here. Upon increasing C_{PC}, the moduli of the

photocrosslinked hydrogels increased owing to denser covalent networks (**Figure 4-S17**). Similarly, increasing C_{PC} continually strengthened the shear moduli of the IPN hydrogels.

It is plausible that the crosslinking of the photocrosslinkable precursors is hindered when pursued amidst the PEC network, owing to reduced mobility of the precursors, steric hindrance by the PEC network, and higher optical density of the PEC+precursor hydrogels as compared to the nearly transparent aqueous precursor solutions. This will imply a lower moduli contribution from partially crosslinked covalent networks to the moduli of the IPN hydrogels. At the same time, entanglements between the PEC and the covalent networks are expected to contribute to the shear strength of the IPN hydrogels. Notably, the shear moduli of all the IPN hydrogels considered here (red circles in **Figure 4-4**) were larger than the sum of shear moduli of individual covalent hydrogels and PEC hydrogels (purple diamonds in **Figure 4-4**). Thus, it can be argued that the excess entanglements emerging from the interpenetration of the two networks not only compensate for the loss of the shear strength caused by deficiencies in the crosslinking of the covalent network but also contribute an excess shear strength than those achievable by a linear combination of the strengths of the constituent networks.

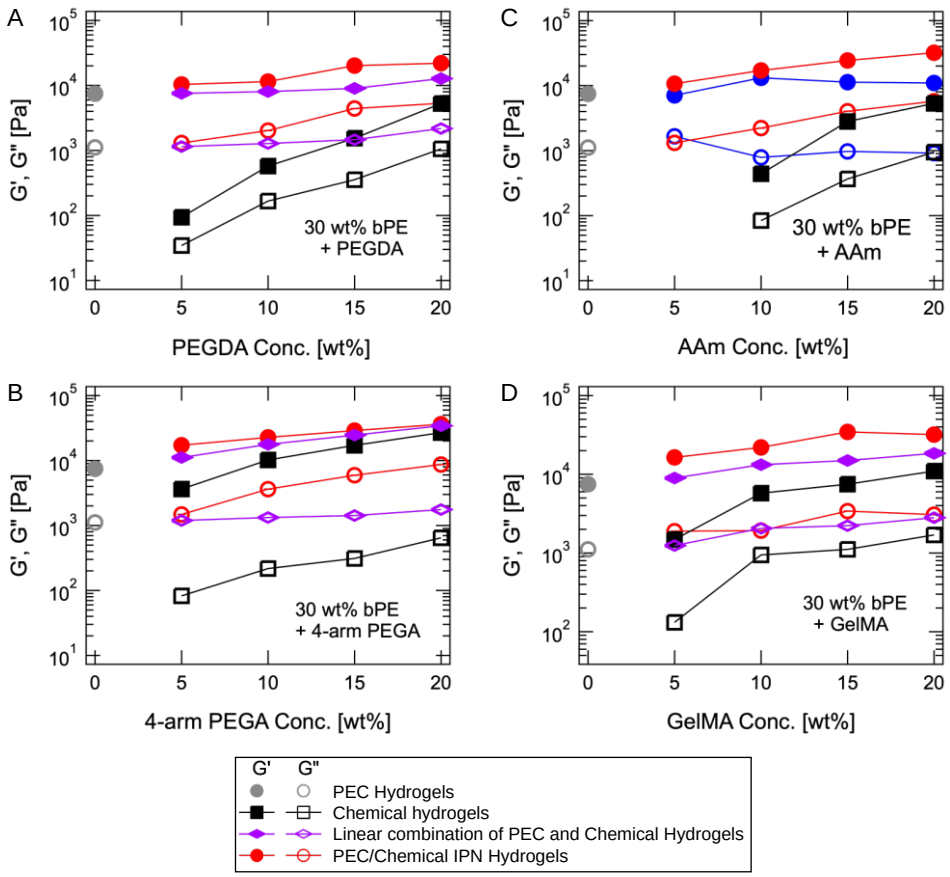

Figure 4-4. Shear moduli tunability and synergistic effects in IPN hydrogels. Storage moduli (G') and loss moduli (G'') of covalent (black squares) and PEC/covalent IPN hydrogels (comprising 30 wt% bPEs, red circles), measured at ω = 1.12 rad/s and γ = 0.8%, as a function of precursor concentration. The shear moduli of the corresponding 30 wt% PEC hydrogels are also shown with grey circles. Purple diamonds depict the linear combination of the moduli of PEC and covalent hydrogels. (A) PEGDA-based hydrogels, (B) 4-arm PEGA-based hydrogels, (C) AAm-based hydrogels, and (D) GelMA-based hydrogels.

The hindrance of crosslinking is expected to be proportional to the mobility limitations that the precursor molecules encounter in the PEC network, which in turn is expected to be inversely proportional to the size of the precursor molecules. Thus, small AAm molecules are expected to form a robust network in the presence of the PEC network, while the long PEGDA chains are expected to face the most significant hindrance. 4-arm PEGA chains should face similar transport limitations as the PEGA chains, with faster transport owing to their slightly smaller size offset by the participation of each chain in twice the number of crosslinks. Concomitantly, the moduli enhancements are the largest for PEC/AAm IPN hydrogels, followed by comparable enhancements for PEC/PEGDA IPN hydrogels and PEC/4-arm PEGA IPN hydrogels (see **Figures 4-S15, 4-S16, and 4-S18**). In addition, covalent networks carrying functional groups that interact with the charge-bearing moieties on the bPEs can contribute further enhancements to the IPN hydrogel moduli. For example, PEC/GelMA IPN hydrogels exhibited larger improvement in G' compared with IPN hydrogels comprising neutral covalent chains, attributable to the interactions between the guanidinium and carboxylic acid groups on the GelMA network and the sulfonate and the guanidinium moieties on the bPEs, contributing another mechanism for stress dissipation.

In summary, the shear strength of the photocrosslinked hydrogels benefit markedly from interpenetration by the PEC networks. Tuning C_{bPE} enables further modulation of these PEC IPN hydrogels. Upon increasing C_{bPE}, the shear moduli of PEC IPN hydrogels grew (irrespective of the chemical nature of the covalent network), owing to denser PEC networks with a higher density of PEC domains and greater extent of entanglements among the PEC and covalent networks (**Figure 4-S13**). Thus, the shear moduli of the IPN hydrogels can be tuned by changing either C_{PC} or C_{bPE} or both, providing flexibility to match the mechanical properties required in applications while also regulating the shear properties of the uncrosslinked PEC+precursors hydrogels, the

tensile properties of the IPN hydrogels, and the microstructure of the PEC network, as discussed in the following sections.

4.4.3 Enhancing the Tensile Properties of Photocrosslinked Hydrogels

The ultimate tensile strength and the Young's modulus of chemically crosslinked hydrogels can be typically enhanced by simply increasing the precursor concentrations. However, such enhancements are usually accompanied by a loss of extensibility due to a higher crosslinking density and denser covalent networks. Thus, improving the toughness of such hydrogels becomes particularly challenging owing to this strength-extensibility tradeoff.[52-56]

The interpenetration of the covalent networks with the PEC networks mitigated the tensile strength-extensibility tradeoff by enabling independent modulation of strength and extensibility of the resulting IPN hydrogels (**Figure 4-5)**. Moreover, the linear elastic response of the photocrosslinked hydrogels transitioned to a markedly non-linear response upon the introduction of the PEC networks (representative stress-strain curves are shown in **Figure 4-5, *row* 1**, see also **Figures 4-S19** and **4-S20**). The tensile properties of the covalent and the IPN hydrogels with $C_{PC} = 15$ wt% and $C_{tbPE} = 30$ wt%, as extracted from the uniaxial tensile testing, are shown in **Figure 4-5, *rows* 2-5**. In general, improvements in ultimate strength, extensibility, Young's moduli, and toughness were noted upon introducing the PEC networks. However, the magnitude of the improvements depended on the molecular structure of the precursors and their interactions with the bPE chains.

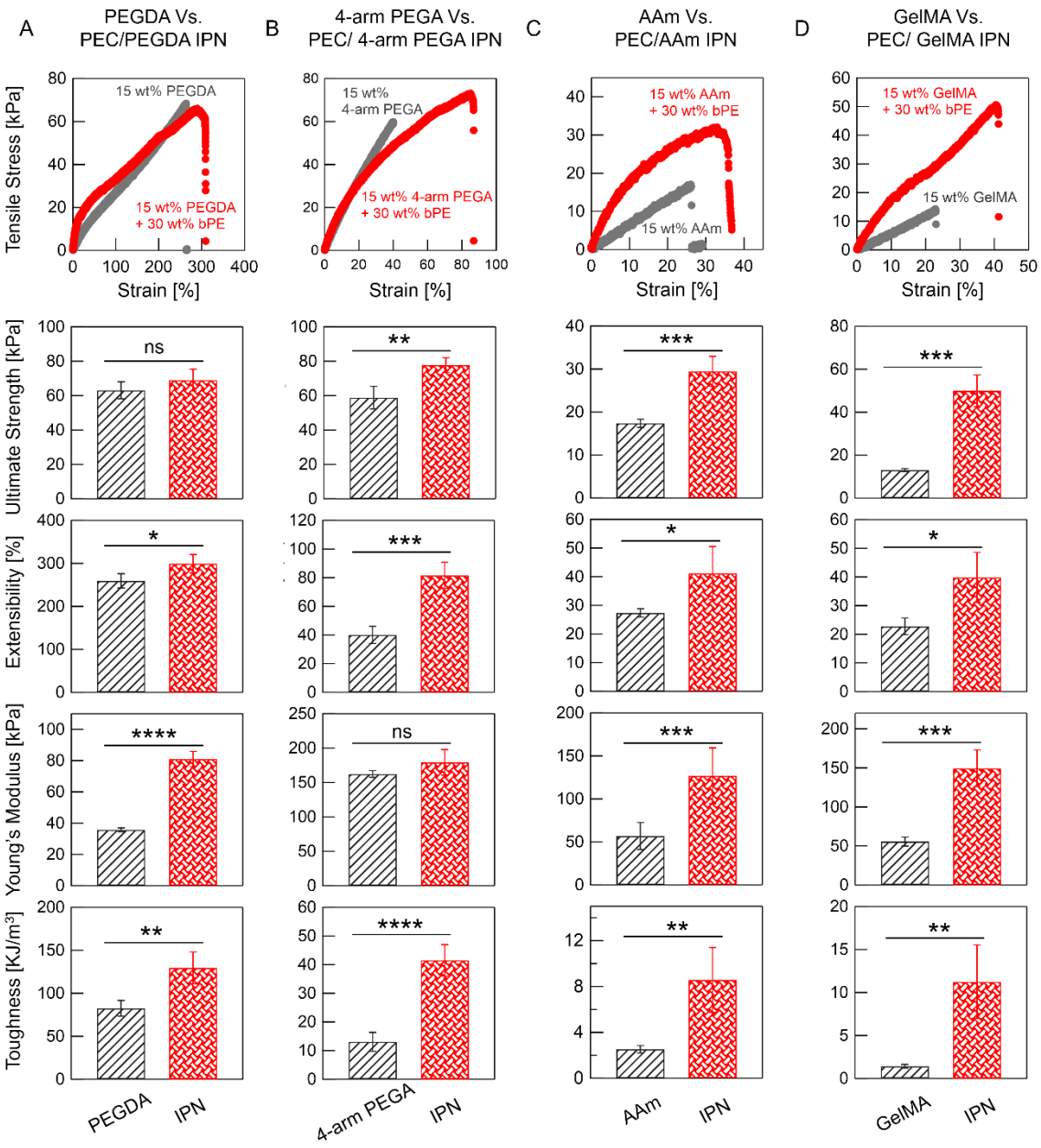

Figure 4-5. Comparing the tensile properties of covalent and IPN hydrogels. Representative tensile stress-strain curves, ultimate strength, extensibility, Young's modulus, and toughness of covalent hydrogels (grey data) and PEC/covalent IPN hydrogels (red data), with C_{PC} = 15 wt% and C_{bPE} = 30 wt%. (A) PEGDA-based hydrogels (B) 4-arm PEGA-based hydrogels, (C) AAm-based hydrogels, (D) GelMA-based hydrogels. Samples tested ≥4. The data are shown as mean ±

standard deviation (Not significant (ns): $p > 0.1$, *: $0.1 > p > 0.05$, **: $0.05 > p > 0.01$, ***: $0.01 > p > 0.001$, ****: $0.001 > p$).

The tensile strength of the IPN hydrogels is expected to have contributions from the stress-bearing covalent networks, the stress-dissipative PEC networks, and the entanglements between the two interpenetrated networks. Expectedly, enhancements in tensile strength in the IPN hydrogels over the covalent hydrogels were observed (**Figure 4-5, *row* 2**). Commensurate with the trends in the shear strength, PEC/AAm IPN hydrogels and PEC/GelMA IPN hydrogels exhibited notable improvements in the tensile strength, ascribable to the robustness of the AAm network and the favorable interactions between GelMA and bPE chains, respectively. At the same time, PEC/PEGDA and PEC/4-arm PEGA IPN hydrogels experienced hindrances in covalent crosslinking, and smaller enhancements in the tensile strengths.

Enhancements in extensibility were also noted in the IPN hydrogels as compared the corresponding covalent hydrogels (**Figure 4-5, *row* 3**). Extensibility of the IPN hydrogels is expected to be dictated by the crosslink density of the covalent network, with the additional entanglements contributed by interpenetrating PEC network contributing to inhibit chain relaxation and reducing the extensibility. Thus, the observed enhancements indicated a lower crosslinking density of covalent networks caused by topological constraints introduced by the PEC network. These enhancements were subtle in IPN hydrogels comprising PEGDA or AAm, while marked in IPN hydrogels comprising 4-arm PEGA or GelMA networks, commensurate with the stronger constraints that the 4-arm PEGA or the GelMA chains faced, owing to a high crosslink density or additional constraints owing to electrostatic interactions with the bPEs, respectively.

Entanglements between the interpenetrating networks also improved the Young's modulus of the IPN hydrogels owing to their contributions to the initial resistance to deformation (**Figure 4-5, *row* 4**). In covalent hydrogels, the crosslinking density dictates the Young's modulus – the Young's modulus of 4-arm PEGA hydrogels were three-fold higher than that of PEGDA hydrogels.

The polymer entanglements serve as additional crosslinks, resulting in notable improvement in Young's modulus of IPN hydrogels comprising PEGDA or AAm networks, while the electrostatic interactions between the GelMA and bPE chains further enhance the modulus of the PEC/GelMA IPN hydrogels. The PEC/4-arm PEGA IPN hydrogels only had a subtle improvement in Young's modulus, which can again be attributed to the incomplete crosslinking of the 4-arm PEGA networks in the IPN hydrogels.

Enhancements in both ultimate strength and extensibility in IPN hydrogels led to their higher toughness. As shown in **Figure 4-5, *row* 5**, IPN hydrogels comprising non-interacting covalent and bPE networks experienced one- to four-fold improvement in toughness compared to the covalent hydrogels. Toughness of PEC/GelMA IPN hydrogel was increased by nearly eight-fold, attributable to the toughening contributed by the reversible electrostatic interactions between the bPE and GelMA chains. Thus, by selecting appropriate photocrosslinkable precursors, IPN hydrogels with targeted tensile properties can be fabricated.

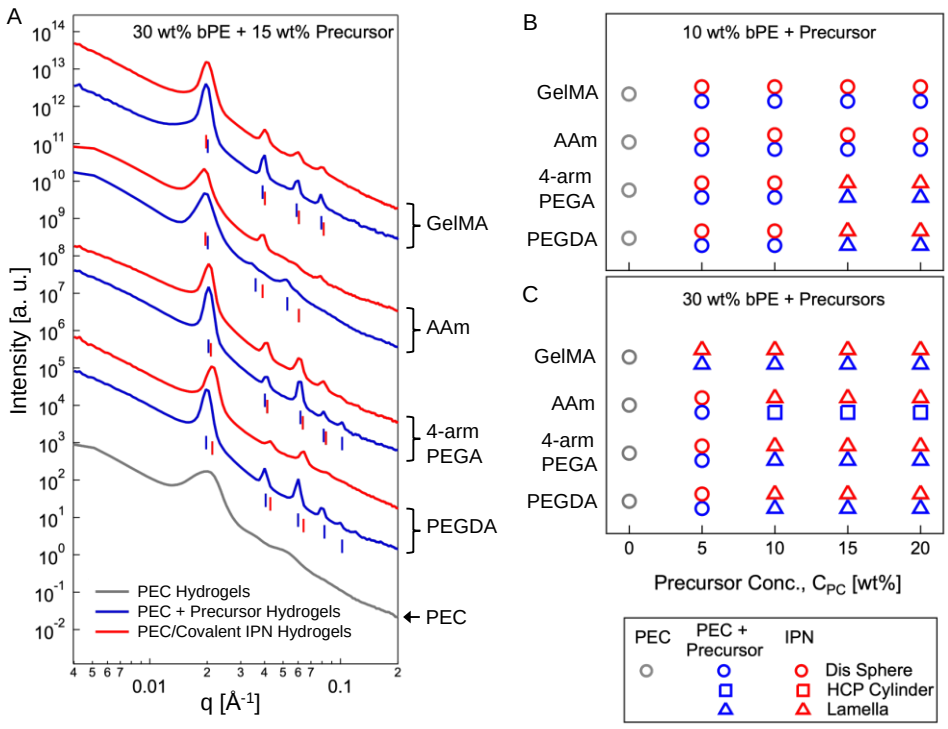

Figure 4-6. Microstructural evolution of PEC, PEC+precursor, and IPN hydrogels. (A) Representative one-dimensional small-angle X-ray scattering spectra from PEC hydrogels (grey) with C_{bPE} = 30 wt%, and the PEC+precursor (blue) and PEC IPN (red) hydrogels with C_{bPE} = 30 wt% and C_{PC} = 15 wt%. Spectra from hydrogels comprising PEGDA, 4-arm PEGA, AAm, and GelMA-based are shown from bottom to top. The spectra are shifted vertically for clarity. The vertical bars denote the positions of primary and secondary Bragg peaks. Bragg peak locations are summarized in Tables S1-S6. (B-C) The microstructural evolution of PEC, PEC + precursor, and IPN hydrogels with (B) C_{bPE} = 10 wt% and (C) C_{bPE} = 30 wt% as a function of C_{PC}.The symbols represent the following: circles - disordered spheres; squares - hexagonally packed cylinders; and triangles - lamellae.

4.4.4 Imbuing Hierarchical Microstructure to Photocrosslinked Hydrogels

The scaffolding and the enhancements provided to the photocrosslinkable precursors and the crosslinked hydrogels, respectively, emerge from the PEC network that form upon mixing of the oppositely charged bPEs. This self-assembly of bPEs results in formation of PEC domains comprising the oppositely charged blocks of the bPEs and interconnected by the neutral blocks. We argue that this self-assembled network also imbues a hierarchical microstructure to the IPN hydrogels, which is a distinct improvement over the molecular-scale crosslinking among the photocrosslinkable chains.

Small-angle X-ray scattering (SAXS) measurements were employed to seek further insights into the structure of the PEC network, specifically the size and structural arrangement of PEC domains and the average distance between them, and how they evolve upon interpenetration with the covalent networks. **Figure 4-6A** shows representative SAXS spectra from PEC hydrogels with $C_{bPE} = 30$ wt% (grey trace), PEC+precursor hydrogels with $C_{bPE} = 30$ wt% and $C_{PC} = 15$ wt% (blue traces), and the corresponding IPN hydrogels (red traces). The broad primary (near q = 0.0201 $Å^{-1}$) in the SAXS spectra of 30 wt% PEC hydrogels indicated a disordered sphere microstructure of PEC domains. Upon the introduction of the photocrosslinkable precursors, the primary peak sharpened, transforming into a Bragg reflection peak and accompanied with the emergence of secondary peaks. These sharp peaks persisted upon crosslinking of the precursors and formation of the IPN hydrogels. The relative positioning of the primary and secondary peaks revealed parallelly stacked lamellar morphology of the PEC domains in the PEC+precursor hydrogels and the IPN hydrogels with $C_{bPE} = 30$ wt% and $C_{PC} = 15$ wt%, except for PEC+AAm hydrogels which featured hexagonally close-packed arrangements of cylindrical PEC domains.

Tunability in the PEC network microstructure (PEC domain morphology and arrangements) was achieved by varying the bPE and the precursor concentrations. As illustrated in **Figure 4-6B, 4-6C**, increasing C_{PC} induced morphological evolution accompanied with an ordering transition, depending on the precursor type. Initially, a disordered arrangement of spherical PEC domains was observed in PEC hydrogels across C_{bPE} ranging from 10 to 40 wt% (**Figure 4-S21 and 4-S22**). The incorporation of precursors, up to $C_{PC} = 10$ wt% in $C_{bPE} = 10$ wt% PEC hydrogels (**Figure 4-6B,** see also **Figure 4-S23**) or up to $C_{PC} = 5$ wt% in $C_{bPE} = 30$ wt% PEC hydrogels (**Figure 4-6C**, see also **Figure 4-S24**), and their subsequent crosslinking preserved the PEC domain morphology (yellow shaded region in **Figures 4-6B, 4-6C**). At higher C_{PC}, a transition to parallelly-stacked lamellar morphology was observed in nearly all PEC+precursor and IPN hydrogels (green shaded region in **Figures 4-6B, 4-6C**), with a few exceptions as discussed below.

The morphological and ordering transitions are hypothesized to emerge from the macromolecular crowding contributed by the precursor molecules between the PEC domains, increasing the effective volume fraction of the bPE chains. Similar transitions have been reported earlier in PEC hydrogels with increasing bPE concentration[63, 64] or upon inclusion of polymeric additives.[64] With increasing size of the precursor molecules (AAm<4-arm PEGA<PEGDA), the crowding is expected to be more significant, resulting in morphological transitions at smaller C_{PC} values. This trend is illustrated in **Figure 4-6B**, wherein morphological transitions of the PEC domains are observed only in 4-arm PEGA or PEGDA containing PEC hydrogels or IPN hydrogels, but not in AAm containing hydrogels. Moreover, as shown in **Figure 4-6C**, the PEC domains transform from spheres into cylinders upon incorporation of >10 wt% AAm monomers followed by a transition into lamellae upon photocrosslinking, commensurate with the enhanced crowding effects upon AAm network formation (blue shaded region in **Figure 4-6C**). At the same time, the evolution of

PEC network microstructure is further convoluted by the interactions between GelMA and bPE chains. At low C_{bPE}, GelMA did not have any effect on the PEC domain morphology (**Figure 4-6B**). However, at higher C_{bPE} ($\geq$ 30 wt%, **Figure 4-6C,** see also **Figure 4-S21**), introduction of even 5 wt% of GelMA induced a transition of the PEC domains from disordered sphere to lamellar morphology (red shaded region in **Figure 4-6C**).

Overall, it can be surmised that the PEC networks are compatible with and resilient towards introduction of different types of precursors, with distinct molecular structures, crosslinking mechanisms, functional groups, and polymer origins, and their corresponding covalent networks.

4.5 Design Guidelines for PEC IPN Hydrogels

This work provides a design paradigm to improve the properties of photocrosslinked hydrogels, pre- and post-crosslinking, by employing PEC hydrogels, composed of oppositely charged block polyelectrolytes, as functional scaffoldings. Here, we have demonstrated the fabrication of PEC+precursor hydrogels and PEC/covalent IPN hydrogels with four kinds of photocrosslinkable precursors (PEGDA, 4-arm PEGA, GelMA, and AAm), demonstrating the suitability of PEC hydrogels as a scaffolding for photocrosslinkable hydrogels. No modification of the precursors was required to make them compatible with the bPEs, and the four types of PEC+precursor hydrogels and the IPN hydrogels all featured improvements in their material properties while retaining the PEC microstructure. These improvements are surmised in the schematic shown in **Figure 4-7**.

We note that the extent of improvements in the shear properties of the PEC+precursor hydrogels and of the shear and the tensile properties of the IPN hydrogels depend on the chemical nature and the size of the precursor molecules, which in turn is posited to influence the extent of bridging in

the PEC network and the completeness of the covalent network. Thus, the shear and tensile properties of the photocrosslinked IPN hydrogels can be tuned by varying the concentration and sizes of the bPEs and the precursor molecules. Moreover, precursors carrying ionizable functional groups (e.g., GelMA) can interact with the bPE chains, resulting in further improvements of the shear and the tensile properties of the IPN hydrogels.

Systematic tuning of the shear properties of the precursors by dispersing them in PEC hydrogels prior to photocrosslinking, creating PEC+precursor hydrogels, enables their application and curing in aqueous environments.[64] Increasing the bPE concentration leads to higher shear moduli, while increasing the precursor concentration leads to a reduction of the shear moduli. The extent of the latter, however, is dependent on the chemical nature and size of the precursor molecules. A small molecular precursor (e.g., AAm) was shown to have negligible influence on the shear moduli, while a large molecule (e.g., PEGDA with 20,000 g/mol) lowered the shear moduli of PEC+precursor hydrogels notably. Additionally, the reversible and recoverable nature of the self-assembled PEC network imparted strong shear-thinning and quick recovery upon cessation of shear, enabling facile injectability and fast recovery upon deposition of the PEC+precursor hydrogels.[58, 62] The improved viscosity and shear properties of the photocrosslinkable precursors can improve their utility in extrusion-based 3D bioprinting, wherein enhancement of inter-layer bonding, prevention of secondary flow, and mitigation of the need to photocrosslink after deposition of each layer can offer improved printing resolution and enable construction of intricate architectures. Similarly, the PEC+precursors hydrogels can be molded to conform to an irregular substrate (wound site) and prevent secondary flow at target sites, improving the functionality of existing photocrosslinkable bioadhesives.

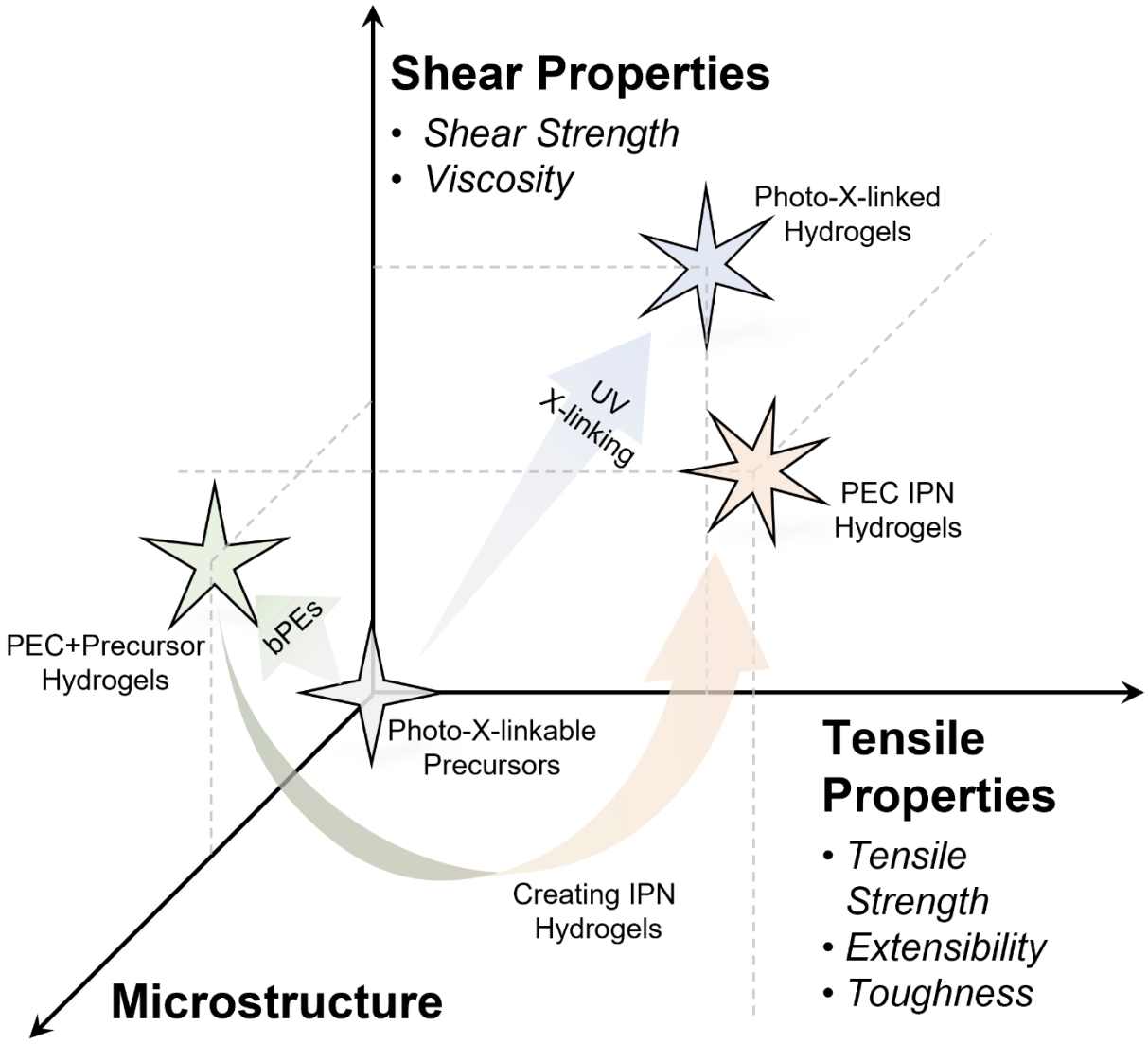

Figure 4-7. Design guidelines for PEC-based hydrogels. Photocrosslinking imbues both shear and tensile properties to covalent hydrogels, but no microstructure. Combining of bPEs with precursors introduce microstructural diversity, stronger shear strength, and higher viscosity to the precursor solutions. Upon photocrosslinking, the IPN hydrogels acquire improvements in both tensile and shear properties owing to formation of interpenetrating covalent and PEC networks.

The improvements in the shear properties of the PEC+precursor hydrogels translate into enhanced shear and tensile performance of the IPN hydrogels fabricated by photoirradiation of the PEC+precursor hydrogels. Interpenetration of the PEC and covalent networks reinforces the shear and tensile properties of the resulting IPN hydrogels while preserving the PEC network microstructure (**Figure 4-7**). We note that while the mixing of the bPEs with the photocrosslinkable precursors can reduce the transparency of the PEC+precursor hydrogels as compared to the precursor solutions, the optical density of the PEC+precursor hydrogels was tuneable by regulating bPEs concentration (**Figure 4-S25**). Moreover, the lowered transparency wasn't found to influence the photocrosslinking of the precursors noticeably, as ascertained from the performance of the IPN hydrogels under shear or tensile loads.

In the IPN hydrogels, both the shear and the tensile performance can be modulated by varying the bPE or precursor contents. Higher bPE or precursors concentration strengthen the shear moduli of the IPN hydrogels, ascribable to higher crosslink density in the PEC or the covalent network, respectively. The shear moduli of the IPN hydrogels were found to be higher than the linear combination of the moduli of the two networks, highlighting the synergistic contribution of the additional entanglements between the interpenetrated PEC and covalent networks to the shear performance of the IPN hydrogels. At the same time, reversible assembly of the PEC domains comprising the PEC network contribute for additional mechanism for stress-dissipation in the IPN hydrogels. Hence, in cases wherein the covalent network formation was not inhibited significantly (e.g., PEC/AAm IPN hydrogels), the tensile strength of the IPN hydrogels improved notably. In contrast, IPN gels wherein the covalent network formation was partially inhibited (e.g., PEC/PEGDA and PEC/4-arm PEGA IPN hydrogels) benefitted from improvements in extensibility while the loss of tensile strength from the incomplete covalent network formation

were compensated by the enhancements in strength from the PEC network and the additional entanglements between the PEC and the covalent networks. In all cases, the hydrogel toughness improved.

The self-assembled PEC domains constituting the PEC network contribute to additional attributes beyond providing mechanical reinforcement in PEC+precursor hydrogels and IPN hydrogels by serving as reversible physical multi-linkages that aid in energy dissipation and enhance the bulk strength and toughness. The PEC domains provide a richer microstructural diversity to the IPN hydrogels and also can serve as repositories for controlled encapsulation and release of charged macromolecules (drugs, growth factors)[63] to enable photocrosslinked hydrogels with therapeutic attributes.

4.6 Supplementary Information

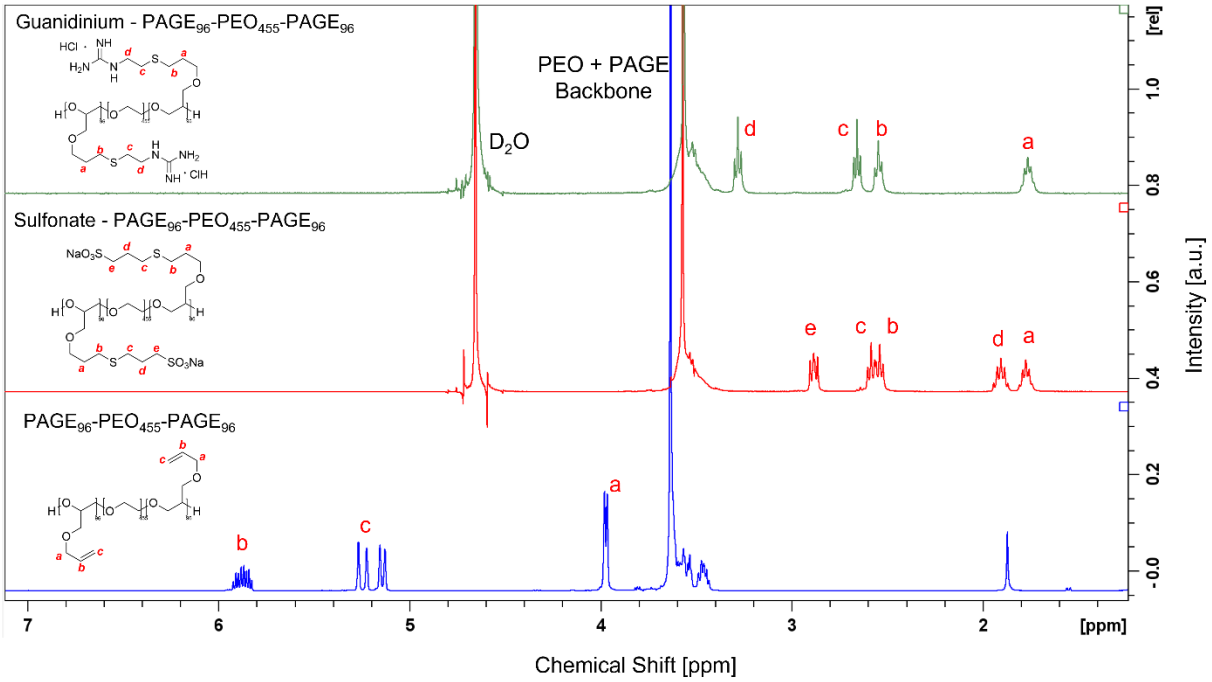

Figure 4-S1. ^{1}H NMR spectra of $PAGE_{96}$-PEO_{455}-$PAGE_{96}$, sulfonate-functionalized $PAGE_{96}$-PEO_{455}-$PAGE_{96}$, and guanidinium-functionalized $PAGE_{96}$-PEO_{455}-$PAGE_{96}$.

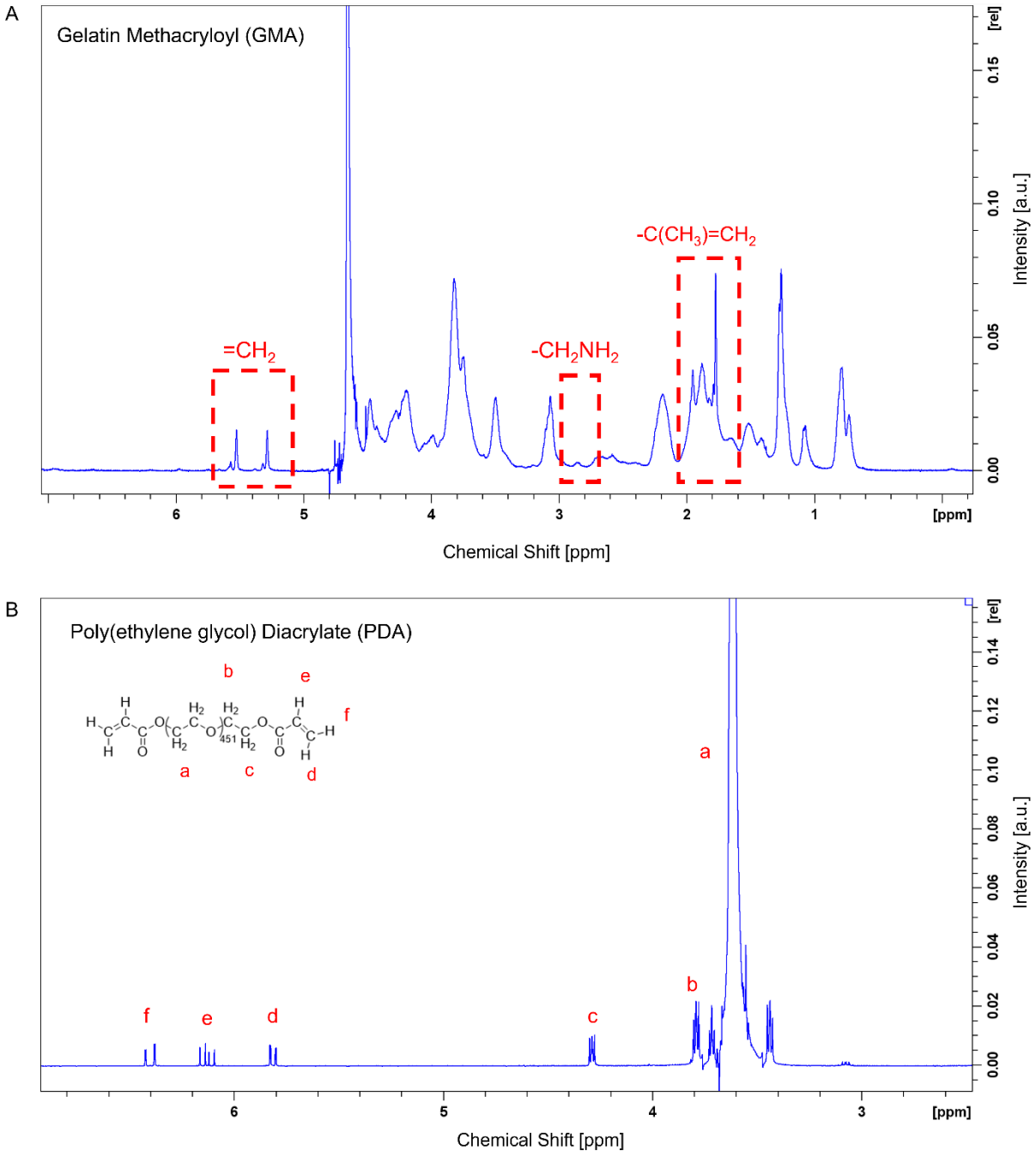

Figure 4-S2. ^{1}H NMR spectra of (A) Gelatin Methacryloyl (GelMA) and (B) Poly(ethylene glycol) diacrylate (PEGDA).

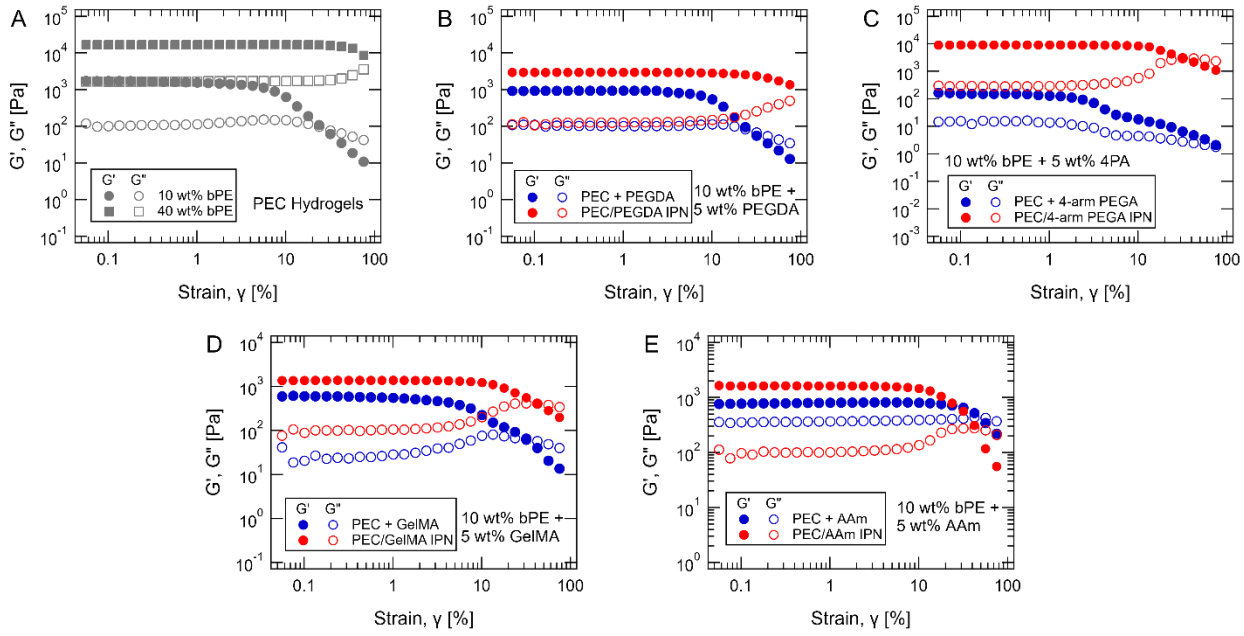

Figure 4-S3. Representative amplitude sweeps showing G' and $G"$ as a function of strain for PEC, PEC + precursors, and IPN hydrogels. **(A)** PEC hydrogels with C_{bPE} = 10 wt% and 40 wt%. **(B)** PEC + PEGDA and PEC/PEGDA IPN hydrogels with C_{bPE} = 10 wt% and C_{PC} = 5 wt%. **(C)** PEC + 4-arm PEGPA and PEC/4-arm PEGPA IPN hydrogels with C_{bPE} = 10 wt% and C_{PC} = 5 wt%. **(D)** PEC+AAm and PEC/AAm IPN hydrogels with C_{bPE} = 10 wt% and C_{PC} = 5 wt%. **(E)** PEC+GelMA and PEC/GelMA IPN hydrogels with C_{bPE} = 10 wt% and C_{PC} = 5 wt%.

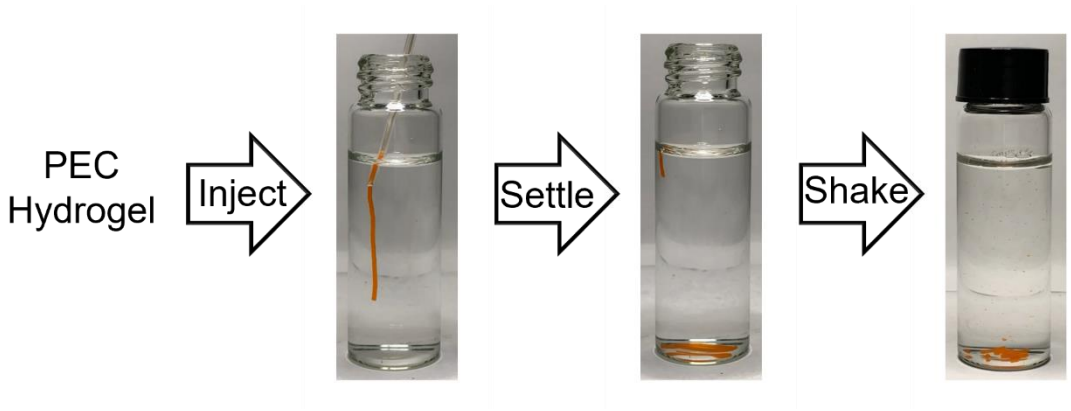

Figure 4-S4. Photos showing injectability of polyelectrolyte complex (PEC) hydrogel and its interim resistance against dissolution upon shaking in water.

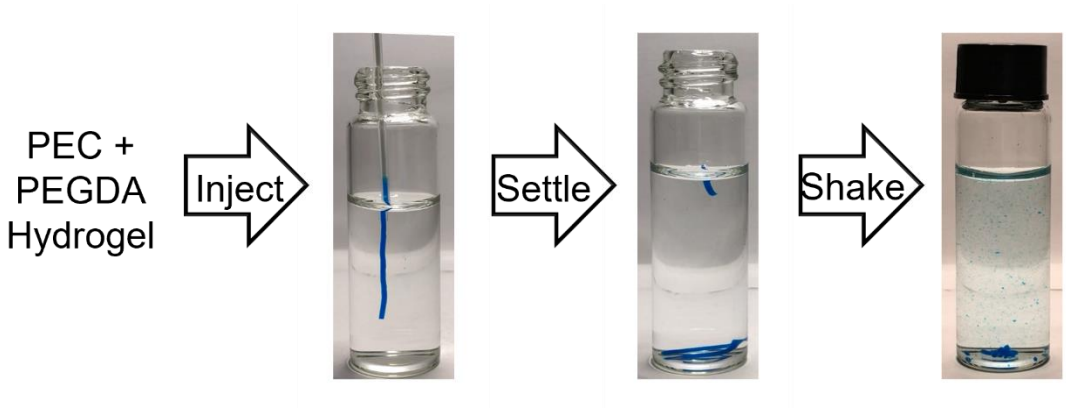

Figure 4-S5. Photos showing injectability and interim insolubility of PEC+PEGDA hydrogel in water.

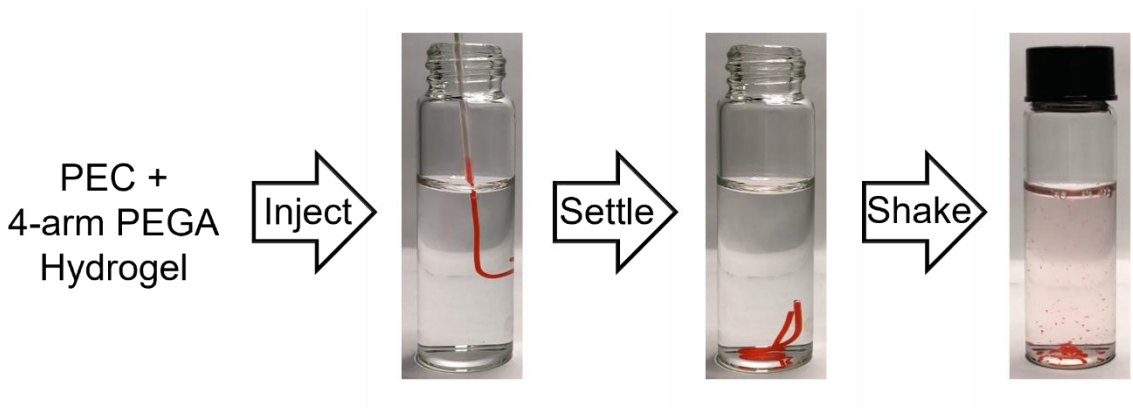

Figure 4-S6. Photos showing injectability and interim insolubility of PEC+4-arm PEGA hydrogel in an aqueous environment.

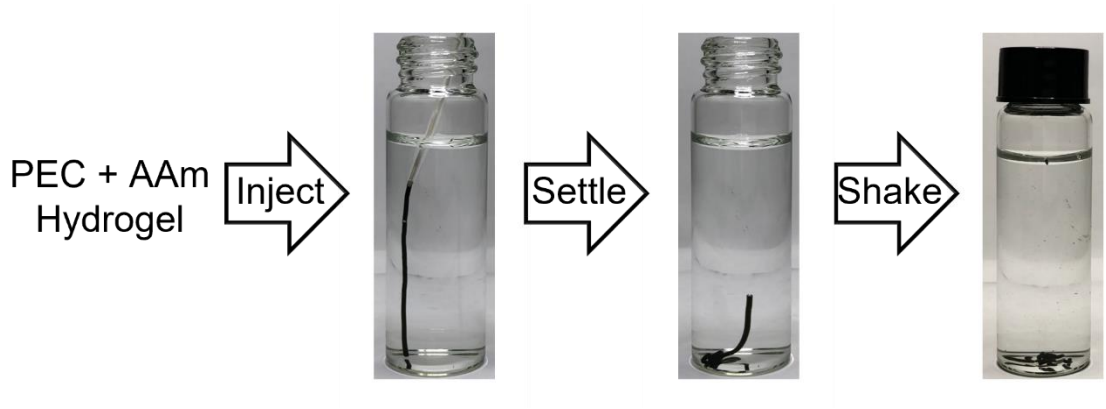

Figure 4-S7. Photos showing injectability and interim insolubility of PEC+AAm hydrogel in an aqueous environment.

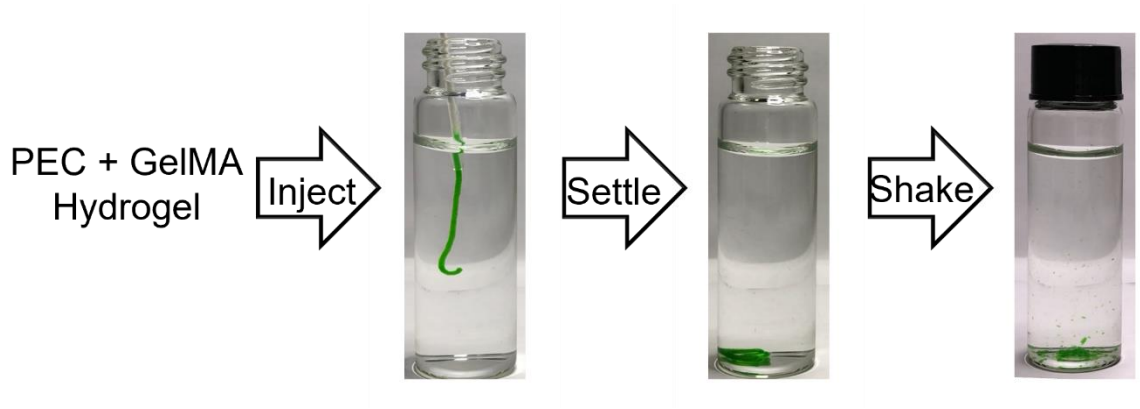

Figure 4-S8. Photos showing injectability and interim insolubility of PEC+GelMA hydrogel in an aqueous environment.

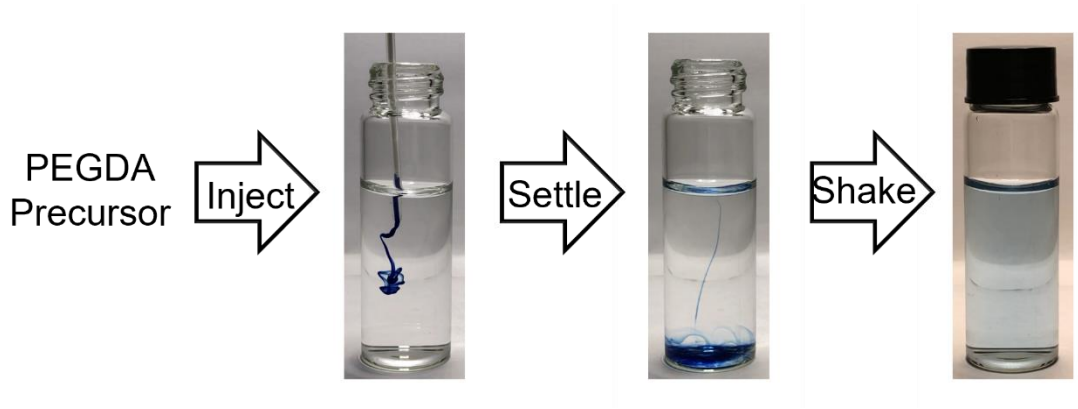

Figure 4-S9. Photos showing swift dilution of PEGDA precursor upon injection in water.

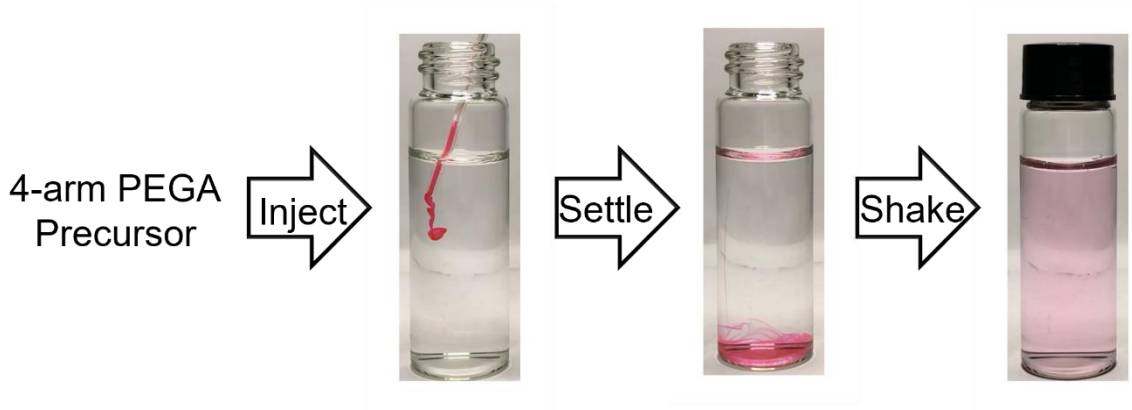

Figure 4-S10. Photos showing swift dilution of 4-arm PEGA precursor upon injection in water.

Figure 4-S11. Photos showing swift dilution of AAm precursor upon injection in water.

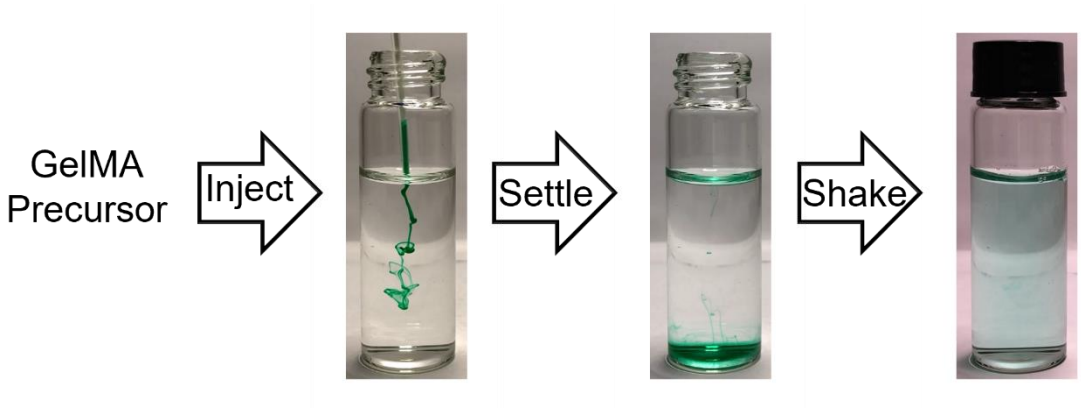

Figure 4-S12. Photos showing swift dilution of GelMA precursor upon injection in water.

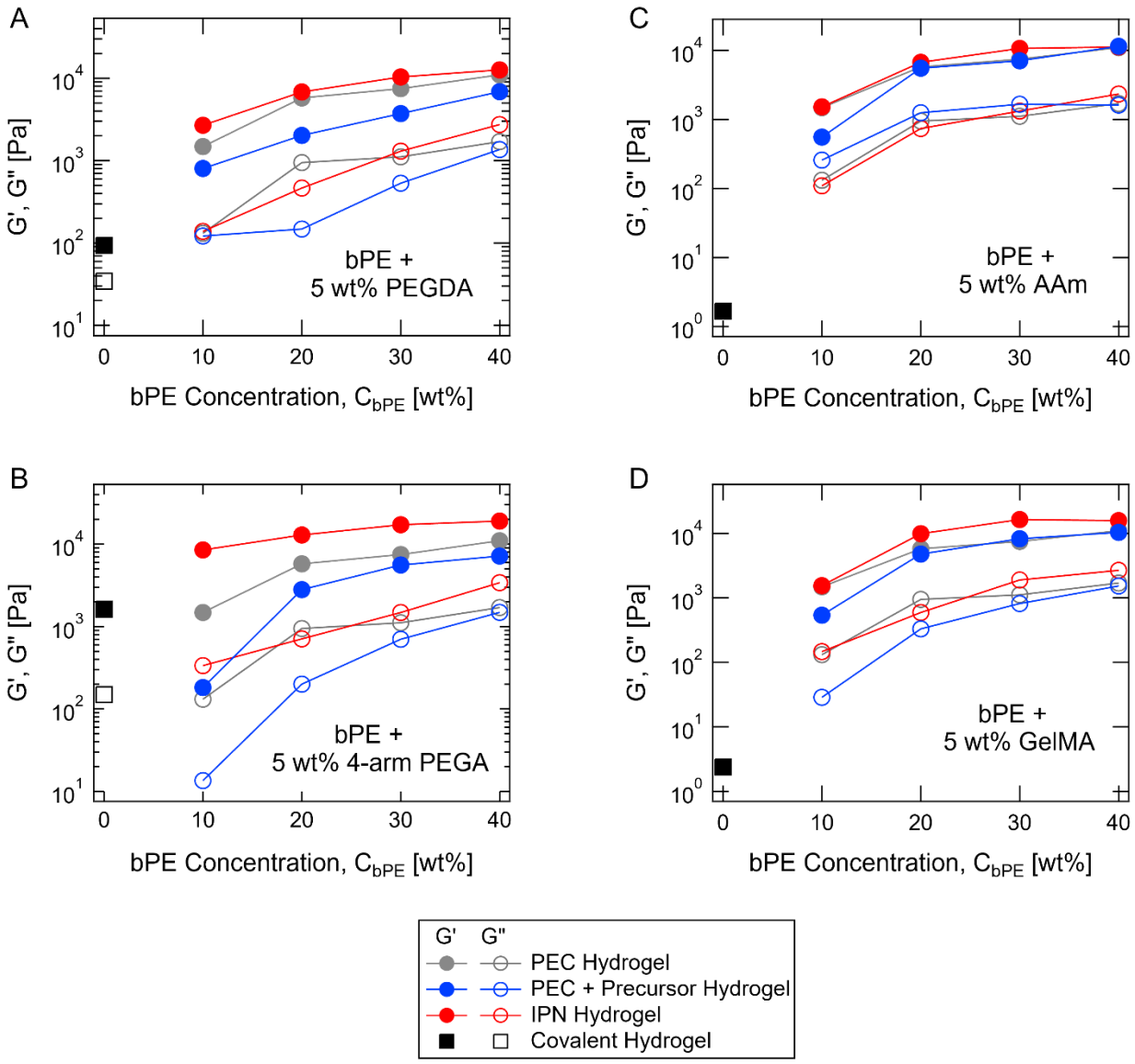

Figure 4-S13. Storage moduli (G') and loss moduli ($G"$) of PEC (grey circles), PEC + precursor (blue circles), IPN (red circles), and covalent hydrogels (black squares) measured at ω = 1.12 rad/s and γ = 0.8%, C_{bPE} varying from 10 wt% to 40 wt% and a constant $C_{PC} = 5$ wt% . **(A-D)** PEGDA, 4-arm PEGA, AAm, and GelMA-based hydrogels. Open and close symbols represent storage moduli G' and loss moduli $G"$, respectively.

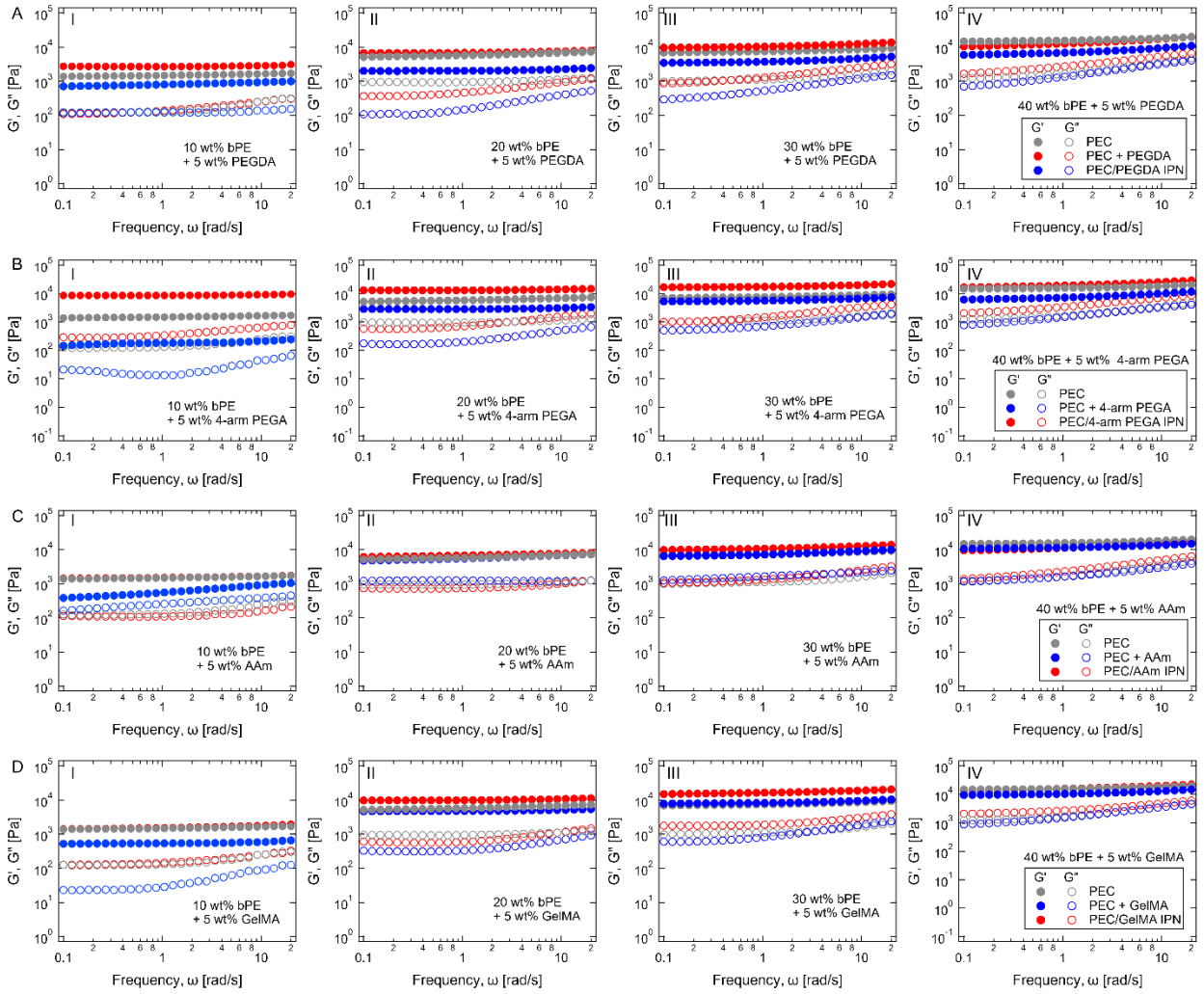

Figure 4-S14. G' and $G"$ as a function of ω, measured at γ = 0.8%, for PEC (grey symbols), PEC+precursor (blue symbols), and IPN (red symbols) hydrogels. In the figures (I) to (IV) in each row, C_{bPE} varies from 10 wt% to 40 wt% with a constant C_{PC} = 5 wt%. (A) PEGDA-based hydrogels. (B) 4-arm PEGA based hydrogels. (C) AAm-based hydrogels. (D) GelMA-based hydrogels. The open and close symbols represent the storage and loss moduli, respectively.

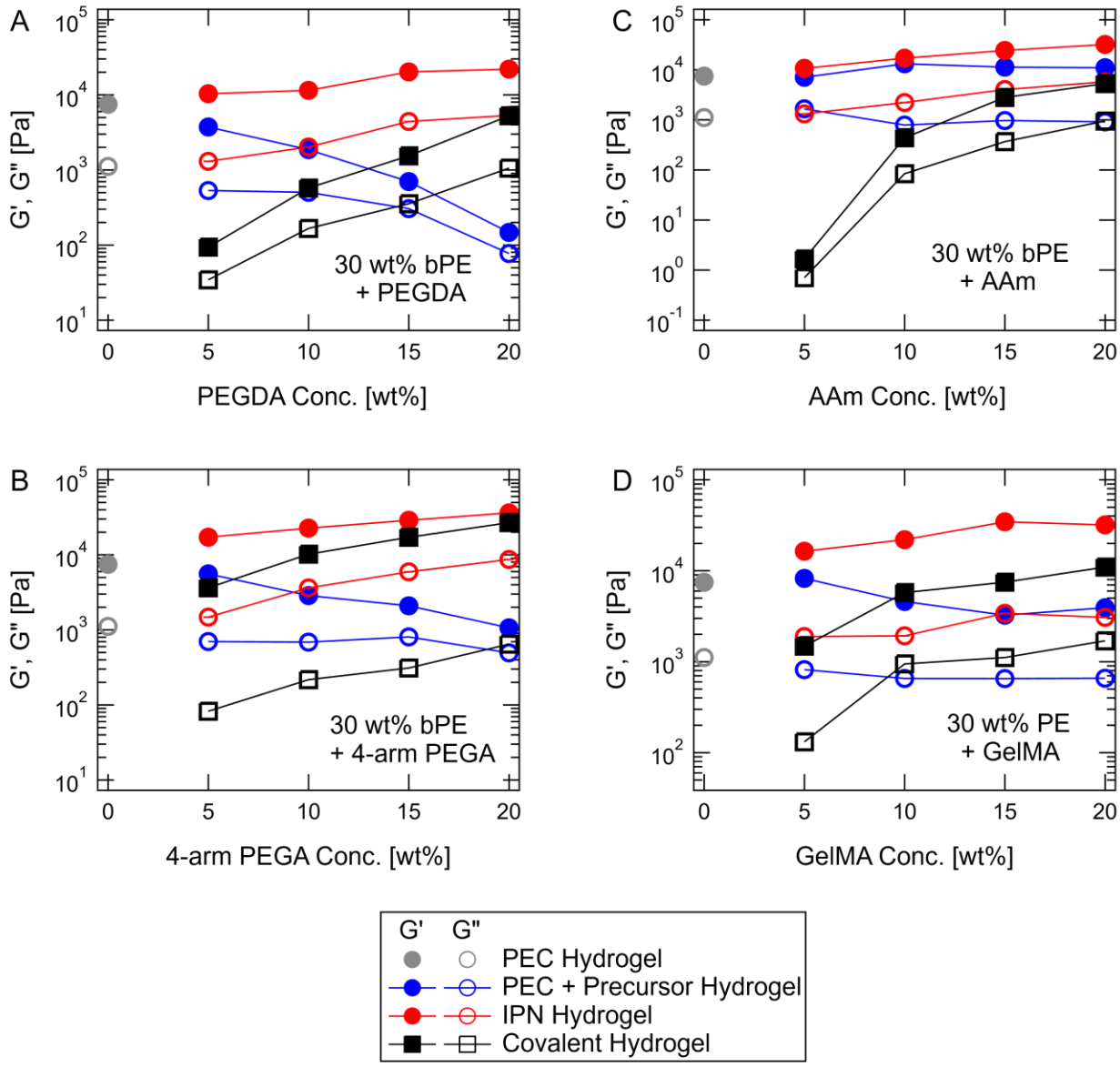

Figure 4-S15. Storage moduli (G') and loss moduli (G'') of covalent (black squares), PEC+precursor and PEC/covalent IPN hydrogels (comprising 30 wt% tbPEs, blue and red circles), measured at ω = 1.12 rad/s and γ = 0.8%, as a function of precursor concentration. The shear moduli of the corresponding 30 wt% PEC hydrogels are also shown with grey circles. (A) PEGDA-based hydrogels, (B) 4-arm PEGA-based hydrogels, (C) AAm-based hydrogels, and (D) GelMA-based hydrogels.

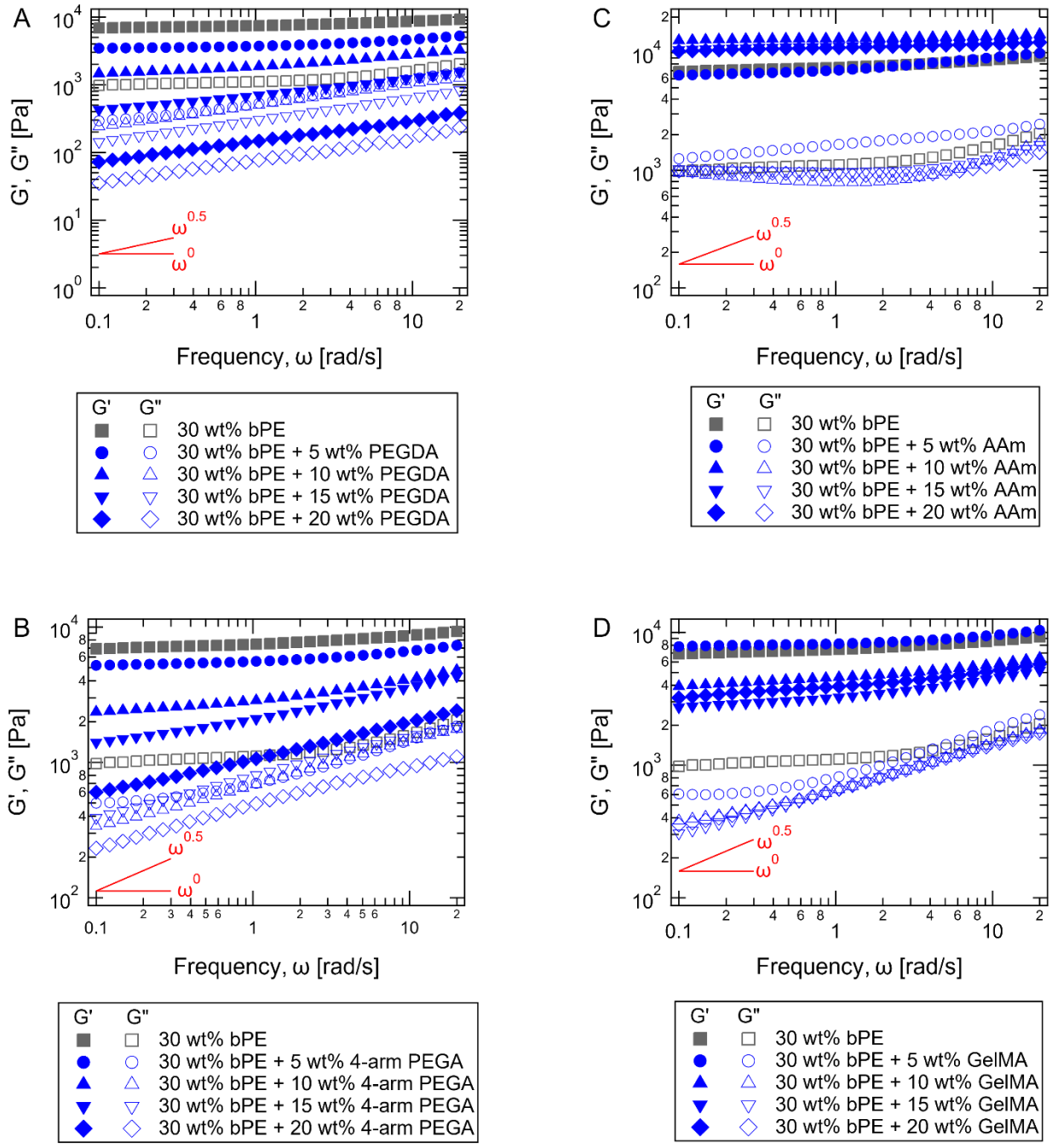

Figure 4-S16. G' and G'' of PEC (C_{bPE} = 30 wt%, grey symbols) and PEC+precursor (C_{bPE} = 30 wt% and varying C_{PC}, blue symbols) hydrogels as a function of ω with γ = 0.8%. (A) PEC + PEGDA hydrogels. (B) PEC + 4-arm PEGA hydrogels. (C) PEC + AAm hydrogels. (D) PEC + GelMA hydrogels.

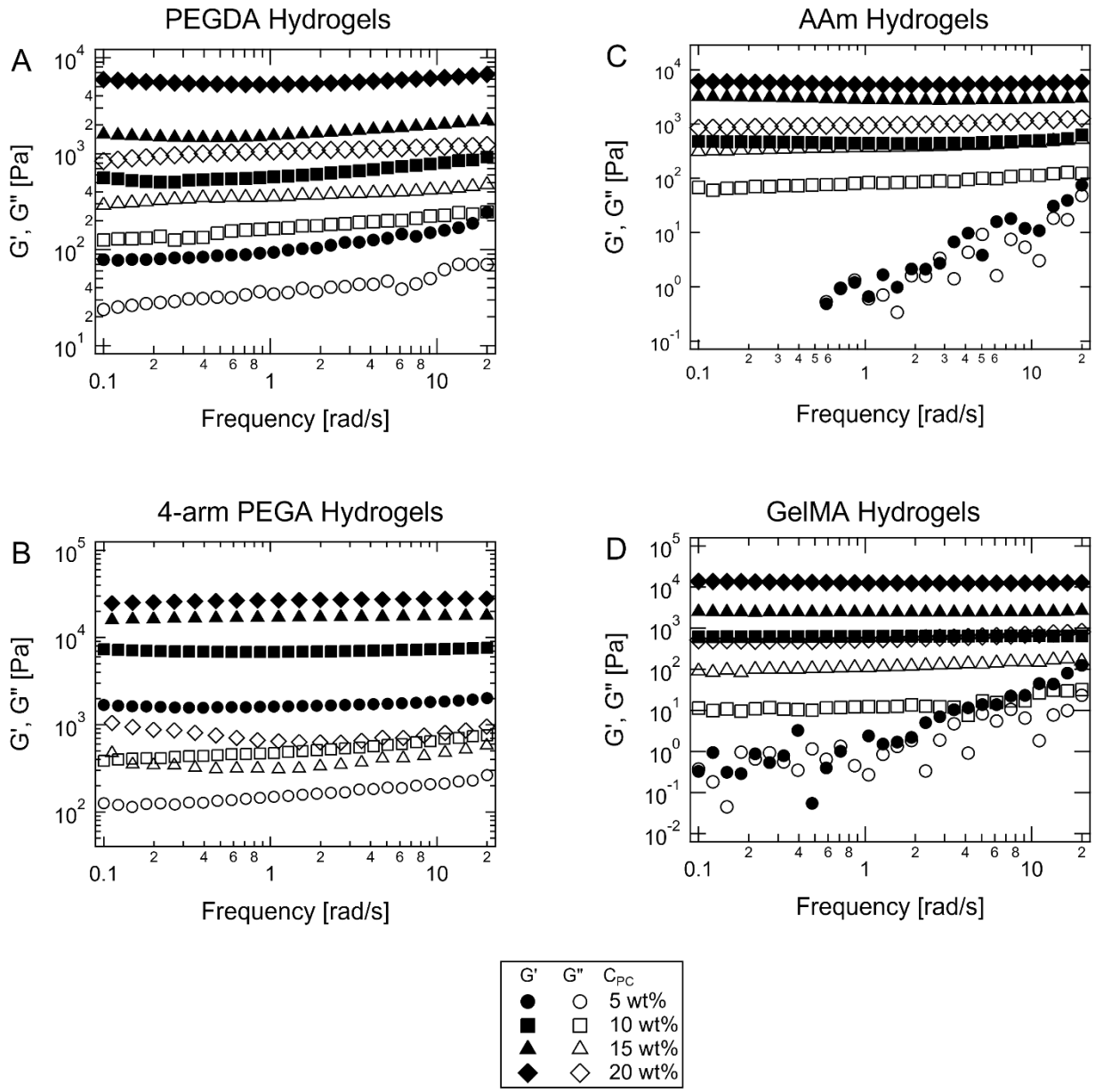

Figure 4-S17. G' and G'' of covalent hydrogels (varying C_{PC}) as a function of ω with γ = 0.8%. (A) PEGDA hydrogels. (B) 4-arm PEGA hydrogels. (C) AAm hydrogels. (D) GelMA hydrogels.

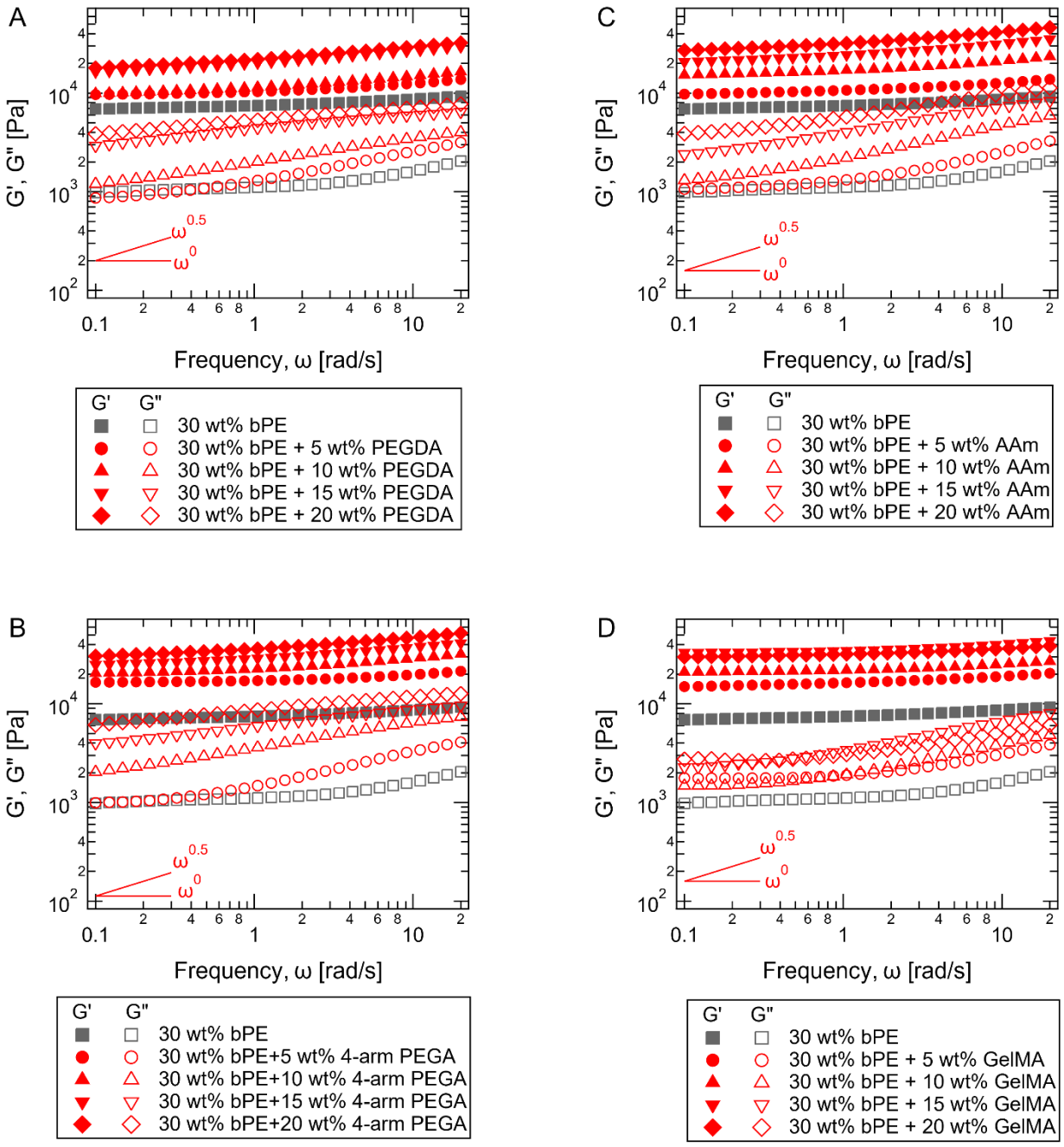

Figure 4-S18. G' and G'' of PEC (C_{bPE} = 30 wt%, grey symbols) and PEC/covalent (C_{bPE} = 30 wt% and varying C_{PC}, red symbols) hydrogels as a function of ω with γ = 0.8%. (A) PEC/PEGDA IPN hydrogels. (B) PEC/4-arm PEGA IPN hydrogels. (C) PEC/AAm IPN hydrogels. (D) PEC/GelMA IPN hydrogels.

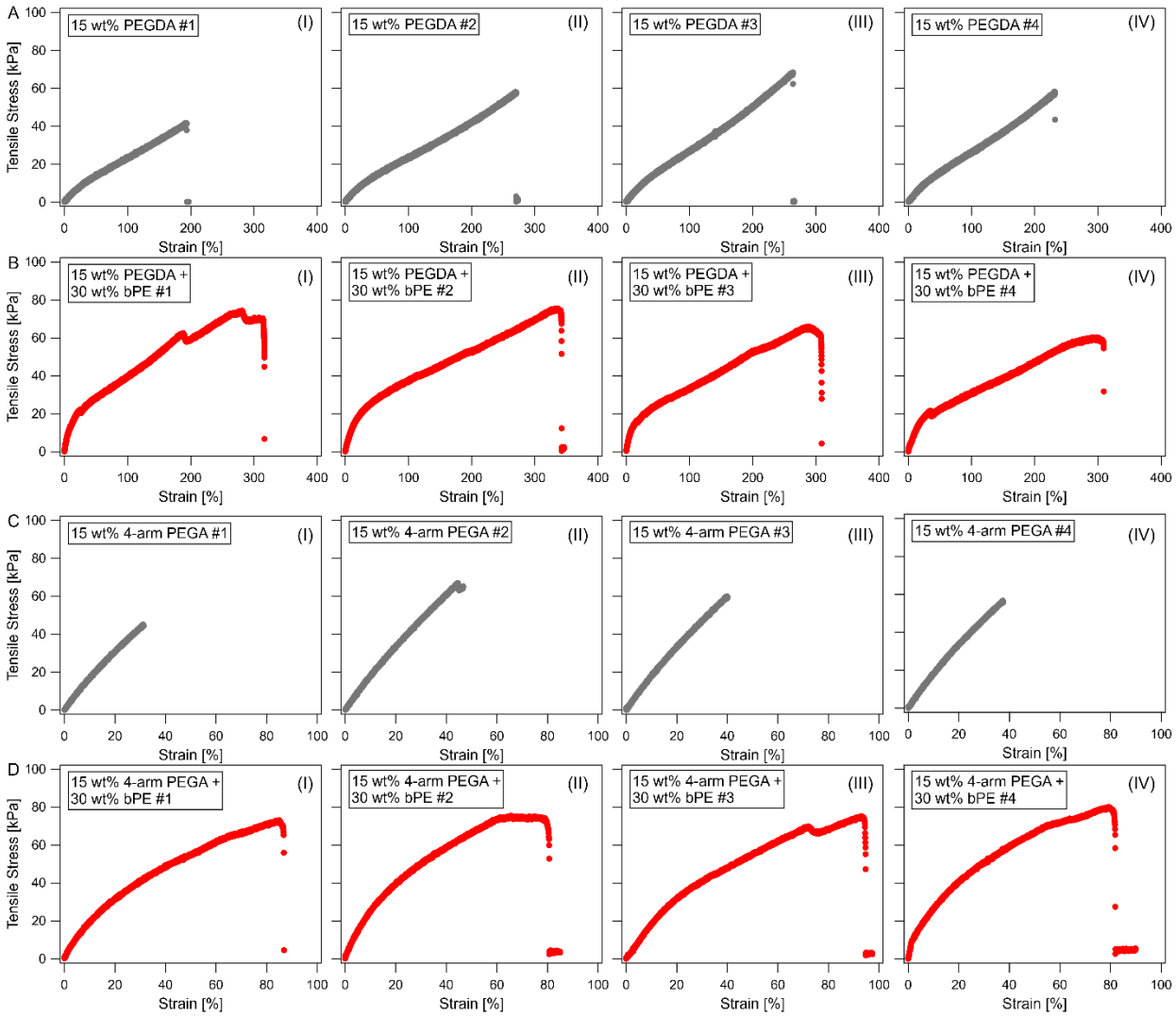

Figure 4-S19. Stress versus strain curves for covalent and IPN hydrogels. (A) PEGDA hydrogels with C_{PC} = 15 wt%, (B) PEC/PEG IPN hydrogels with C_{PC} = 15 wt% and C_{bPE} = 30 wt%, (C) 4-arm PEGA hydrogels with C_{PC} = 15 wt%, (D) PEC/4-arm PEGA IPN hydrogels with C_{PC} = 15 wt% and C_{bPE} = 30 wt%.

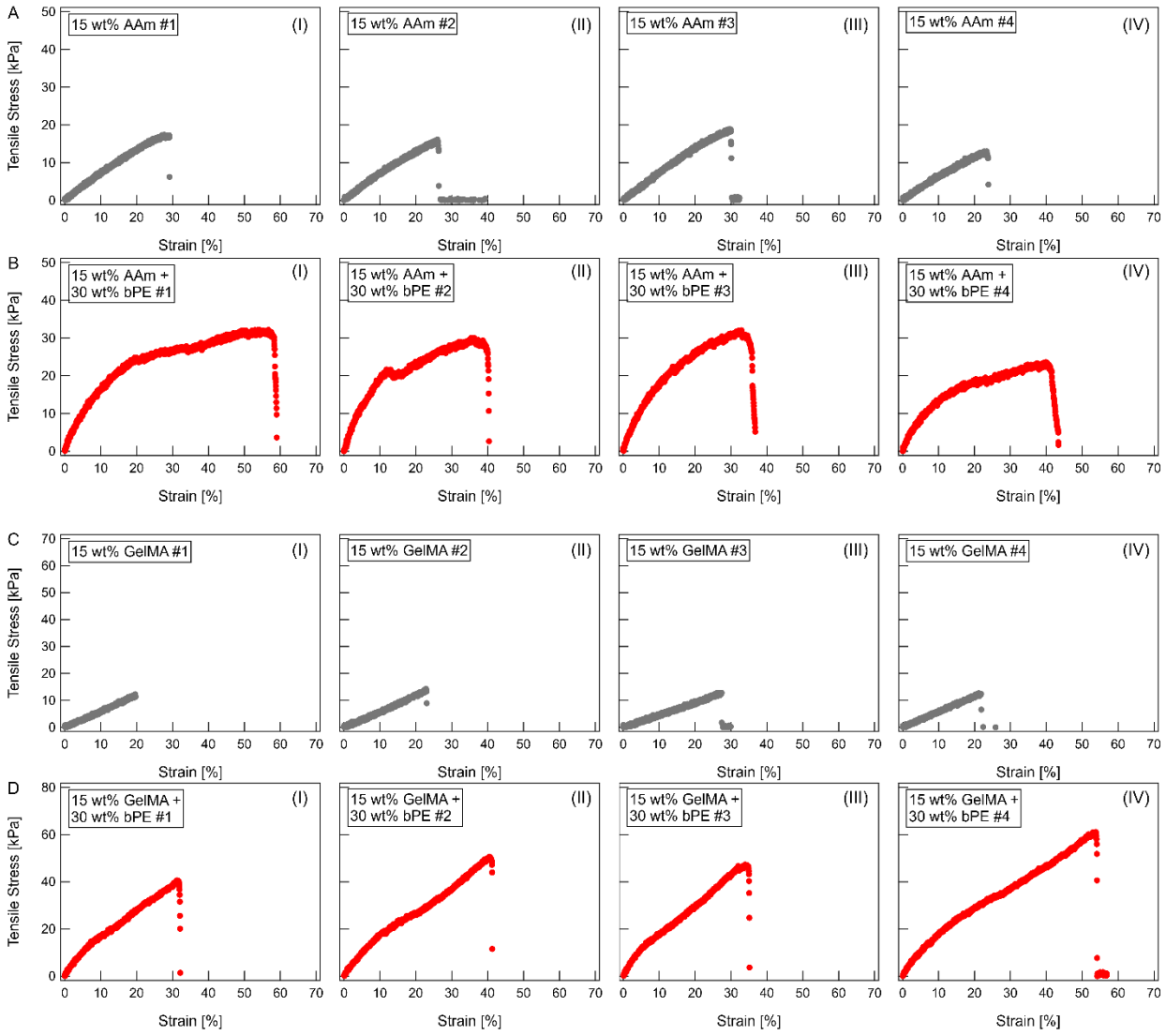

Figure 4-S20. Stress versus strain curves for covalent and IPN hydrogels. (A) AAm hydrogels with C_{PC} = 15 wt%, (B) PEC/AAm IPN hydrogels with C_{PC} = 15wt% and C_{bPE} = 30 wt%. (C) GelMA hydrogels with C_{PC} = 15 wt%. (D) PEC/GelMA IPN hydrogels with C_{PC} = 15 wt% and C_{bPE} = 30 wt%.

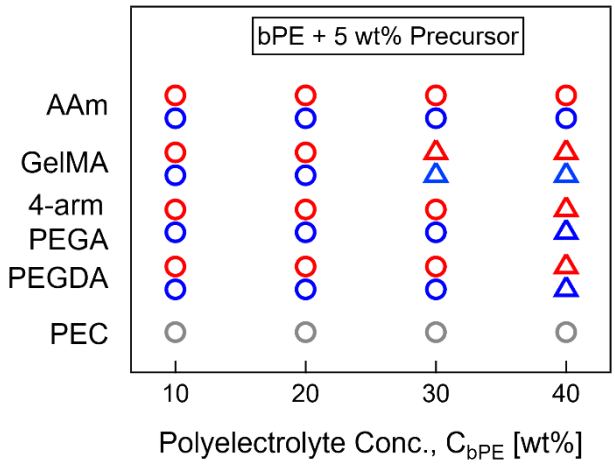

Figure 4-S21. Microstructural map for PEC+precursor and IPN hydrogels with a constant C_{PC} = 5 wt% and varying C_{bPE}. Circles represent disordered spheres, and triangles represent lamellae.

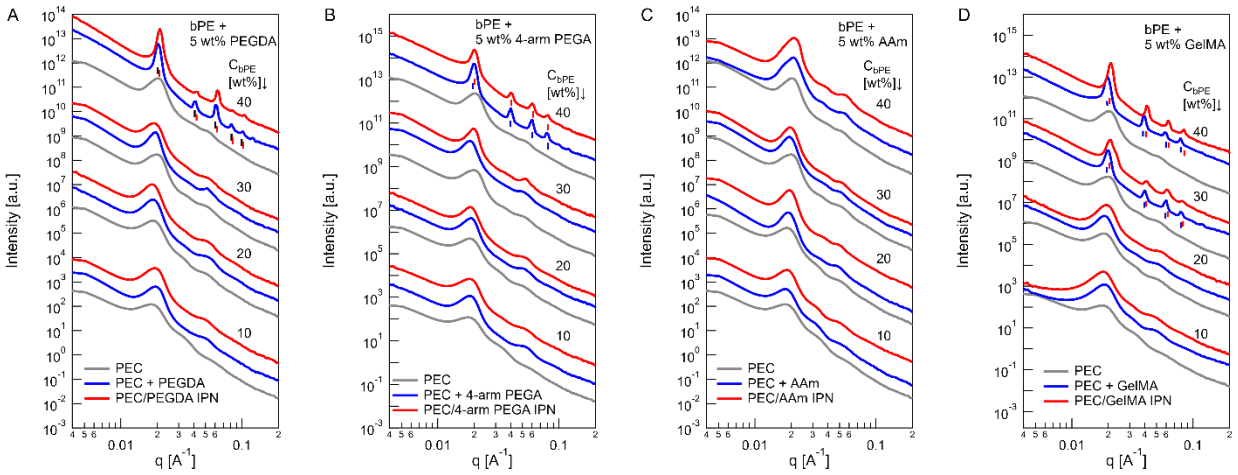

Figure 4-S22. One-dimensional SAXS scattering $I(q)$ as a function of q for the PEC (grey), PEC + precursors (blue), and IPN (red) hydrogels with varying bPE concentration. All PEC+precursor and IPN hydrogels contain 5 wt% precursor content. (A) PEGDA-based hydrogels, (B) 4-arm PEGA-based hydrogels, (C) AAm-based hydrogels, (D) GelMA-based hydrogels. The SAXS scattering curves were shifted vertically for clarity. The details of Bragg peak positions are summarized in Table 4-S1 to Table 4-S6.

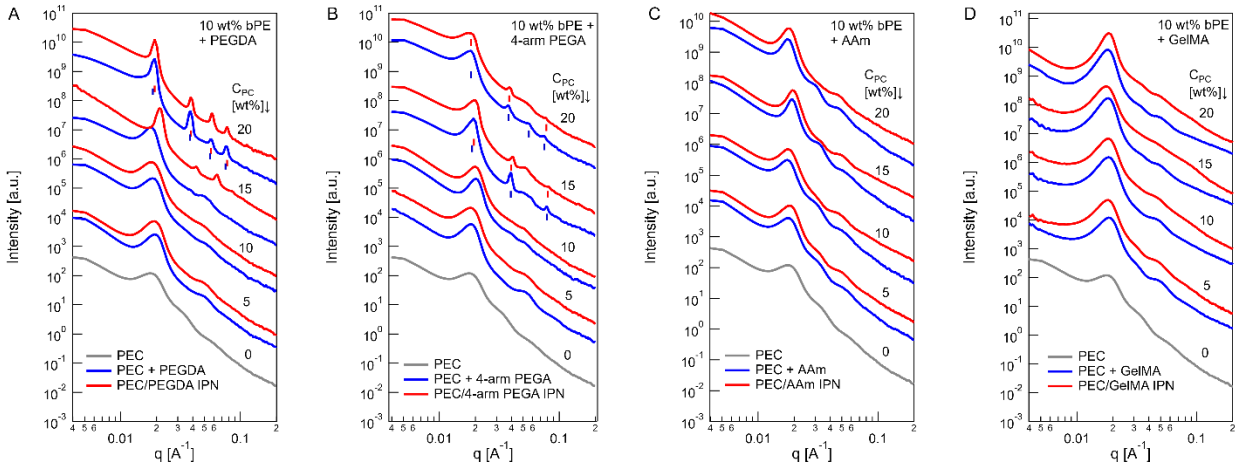

Figure 4-S23. One-dimensional SAXS scattering $I(q)$ as a function of q for the PEC (grey), PEC + precursors (blue), and IPN (red) hydrogels with varying precursor concentration. hydrogels contain 10 wt% tbPE content. (A) PEGDA-based hydrogels, (B) 4-arm PEGA-based hydrogels, (C) AAm-based hydrogels, (D) GelMA-based hydrogels. The SAXS scattering curves were shifted vertically for clarity. The details of Bragg peak positions are summarized in Table 4-S1 to Table 4-S6.

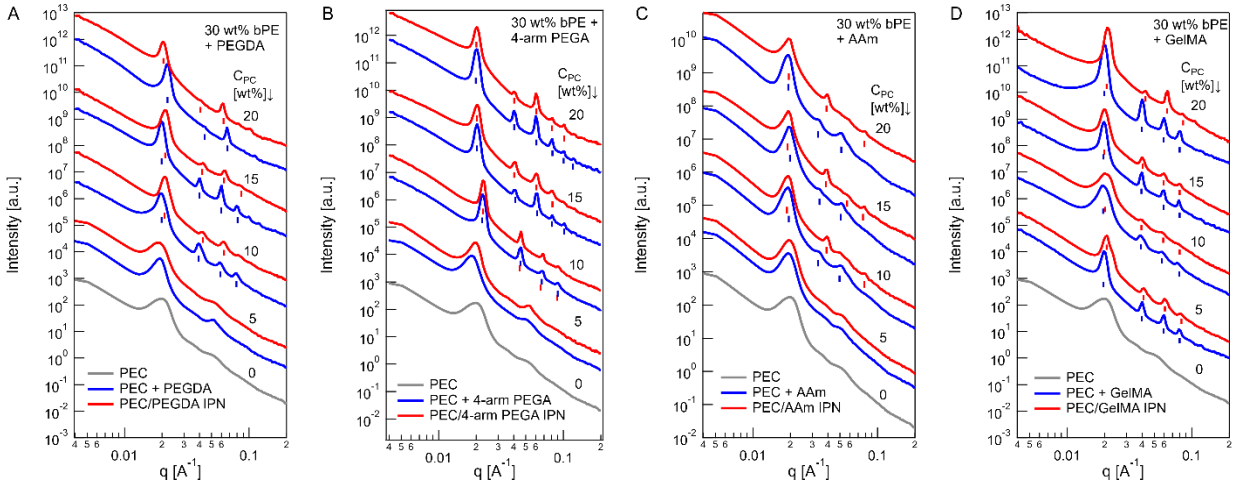

Figure 4-S24. One-dimensional SAXS scattering $I(q)$ as a function of q for the PEC (grey), PEC + precursors (blue), and IPN (red) hydrogels with varying precursor concentration. hydrogels contain 30 wt% tbPE content. (A) PEGDA-based hydrogels, (B) 4-arm PEGA-based hydrogels, (C) AAm-based hydrogels, (D) GelMA-based hydrogels. The SAXS scattering curves were shifted vertically for clarity. The details of Bragg peak positions are summarized in Table 4-S1 to Table 4-S6.

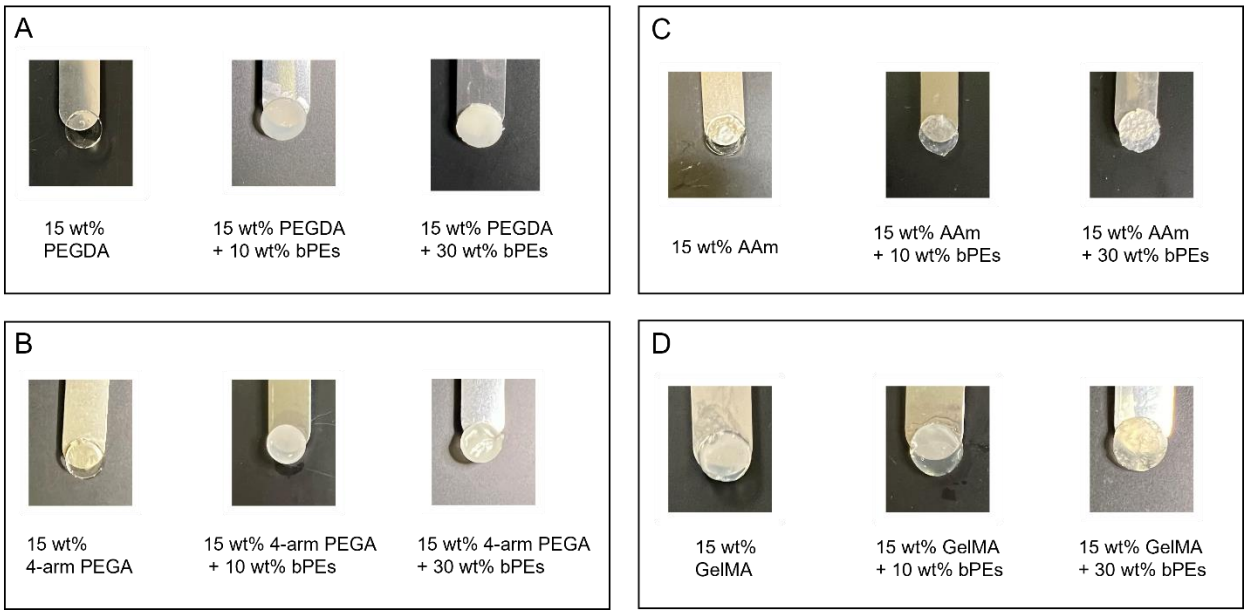

Figure 4-S25. Photos of covalent and IPN hydrogels showing differences in optical density upon addition of tbPEs. All covalent hydrogels contained C_{PC} = 15 wt%. IPN hydrogels contained a constant C_{PC} = 15 wt% and varying C_{bPE} = 10 wt% or 30 wt%. (A) PEGDA-based hydrogels, (B) 4-arm PEGA-based hydrogels, (C) AAm-based hydrogels, (D) GelMA-based hydrogels.

Table 4-S1. Bragg peak positions and microstructural details for PEC+4-arm PEGA hydrogels and PEC/4-arm PEGA IPN hydrogels with C_{bPE} = 30 wt%.

Hydrogel Description	q [Å^{-1}]	$\frac{q}{q^*}$	Expected $\frac{q}{q^*}$	**Microstructure**
PEC+4-arm PEGA hydrogels with C_{bPE} = 30 wt% and C_{PC} = 10 wt%, q^*= 0.0225 Å^{-1}	0.0459	2.04	2	LAM
	0.0689	3.06	3	
	0.0903	4.01	4	
PEC/4-arm PEGA IPN hydrogels with C_{bPE} = 30 wt% and C_{PC} = 10 wt%, q^*= 0.0225 Å^{-1}	0.0459	2.04	2	LAM
	0.0689	3.06	3	
	0.0903	4.01	4	
PEC+4-arm PEGA hydrogels with C_{bPE} = 30 wt% and C_{PC} = 15 wt%, q^*= 0.0204 Å^{-1}	0.0415	2.04	2	LAM
	0.0622	3.06	3	
	0.0816	4.01	4	
	0.102	5.01	5	
PEC/4-arm PEGPA IPN hydrogels with C_{bPE} = 30 wt% and C_{PC} = 15 wt%, q^*= 0.0204 Å^{-1}	0.0415	2.04	2	LAM
	0.0602	2.96	3	
	0.0816	4.01	4	
	0.102	5.01	5	
	0.0401	1.97	2	LAM
	0.0602	2.96	3	

PEC+4-arm PEGA hydrogels with C_{bPE} = 30 wt% and C_{4PA} = 20 wt%, q^*= 0.0204 Å^{-1}	0.0816	4.01	4	
	0.102	5.01	5	
	0.122	5.99	6	
PEC/4-arm PEGPA IPN hydrogels with C_{bPE} = 30 wt% and C_{PC} = 20 wt%, q^*= 0.0204 Å^{-1}	0.0401	1.97	2	LAM
	0.0602	2.96	3	
	0.0816	4.01	4	
	0.102	5.01	5	
	0.124	6.09	6	

Table 4-S2. Bragg peak positions and microstructural details for PEC+PEGDA hydrogels and PEC/PEGDA IPN hydrogels with C_{bPE} = 30 wt%.

Hydrogel Description	q **[Å^{-1}]**	$\frac{q}{q^*}$	**Expected** $\frac{q}{q^*}$	**Microstructure**
PEC+PEGDA hydrogels with C_{bPE} = 30 wt% and C_{PC} = 10wt%, q^*= 0.0197 Å^{-1}	0.0401	2.04	2	LAM
	0.0582	2.96	3	
	0.0789	4.01	4	
PEC/PEGDA IPN hydrogels with C_{bPE} = 30 wt% and C_{PC} = 10 wt%, q^*= 0.0211 Å^{-1}	0.0429	2.04	2	LAM
	0.0622	2.96	3	
	0.0844	4.01	4	
PEC+PEGDA hydrogels with C_{bPE} = 30 wt% and C_{PC} = 15wt%, q^*= 0.0197 Å-1	0.0401	2.04	2	LAM
	0.0602	3.06	3	
	0.0789	4.01	4	
PEC/PEGDA IPN hydrogels with C_{bPE} = 30 wt% and C_{PC} = 15 wt%, q^*= 0.0218 Å^{-1}	0.0429	1.97	2	LAM
	0.0644	2.96	3	
	0.0873	4.01	4	
PEC+PEGDA hydrogels with C_{bPE} = 30 wt% and C_{PC} = 20 wt%, q^*= 0.0225 Å^{-1}	0.0444	1.97	2	LAM
	0.0666	2.96	3	

PEC/PEGDA IPN hydrogels with C_{bPE} = 30 wt% and C_{pc} = 20 wt%, q^*= 0.0204 Å^{-1}	0.0415	2.04	2	LAM
	0.0622	3.06	3	

Table 4-S3. Bragg peak positions and microstructural details for PEC+AAm hydrogels and PEC/AAm IPN hydrogels with C_{bPE} = 30 wt%.

Hydrogel Description	q [Å^{-1}]	$\frac{q}{q^*}$	Expected $\frac{q}{q^*}$	Microstructure	Comments
PEC+AAm hydrogels with C_{bPE} = 30 wt% and C_{PC} = 10 wt%, q^*= 0.0193 Å^{-1}	0.0343	1.78	1.73	HCP	
	0.0508	2.63	2.65		
PEC/AAm IPN hydrogels with C_{bPE} = 30 wt% and C_{PC} = 10 wt%, q^*= 0.0193 Å^{-1}	0.0397	2.06	2	LAM	Missing peak at $3q^*$
	0.0788	4.09	4		
PEC+AAm hydrogels with C_{bPE} = 30 wt% and C_{PC} = 15 wt%, q^*= 0.0193 Å^{-1}	0.0343	1.78	1.73	HCP	
	0.0522	2.71	2.65		
PEC/AAm IPN hydrogels with C_{bPE} = 30 wt% and C_{PC} = 15 wt%, q^*= 0.0193 Å^{-1}	0.0397	2.06	2	LAM	
	0.0578	3.00	3		
	0.0788	4.09	4		
PEC+AAm hydrogels with C_{bPE} = 30 wt% and C_{PC} = 20 wt%, q^*= 0.0193 Å^{-1}	0.0343	1.78	1.73	HCP	
	0.0508	2.63	2.65		

PEC/AAm IPN hydrogels with C_{bPE} = 30 wt% and C_{PC} = 15 wt%, q^*= 0.0201 Å^{-1}	0.0397	1.97	2	LAM	Missing peak at 3q^*
	0.0805	4.00	4		

Table 4-S4. Bragg peak positions and microstructural details for PEC+GelMA hydrogels and PEC/GelMA IPN hydrogels with C_{bPE} = 30 wt%.

Hydrogel Description	q **[Å^{-1}]**	$\frac{q}{q^*}$	**Expected** $\frac{q}{q^*}$	**Microstructure**
PEC+GelMA hydrogels with C_{bPE} = 30 wt% and C_{PC} = 5 wt%, q^*= 0.0197 Å^{-1}	0.0401	2.04	2	LAM
	0.0602	3.06	3	
	0.0789	4.01	4	
PEC/GelMA IPN hydrogels with C_{bPE} = 30 wt% and C_{PC} = 5 wt%, q^*= 0.0211 Å^{-1}	0.0415	1.97	2	LAM
	0.0602	2.86	3	
	0.0816	3.87	4	
PEC+GelMA hydrogels with C_{bPE} = 30 wt% and C_{PC} = 10 wt%, q^*= 0.0197 Å^{-1}	0.0387	1.97	2	LAM
	0.0582	2.96	3	
	0.0789	4.01	4	
PEC/GelMA IPN hydrogels with C_{bPE} = 30 wt% and C_{PC} = 10 wt%, q^*= 0.0204 Å^{-1}	0.0401	1.97	2	LAM
	0.0582	2.86	3	
	0.0789	3.87	4	
PEC+GelMA hydrogels with C_{bPE} = 30 wt% and C_{PC} = 15 wt%, q^*= 0.0197 Å^{-1}	0.0401	2.04	2	LAM
	0.0602	3.06	3	
	0.0789	4.01	4	

PEC/GelMA IPN hydrogels with C_{bPE} = 30 wt% and C_{PC} = 15 wt%, q^*= 0.0204 Å^{-1}	0.0401	1.97	2	LAM
	0.0602	2.96	3	
	0.0816	4.01	4	
PEC+GelMA hydrogels with C_{bPE} = 30 wt% and C_{PC} = 20 wt%, q^*= 0.0204 Å^{-1}	0.0429	1.97	2	LAM
	0.0644	2.96	3	
	0.0844	4.01	4	
PEC/GelMA IPN hydrogels with C_{bPE} = 30 wt% and C_{PC} = 20 wt%, q^*= 0.0211 Å^{-1}	0.0429	2.04	2	LAM
	0.0644	3.06	3	
	0.0844	4.01	4	

Table 4-S5. Bragg peak positions and microstructural details for PEC+4-arm PEGA hydrogels and PEC/4-arm PEGA hydrogels with C_{bPE} = 10 wt% and 40 wt%.

Hydrogel Description	q [Å^{-1}]	$\frac{q}{q^*}$	Expected $\frac{q}{q^*}$	**Microstructure**	**Comments**
PEC+4-arm PEGA hydrogels with C_{bPE} = 10 wt% and C_{PC} = 15 wt%, q^*= 0.0193 Å^{-1}	0.0397	2.06	2	LAM	Missing peak at $3q^*$
	0.0788	4.09	4		
PEC/4-arm PEGA IPN hydrogels with C_{bPE} = 10 wt% and C_{PC} = 15 wt%, q^*= 0.0193 Å^{-1}	0.0397	2.06	2	LAM	Missing peak at $3q^*$
	0.0788	4.09	4		
PEC+4-arm PEGA hydrogels with C_{bPE} = 10 wt% and C_{PC} = 20 wt%, q^*= 0.0184 Å^{-1}	0.0374	2.03	2	LAM	
	0.0564	3.06	3		
	0.0737	4	4		
PEC/4-arm PEGA IPN hydrogels with C_{bPE} = 10 wt% and C_{PC} = 20 wt%, q^*= 0.0184 Å^{-1}	0.0383	2.08	2	LAM	Missing peak at $3q^*$
	0.0754	4.09	4		
PEC+4-arm PEGA hydrogels with C_{bPE} = 40 wt% and C_{PC} = 5 wt%, q^*= 0.0204 Å^{-1}	0.0401	1.97	2	LAM	
	0.0602	2.96	3		
	0.0789	3.87	4		

PEC/4-arm PEGA IPN hydrogels with C_{bPE} = 40 wt% and C_{PC} = 5 wt%, q^*= 0.0204 Å^{-1}	0.0401	1.97	2	LAM	
	0.0602	2.96	3		
	0.0816	4.01	4		

Table 4-S6. Bragg peak positions and microstructural details for PEC+PEGDA hydrogels and PEC/PEGDA IPN hydrogels with C_{bPE} = 10 wt% and 40 wt%.

Hydrogel Description	q **[Å^{-1}]**	$\frac{q}{q^*}$	**Expected** $\frac{q}{q^*}$	**Microstructure**
PEC+PEGDA hydrogels with C_{bPE} = 10 wt% and C_{PC} = 20wt%, q^*= 0.0193 Å^{-1}	0.0383	1.99	2	LAM
	0.0564	2.93	3	
	0.0771	4.00	4	
PEC/PEGDA IPN hydrogels with C_{bPE} = 10 wt% and C_{PC} = 20 wt%, q^*= 0.0193 Å^{-1}	0.0383	1.99	2	LAM
	0.0578	3	3	
	0.0771	4	4	
PEC+PEGDA hydrogels with C_{bPE} = 40 wt% and C_{PC} = 5wt%, q^*= 0.0204 Å^{-1}	0.0415	2.03	2	LAM
	0.0602	2.96	3	
	0.0816	4.01	4	
	0.1020	5.01	5	
PEC/PEGDA IPN hydrogels with C_{bPE} = 40 wt% and C_{PC} = 5 wt%, q^*= 0.0211 Å^{-1}	0.0429	2.03	2	LAM
	0.0622	2.94	3	
	0.0844	4.00	4	
	0.1060	5.02	5	

Supplementary Movies

Movie 4-SM1. Video showing injectability of PEC hydrogels and their interim resistance against dilution and material loss in water.

Movie 4-SM2. Video showing injectability of PEC+PEGDA hydrogels and their interim resistance against dilution and material loss in water.

Movie 4-SM3. Video showing injectability of PEC+4-arm PEGA hydrogels and their interim resistance against dilution and material loss in water.

Movie 4-SM4. Video showing injectability of PEC+AAm hydrogels and their interim resistance against dilution and material loss in water.

Movie 4-SM5. Video showing injectability of PEC+GelMA hydrogels and their interim resistance against dilution and material loss in water.

Movie 4-SM6. Video demonstrating immediate dilution of PEGDA precursors in water.

Movie 4-SM7. Video demonstrating immediate dilution of 4-arm PEGA precursors in water.

Movie 4-SM8. Video demonstrating immediate dilution of AAm precursors in water.

Movie 4-SM9. Video demonstrating immediate dilution of GelMA precursors in water.

4.7 Reference

(1) Yang, J.; Bai, R.; Chen, B.; Suo, Z. Hydrogel Adhesion: A Supramolecular Synergy of Chemistry, Topology, and Mechanics. *Advanced Functional Materials* **2020**, *30* (2), 1901693. DOI: 10.1002/adfm.201901693.

(2) Mehdizadeh, M.; Yang, J. Design Strategies and Applications of Tissue Bioadhesives. *Macromolecular Bioscience* **2013**, *13* (3), 271-288. DOI: 10.1002/mabi.201200332.

(3) Annabi, N.; Yue, K.; Tamayol, A.; Khademhosseini, A. Elastic sealants for surgical applications. *European Journal of Pharmaceutics and Biopharmaceutics* **2015**, *95* (Pt A), 27-39. DOI: 10.1016/j.ejpb.2015.05.022.

(4) Jeon, O.; Samorezov, J. E.; Alsberg, E. Single and dual crosslinked oxidized methacrylated alginate/PEG hydrogels for bioadhesive applications. *Acta Biomaterialia* **2014**, *10* (1), 47-55. DOI: 10.1016/j.actbio.2013.09.004.

(5) Shirzaei Sani, E.; Kheirkhah, A.; Rana, D.; Sun, Z.; Foulsham, W.; Sheikhi, A.; Khademhosseini, A.; Dana, R.; Annabi, N. Sutureless repair of corneal injuries using naturally derived bioadhesive hydrogels. *Science Advances* **2019**, *5* (3), eaav1281. DOI: 10.1126/sciadv.aav1281.

(6) Bal-Ozturk, A.; Cecen, B.; Avci-Adali, M.; Topkaya, S. N.; Alarcin, E.; Yasayan, G.; Li, Y.-C. E.; Bulkurcuoglu, B.; Akpek, A.; Avci, H. Tissue adhesives: From research to clinical translation. *Nano Today* **2021**, *36*, 101049. DOI: 10.1016/j.nantod.2020.101049.

(7) Mei, Q.; Rao, J.; Bei, H. P.; Liu, Y.; Zhao, X. 3D bioprinting photo-crosslinkable hydrogels for bone and cartilage repair. *International Journal of Bioprinting* **2021**, *7* (3), 367. DOI: 10.18063/ijb.v7i3.367.

(8) Pepelanova, I.; Kruppa, K.; Scheper, T.; Lavrentieva, A. Gelatin-Methacryloyl (GelMA) Hydrogels with Defined Degree of Functionalization as a Versatile Toolkit for 3D Cell Culture and Extrusion Bioprinting. *Bioengineering* **2018**, *5* (3), 55. DOI: 10.3390/bioengineering5030055.

(9) Ouyang, L.; Highley, C. B.; Sun, W.; Burdick, J. A. A Generalizable Strategy for the 3D bioprinting of Hydrogels from Nonviscous Photo-Crosslinkable Inks. *Advanced Materials* **2017**, *29* (8), 1604983. DOI: 10.1002/adma.201604983.

(10) Kačarević, Ž. P.; Rider, P. M.; Alkildani, S.; Retnasingh, S.; Smeets, R.; Jung, O.; Ivanišević, Z.; Barbeck, M. An Introduction to 3D Bioprinting: Possibilities, Challenges and Future Aspects. *Materials* **2018**, *11* (11), 2199. DOI: 10.3390/ma11112199.

(11) Sarker, M.; Naghieh, S.; Sharma, N.; Chen, X. 3D Biofabrication of Vascular Networks for Tissue Regeneration: A Report on Recent Advances. *Journal of Pharmaceutical Analysis* **2018**, *8* (5), 277-296. DOI: 10.1016/j.jpha.2018.08.005.

(12) Galarraga, J. H.; Kwon, M. Y.; Burdick, J. A. 3D Bioprinting via an in situ Crosslinking Technique towards Engineering Cartilage Tissue. *Scientific Reports* **2019**, *9* (1), 1-12. DOI: 10.1038/s41598-019-56117-3.

(13) Derakhshanfar, S.; Mbeleck, R.; Xu, K.; Zhang, X.; Zhong, W.; Xing, M. 3D Bioprinting for Biomedical Devices and Tissue Engineering: A Review of Recent Trends and Advances. *Bioactive Materials* **2018**, *3* (2), 144-156. DOI: 10.1016/j.bioactmat.2017.11.008.

(14) Leu Alexa, R.; Iovu, H.; Ghitman, J.; Serafim, A.; Stavarache, C.; Marin, M.-M.; Ianchis, R. 3D-Printed Gelatin Methacryloyl-Based Scaffolds with Potential Application in Tissue Engineering. *Polymers* **2021**, *13* (5), 727. DOI: 10.3390/polym13050727.

(15) Jungst, T.; Smolan, W.; Schacht, K.; Scheibel, T.; Groll, J. Strategies and Molecular Design Criteria for 3D Printable Hydrogels. *Chemical Reviews* **2016**, *116* (3), 1496-1539. DOI: 10.1021/acs.chemrev.5b00303.

(16) Pereira, R. F.; Bártolo, P. J. 3D bioprinting of photocrosslinkable hydrogel constructs. *Journal of Applied Polymer Science* **2015**, *132* (48). DOI: Artn 42458

10.1002/App.42458.

(17) Bedell, M. L.; Navara, A. M.; Du, Y.; Zhang, S.; Mikos, A. G. Polymeric Systems for Bioprinting. *Chemical Reviews* **2020**, *120* (19), 10744-10792. DOI: 10.1021/acs.chemrev.9b00834.

(18) Knowlton, S.; Yenilmez, B.; Anand, S.; Tasoglu, S. Photocrosslinking-based bioprinting: Examining crosslinking schemes. *Bioprinting* **2017**, *5*, 10-18. DOI: 10.1016/j.bprint.2017.03.001.

(19) GhavamiNejad, A.; Ashammakhi, N.; Wu, X. Y.; Khademhosseini, A. Crosslinking strategies for 3D bioprinting of polymeric hydrogels. *Small* **2020**, *16* (35), 2002931.

(20) Ashammakhi, N.; Ahadian, S.; Xu, C.; Montazerian, H.; Ko, H.; Nasiri, R.; Barros, N.; Khademhosseini, A. Bioinks and bioprinting technologies to make heterogeneous and biomimetic tissue constructs. *Materials Today Bio* **2019**, *1*, 100008. DOI: 10.1016/j.mtbio.2019.100008.

(21) Aubert, S.; Bezagu, M.; Spivey, A. C.; Arseniyadis, S. Spatial and temporal control of chemical processes. *Nature Reviews Chemistry* **2019**, *3* (12), 706-722. DOI: 10.1038/s41570-019-0139-6.

(22) Wang, Y.; Zhang, S.; Wang, J. Photo-crosslinkable hydrogel and its biological applications. *Chinese Chemical Letters* **2021**, *32* (5), 1603-1614. DOI: 10.1016/j.cclet.2020.11.073.

(23) Elisseeff, J.; Anseth, K.; Sims, D.; McIntosh, W.; Randolph, M.; Langer, R. Transdermal photopolymerization for minimally invasive implantation. *Proceedings of the National Academy of Sciences* **1999**, *96* (6), 3104-3107. DOI: 10.1073/pnas.96.6.3104.

(24) Bhattarai, N.; Gunn, J.; Zhang, M. Chitosan-based hydrogels for controlled, localized drug delivery. *Advanced Drug Delivery Reviews* **2010**, *62* (1), 83-99. DOI: 10.1016/j.addr.2009.07.019.

(25) Dimatteo, R.; Darling, N. J.; Segura, T. In situ Forming Injectable Hydrogels for Drug Delivery and Wound Repair. *Advanced Drug Delivery Reviews* **2018**, *127*, 167-184. DOI: 10.1016/j.addr.2018.03.007.

(26) Matricardi, P.; Di Meo, C.; Coviello, T.; Hennink, W. E.; Alhaique, F. Interpenetrating polymer networks polysaccharide hydrogels for drug delivery and tissue engineering. *Advanced Drug Delivery Reviews* **2013**, *65* (9), 1172-1187. DOI: 10.1016/j.addr.2013.04.002.

(27) Rizzo, F.; Kehr, N. S. Recent Advances in Injectable Hydrogels for Controlled and Local Drug Delivery. *Advanced Healthcare Materials* **2021**, *10* (1), 2001341. DOI: 10.1002/adhm.202001341.

(28) Schesny, M. K.; Monaghan, M.; Bindermann, A. H.; Freund, D.; Seifert, M.; Eble, J. A.; Vogel, S.; Gawaz, M. P.; Hinderer, S.; Schenke-Layland, K. Preserved bioactivity and tunable release of a SDF1-GPVI bi-specific protein using photo-crosslinked PEGda hydrogels. *Biomaterials* **2014**, *35* (25), 7180-7187. DOI: 10.1016/j.biomaterials.2014.04.116.

(29) Clark, E. A.; Alexander, M. R.; Irvine, D. J.; Roberts, C. J.; Wallace, M. J.; Sharpe, S.; Yoo, J.; Hague, R. J.; Tuck, C. J.; Wildman, R. D. 3D printing of tablets using inkjet with UV photoinitiation. *International Journal of Pharmaceutics* **2017**, *529* (1-2), 523-530. DOI: 10.1016/j.ijpharm.2017.06.085.

(30) Lim, W. S.; Chen, K.; Chong, T. W.; Xiong, G. M.; Birch, W. R.; Pan, J.; Lee, B. H.; Er, P. S.; Salvekar, A. V.; Venkatraman, S. S. A bilayer swellable drug-eluting ureteric stent: Localized drug delivery to treat urothelial diseases. *Biomaterials* **2018**, *165*, 25-38. DOI: 10.1016/j.biomaterials.2018.02.035.

(31) Liu, S.; Yeo, D. C.; Wiraja, C.; Tey, H. L.; Mrksich, M.; Xu, C. Peptide delivery with poly (ethylene glycol) diacrylate microneedles through swelling effect. *Bioengineering & Translational Medicine* **2017**, *2* (3), 258-267. DOI: 10.1002/btm2.10070.

(32) Aycan, D.; Alemdar, N. Development of pH-responsive chitosan-based hydrogel modified with bone ash for controlled release of amoxicillin. *Carbohydrate Polymers* **2018**, *184*, 401-407. DOI: 10.1016/j.carbpol.2017.12.023.

(33) Modaresifar, K.; Hadjizadeh, A.; Niknejad, H. Design and fabrication of GelMA/chitosan nanoparticles composite hydrogel for angiogenic growth factor delivery. *Artificial cells, Nanomedicine, and Biotechnology* **2018**, *46* (8), 1799-1808. DOI: 10.1080/21691401.2017.1392970.

(34) Qi, C.; Liu, J.; Jin, Y.; Xu, L.; Wang, G.; Wang, Z.; Wang, L. Photo-crosslinkable, injectable sericin hydrogel as 3D biomimetic extracellular matrix for minimally invasive repairing cartilage. *Biomaterials* **2018**, *163*, 89-104. DOI: 10.1016/j.biomaterials.2018.02.016.

(35) Klotz, B. J.; Gawlitta, D.; Rosenberg, A. J.; Malda, J.; Melchels, F. P. Gelatin-methacryloyl hydrogels: towards biofabrication-based tissue repair. *Trends in Biotechnology* **2016**, *34* (5), 394-407. DOI: 10.1016/j.tibtech.2016.01.002.

(36) Wang, Y.; Koole, L. H.; Gao, C.; Yang, D.; Yang, L.; Zhang, C.; Li, H. The potential utility of hybrid photo-crosslinked hydrogels with non-immunogenic component for cartilage repair. *NPJ Regenerative Medicine* **2021**, *6* (1), 1-14. DOI: 10.1038/s41536-021-00166-8.

(37) Sun, M.; Sun, X.; Wang, Z.; Guo, S.; Yu, G.; Yang, H. Synthesis and Properties of Gelatin Methacryloyl (GelMA) Hydrogels and Their Recent Applications in Load-Bearing Tissue. *Polymers* **2018**, *10* (11), 1290. DOI: 10.3390/polym10111290.

(38) Tan, H.; Marra, K. G. Injectable, biodegradable hydrogels for tissue engineering applications. *Materials* **2010**, *3* (3), 1746-1767. DOI: 10.3390/ma3031746.

(39) Nguyen, Q. T.; Hwang, Y.; Chen, A. C.; Varghese, S.; Sah, R. L. Cartilage-like mechanical properties of poly (ethylene glycol)-diacrylate hydrogels. *Biomaterials* **2012**, *33* (28), 6682-6690. DOI: 10.1016/j.biomaterials.2012.06.005.

(40) Levett, P. A.; Melchels, F. P.; Schrobback, K.; Hutmacher, D. W.; Malda, J.; Klein, T. J. A biomimetic extracellular matrix for cartilage tissue engineering centered on photocurable gelatin, hyaluronic acid and chondroitin sulfate. *Acta Biomaterialia* **2014**, *10* (1), 214-223. DOI: 10.1016/j.actbio.2013.10.005.

(41) Meinert, C.; Schrobback, K.; Hutmacher, D. W.; Klein, T. J. A novel bioreactor system for biaxial mechanical loading enhances the properties of tissue-engineered human cartilage. *Scientific Reports* **2017**, *7* (1), 1-14. DOI: 10.1038/s41598-017-16523-x.

(42) Brown, G. C.; Lim, K. S.; Farrugia, B. L.; Hooper, G. J.; Woodfield, T. B. Covalent incorporation of heparin improves chondrogenesis in photocurable gelatin - methacryloyl hydrogels. *Macromolecular Bioscience* **2017**, *17* (12), 1700158. DOI: 10.1002/mabi.201700158.

(43) Mouser, V. H.; Melchels, F. P.; Visser, J.; Dhert, W. J.; Gawlitta, D.; Malda, J. Yield stress determines bioprintability of hydrogels based on gelatin-methacryloyl and gellan gum for cartilage bioprinting. *Biofabrication* **2016**, *8* (3), 035003. DOI: 10.1088/1758-5090/8/3/035003.

(44) Bian, L.; Guvendiren, M.; Mauck, R. L.; Burdick, J. A. Hydrogels that mimic developmentally relevant matrix and N-cadherin interactions enhance MSC chondrogenesis.

Proceedings of the National Academy of Sciences **2013**, *110* (25), 10117-10122. DOI: 10.1073/pnas.1214100110.

(45) Hayami, J. W.; Waldman, S. D.; Amsden, B. G. Chondrocyte generation of cartilage-like tissue following photoencapsulation in methacrylated polysaccharide solution blends. *Macromolecular Bioscience* **2016**, *16* (7), 1083-1095. DOI: 10.1002/mabi.201500465.

(46) Buwalda, S. J.; Boere, K. W. M.; Dijkstra, P. J.; Feijen, J.; Vermonden, T.; Hennink, W. E. Hydrogels in a Historical Perspective: From Simple Networks to Smart Materials. *Journal of Controlled Release* **2014**, *190*, 254-273. DOI: 10.1016/j.jconrel.2014.03.052.

(47) Choi, J. R.; Yong, K. W.; Choi, J. Y.; Cowie, A. C. Recent Advances in Photo-Crosslinkable Hydrogels for Biomedical Applications. *BioTechniques* **2019**, *66* (1), 40-53. DOI: 10.2144/btn-2018-0083.

(48) Hua, Y.; Xia, H.; Jia, L.; Zhao, J.; Zhao, D.; Yan, X.; Zhang, Y.; Tang, S.; Zhou, G.; Zhu, L. Ultrafast, tough, and adhesive hydrogel based on hybrid photocrosslinking for articular cartilage repair in water-filled arthroscopy. *Science Advances* **2021**, *7* (35), eabg0628. DOI: 10.1126/sciadv.abg0628.

(49) Thakur, T.; Xavier, J. R.; Cross, L.; Jaiswal, M. K.; Mondragon, E.; Kaunas, R.; Gaharwar, A. K. Photocrosslinkable and elastomeric hydrogels for bone regeneration. *Journal of Biomedical Materials Research Part A* **2016**, *104* (4), 879-888. DOI: 10.1002/jbm.a.35621.

(50) Bian, S.; Zheng, Z.; Liu, Y.; Ruan, C.; Pan, H.; Zhao, X. A Shear-Thinning Adhesive Hydrogel Reinforced by Photo-Initiated Crosslinking as a Fit-to-Shape Tissue Sealant. *Journal of Materials Chemistry B* **2019**, *7* (42), 6488-6499. DOI: 10.1039/C9TB01521C.

(51) Townsend, J. M.; Beck, E. C.; Gehrke, S. H.; Berkland, C. J.; Detamore, M. S. Flow Behavior Prior to Crosslinking: The Need for Precursor Rheology for Placement of Hydrogels in Medical

Applications and for 3D Bioprinting. *Progress in Polymer Science* **2019**, *91*, 126-140. DOI: 10.1016/j.progpolymsci.2019.01.003.

(52) Creton, C. 50th anniversary perspective: Networks and gels: Soft but dynamic and tough. *Macromolecules* **2017**, *50* (21), 8297-8316.

(53) Khare, E.; Holten-Andersen, N.; Buehler, M. J. Transition-metal coordinate bonds for bioinspired macromolecules with tunable mechanical properties. *Nature Reviews Materials* **2021**, *6* (5), 421-436. DOI: 10.1038/s41578-020-00270-z.

(54) Lin, X.; Wang, X.; Zeng, L.; Wu, Z. L.; Guo, H.; Hourdet, D. Stimuli-Responsive Toughening of Hydrogels. *Chemistry of Materials* **2021**.

(55) Cao, J.; Li, J.; Chen, Y.; Zhang, L.; Zhou, J. Dual physical crosslinking strategy to construct moldable hydrogels with ultrahigh strength and toughness. *Advanced Functional Materials* **2018**, *28* (23), 1800739. DOI: ARTN 1800739

10.1002/adfm.201800739.

(56) Meng, Z.-J.; Liu, J.; Yu, Z.; Zhou, H.; Deng, X.; Abell, C.; Scherman, O. A. Viscoelastic Hydrogel Microfibers Exploiting Cucurbit [8] uril Host–Guest Chemistry and Microfluidics. *ACS Applied Materials & Interfaces* **2020**, *12* (15), 17929-17935. DOI: 10.1021/acsami.9b21240.

(57) Zhang, Y. S.; Khademhosseini, A. Advances in Engineering Hydrogels. *Science* **2017**, *356* (6337), eaaf3627. DOI: 10.1126/science.aaf3627.

(58) Hunt, J. N.; Feldman, K. E.; Lynd, N. A.; Deek, J.; Campos, L. M.; Spruell, J. M.; Hernandez, B. M.; Kramer, E. J.; Hawker, C. J. Tunable, High Modulus Hydrogels Driven by Ionic Coacervation. *Advanced Materials* **2011**, *23* (20), 2327-2331. DOI: 10.1002/adma.201004230.

(59) Appel, E. A.; del Barrio, J.; Loh, X. J.; Scherman, O. A. Supramolecular polymeric hydrogels. *Chemical Society Reviews* **2012**, *41* (18), 6195-6214.

(60) Fan, H.; Gong, J. P. Fabrication of Bioinspired Hydrogels: Challenges and Opportunities. *Macromolecules* **2020**, *53* (8), 2769-2782. DOI: 10.1021/acs.macromol.0c00238.

(61) Hu, W.; Wang, Z.; Xiao, Y.; Zhang, S.; Wang, J. Advances in crosslinking strategies of biomedical hydrogels. *Biomaterials science* **2019**, *7* (3), 843-855.

(62) Srivastava, S.; Andreev, M.; Levi, A. E.; Goldfeld, D. J.; Mao, J.; Heller, W. T.; Prabhu, V. M.; de Pablo, J. J.; Tirrell, M. V. Gel Phase Formation in Dilute Triblock Copolyelectrolyte Complexes. *Nature Communications* **2017**, *8* (1), 14131. DOI: 10.1038/ncomms14131.

(63) Srivastava, S.; Levi, A. E.; Goldfeld, D. J.; Tirrell, M. V. Structure, Morphology, and Rheology of Polyelectrolyte Complex Hydrogels Formed by Self-Assembly of Oppositely Charged Triblock Polyelectrolytes. *Macromolecules* **2020**, *53* (14), 5763-5774. DOI: 10.1021/acs.macromol.0c00847.

(64) Li, D. F.; Gockler, T.; Schepers, U.; Srivastava, S. Polyelectrolyte Complex-Covalent Interpenetrating Polymer Network Hydrogels. *Macromolecules* **2022**, *55* (11), 4481-4491. DOI: 10.1021/acs.macromol.2c00590.

(65) Mostafavi, A.; Samandari, M.; Karvar, M.; Ghovvati, M.; Endo, Y.; Sinha, I.; Annabi, N.; Tamayol, A. Colloidal multiscale porous adhesive (bio) inks facilitate scaffold integration. *Applied Physics Reviews* **2021**, *8* (4), 041415. DOI: 10.1063/5.0062823.

(66) Ghovvati, M.; Baghdasarian, S.; Baidya, A.; Dhal, J.; Annabi, N. Engineering a highly elastic bioadhesive for sealing soft and dynamic tissues. *Journal of Biomedical Materials Research Part B: Applied Biomaterials* **2022**, *110* (7), 1511-1522. DOI: 10.1002/jbm.b.35012.

(67) Cruise, G. M.; Scharp, D. S.; Hubbell, J. A. Characterization of permeability and network structure of interfacially photopolymerized poly (ethylene glycol) diacrylate hydrogels. *Biomaterials* **1998**, *19* (14), 1287-1294. DOI: 10.1016/s0142-9612(98)00025-8.

(68) Van der Gucht, J.; Spruijt, E.; Lemmers, M.; Stuart, M. A. C. Polyelectrolyte complexes: Bulk phases and colloidal systems. *Journal of colloid and interface science* **2011**, *361* (2), 407-422. DOI: 10.1016/j.jcis.2011.05.080.

(69) Srivastava, S.; Tirrell, M. V. Polyelectrolyte complexation. *Advances in chemical physics* **2016**, *161*, 499-544. DOI: Book_Doi 10.1002/9781119290971.

(70) Sing, C. E.; Perry, S. L. Recent progress in the science of complex coacervation. *Soft Matter* **2020**, *16* (12), 2885-2914.

(71) Kirsch, M.; Birnstein, L.; Pepelanova, I.; Handke, W.; Rach, J.; Seltsam, A.; Scheper, T.; Lavrentieva, A. Gelatin-methacryloyl (GelMA) formulated with human platelet lysate supports mesenchymal stem cell proliferation and differentiation and enhances the hydrogel's mechanical properties. *Bioengineering* **2019**, *6* (3), 76. DOI: 10.3390/bioengineering6030076.

(72) Zhu, M.; Wang, Y.; Ferracci, G.; Zheng, J.; Cho, N.-J.; Lee, B. H. Gelatin methacryloyl and its hydrogels with an exceptional degree of controllability and batch-to-batch consistency. *Scientific reports* **2019**, *9* (1), 1-13.

Chapter 5

Hydrogel Scaffoldings Enable Extrusion-based 3D Bioprinting of Low Viscosity Bioinks

Reproduced from a manuscript in preparation. “Hydrogel Scaffoldings Enable Extrusion-based 3D Bioprinting of Low Viscosity Bioinks”, Tobias Göckler, Defu Li, Alisa Grimm, Felix Mecklenburg, Michael Grün, Ute Schepers, Samanvaya Srivastava. *Submitted*.

Contribution from Defu Li: Synthesis of diblock and triblock polyelectrolytes, NMR characterization of polyelectrolytes, rheology, SAXS, tensile, and SEM characterization oh hydrogel inks.

Abstract

We generate biocompatible scaffolds with excellent structural integrity based on complex-forming block polyelectrolytes that enables extrusion-based 3D bioprinting of large tissues from low viscosity bioinks. Despite remarkable progress of biofabrication techniques in tissue engineering, the development of extrudable bioinks that perform optimally at physiological temperatures remains a major challenge. Most biopolymer and photocurable precursor solutions exhibit low viscosities at 37 °C, resulting in undesirable flows and loss of form prior to chemical crosslinking. Temperature-sensitive bioinks, such as gelatin methacryloyl (GelMA), can be deposited near their gelling point, but suffer from suboptimal temperature-induced pre-gelation, poor cell viability emerging from long holding times in the cooled cartridges, inefficient temperature transfer from the print bed, and discontinuous layer-by-layer fabrication. Here, we demonstrate that block polyelectrolyte additives serve as effective viscosity enhancers when added to non-extrudable

precursor solutions. Rapid, charge-driven self-assembly of block polyelectrolytes into either micelles or interconnected networks provides a hydrogel scaffolding that forms nearly instantly, lends initial structural robustness upon deposition, and enhances shear and tensile strength of the deposited bioinks. Moreover, our approach enables continuous extrusion without the need of chemical crosslinking between individual layers, paving the way for fast biomanufacturing of human-scale tissue constructs with improved inter-layer bonding.

5.1 Introduction

The design of suitable bioinks that balance three-dimensional (3D) printability and biocompatibility (the biofabrication window[1]) remains critical for the expansion of additive manufacturing (AM) in biomedicine.[2 3 4 5 6 7] AM techniques have found application in a growing number of disciplines, including mechanical engineering[8], aviation and aerospace engineering[9 10], architecture[11 12 13], electronics[14 15], arts[16], food industry[17 18], and medicine[19 20 21]. In the life sciences, AM technologies have enabled customized macro- and micro-scale fabrication, ranging from prosthetics[22 23 24] to highly defined and complex microarchitectures for 3D cell culture[25 26 27] to the precise deposition of cells and biomolecules[1 28 29]. Among various biofabrication techniques (inkjet, laser-assisted, stereolithography), extrusion-based bioprinting is the most commonly used method due to its rapid print speed and possibility to encapsulate high cell densities (10^8-10^9 cells·mL^{-1}) within extracellular matrix (ECM)-mimicking hydrogel inks.[6 30] Consequently, cell-laden tissue and organ constructs[31 32] have been fabricated through extrusion-based bioprinting, including skin[33], liver[34], kidney[35], heart[36], blood vessels[37], cartilage[38], and bone[39] constructs.

However, despite immense efforts in the development of diverse hydrogel-based inks for extrusion-based bioprinting, "printable" inks that possess the optimal rheological properties along with cell-friendly microstructures, controlled swelling response, biocompatibility and biodegradability remain elusive. Ideally, cell-encapsulating extrusion inks should exhibit high zero-shear viscosity (10^1-10^7 mPa·s) to ensure fiber formation and multilayer stacking during printing[40] while exhibiting shear-thinning properties to achieve low viscosities under high shear and minimize the shear stress on cells during extrusion.[41 42 43] Upon deposition, rapid viscosity recovery and high yield stress (10^1-10^3 Pa) [44 45 46] are crucial to maintain structural integrity and avoid undesirable flows and loss of form.[47 48 49]

Physical hydrogelation in biopolymer (gelatin, alginate, collagen, etc.) solutions has emerged as an avenue to enhance printability while retaining ECM-mimicking microstructures, biocompatibility, and biodegradability. When combined with functionalization of biopolymers (e.g., methacrylation[50 51 52], norbornene[53 54 55] or thiol modification[56 57]) to enable secondary crosslinking, these approaches have been shown to improve ink printability and enhance shape fidelity by "locking" the printed microstructures. For instance, cooling biopolymer solutions below their gelation temperatures[58 50], crosslinking them with multivalent ions[59 60 61], or incorporating additives such as nanocellulose[62 63 64] and nanoclay[65 66 67] have been employed to enhance the viscosity of precursor solutions. However, these strategies suffer from reduced cell survival in the cooled cartridges[68 69], long-term nanotoxicity and limited biodegradability of the additives[70 71 72], and do not confer any advantageous properties to the hydrogel inks after secondary crosslinking. Although huge efforts have been put over the last decade into the design of increasingly sophisticated and multicomponent hydrogel systems[73 74 75 76 53], there is still a lack of extrudable and highly tunable bioinks that perform optimally at physiological temperatures, which is highly desirable in tissue engineering.

Here, we present a versatile strategy to imbue printability to photocurable low viscosity inks at 37 °C by inclusion of polyelectrolyte complex (PEC) self-assemblies. In the model system demonstrated here, oppositely charged diblock or triblock polyelectrolytes (DbPEs and TbPEs) serve as building blocks of electrostatic self-assemblies – micelles or network, respectively[77 78 79]– while gelatin methacryloyl (GelMA) at 37 °C serves as a representative low viscosity ink. Mixing of the three ink constituents (the oppositely charged block polyelectrolytes and the crosslinkable precursors) results in swift assembly of GelMA-containing viscous and extrudable PEC hydrogel inks. The PEC hydrogels recover quickly upon deposition and provide interim insolubility in water,

conserving the photopolymerizable precursors and limiting their dilution or loss of structural integrity.[80] Moreover, the combination of covalent network and non-covalent assemblies in the crosslinked 3D printed manifolds exhibit improvements in shear and tensile properties, including shear and tensile moduli, toughness, and extensibility, as well as provide control over their swelling response. Suitable GelMA/DbPE and GelMA/TbPE formulations for 3D bioprinting are demonstrated, as identified by rheological screening, and enable continuous extrusion of 3D structures which require only a single photocrosslinking step in the end, paving the way for fast biomanufacturing of human-scale tissue constructs with improved inter-layer bonding. Due to the ease of transferability of our approach, we envision the PEC micelles and network as powerful additives to any type of liquid-like precursor solution that will expand the future availability of extrusion bioinks for tissue engineering.

5.2 Results and Discussion

5.2.1 Diblock and Triblock Polyelectrolytes as Viscosity Enhancers for Liquid-Like Precursor Solutions

Ink additives based on oppositely charged bPEs were synthesized from poly(ethylene glycol) in a two-step process. In the first step, methoxy poly(ethylene glycol)$_{113}$-poly(allyl glycidyl ether)$_{45}$ (mPEO$_{113}$-PAGE$_{45}$) *AB* diblock copolymers or poly(ally glycidyl ether)$_{30}$-poly(ethylene glycol)$_{455}$-poly(ally glycidyl ether)$_{30}$ (PAGE$_{30}$-PEO$_{455}$-PAGE$_{30}$) *ABA* triblock copolymers were synthesized by ring-opening anionic polymerization. In the second step, the PAGE blocks were functionalized with ionic (guanidinium or sulfonate) moieties using thiol-ene click chemistry to yield diblock or triblock polyelectrolytes (DbPE or TbPE, respectively) (**Figures 5-S1,2,3,4**). Mixing equimolar aqueous solutions of cationic and anionic bPEs resulted in swift electrostatic

self-assembly of polyelectrolyte complex (PEC) hydrogels with characteristic PEC microstructures. DbPEs assembled into micelles with the charged *A* blocks forming the micelle core and the neutral *B* blocks forming the corona, while TbPEs formed interconnected networks, wherein the neutral *B* midblocks bridged the PEC domains comprising the charged *A* endblocks (**Figure 5-1**).[77 79 81]

Aqueous self-assembly of the oppositely charged pairs of DbPEs or TbPEs was harnessed to create a hydrogel scaffolding for the low viscosity, non-extrudable solutions of crosslinkable precursors, thus providing structural stability and interim protection against uncontrolled dilution. Previously, we have shown that inclusion of photocurable precursor polymers does not impede with the PEC self-assembly.[80] In this work, GelMA was used as a representative photocrosslinkable precursor. While GelMA solutions exhibit excellent printing performance near the gelling point (~ 22 °C) and has therefore become a widely used ink for 3D bioprinting[82 4 83], its water-like viscosity at 37 °C is similar to most synthetic precursors which suffer from poor printability. Mixing the GelMA precursor with the oppositely charged DbPEs resulted extrudable GelMA/DbPE hydrogels comprising GelMA chains interspersed among jammed PEC micelles. Subsequent photocrosslinking of the GelMA precursors was induced by ultraviolet/visible light irradiation and led to the formation of hybrid GelMA/DbPE hydrogels (**Figure 5-1A**). Similarly, mixing of GelMA with the oppositely charged TbPEs resulted in homogenous and extrudable GelMA/TbPE hydrogels comprising an interconnected PEC network with dispersed GelMA chains. After photocrosslinking, hybrid GelMA/TbPE hydrogels with interpenetrating covalent and non-covalent networks were formed (**Figure 5-1B**).

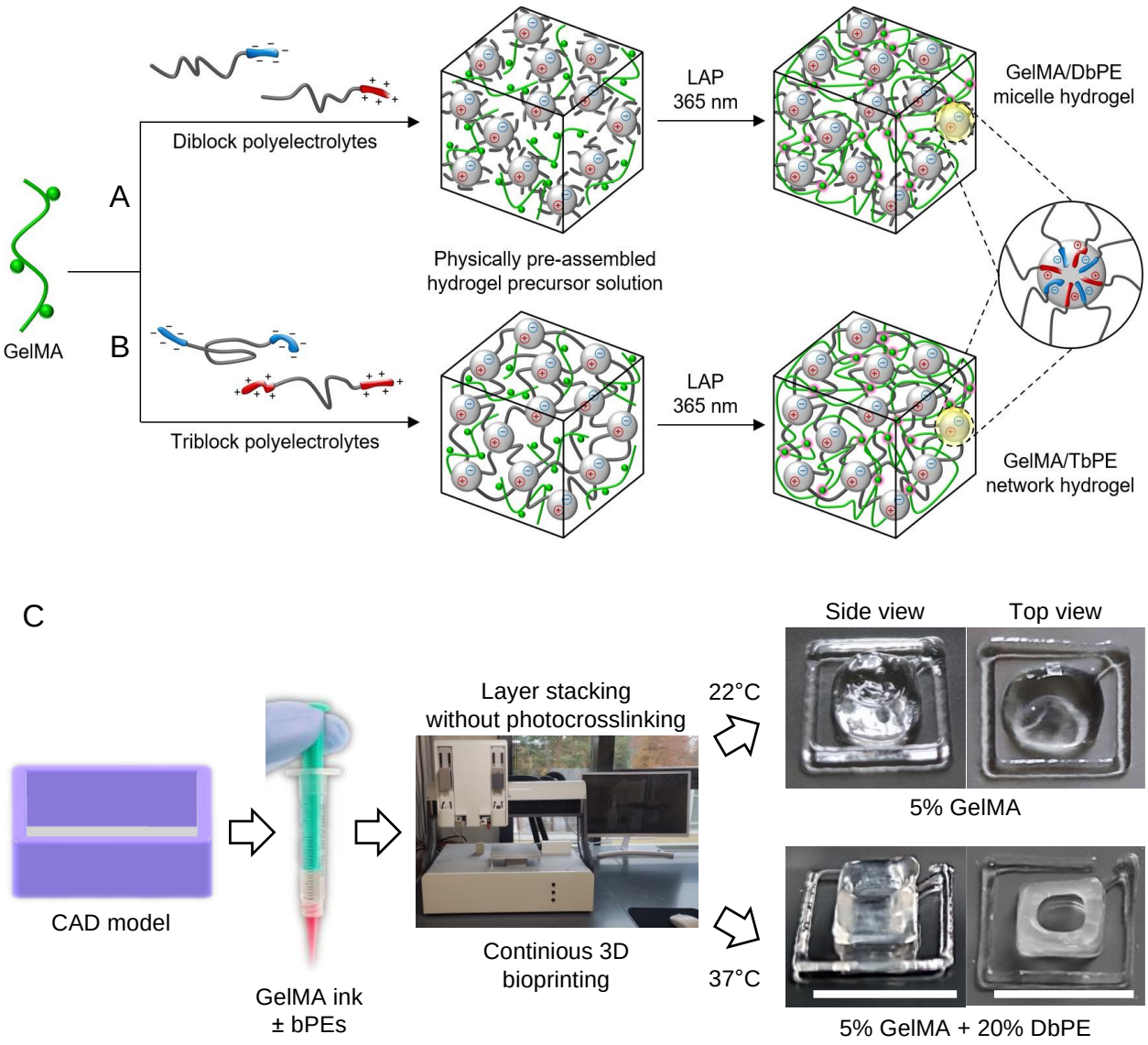

Figure 5-1. Schematics representing a versatile strategy to improve 3D printability of low viscosity bioinks (e.g., GelMA at 37 °C) by inclusion of complex-forming block polyelectrolyte additives. Electrostatic self-assembly of oppositely charged **(A)** diblock PE (DbPE) and **(B)** triblock PE (TbPE) resulted in either micelle or network formation while increasing the viscosity of the GelMA precursor solution. After photocrosslinking, covalently and electrostatically double-crosslinked hydrogels were formed. **(C)** Proof-of-concept of employing electrostatically reinforced bioinks in 3D bioprinting. A 5 wt% GelMA precursor solution was supplemented with

20 wt% DbPE that forms a protective hydrogel scaffolding to enable continuous extrusion of a hollow square structure (11 layers) at 37 °C, followed by a single photocrosslinking step in the end. Shape fidelity of the hybrid ink was compared to the print result of bPE-free GelMA which relies solely on thermally induced gelation by a cooled cartridge and print bed and hence suffers from loss of structural integrity with increasing layer stacking (scale bar: 10 cm).

Reinforcement of the GelMA precursor with either PEC micelles or PEC network improved 3D printability to such an extent that biomanufacturing at a physiological temperature became possible. In a *proof-of-principle* experiment, we demonstrated that the protective hydrogel scaffolding which forms within seconds provides advanced structural robustness to the ink over hours prior to secondary crosslinking, making immediate photocuring upon deposition obsolete. Moreover, electrostatic reinforcement overcomes current shortcomings of temperature-sensitive bioinks (e.g., GelMA) used for extrusion-based printing, particularly the remarkably deteriorating shape fidelity and resolution with increasing layer stacking due to the poor temperature transfer from the print bed to the top layers. Printing a hollow square structure consisting of eleven layers and without photocuring between individual layers revealed insufficient cooling of the top layers of a bPE-free GelMA construct. As a consequence, inward bending and eventual collapse of the structure was promoted due to slow viscosity recovery, underlining the need of *in situ* photocrosslinking for GelMA after each deposited layer (**Figure 5-1C**). In contrast, GelMA inks supplemented with appropriate amounts of bPEs do no longer rely on thermally induced pre-gelation by a cooled cartridge (22 °C) and print bed (17 °C) but benefit the from the instantaneous formation of the PEC assemblies. Hence, using electrostatically reinforced bioinks enabled continuous fabrication at 37 °C of 3D structures with improved inter-layer adhesion and only a single photocrosslinking step in the end, thus leading to reduced manufacturing time and UV exposure to encapsulated cells (**Figure 5-1C**). In the following, we discuss the benchmarks for printable formulations in bioink design and evaluate the impact of the additives on material properties to highlight the utility and the potential of self-assembling bPEs in 3D bioprinting.

5.2.2 Rheological Screening for Printable GelMA/bPE Bioinks

Rheology has established itself as a powerful method to assess and predict printability of bioinks for extrusion-based printing, while benefiting from minimal material consumption.[40 48 84 47] The rheological benchmarks for bioink printability were established through oscillatory and rotational rheology of 22 °C GelMA precursor hydrogels, which served as the basis for the development of printable GelMA/bPE formulations. GelMA solutions with concentrations between 5 wt% and 10 wt% when cooled near their gelling temperature are typically considered to lie within the "bioprintability window" and are commonly used for 3D bioprinting. While lower GelMA concentration formulations suffer from poor structural stability after photocrosslinking, higher GelMA concentrations limit the available space for cell encapsulation and spreading.[41 50 85]

First, small amplitude oscillatory strain measurements were carried out at 22 °C for pre-gelled GelMA solutions (its optimal temperature for extrusion-based printing) to determine the printability window in shear moduli (storage modulus G': 20-700 Pa). Then, 5 wt% of a low viscosity GelMA solution at 37 °C was supplemented with increasing amounts of either DbPEs or TbPEs to obtain formulations whose moduli were within the printability moduli window. Both DbPEs and TbPEs represented suitable ink additives; their addition resulted in an immediate increase in the shear moduli of the hybrid inks (**Figure 5-2A, 5-S6**). However, the respective quantities of DbPEs and TbPEs required to achieve ink formulations with moduli within the printability window were very different, ascribable to the different PEC microstructures (jammed micelles vs. interconnected networks) they form. For TbPEs, even small concentrations ($C_{TbPE} \leq 10$ wt%) had a significant impact on the ink moduli, while DbPE concentrations $C_{DbPE} \geq 20$ wt% were required to achieve moduli commensurate to printable inks.

Numerous promising GelMA/bPE formulations were identified by the small amplitude oscillatory strain measurements, however, the investigation was limited to the properties of the static bulk material prior and after extrusion, wherein the respective microstructure is expected to be unperturbed. Hence, in addition to shear moduli determined within the linear viscoelastic (LVE) regime, further rheological key parameters describing the shear conditions present during extrusion through a small orifice, including yield stress, complex viscosity, and post-shearing recovery, of the 37 °C GelMA/bPE inks were examined and compared with 22 °C GelMA inks. The yield stress is defined as the minimum stress required for a material to start to flow and thus influences the required extrusion pressure in 3D printing. In a stress ramp experiment, yielding occurs when an initially elastic material (plateau-region) displays a steep decrease in viscosity (viscosity-drop region) above a characteristic stress threshold (**Figure 5-2B, 5-S8**). It is primarily observed for entangled polymer networks or physically pre-crosslinked materials, where non-covalent bonds must first be broken to enable macroscopic flow. A large yield stress of an ink generally promotes syringeability, fiber formation during extrusion as well as post-printing shape fidelity (i.e., no flow in absence of applied force). However, if the yield stress exceeds a critical value, it can impede dispensing, hinder miscibility with cells, and negatively impact cell viability because of the high pressure that is needed for extrusion.[47 48]

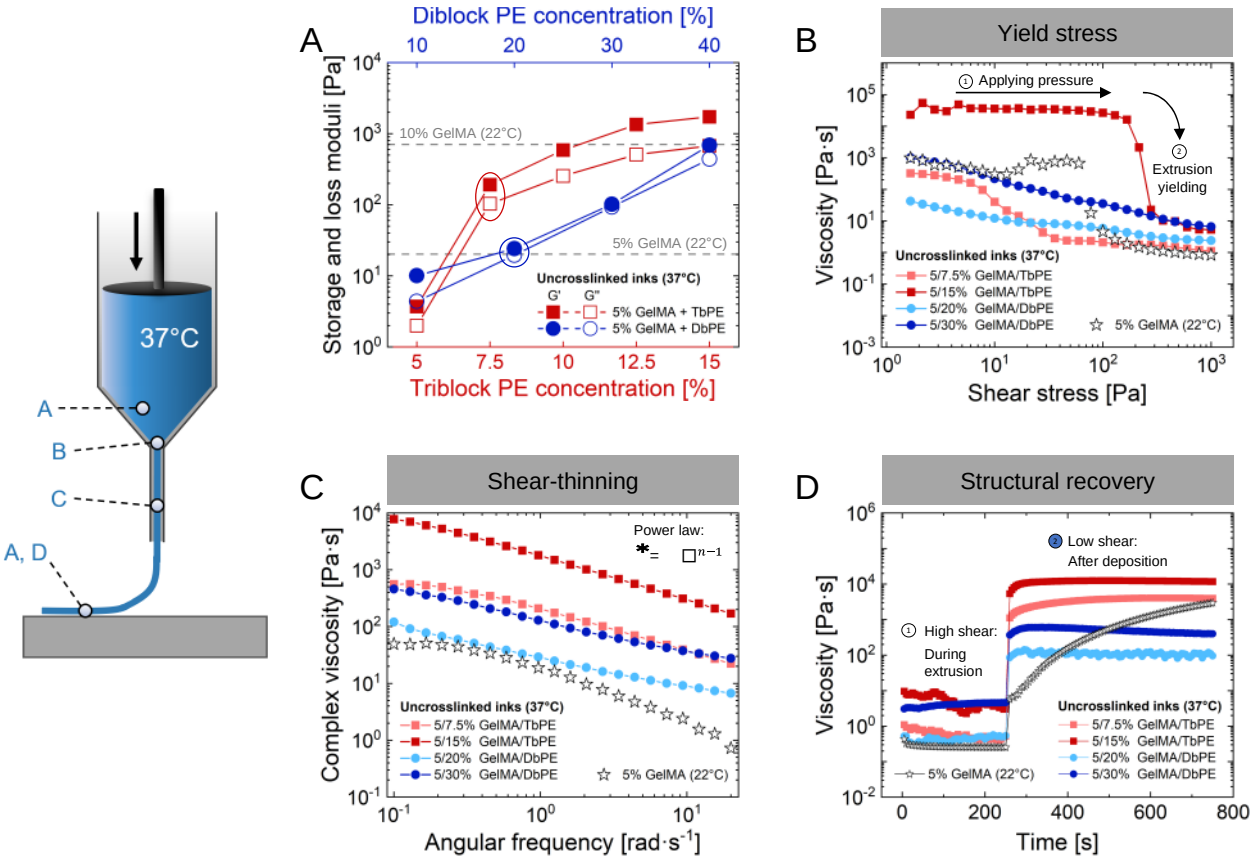

Figure 5-2. Rheological characterization of GelMA/bPE precursor solutions with increasing DbPE and TbPE concentration at 37 °C. **(A)** Screening for printable inks within the biofabrication window of GelMA (5-10 wt%, 22 °C). Shear moduli (G', G'') were derived from frequency sweeps at ω = 1.25 rad·s^{-1}. Representative formulations were further characterized in terms of their **(B)** yield stress, **(C)** shear-thinning behavior, and **(D)** structural recovery post-shearing. GelMA inks are depicted in black stars, whereas GelMA/TbPE and GelMA/DbPE inks are shown in red squares and blue circles, respectively.

As gelatin chains assemble into triple helices near the gelling point, GelMA demonstrates a distinct yield point at which the ink transitions from elastic to flow behavior (black stars in **Figure 5-2B**). Likewise, GelMA/TbPE inks exhibited characteristic yield stress points that continuously rose with TbPE loading (C_{TbPE} = 7.5-15 wt%, red squares in **Figure 5-2B**), owing to the increasing number of PEC crosslinks. In contrast, the GelMA/DbPE inks did not exhibit either a plateau or a steep viscosity-drop region, but rather a continuous and slow decline in viscosity (blue circles in **Figure 5-2B**). The absence of a specific stress required for flow initiation was ascribed to the lack of both physical gelation of GelMA at 37 °C and the lack of interconnection among the PEC micelles. Nevertheless, comparable viscosities of the 22 °C GelMA inks and 37 °C GelMA/DbPE inks in the low and high stress regimes (corresponding to the pre- and post-yield states of 22 °C GelMA inks) engendered confidence towards printability of GelMA/DbPE inks.

Once the flow is initiated, shear-thinning behavior is required to facilitate extrusion through a small diameter nozzle and to prevent excessive shear stress on cells. Shear-thinning is a non-Newtonian fluid behavior characterized in different solvents prior and after photocrosslinking of the GelMA precursors by a decrease in viscosity with increasing shear rate or angular frequency. Here, it was quantified by describing the linear region of the double-logarithmic angular frequency - complex viscosity profiles with a power law ($\eta^* = K \cdot \omega^{n-1}$) and determining the shear-thinning exponent *n* (**Figure 5-2C, 5-S9**), wherein $n = 1$ applies to Newtonian fluids and $0 < n < 1$ describes shear-thinning fluids. 22 °C GelMA inks and 37 °C GelMA/TbPE inks both displayed strong shear-thinning properties with $n \leq 0.2$, ascribable to their physically crosslinked microstructures. At the same time, the jammed microstructure of the disjointed PEC micelles in the 37 °C GelMA/DbPE inks resulted in milder shear-thinning behavior, with $n \approx 0.5$. In both

DbPE and TbPE containing inks, sufficient shear-thinning was observed to enable printing while preserving cell viability.

After shearing, it is important for the ink to regain its original properties prior to extrusion. The time required for returning to the equilibrium state is referred to as the recovery or the self-healing time.[45] [86] Post-printing viscosity recovery (i.e., transition from fluid-like flow to elastic shape retention) of 22 °C GelMA and 37 °C GelMA/bPE inks was studied by applying a high shear rate, followed by a low shear rate to simulate the dispensing process (**Figure 5-2D**). Immediate flow discontinuation and buildup of internal resistance after deposition is crucial to prevent undesirable flows and loss of form prior to secondary photocrosslinking. GelMA inks exhibited slow recovery kinetics (≥ 8 min) at 22 °C, owing to the long recovery timescale of the triple helix microstructure. In typical printing setups, the print bed is therefore cooled to temperatures below the gelling point of gelatin (17 °C) to accelerate gelation upon deposition. In contrast, both GelMA/DbPE and GelMA/TbPE inks displayed near-instant viscosity recovery at 37 °C (80% recovery within 20 s), resulting from the rapid recovery of the PEC self-assemblies.

These tunable rheological characteristics of GelMA/bPE inks highlight the advantages of employing these hybrid inks in 3D bioprinting. Hence, several bPE-based ink formulations within the printability window were selected for further investigation of their physico-mechanical properties, biocompatibility, and 3D bioprintability.

5.2.3 Enhanced Tensile Performance of GelMA/bPE Double Network Hydrogels

Photochemical crosslinking of the GelMA precursors provides almost immediate structural stability in wet environments and at temperatures above the gelling point. However, compared to other photocurable hydrogels, GelMA suffers from inherently poor mechanical and adhesive

properties, limited stretchiness, and lack of robustness against external forces. As soon as stress is applied, their structures easily fall apart, thus making damage-free transfer of hydrogel constructs quite challenging.

Reinforcement of the covalent network with either PEC micelles or PEC network rendered improved tensile performance to the GelMA hydrogels. Stress-strain curves from uniaxial tensile tests (**Figure 5-3A, 5-S11**) revealed significant enhancements in ultimate stress (up to 572%, **Figure 5-3B**), extensibility (up to 42%, **Figure 5-3C**), Young's modulus (up to 1147%, **Figure 5-S12**), and toughness (up to 772%, **Figure 5-3D**) for GelMA/bPE hydrogels. In these hybrid hydrogels, the self-assembled bPEs served as energy-dissipating scaffolds within the brittle GelMA network. Due to the reversible nature of electrostatic interactions, the PEC domains were hypothesized to undergo repeated sequences of disassembly and reassembly without influencing the integrity of the GelMA network. Higher bPE loading enhanced the overall network resilience, hence why more energy was required to break the network.

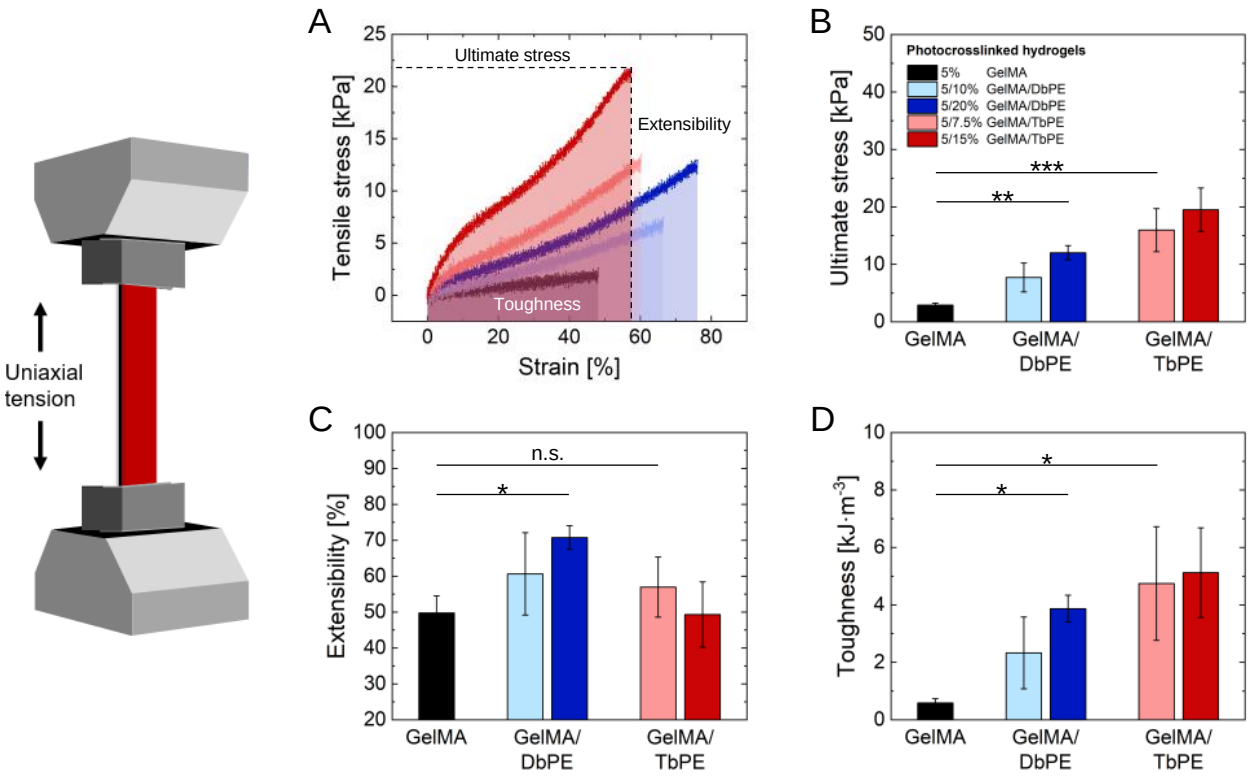

Figure 5-3. Tensile tests for photocrosslinked GelMA and GelMA/bPE hydrogels with increasing DbPE and TbPE concentration ($n \geq 3$). **(A)** Representative stress curves as a function of strain, from which **(B)** ultimate stress **(C)** extensibility, and **(D)** toughness were determined. GelMA hydrogels are depicted in black, whereas GelMA/TbPE and GelMA/DbPE hydrogels are shown in red and blue, respectively. Data were presented as mean ± SD and statistically evaluated by one-way ANOVA. *, **, *** represent $p < 0.05$, 0.01, and 0.001, respectively.

Subtle differences in the improvements of the tensile performance of GelMA/bPE hydrogels over GelMA hydrogels were observed. While GelMA/DbPE hydrogels showed improved ultimate stress and extensibility in comparison to GelMA hydrogels, GelMA/TbPE hydrogels exhibited further improvements in ultimate stress in comparison with GelMA/DbPE hydrogels but with a loss in extensibility, such that their extensibility was comparable to GelMA hydrogels. These differences can again be ascribed to the PEC microstructure – disjointed micelles vs. interconnected networks – formed by DbPEs and TbPEs, respectively. The former is expected to exhibit higher restructurability but at the expense of lower stress threshold for restructuring, while the latter is expected to exhibit a larger threshold for network restructuring and lower restructurability owing to the interconnected microstructure. Overall, we surmise that the incorporation of bPEs into the covalent network overcame the low mechanical resilience of GelMA bioinks after photocrosslinking and facilitated their post-printing processability for applications that require relocation of the bioprinted constructs (e.g., transplantation).

5.2.4 Tunability of Mechanical Properties and Swelling Characteristics of Photocrosslinked GelMA/bPE Hydrogels

In addition to tensile strength, further physico-mechanical properties of hydrogels must meet specific demands to ensure cytocompatibility, which include a matrix stiffness matching to the target tissue, a sufficiently high hydration degree for fast nutrient diffusion, and structural robustness in physiological environments. Hence, shear moduli and swelling behavior of photocrosslinked GelMA/bPE hydrogels were studied for different compositions and solvents (**Figure 5-4**).

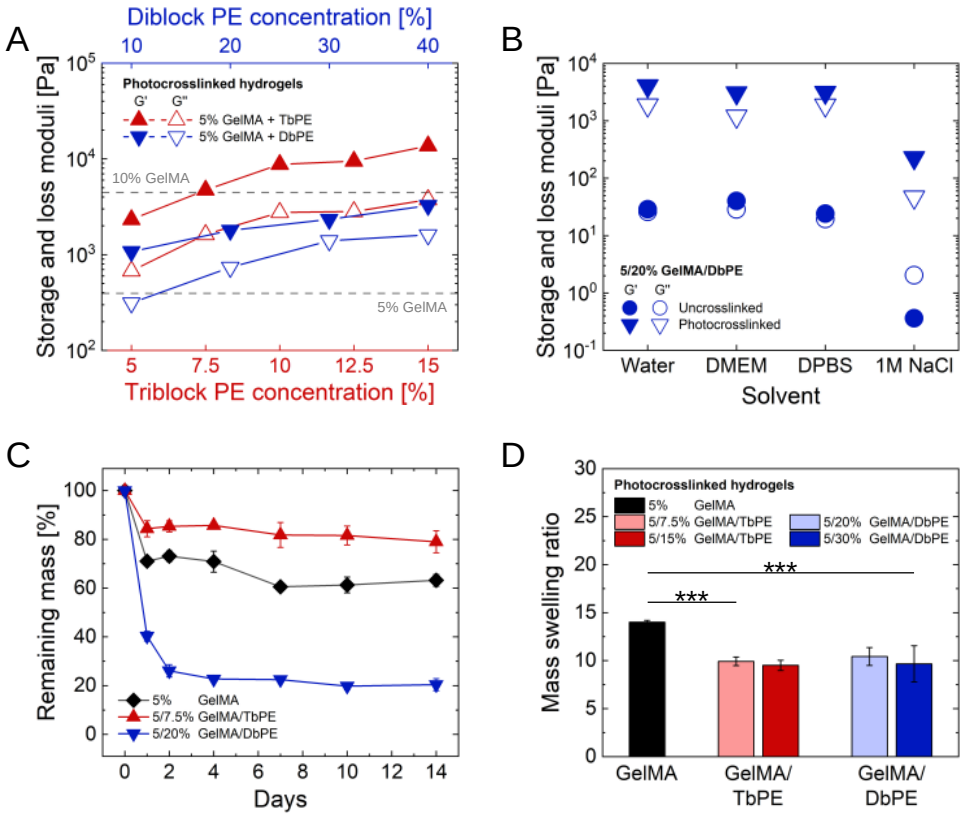

Figure 5-4. Impact of bPE additives on hydrogel properties. **(A)** Shear moduli (storage and loss moduli, G' and G'') of photocrosslinked GelMA/bPE hydrogels with increasing DbPE and TbPE concentration, obtained from frequency sweeps at ω = 1.25 rad·s^{-1}. **(B)** Shear moduli (storage and loss moduli, G' and G'') of 5/20% GelMA/DbPE hydrogels incubated in different solvents prior and after photocrosslinking of the GelMA precursors, obtained from frequency sweeps at ω = 1.25 rad·s^{-1}. **(C)** Mass release in GelMA and GelMA/bPE hydrogels in DPBS at 37 °C over a period of 14 days (n = 3). **(D)** Mass swelling ratio taking into account the mass release within the first 24 h (n = 5). GelMA hydrogels are depicted in black, whereas GelMA/TbPE and GelMA/DbPE hydrogels are shown in red and blue, respectively. Data were presented as mean ± SD and statistically evaluated by one-way ANOVA. *, **, *** represent $p < 0.05$, 0.01, and 0.001, respectively.

After photocuring, the GelMA/bPE hydrogels displayed enhanced shear strength owing to the synergistic contributions of covalent network and electrostatic self-assemblies (**Figure 5-4A**). Precise tuning of shear properties could be achieved by variation in bPE loading, thus granting access to suitable matrices for a wide range of tissue substrates (e.g., ~300 Pa for brain, ~600 Pa for liver, ~2.5 kPa for kidney, 12-100 kPa for skeletal muscle, ~900 kPa for cartilage).[87] [88] Moreover, the electrostatic self-assemblies based on strongly interacting guanidinium and sulfonate moieties demonstrated excellent robustness of shear strength in physiological salt conditions (approx. 0.1 M NaCl), such as in Dulbecco's phosphate-buffered saline (DPBS) or Dulbecco's modified eagle's medium (DMEM). GelMA/bPE precursor solutions and hydrogels, however, were prone to highly salty environments (1 M NaCl) as a consequence of increasing charge screening, leading to the eventual breakdown of the PEC self-assemblies (**Figure 5-4B**). As shown in previous studies, the level of salt and pH responsiveness is dependent on the strength of the ionic pair of the bPEs (strong: guanidinium and sulfonate vs. weak: ammonium and carboxylate), thus providing a flexible platform for future design of adaptive hybrid hydrogels.[77] [89]

In addition, interlacing the electrostatically assembled bPEs with the covalent GelMA scaffold led to protection against indefinite swelling – a drawback typically faced by PEC hydrogels. When exposed to a solvent bath, the GelMA/bPE hydrogels swelled until they reached equilibrium within several hours. In order to check whether bPEs were kept inside or diffused out of the hydrogel, mass release during and after completion of swelling was monitored over a period of 14 days (**Figure 5-4C**). For both GelMA and hybrid hydrogels, an initial loss of material was expected attributed to the release of unfunctionalized gelatin chains as well as photoinitiator residues. Since

GelMA/TbPE hydrogels did not show any additional mass release, we concluded that the interpenetration of electrostatic and covalent networks prevented the escape of TbPEs. In contrast, high mobility of the disjointed micelles in GelMA/DbPE hydrogels resulted in their fast and almost complete release. Hence, the DbPE additives can be considered as a sacrificial scaffolding which temporarily improves material properties for 3D printing. Accounting for the respective mass loss within the first 24 hours, an "effective" swelling ratio was calculated. The hybrid hydrogels exhibited slightly reduced swelling properties (~ 30%) compared to the GelMA hydrogels (**Figure 5-4D**), attributable to a combination of increased polymer concentration, entanglements, and crosslink density in the hydrogels that limited network expansion and reduced swelling.

5.2.5 Biocompatibility of GelMA/bPE Bioinks

Among the numerous extrudable GelMA/bPE ink formulations, those with the lowest possible bPE concentration within the window of printability were chosen to reduce the exposure of cells to potentially toxic materials. Hence, we considered 7.5 wt% TbPEs and 20 wt% DbPEs as suitable polymer concentrations to supplement the GelMA ink in the following biocompatibility studies.

The addition of bPEs resulted in an almost negligible decrease in optical transparency, allowing for fluorescent cell staining and subsequent confocal microscopy (**Figure 5-5A, 5-S10**). Changes in the GelMA microstructure after photocrosslinking, which were induced by incorporation of the bPEs, were visualized by scanning electron microscopy (SEM) of the lyophilized hydrogel samples (**Figure 5-5A**). In the GelMA/DbPE hydrogel, the high PEC micelle content led to polymer accumulation around the GelMA pores, although, without influencing the micropore sizes significantly. In comparison, interpenetration with PEC network composed of TbPEs revealed a less uniform GelMA network structure with noticeable changes in pore size distribution.

Cytocompatibility of the bPEs and their complexes was evaluated in two- and three-dimensional (2D and 3D) toxicity studies using the human hepatocarcinoma cell line HepG2. HepG2 is a fast-growing cell line which is a well-established model system for liver cell function *in vitro* and shares many of the characteristics of primary hepatocytes, including metabolism and processing of xenobiotics.[90 91] A colorimetric assay for assessing metabolic activity (MTT) was conducted to determine viability of HepG2 cells, which were grown in 2D on standard cell culture plasticware and exposed to the bPEs for 72 hours (**Figure 5-5B**). bPEs were tested both in individual solutions (only sulfonate or guanidinium bPEs) and in the complexed state to investigate the impact of excess charge and macromolecular charge complexation on cell fate. As oppositely charged bPEs self-assemble into hydrogels even at concentrations as low as 5 wt%[78] and would have thus hindered diffusion and potential cellular uptake in the toxicity studies, a concentration of 0.5 wt% for the individual bPEs and 1 wt% for the oppositely charged complexes was chosen, that did not result in any apparent viscosity increase. The cytotoxicity of the bPEs was found to be highly dependent on the type of bPEs, with high survival rates for the sulfonate bPEs and complete cell death for the guanidinium bPEs (**Figure 5-5B**). This strikingly detrimental impact of positive charge on cell fate has been previously reported, especially in the context of cell penetrating peptides (CPP) rich in lysine or arginine. Their strong affinity to the negatively charged cell membrane as well as cellular internalization can cause cell membrane leakage and other toxic side effects.[92 93 94] However, upon the complexation of the positively and negatively charged bPEs, charge compensation led to remarkably increased cell viability (**Figure5- 5B**). Following self-assembly, the guanidinium groups were hypothesized to be primarily confined in the PEC domains, preventing interaction with the cells in the water-filled inter-domain space. We note that despite the use of identical polymer concentrations of DbPEs and TbPEs, their respective cytotoxicity

varied marginally due to their different chemical structure (i.e., varying lengths of the PEO block and the charged blocks).

Cytocompatibility of the hybrid hydrogels was further examined through a comparative biocompatibility study in 3D, where HepG2 cells were encapsulated in the hybrid hydrogels and cultured over a period of 14 days (**Figure 5-5D**). Live/dead staining revealed superior cell survival in DbPE-based hybrid hydrogels. Initial exposure of DbPEs resulted in moderate cell viability, however, the proportion of live cells progressively increased to > 60% over the period of cultivation. A substantial portion of the DbPE micelles escaped from the hybrid hydrogels upon incubation in the culture medium within 72 hours (**Figure 5-4C**), thus reducing both effective polymer concentration in the gel and exposure of embedded cells to the DbPEs, resulting in improved cell viability. Therefore, the DbPEs additive can be surmised to serve as a sacrificial scaffolding material in the hybrid gels. In contrast, a high cell death rate was observed in TbPE-based hybrid gels at day 1 post-encapsulation. TbPEs were more resistant against dilution due to presence of the interconnected nanoscale PEC network (not visible in SEM).[78 79 80 95] Limited space for cells and long-term exposure to TbPEs hence led to poorer cell viability initially. However, as network remodeling and enzymatic biodegradation of the gelatin scaffold proceeded, cells gained more space, resulting in strongly increased viability after 14 days (**Figure 5-5C and 5-5D**).

5.2.6 Extrusion-based 3D Bioprinting with GelMA/bPE Bioinks

The suitability of GelMA/bPE hybrid hydrogels as bioinks, beyond their rheological screening (**Figure 5-2A**), was validated in extrusion-based 3D printing (**Figure 5-6A**). First, cell-free hybrid inks with 5 wt% GelMA precursor solutions supplemented with increasing amounts of DbPEs and

TbPEs were extruded at 37 °C to create a grid that served as a model structure to evaluate printing performance (**Figure 5-6B**). As expected, the low viscosity GelMA ink was not printable at 37 °C. Increasing amounts of electrostatically self-assembling bPEs improved extrudability of the GelMA ink and shape fidelity after deposition, commensurate with expectations from the rheological screening.

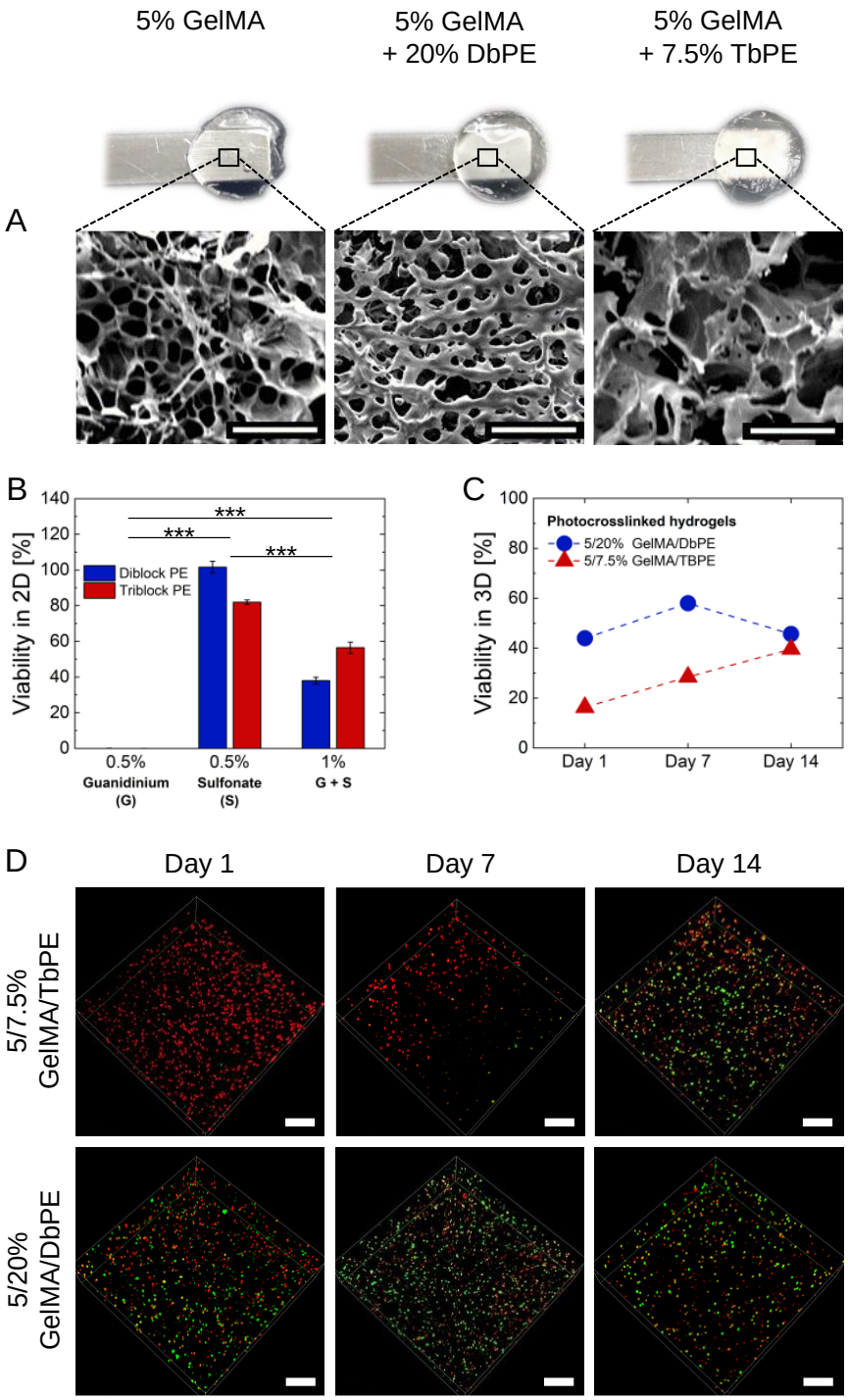

Figure 5-5. Biocompatibility studies in 2D and 3D of GelMA/bPE bioinks. **(A)** Photographs and scanning electron microscopy images of GelMA and GelMA/bPE hydrogels after

photocrosslinking (scale bar: 50 µm). **(B)** Cytotoxicity of DbPEs and TbPEs assessed by a MTT proliferation assay with HepG2 cells after 72 h exposure time (n = 6). Data were presented as mean ± SD and statistically evaluated by one-way ANOVA, wherein *** represents $p < 0.001$. **(D)** Live/dead staining of embedded HepG2 cells with calcein-AM (green, live cells) and propidium iodide (red, dead cells) 1, 7, and, 14 days post-encapsulation, followed by confocal microscopy (scale bar: 200 µm) and **(C)** cell viability analysis. Viability was determined by the percentage of live cells over the total cell count.

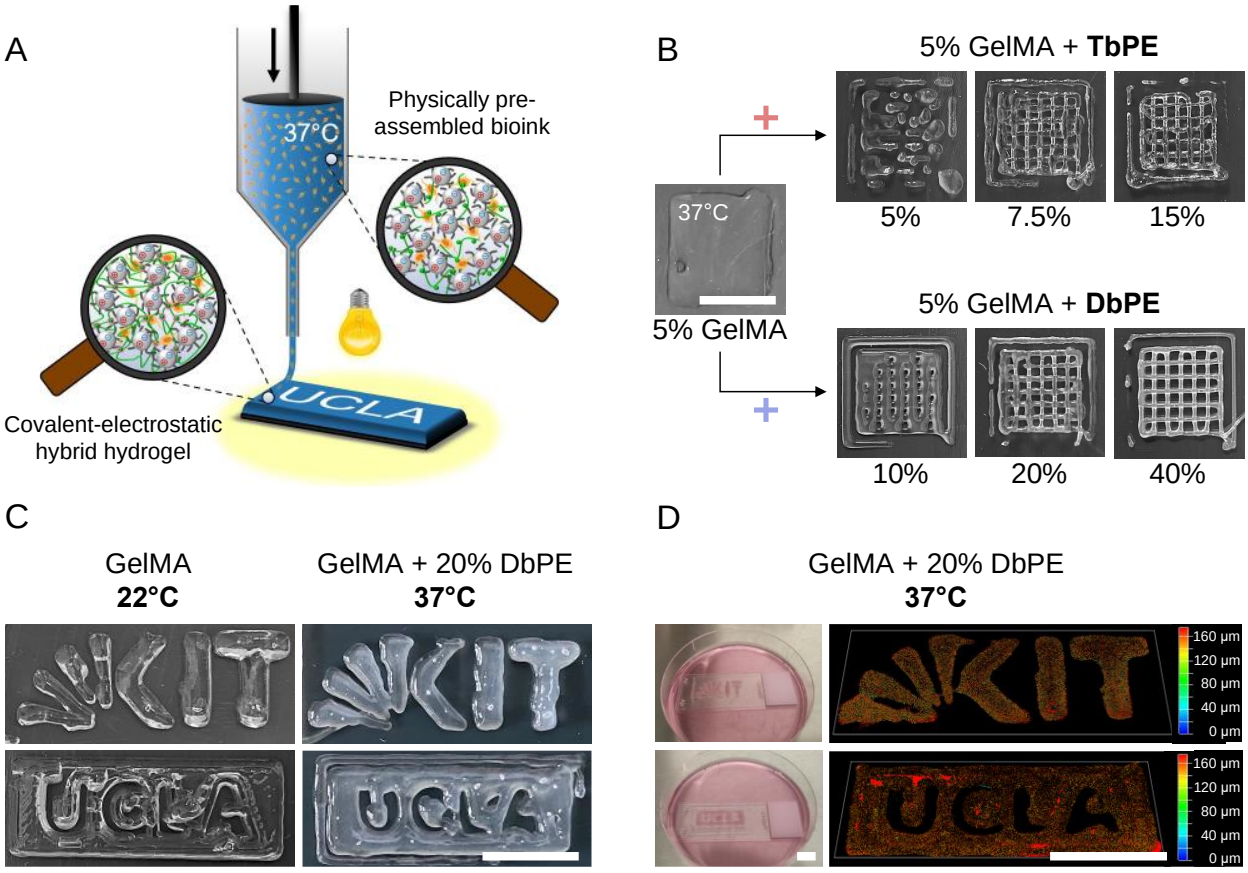

Figure 5- 6. Extrusion-based 3D bioprinting with GelMA/bPE ink formulations. **(A)** Schematic overview of employing GelMA/DbPE bioinks. **(B)** Shape fidelity of extruded grids (cartridge: 37 °C) using GelMA/TbPE and GelMA/DbPE inks with increasing bPE loading. **(C)** Performance comparison between GelMA at 22 °C and GelMA/DbPE inks at 37 °C when printing the KIT and UCLA logos. **(D)** Bioprinted HepG2 cells using GelMA/DbPE bioinks, followed by visualization of cell distribution along the z-axis (depth coding) after 7 days of cultivation (scale bar: 10 cm).

The printability of these hybrid hydrogel bioinks also emphasizes particularly the high accuracy of the rheological screening methodology. Ink compositions which were considered below the lower limit of printability according to rheology screening (i.e., 5 wt% GelMA + 10 wt% DbPE and 5 wt% GelMA + 5 wt% TbPE inks) turned out to be too fluid-like for printing and immediately started to flow and spread on the glass slide after deposition. The best resolution was achieved with the 5 wt% GelMA + 40 wt% DbPE gels; however, such high micelle concentration impeded with photochemical crosslinking of the GelMA precursor, thus leading to reduced crosslink density and loss of structural integrity during swelling. When comparing the two types of bPE additives, we observed that GelMA/DbPE formulations benefited from higher ink homogeneity during extrusion. Although both additives promoted fiber formation, printing of the GelMA/TbPE ink turned out to be less consistent with several fiber breaks during extrusion. Since these inhomogeneities persisted over a wide range of different extrusion rates, we attribute this to the challenge of extruding highly interconnected TbPE networks through a small orifice.

Considering the results from the extrusion screening as well as the better biocompatibility of the DbPE additive, we selected the 20 wt% DbPE composition for further cell-based 3D printing experiments (**Figure 5-6A**). Bioinks were prepared by suspending HepG2 cells in GelMA and GelMA/DbPE precursor solutions and were subsequently held in the cartridge until their respective printing temperature (22 °C or 37 °C) was reached. The achievable resolution in 3D bioprinting was found to be very similar for the GelMA ink at 22 °C and for the hybrid ink at 37 °C, as exemplified by printing the two logos of the collaborating universities (**Figure 5-6C, Movies 5-SM1 and 5-SM2**). Moreover, as gelation of the GelMA ink does typically not happen instantaneously upon cooling (~ 20 min), cells could potentially sink and accumulate at the bottom of the cartridge, resulting in inhomogeneous cell distribution in the printed construct. In the hybrid

inks, the high viscosity and the high yield stress of the ink, both of which are attained nearly instantaneously after mixing of the polymeric components, prevented cell sedimentation in the cartridge during temperature modulation (analogous to the herbs in the "Italian dressing"). Therefore, bioprinted HepG2 cells displayed a very homogeneous cell distribution along the z-axis in the extruded hybrid hydrogels as a result of immediate pre-gelation in the cartridge as well as provision of adhesion sites (RGD) by the gelatin biopolymer (**Figure 5-6D**). Our approach, based on electrostatic self-assembly, hence exceled by requiring only a single crosslinking step in the end and addressed current shortcomings faced by the GelMA ink, particularly long holding times in the cartridge for cooling and inhomogeneous cell distribution in the inks, inefficient temperature transfer from the print bed to the top layers of the deposited ink, and discontinuous fabrication accompanied by stacking of disjointed layers.

5.3 Conclusions

In summary, we have demonstrated a facile approach based on complex-forming and viscoelasticity enhancing bPEs to render very liquid-like bioinks applicable for extrusion-based 3D bioprinting at a physiological temperature (37 °C). Swift self-assembly of oppositely charged bPEs was harnessed to lend initial structural robustness to photocurable precursor solutions, improve their extrudability as well as post-printing recovery, and support inter-layer adhesion in the printed structures. This, to the best of our knowledge, is the first demonstration of harnessing electrostatic self-assembly of block polyelectrolytes to create a scaffolding for cell-containing bioinks. Depending on the chemical composition, bPEs were able to either provide long-term tensile strength to the hydrogel by interpenetration of the covalent network or serve as sacrificial micellar additives, which were quickly removed by diffusion post-printing. Further improvements in the already satisfactory biocompatibility of the PEC hydrogels are envisioned by varying the

lengths of the neutral and the charged blocks and the nature of the charged moieties as well as incorporation of enzyme- or photocleavable sites along the PEO backbone. Additional physico-mechanical features provided by the PEC network, such as tunable shear moduli and salt responsiveness, enabled the flexible platform to meet the increasing demands on advanced materials for biomedical applications and tissue engineering. Our pioneering approach based on electrostatic self-assembly of bPEs thus represents a competitive alternative to state-of-the-art approaches of temperature-induced pre-gelation, mitigating their drawbacks and offering new perspectives for future bioink design. Since any aqueous biopolymer solution – especially those which are currently not extrudable due to their liquid-like properties – can be supplemented with bPEs, the strategy demonstrated here excels by its unique versatility and feasibility.

5.4 Experimental Section

Materials: Potassium (99.5% trace metals basis), naphthalene, poly(ethylene glycol) (M_n = 20,000 g mol^{-1}), poly(ethylene glycol) monomethyl ether (M_n = 5,000 g mol^{-1}), allyl glycidyl ether (AGE), calcium hydride, sodium 3-mercapto-1-propanesulfonate (technical grade, 90%), 1H-pyrazole-1-carboxamidine hydrochloride (99%), cysteamine hydrochloride (≥ 98%), gelatin (type A, gel strength ~300 g bloom, from porcine skin), methacrylic anhydride, propidium iodide, 2,2-dimethoxy-2-phenylacetophenone (DMPA), and Irgacure 2959 were purchased from Sigma-Aldrich. Lithium phenyl(2,4,6-trimethylbenzoyl)phosphinate (LAP) was obtained from TCI Deutschland. Tetrahydrofuran (THF) and dimethylformamide (DMF) were purchased from Fisher Scientific. DPBS$^{-/-}$, DMEM, fetal calf serum (FCS), penicillin-streptomycin (10 000 U mL^{-1}), trypsin-EDTA (0.05%), phenol red, calcein-AM were purchased from Thermo Fisher Scientific. The CellTiter 96 non-radioactive cell proliferation assay (MTT) was provided by Promega.

Dialysis tubes were obtained from VWR International and Fisher Scientific. The human hepatocarcinoma cell line HepG2 was received from PromoCell.

Block Polyelectrolyte Synthesis: *Triblock Polyelectrolyte Synthesis*: Guanidinium and sulfonate functionalized poly(ally glycidyl ether)-*b*-poly(ethylene glycol)-*b*-poly(ally glycidyl ether) (PAGE-PEO-PAGE) were synthesized following previously published protocols.[77] Poly(ethylene glycol) (PEO, M_n = 20,000 g mol^{-1}) was dried in a vacuum oven at 25 °C for one day before use. Allyl glycidyl ether (AGE) was mixed with calcium hydride, stirred overnight to remove trace amounts of water, and degassed by three cycles of freeze-pump-thaw, followed by distillation. All anhydrous reagents were transferred inside a glove box with argon. An appropriate amount of PEO was dissolved in 50 mL anhydrous THF and titrated with potassium naphthalenide (0.4 M in anhydrous THF) until the solution turned light green. Then, AGE was added, and the reaction mixture was stirred at 45 °C for 48 h. The anionic polymerization was terminated by addition of degassed methanol. The product PAGE-PEO-PAGE was precipitated in hexane, filtered, and dried under vacuum prior to further functionalization. The degree of polymerization of the PAGE blocks was calculated from the relative peak intensities in the NMR spectra, yielding $PAGE_{30}$-PEO_{455}-$PAGE_{30}$.

For post-functionalization via thiol-ene click chemistry, $PAGE_{30}$-PEO_{455}-$PAGE_{30}$, photoinitiator 2,2-dimethoxy-2-phenylacetophenone (DMPA) and a functional thiol reagent (cysteamine hydrochloride or sodium 3-mercapto-1-propanesulfonate, 5 equiv. per alkene group) were dissolved in a DMF/water (1:1) mixture. The solution was degassed with nitrogen and then exposed to UV light (365 nm, 8 W) for at least 6 h. The product solutions of $PAGE_{30}$-PEO_{455}-$PAGE_{30}$ functionalized with either ammonium or sulfonate moieties were dialyzed (MWCO: 3.5 kDa) against deionized water for 10 cycles of 8 h each, followed by lyophilization.

Guanidinilated $PAGE_{30}$-PEO_{455}-$PAGE_{30}$ was obtained by dissolving an appropriate amount of the ammonium functionalized block copolymer and 1H-pyrazole-1-carboxamidine in phosphate-buffered saline (PBS) solution. After adjusting the pH to 10 with NaOH, the reaction mixture was stirred for 3 days at room temperature. The product solution was dialyzed (MWCO: 3.5 kDa) against deionized water for 10 cycles of 8 h each, followed by lyophilization.

Diblock Polyelectrolyte Synthesis: DbPEs were prepared and functionalized following the same protocol used for the TbPE synthesis except for replacing the initiator PEO with poly(ethylene glycol) monomethyl ether (M_n = 5,000 g mol^{-1}). ^{1}H NMR spectra of all block copolymers prior and after functionalization are provided in the supplementary information (**Figure 5-S2 and 5-S4**).

Gelatin Methacryloyl Synthesis: GelMA was synthesized following previously published protocols.[58 53] 10 g gelatin (type A, gel strength ~300 g bloom, from porcine skin, 0.266 mmol NH_2 groups, 1 equiv.) was dissolved in 100 mL DPBS. The solution was heated to 50 °C until complete dissolution of gelatin. Then, 3.17 mL methacrylic anhydride (2.13 mmol, 8 equiv.) was added dropwise and the mixture was stirred at 50 °C for 2 h, followed by dilution with 100 mL DPBS. The solution was transferred into dialysis tubes (MWCO: 12-14 kDa) and dialyzed against deionized water at 40 °C for 12 cycles of 8 h each. After lyophilization, the product was obtained as a white solid and stored at −20 °C.

^{1}H NMR (400 MHz, D_2O, 315 K, δ): 7.60-7.40 ($H_{aromtic}$, gelatin), 5.88 (1H, H_a, vinyl), 5.64 (1H, H_b, vinyl), 5.24-0.99 (gelatin), 3.20 (bs, 2H, NH_2), 2.11 (s, 3H, CH_3, H_c).

Preparation of GelMA/bPE Hydrogels: Stock solutions of the block polyanion (sulfonate functionalized bPEs), block polycation (guanidinium functionalized bPEs), GelMA precursor, and photoinitiator Irgacure 2959 or LAP were prepared in DBPS. GelMA/DbPE and GelMA/TbPE

hydrogels were prepared by mixing the block polyanion with an aqueous solution of GelMA precursor and photoinitiator, followed by the addition of the block polycation. Each addition step was followed by thorough mixing to ensure homogeneity of the sample. The bPEs were mixed in proportion such that the molar charge ratio of cationic and anionic moieties was 1:1.

Rheology: Rheological measurements were performed on an Anton Paar MCR 302 rheometer (Anton Paar, Torrance, USA) using a cone-and-plate geometry (diameter: 10 mm, cone angle: 2°) for precursor solutions and a parallel plate geometry (diameter: 8 mm, gap size: 0.6 mm) for photocrosslinked hydrogels. Hydrogels were prepared by pipetting 75 µL in a cylindrical polydimethylsiloxane (PDMS) mold (diameter: 8 mm, height: 1.5 mm), followed by UV light exposure for 5 min (302 nm, 8 W). For the rheological characterization, the hydrogel slab or an appropriate amount of precursor solution was placed on the lower plate. Excess sample volume of the precursor solution was trimmed after reaching the measuring gap between cone and plate. A solvent trap was employed to minimize water evaporation. Rheology data was acquired at 22 °C for the GelMA precursor and at 37 °C for GelMA/bPE formulations and hydrogels. All samples were pre-sheared by employing an oscillatory shear γ = 100% for 30 s, followed γ = 1% for 5 min to reach steady state. Amplitude sweeps (**Figure 5-S6 and 5-S7**), with a strain amplitude γ ranging from 0.01-100%, were carried out at a frequency ω = 1 rad·s^{-1} to assess the linear viscoelastic (LVE) regime. Frequency sweeps (ω = 0.1-20 rad·s^{-1}) were performed at γ = 1% (within the LVE regime), leading to the frequency-dependent shear moduli G' and G'' (**Figure 5-S6 and 5-S7**) and the oscillatory complex viscosity. Shear-thinning behavior was quantified by fitting the linear region of the angular frequency-complex viscosity plot with the power law model (**Figure 5-S9**). A shear stress ramp ranging from 1-1000 Pa was applied to all precursor solutions to determine the yield point. In the shear stress-viscosity diagram, the flow initiation point was computed by

the intersection point between two linear regressions at the plateau-region and the viscosity-drop region (**Figure 5-S8**). Rotational recovery measurements were conducted to simulate the recovery behavior post-extrusion by applying a high shear rate at 100 s^{-1} for 250 s, followed by a low shear rate of 0.01 s^{-1} for 500 s.

Tensile Test: Tensile properties of GelMA, GelMA/DbPE and GelMA/TbPE hydrogels were characterized by an Instron 5542 tensile tester. 120 µL precursor solution was pipetted into a rectangular PDMS mold (18 mm × 4.5 mm × 1.5 mm) and exposed to UV light (302 nm, 8 W) for photocrosslinking. The hydrogel samples were affixed to the machine tension grips with double-sided tape and stretched with an extension rate of 6 mm min^{-1}. Ultimate stress was the maximum stress that a hydrogel sample could withstand before fracture, and its corresponding strain indicated its extensibility. Young's modulus was determined by computing the slope of the linear region of the stress-strain curves (**Figure 5-S12**). Toughness was calculated by integrating the area under the stress-strain curve, wherein the strain is unitless.

Release Study: Mass release of GelMA, GelMA/DbPE and GelMA/TbPE hydrogels was monitored over a period of 14 days. 200 µL precursor solution was pipetted onto a PDMS surface and photocrosslinked by UV light irradiation (302 nm, 8 W). Following lyophilization, dry weight was measured, and samples were incubated in DPBS at 37 °C. The DPBS solution was exchanged every 2-3 days. After 0, 1, 2, 4, 7, 10, and 14 days, hydrogel samples were lyophilized and weighed after carefully removing residual water from the surface. The remaining mass was calculated from the following equation, where w_i is the initial dry weight and w_t is the dry weight at time t.

$$Remaining\ mass\ [\%] = \frac{w_t}{w_i} \times 100\% \quad (1)$$

Mass Swelling Ratio: 60 µL precursor solution of GelMA, GelMA/DbPE and GelMA/TbPE was pipetted into a cylindrical PDMS mold (diameter: 5 mm, height: 3 mm) and photocrosslinked by UV light irradiation (302 nm, 8 W). The hydrogel pads were swollen in DBPS for 24 h at room temperature and weighed after carefully removing residual water from the surface. Then, the samples were lyophilized, and dry weight was measured. Mass swelling ratio – taking into account the mass release within the first 24 h – was calculated from the following equation, where $w_{swollen}$ is the weight after complete swelling, and w_{dry} is the weight after lyophilization.

$$Mass\ swelling\ ratio = \frac{w_{swollen}}{w_{dry}} \tag{2}$$

Scanning Electron Microscopy: 60 µL precursor solution of GelMA, GelMA/DbPE and GelMA/TbPE was pipetted into a cylindrical PDMS mold (diameter: 5 mm, height: 3 mm) and photocrosslinked by UV light irradiation (302 nm, 8 W). Then, the hydrogel pads were frozen with liquid nitrogen and cut with a razor blade to reveal their cross-section. The frozen hydrogel slabs were attached to a SEM pin mount holder with a double-sided conductive tape, followed by lyophilization. After sputtering the specimen surface with gold, pore size and morphology was characterized by SEM microscopy (Nova 230 NanoSEM, FEI company, Hillsboro, USA). All images were taken using an acceleration voltage of 5-10 kV and a secondary electron detector.

MTT Cell Viability Assay: HepG2 cells were seeded at a density of 1×10^4 cells per well (1×10^5 cells·mL^{-1}) in a 96-well plate. After 24 h, cell culture medium was removed, and cells were treated with 0.5 wt% (individual solution) or 1 wt% (complexed state) of guanidinium and sulfonate functionalized bPEs. For the positive and negative controls, media was exchanged without addition of any test compound. After incubation for 72 h (37 °C, 5% CO_2), positive controls were treated with 5 µL Triton X-100 (20% v/v). Then, 15 µL of the yellow MTT reagent was added to each

well, followed by incubation for 3 h. The reaction was stopped by addition of 100 µL lysis buffer. The next day, absorption was measured at 595 nm with the SpectraMax ID5 microplate reader (Molecular Devices LLC, San José, USA). Cell viability for each test compound was determined, wherein a viability of 0% and 100% was assigned to the positive and negative controls, respectively.

Cell Encapsulation: For cell encapsulation, stock solutions of 20 wt% GelMA precursor, 70 wt% DbPEs, 20 wt% TbPEs, and 6 wt% of photoinitiator LAP in DPBS were used. GelMA/bPE hydrogels were prepared following the protocol described above. Importantly, HepG2 cell suspension (2,5 x 10^6 cells·mL^{-1}) was added prior to addition of the oppositely charged bPEs to ensure homogenous mixing (sequence of addition: block polyanion, GelMA precursor, LAP, cell suspension, and block polycation). 200 µL of the cell-laden precursor solution with 0.3 wt% LAP was transferred to each well of an ibidi µ-slide, followed by photochemical crosslinking (320-500 nm, 500 mW cm^{-2}) for 60 s using the Omnicure S2000 curing system (*igb-tech* GmbH, Friedelsheim, Germany). Then, the hydrogels were transferred to a 24-well plate, covered with 1 mL DMEM and cultured over a period of 14 days (37 °C, 5% CO_2). Media was exchanged every 2-3 days.

Live/Dead Staining: Cell viability of embedded HepG2 cells was monitored by live/dead staining 1, 7, and 14 days post-encapsulation. The supernatant media was removed, and cells were stained with calcein-AM (4 µg mL^{-1}) and propidium iodide (20 µg mL^{-1}). After incubation for 30 min, the staining solution was removed. Hydrogels were washed twice with DPBS and covered with cell culture medium. Confocal microscopy (Leica Stellaris 5, Leica Microsystems GmbH, Wetzlar, Germany) was used to record *z*-stacks of 300 µm thickness (step size: 5 µm), which were

converted into 3D images with LasX software. Cell viability was calculated from the percentage of live cells over the total cell count.

Extrusion-Based 3D Bioprinting: For 3D bioprinting, an extrusion-based 3D printer (BioSpot BP, Biofluidix GmbH, Freiburg, Germany) equipped with a cooling system, syringe (Injekt Luer Lock Solo, VWR, Bruchsal, Germany), and a dispensing nozzle (cone, diameter: 0.25 mm, Vieweg GmbH, Kranzberg, Germany) was used. Cell-loaded (2.5×10^6 cells·mL^{-1}) precursor solutions (bioinks) were prepared in a 2 mL syringe following the protocol described above. The temperature of the bioinks was set to either 37 °C for GelMA/bPE inks or 22 °C for the GelMA ink and hold for 30 min prior to extrusion. In order to support fast structural recovery upon deposition, adhesive glass slides were cooled to 17 °C. G-codes were written for different model structures, including grid (12 mm × 12 mm), university logos (10 mm × 26 mm), and a hollow square structure of 11 uncrosslinked layers (6 mm × 6 mm). 3D printing was performed at an average extrusion rate of 0.02 mm·s^{-1} and a print speed of 5 mm·s^{-1}, followed by photochemical crosslinking (320-500 nm, 500 mW cm^{-2}) for 60 s using the Omnicure S2000 curing system (*igb-tech* GmbH, Friedelsheim, Germany). The printed structures on the glass slide were washed with DPBS, transferred to a petri dish, and covered with 10 mL DMEM for further cultivation.

Data Analysis and Statistics: Data analysis and statistics were carried out using OriginPro 2021. All data are presented as mean ± standard deviation (SD). Unless stated otherwise, the value of *n* is defined as the number of repeat attempts performed. A two-sample independent Student's *t*-test was conducted when two average values were compared. If more average values needed to be compared, one-way analysis of variance (ANOVA) with Bonferroni correction was carried out across groups. In all cases, significance was defined as $p < 0.05$ ($^*p < 0.05$, $^{**}p < 0.01$, and $^{***}p < 0.001$).

5.5 Supplementary Information

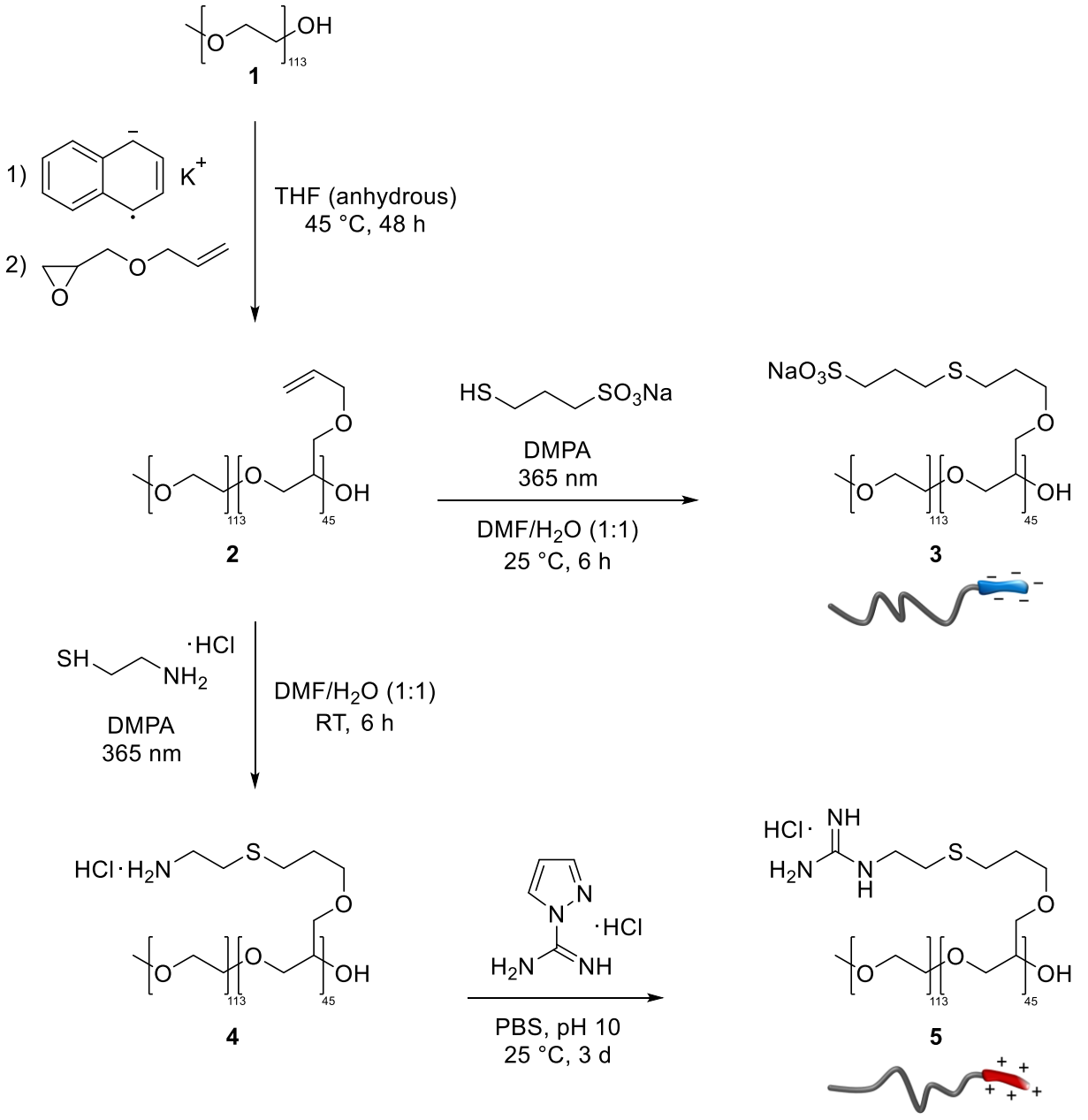

Figure 5-S1. Synthesis of diblock polyelectrolytes. Synthesis of the diblock copolymer precursor **2** ($mPEO_{113}$-$PAGE_{45}$) from poly(ethylene glycol) monomethyl ether by ring-opening anionic polymerization and subsequent functionalization of the PAGE blocks using thiol-ene click

chemistry, yielding oppositely charged AB diblock copolyelectrolytes with **3** (sulfonate), **4** (ammonium), and **5** (guanidinium) moieties.

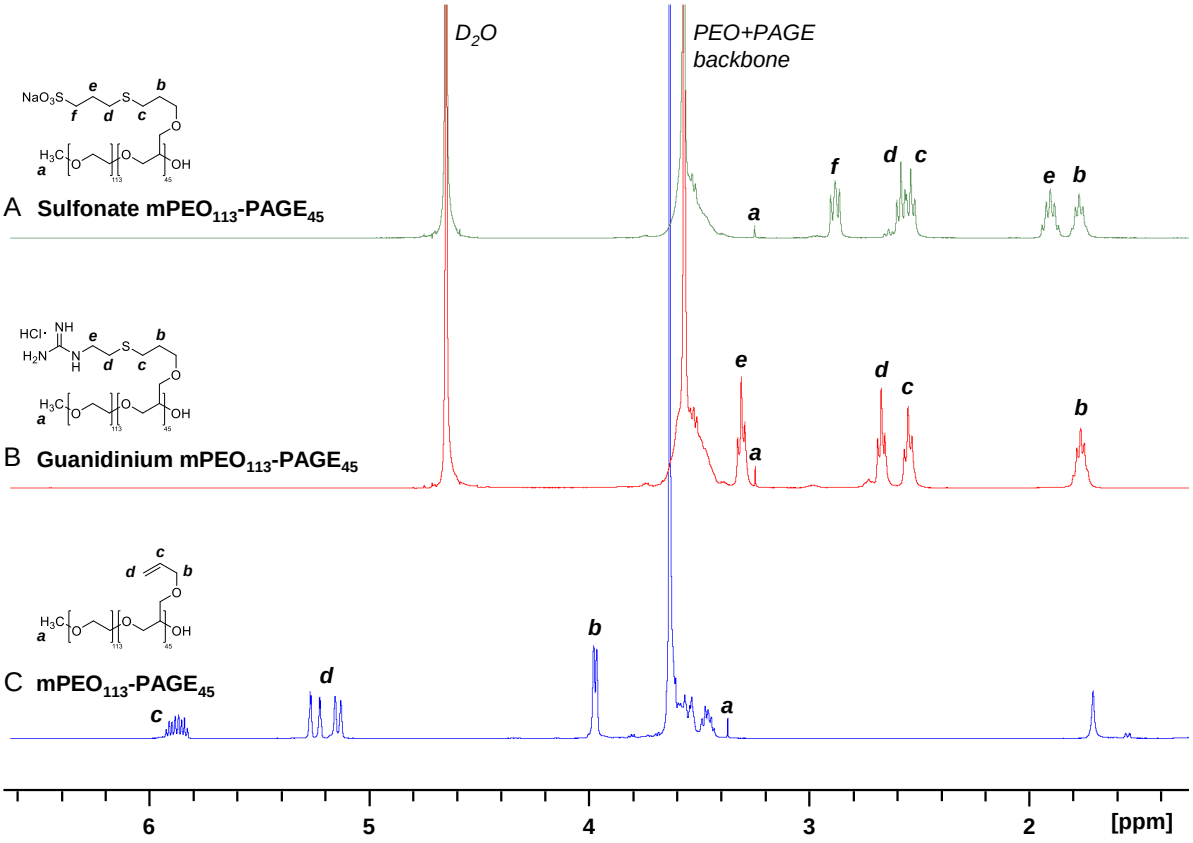

Figure 5-S2. ^{1}H NMR spectra (400 MHz) of diblock copolyelectrolytes **(A)** sulfonate functionalized $mPEO_{113}$-$PAGE_{45}$, **(B)** guanidinium functionalized $mPEO_{113}$-$PAGE_{45}$ in D_2O, and **(C)** $mPEO_{113}$-$PAGE_{45}$ precursor in $CDCl_3$ prior to functionalization.

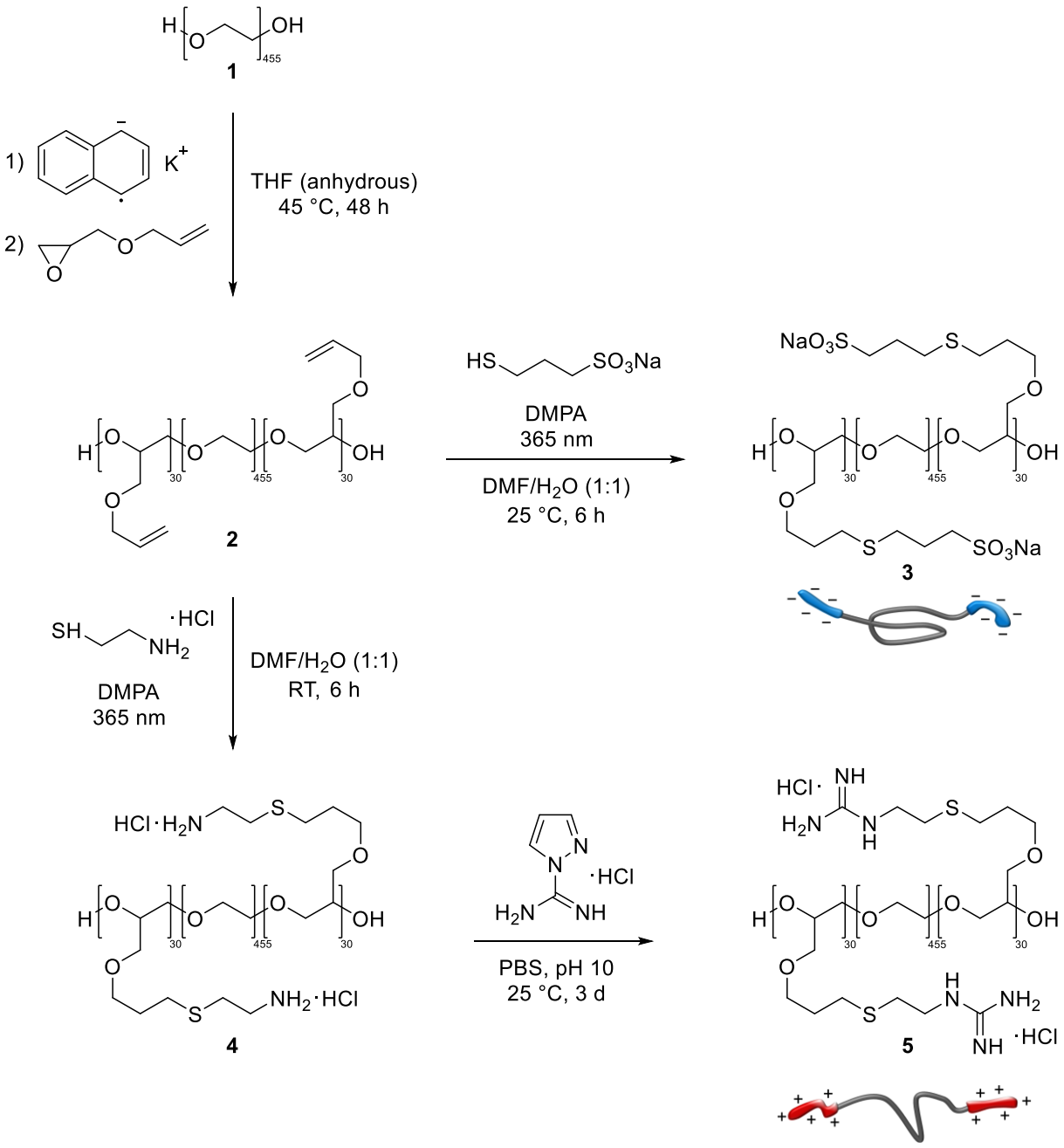

Figure 5-S3. Synthesis of triblock polyelectrolytes. Synthesis of the triblock copolymer precursor **2** ($PAGE_{30}$-PEO_{455}-$PAGE_{30}$) from poly(ethylene glycol) by ring-opening anionic polymerization and subsequent functionalization of the PAGE blocks using thiol-ene click chemistry, yielding

oppositely charged ABA triblock copolyelectrolytes with **3** (sulfonate), **4** (ammonium), and **5** (guanidinium) moieties.

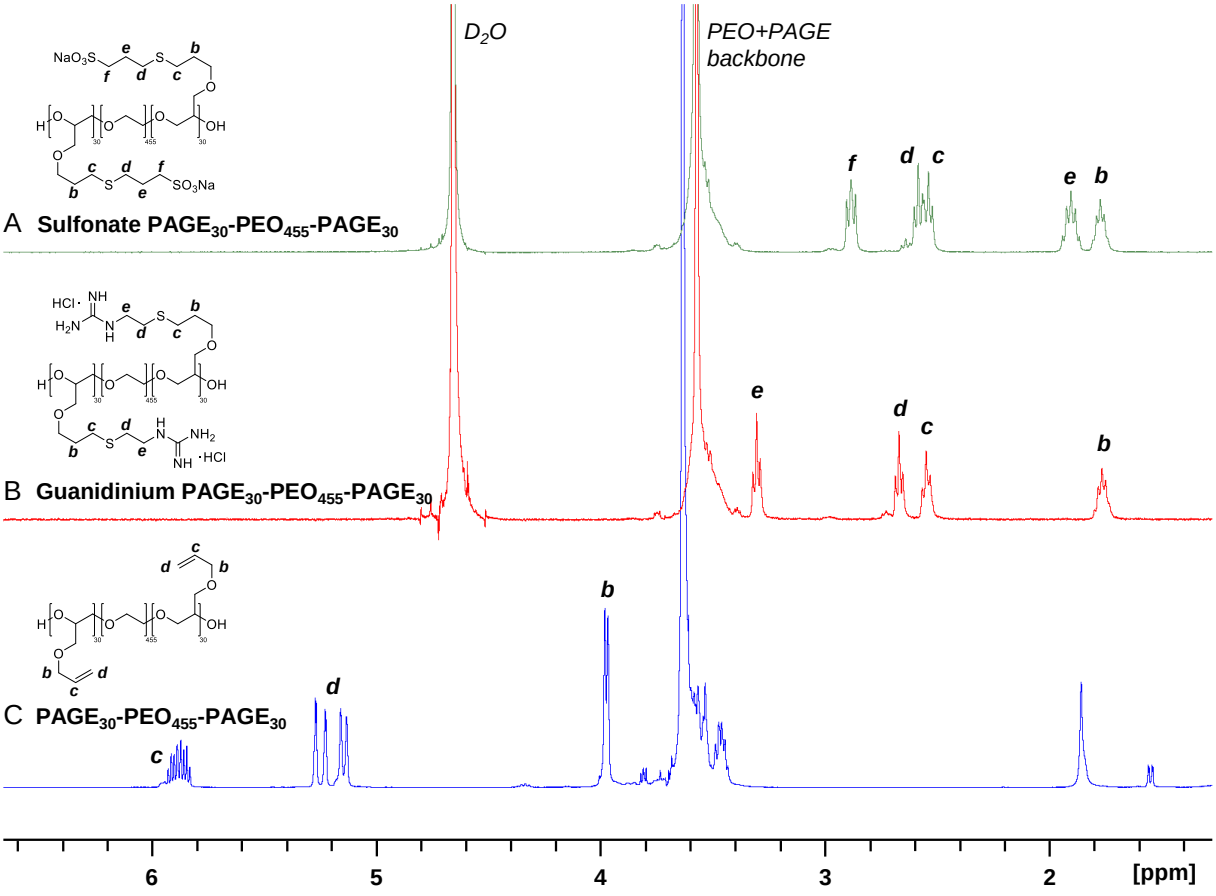

Figure 5-S4. ^{1}H NMR spectra (400 MHz) of triblock copolyelectrolytes: **(A)** sulfonate functionalized $PAGE_{30}$-PEO_{455}-$PAGE_{30}$, **(B)** guanidinium functionalized $PAGE_{30}$-PEO_{455}-$PAGE_{30}$ in D_2O, and **(C)** $PAGE_{30}$-PEO_{455}-$PAGE_{30}$ precursor in $CDCl_3$ prior to functionalization.

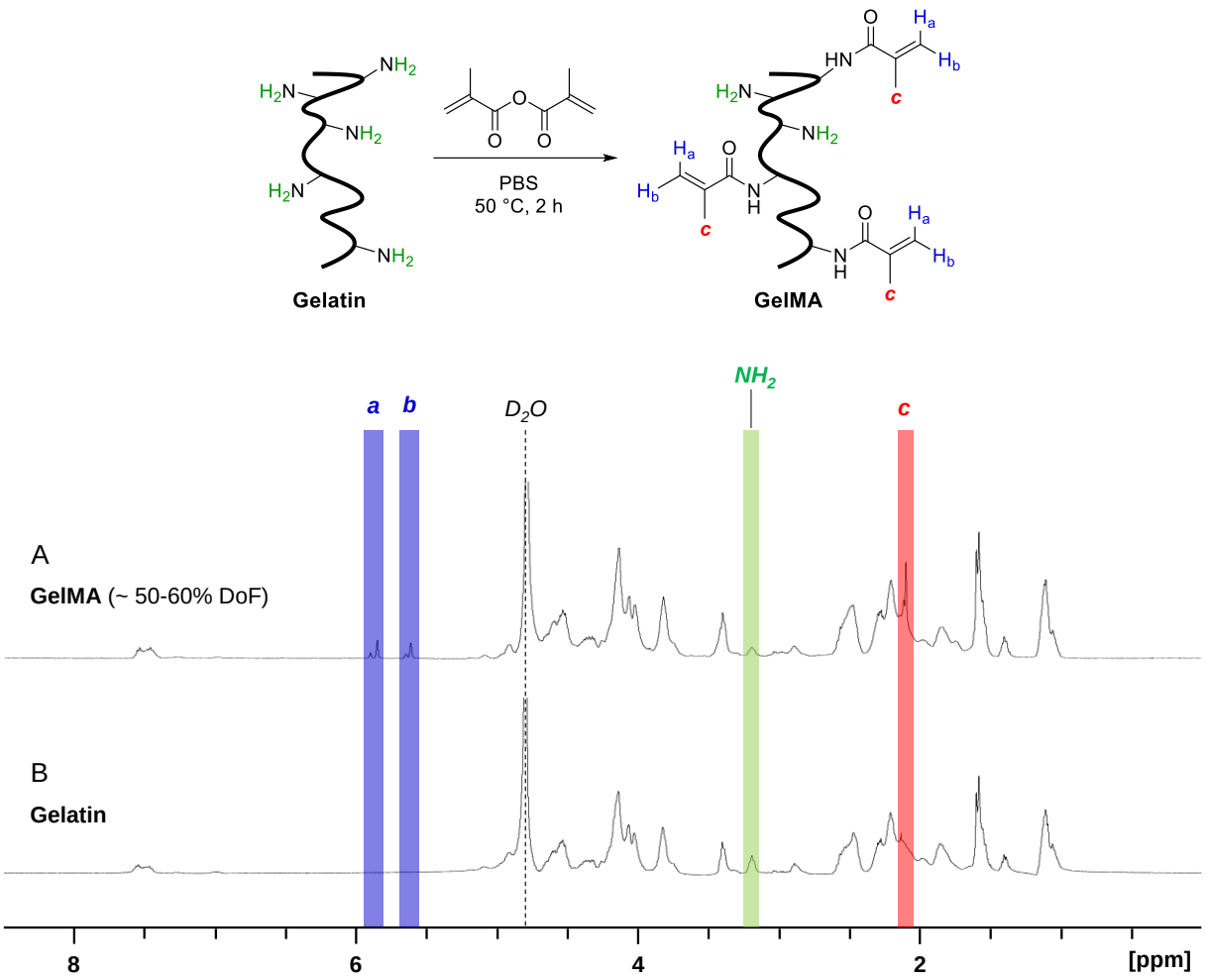

Figure 5-S5. ^{1}H NMR spectra (400 MHz, D_2O, 315 K) of **(A)** GelMA hydrogel precursor and **(B)** unmodified gelatin.

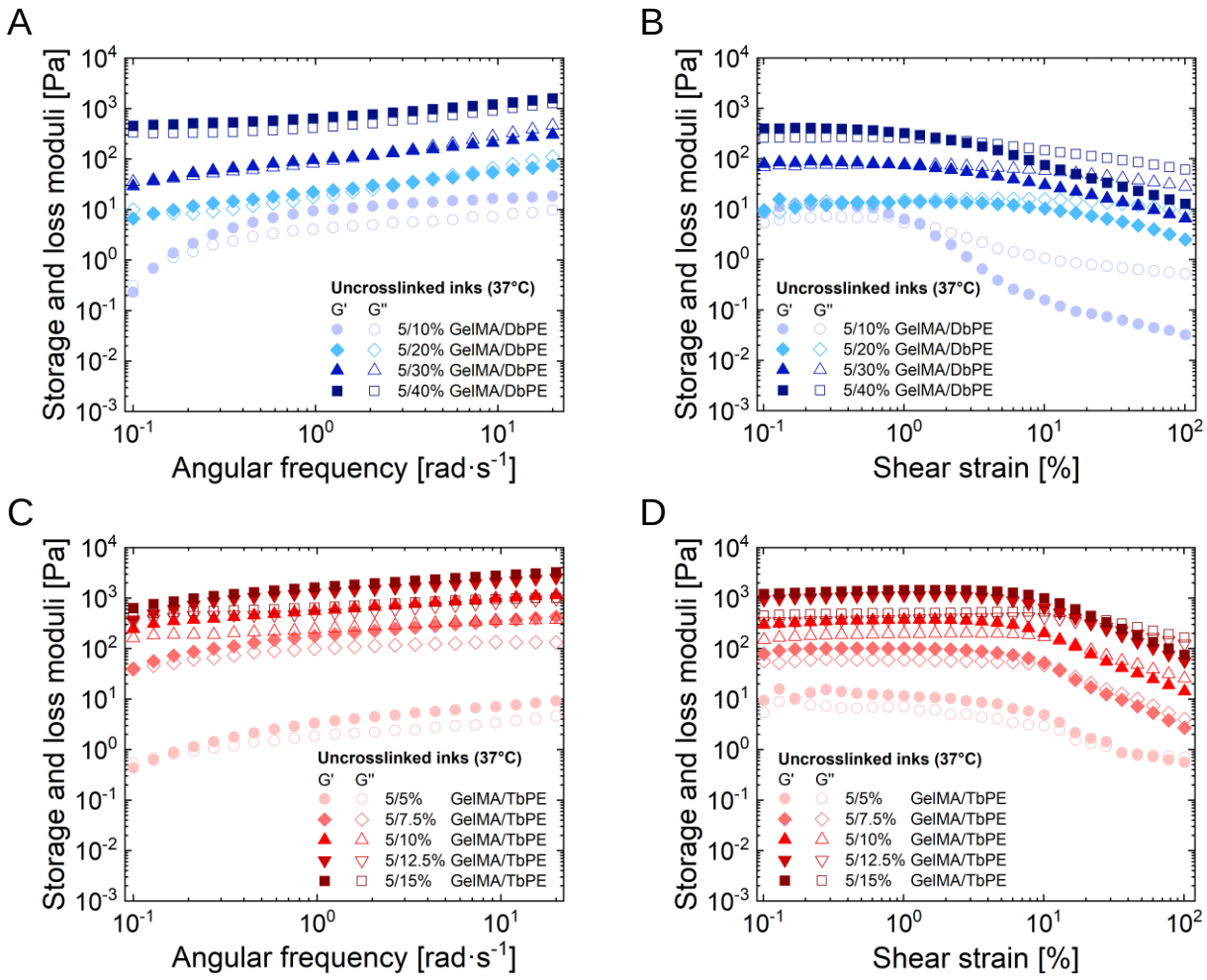

Figure 5-S6. Frequency sweeps and amplitude sweeps of **(A-B)** GelMA/DbPE and **(C-D)** GelMA/TbPE precursor solutions with increasing bPE concentration at 37 °C. Storage (G') and loss (G'') moduli are depicted as a function of (A,C) angular frequency ω and (B,D) shear strain γ. A strain of γ = 1% (within the LVE region) was selected to perform the frequency sweeps.

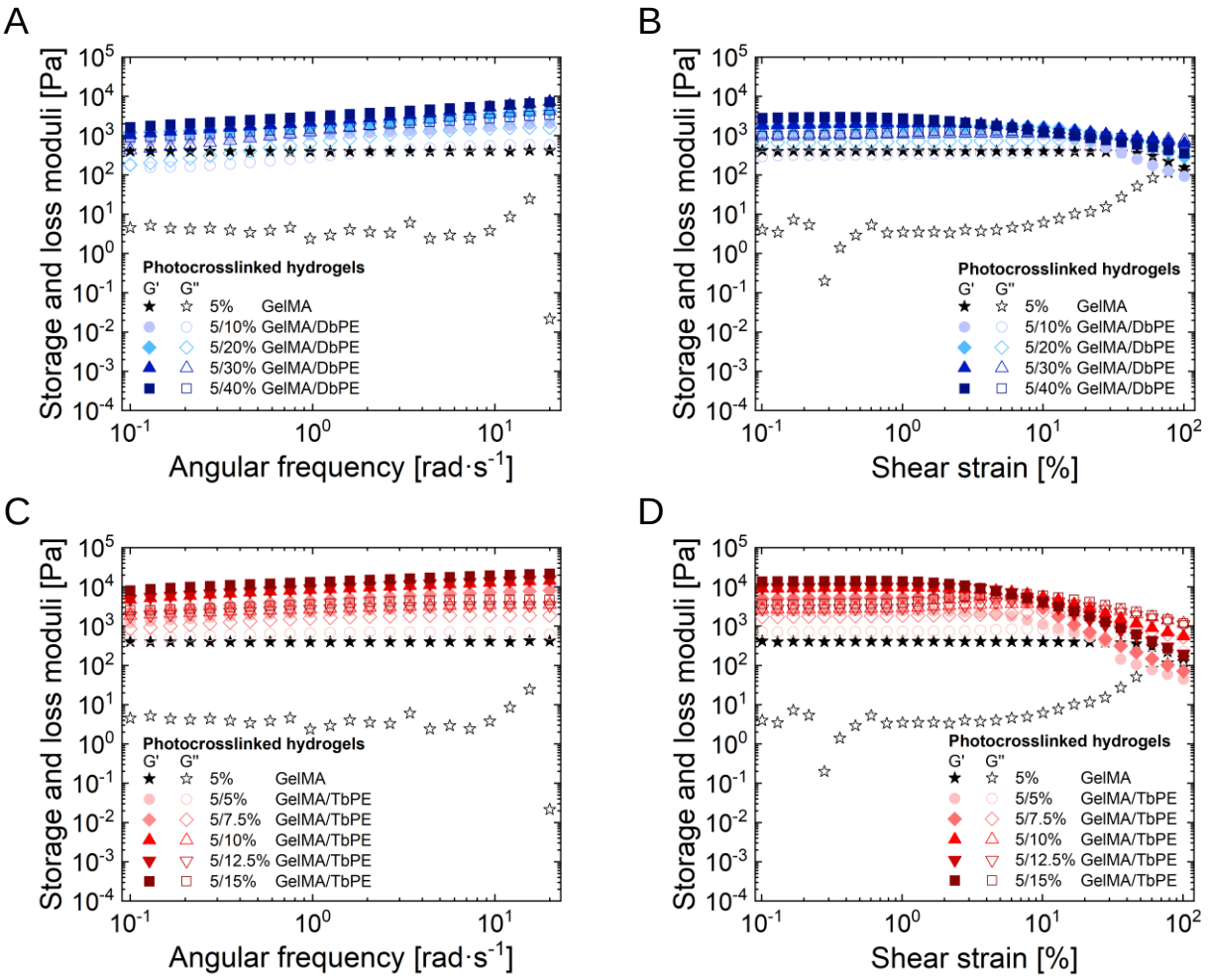

Figure 5-S7. Frequency sweeps and amplitude sweeps of photocrosslinked **(A-B)** GelMA/DbPE and **(C-D)** GelMA/TbPE hydrogels with increasing bPE concentration at 37 °C. Storage (G') and loss (G'') moduli are depicted as a function of (A,C) angular frequency ω and (B,D) shear strain γ. A strain of γ = 1% (within the LVE region) was selected to perform the frequency sweeps.

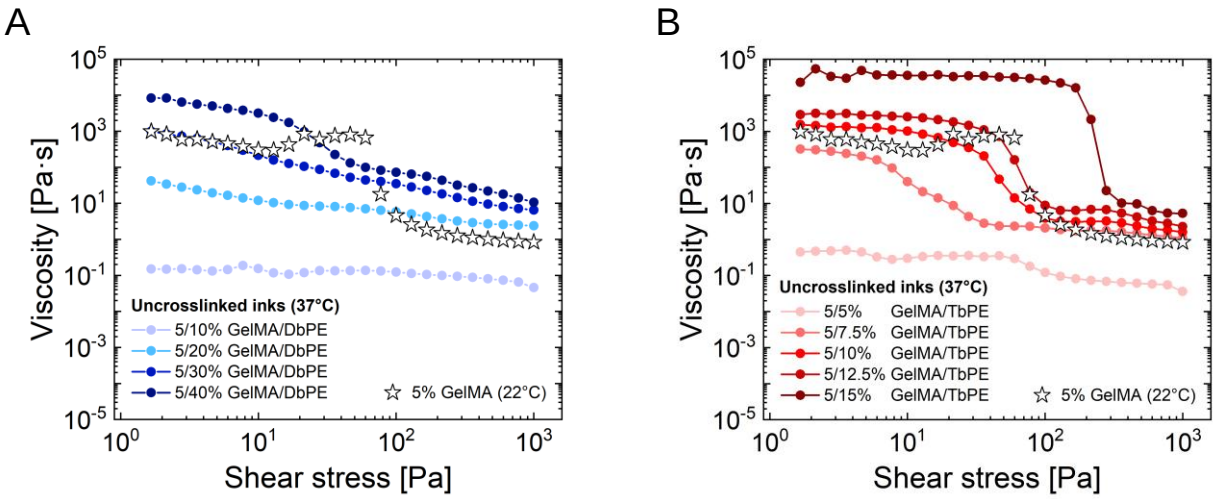

Tangent intersection	Yield stress [Pa]
5/10% GelMA/DbPE	–
5/20% GelMA/DbPE	–
5/30% GelMA/DbPE	–
5/40% GelMA/DbPE	15
5% GelMA (22°C)	60

Tangent intersection	Yield stress [Pa]
5/5% GelMA/TbPE	–
5/7.5% GelMA/TbPE	5.7
5/10% GelMA/TbPE	26
5/12.5% GelMA/TbPE	40
5/15% GelMA/TbPE	185
5% GelMA (22°C)	60

Figure 5-S8. Stress ramp profiles for **(A)** GelMA/DbPE and **(B)** GelMA/TbPE precursor solutions with increasing bPE concentration at 37 °C and GelMA ink without bPEs at 22 °C. Yield stress was determined using the tangent intersection method. Values of yield stress are given in the table below.

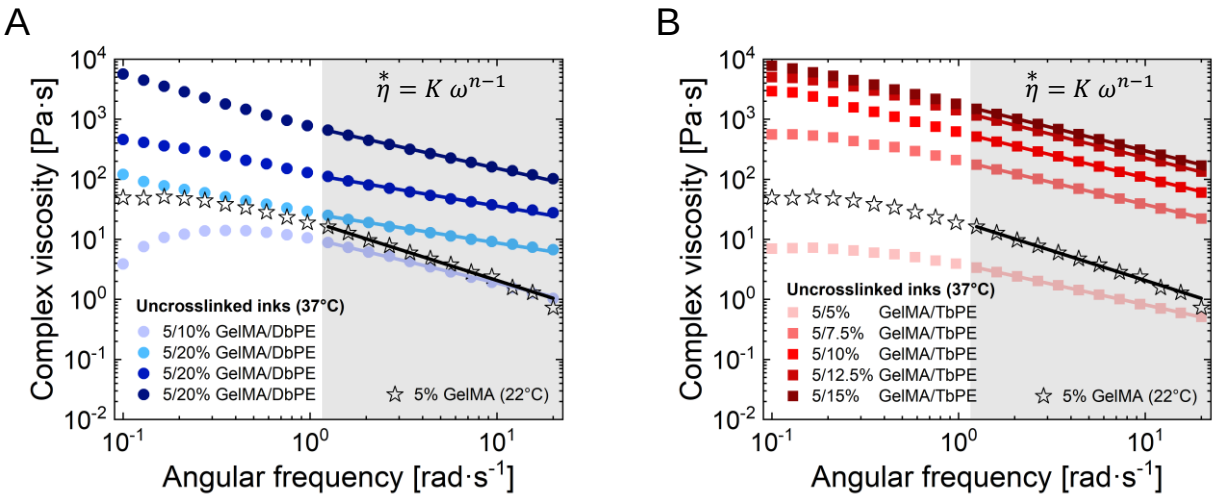

Power law	*n*	*K*
5/10% GelMA/DbPE	0.25	10
5/20% GelMA/DbPE	0.51	27
5/30% GelMA/DbPE	0.47	121
5/40% GelMA/DbPE	0.31	751
5% GelMA (22°C)	0.01	20

Power law	*n*	*K*
5/5% GelMA/TbPE	0.31	3.9
5/7.5% GelMA/TbPE	0.27	206
5/10% GelMA/TbPE	0.24	609
5/12.5% GelMA/TbPE	0.22	1367
5/15% GelMA/TbPE	0.22	1767
5% GelMA (22°C)	0.01	20

Figure 5-S9. Complex viscosity profiles for **(A)** GelMA/DbPE and **(B)** GelMA/TbPE precursor solutions with increasing bPE concentration at 37 °C and GelMA ink without bPEs at 22 °C. Shear-thinning behavior was quantified by power law regression of the linear regions. Values of shear-thinning coefficients are given in the table below.

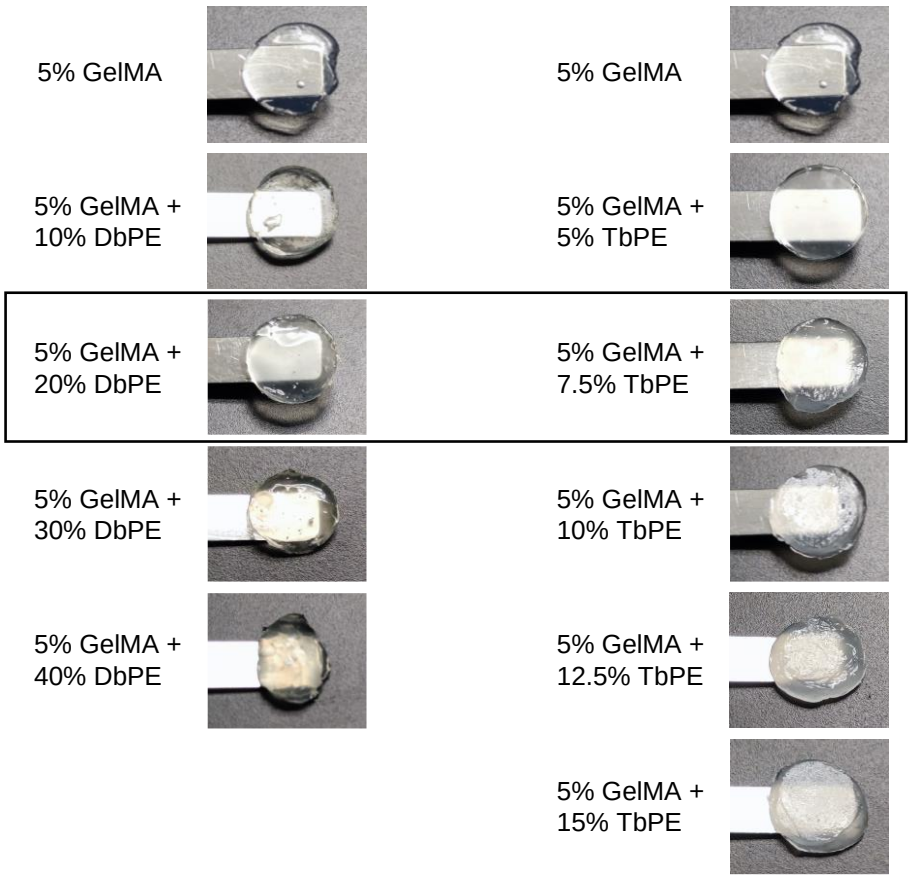

Figure 5-S10. Photographs of GelMA and GelMA/bPE hydrogels after photocrosslinking. Increasing amounts of DbPEs and TbPEs resulted in a gradual decrease in optical transparency. DbPE concentrations of ≥ 30 wt% impeded with photochemical crosslinking of the GelMA precursors, thus leading to reduced crosslink density and a loss of structural integrity.

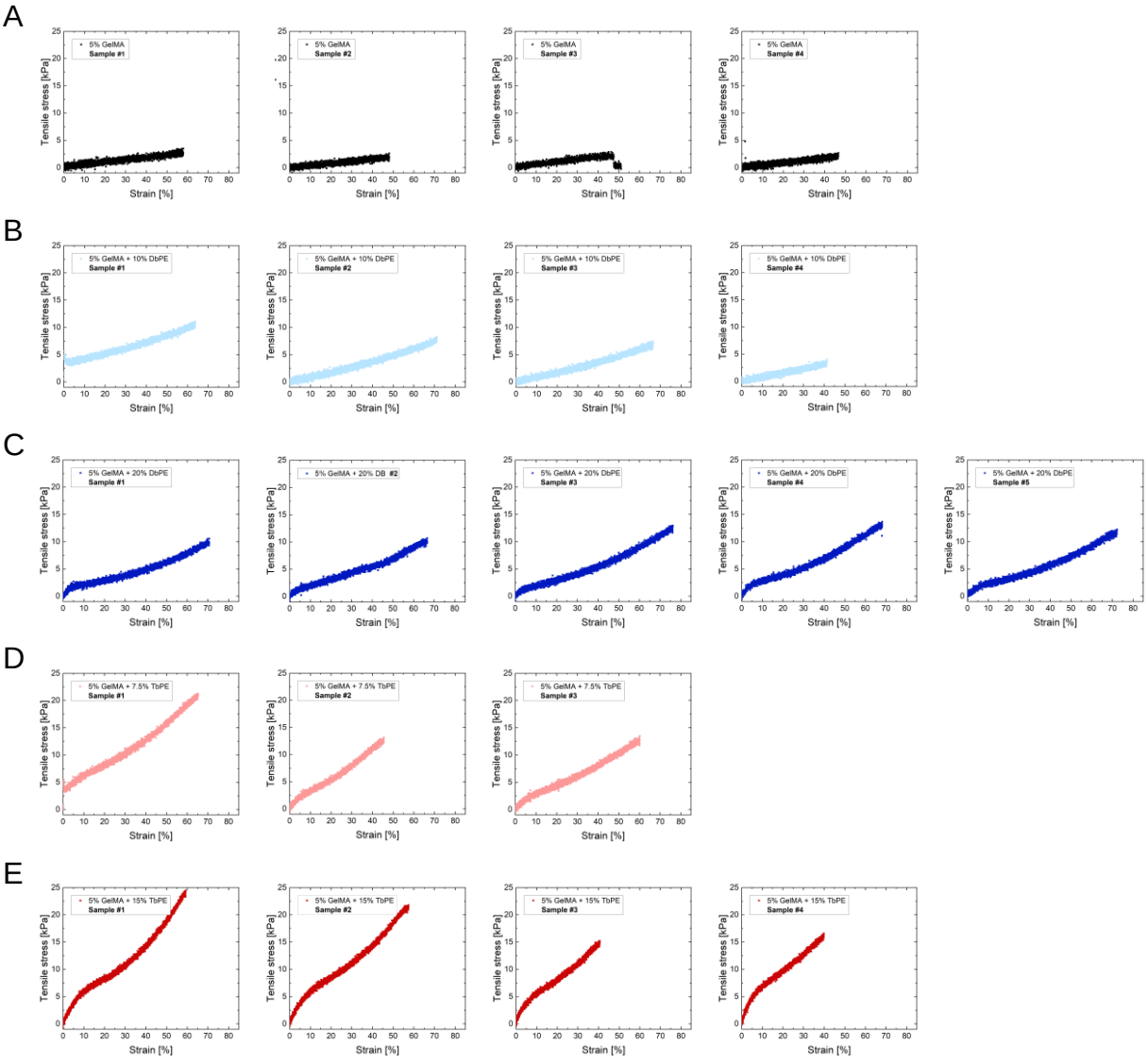

Figure 5-S11. Stress-strain curves from uniaxial tensile tests for photocrosslinked **(A)** GelMA, **(B-C)** GelMA/DbPE, and **(D-E)** GelMA/TbPE hydrogels.

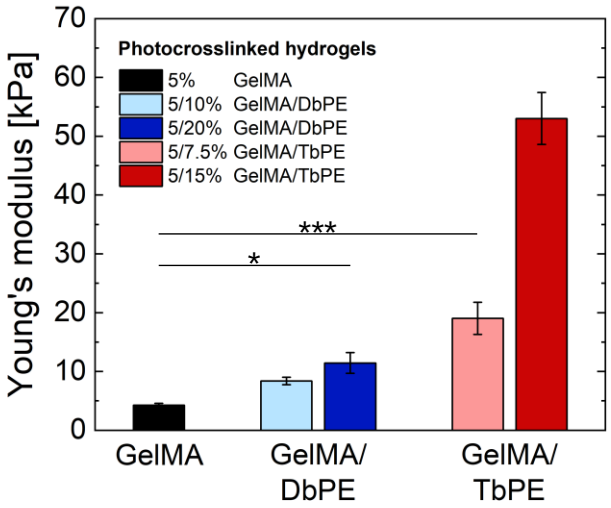

Figure 5-S12. Young's modulus for photocrosslinked GelMA, GelMA/DbPE and GelMA/TbPE hydrogels determined from the slope of the linear region of the stress-strain curves. Data were presented as mean ± SD and statistically evaluated by one-way ANOVA. *, **, *** represent $p < 0.05$, 0.01, and 0.001, respectively.

Supplementary Movies

Movie 5-SM1. Movie depicting extrusion-based 3D printing of the KIT logo at 37 °C using a 5 wt% GelMA ink supplemented with 20 wt% DbPE additives. A green dye was added to the precursor solution to aid visualization.

Movie 5-SM2. Movie depicting extrusion-based 3D printing of the UCLA logo at 37 °C using a 5 wt% GelMA ink supplemented with 20 wt% DbPE additives. A blue dye was added to the precursor solution to aid visualization.

5.6 Reference

(1) Malda, J.; Visser, J.; Melchels, F. P.; Jungst, T.; Hennink, W. E.; Dhert, W. J. A.; Groll, J.; Hutmacher, D. W. 25th Anniversary Article: Engineering Hydrogels for Biofabrication. *Advanced Materials* **2013**, *25* (36), 5011-5028. DOI: 10.1002/adma.201302042.

(2) Moroni, L.; Burdick, J. A.; Highley, C.; Lee, S. J.; Morimoto, Y.; Takeuchi, S.; Yoo, J. J. Biofabrication strategies for 3D in vitro models and regenerative medicine. *Nat Rev Mater* **2018**, *3* (5), 21-37. DOI: 10.1038/s41578-018-0006-y.

(3) Chimene, D.; Kaunas, R.; Gaharwar, A. K. Hydrogel Bioink Reinforcement for Additive Manufacturing: A Focused Review of Emerging Strategies. *Adv Mater* **2020**, *32* (1), e1902026. DOI: 10.1002/adma.201902026.

(4) Kolesky, D. B.; Truby, R. L.; Gladman, A. S.; Busbee, T. A.; Homan, K. A.; Lewis, J. A. 3D bioprinting of vascularized, heterogeneous cell-laden tissue constructs. *Adv Mater* **2014**, *26* (19), 3124-3130. DOI: 10.1002/adma.201305506.

(5) Ashammakhi, N.; Hasan, A.; Kaarela, O.; Byambaa, B.; Sheikhi, A.; Gaharwar, A. K.; Khademhosseini, A. Advancing Frontiers in Bone Bioprinting. *Adv Healthc Mater* **2019**, *8* (7), e1801048. DOI: 10.1002/adhm.201801048.

(6) Bedell, M. L.; Navara, A. M.; Du, Y. Y.; Zhang, S. M.; Mikos, A. G. Polymeric Systems for Bioprinting. *Chemical Reviews* **2020**, *120* (19), 10547-10595. DOI: 10.1021/acs.chemrev.9b00834.

(7) Sun, W.; Starly, B.; Daly, A. C.; Burdick, J. A.; Groll, J.; Skeldon, G.; Shu, W.; Sakai, Y.; Shinohara, M.; Nishikawa, M.; et al. The bioprinting roadmap. *Biofabrication* **2020**, *12* (2), 022002. DOI: 10.1088/1758-5090/ab5158.

(8) Gao, W.; Zhang, Y. B.; Ramanujan, D.; Ramani, K.; Chen, Y.; Williams, C. B.; Wang, C. C. L.; Shin, Y. C.; Zhang, S.; Zavattieri, P. D. The status, challenges, and future of additive manufacturing in engineering. *Comput Aided Design* **2015**, *69*, 65-89. DOI: 10.1016/j.cad.2015.04.001.

(9) Gisario, A.; Kazarian, M.; Martina, F.; Mehrpouya, M. Metal additive manufacturing in the commercial aviation industry: A review. *J Manuf Syst* **2019**, *53*, 124-149. DOI: 10.1016/j.jmsy.2019.08.005.

(10) Kumar, L. J.; Krishnadas Nair, C. G. Current Trends of Additive Manufacturing in the Aerospace Industry. In *Advances in 3D Printing & Additive Manufacturing Technologies*, Wimpenny, D. I., Pandey, P. M., Kumar, L. J. Eds.; Springer Singapore, 2017; pp 39-54.

(11) Craveiro, F.; Duarte, J. P.; Bartolo, H.; Bartolo, P. J. Additive manufacturing as an enabling technology for digital construction: A perspective on Construction 4.0. *Automat Constr* **2019**, *103*, 251-267. DOI: 10.1016/j.autcon.2019.03.011.

(12) Lim, S.; Buswell, R. A.; Le, T. T.; Austin, S. A.; Gibb, A. G. F.; Thorpe, T. Developments in construction-scale additive manufacturing processes. *Automat Constr* **2012**, *21*, 262-268. DOI: 10.1016/j.autcon.2011.06.010.

(13) Rael, R. S. F. V. Printing architecture : innovative recipes for 3D printing. **2018**. From http://worldcat.org.

(14) Lu, B. H.; Lan, H. B.; Liu, H. Z. Additive manufacturing frontier: 3D printing electronics. *Opto-Electron Adv* **2018**, *1* (1), 17000401-17000410. DOI: 10.29026/oea.2018.170004.

(15) Espera, A. H.; Dizon, J. R. C.; Chen, Q.; Advincula, R. C. 3D-printing and advanced manufacturing for electronics. *Progress in Additive Manufacturing* **2019**, 1-23.

(16) Guo, S. Formative Arts Based on 3D Printing Technology. *Journal of Physics: Conference Series* **2020**, *1533* (2), 022031. DOI: 10.1088/1742-6596/1533/2/022031.

(17) Liu, Z. B.; Zhang, M.; Bhandari, B.; Wang, Y. C. 3D printing: Printing precision and application in food sector. *Trends Food Sci Tech* **2017**, *69*, 83-94. DOI: 10.1016/j.tifs.2017.08.018.

(18) Sun, J.; Zhou, W. B.; Huang, D. J.; Fuh, J. Y. H.; Hong, G. S. An Overview of 3D Printing Technologies for Food Fabrication. *Food Bioprocess Tech* **2015**, *8* (8), 1605-1615. DOI: 10.1007/s11947-015-1528-6.

(19) Yan, Q.; Dong, H. H.; Su, J.; Han, J. H.; Song, B.; Wei, Q. S.; Shi, Y. S. A Review of 3D Printing Technology for Medical Applications. *Engineering-Prc* **2018**, *4* (5), 729-742. DOI: 10.1016/j.eng.2018.07.021.

(20) Atala, A.; Forgacs, G. Three-Dimensional Bioprinting in Regenerative Medicine: Reality, Hype, and Future. *Stem Cells Transl Med* **2019**, *8* (8), 744-745. DOI: 10.1002/sctm.19-0089.

(21) Tack, P.; Victor, J.; Gemmel, P.; Annemans, L. 3D-printing techniques in a medical setting: a systematic literature review. *Biomed Eng Online* **2016**, *15* (1), 115. DOI: 10.1186/s12938-016-0236-4.

(22) Ten Kate, J.; Smit, G.; Breedveld, P. 3D-printed upper limb prostheses: a review. *Disabil Rehabil Assist Technol* **2017**, *12* (3), 300-314. DOI: 10.1080/17483107.2016.1253117.

(23) Rengier, F.; Mehndiratta, A.; von Tengg-Kobligk, H.; Zechmann, C. M.; Unterhinninghofen, R.; Kauczor, H. U.; Giesel, F. L. 3D printing based on imaging data: review of medical applications. *Int J Comput Assist Radiol Surg* **2010**, *5* (4), 335-341. DOI: 10.1007/s11548-010-0476-x.

(24) Hoang, D.; Perrault, D.; Stevanovic, M.; Ghiassi, A. Surgical applications of three-dimensional printing: a review of the current literature & how to get started. *Ann Transl Med* **2016**, *4* (23), 456. DOI: 10.21037/atm.2016.12.18.

(25) Hippler, M.; Lemma, E. D.; Bertels, S.; Blasco, E.; Barner-Kowollik, C.; Wegener, M.; Bastmeyer, M. 3D Scaffolds to Study Basic Cell Biology. *Adv Mater* **2019**, *31* (26), e1808110. DOI: 10.1002/adma.201808110.

(26) Selimis, A.; Mironov, V.; Farsari, M. Direct laser writing: Principles and materials for scaffold 3D printing. *Microelectron Eng* **2015**, *132*, 83-89. DOI: 10.1016/j.mee.2014.10.001.

(27) Nikolova, M. P.; Chavali, M. S. Recent advances in biomaterials for 3D scaffolds: A review. *Bioact Mater* **2019**, *4*, 271-292. DOI: 10.1016/j.bioactmat.2019.10.005.

(28) Wilson, W. C., Jr.; Boland, T. Cell and organ printing 1: protein and cell printers. *Anat Rec A Discov Mol Cell Evol Biol* **2003**, *272* (2), 491-496. DOI: 10.1002/ar.a.10057.

(29) Gupta, M. K.; Meng, F.; Johnson, B. N.; Kong, Y. L.; Tian, L.; Yeh, Y. W.; Masters, N.; Singamaneni, S.; McAlpine, M. C. 3D Printed Programmable Release Capsules. *Nano Lett* **2015**, *15* (8), 5321-5329. DOI: 10.1021/acs.nanolett.5b01688.

(30) Ozbolat, I. T.; Hospodiuk, M. Current advances and future perspectives in extrusion-based bioprinting. *Biomaterials* **2016**, *76*, 321-343. DOI: 10.1016/j.biomaterials.2015.10.076.

(31) Murphy, S. V.; Atala, A. 3D bioprinting of tissues and organs. *Nature Biotechnology* **2014**, *32* (8), 773-785. DOI: 10.1038/nbt.2958.

(32) Arslan-Yildiz, A.; El Assal, R.; Chen, P.; Guven, S.; Inci, F.; Demirci, U. Towards artificial tissue models: past, present, and future of 3D bioprinting. *Biofabrication* **2016**, *8* (1), 014103. DOI: 10.1088/1758-5090/8/1/014103.

(33) Vijayavenkataraman, S.; Lu, W. F.; Fuh, J. Y. 3D bioprinting of skin: a state-of-the-art review on modelling, materials, and processes. *Biofabrication* **2016**, *8* (3), 032001. DOI: 10.1088/1758-5090/8/3/032001.

(34) Ma, L.; Wu, Y.; Li, Y.; Aazmi, A.; Zhou, H.; Zhang, B.; Yang, H. Current Advances on 3D-Bioprinted Liver Tissue Models. *Adv Healthc Mater* **2020**, *9* (24), e2001517. DOI: 10.1002/adhm.202001517.

(35) Fransen, M. F. J.; Addario, G.; Bouten, C. V. C.; Halary, F.; Moroni, L.; Mota, C. Bioprinting of kidney in vitro models: cells, biomaterials, and manufacturing techniques. *Essays Biochem* **2021**, *65* (3), 587-602. DOI: 10.1042/EBC20200158.

(36) Liu, N.; Ye, X.; Yao, B.; Zhao, M.; Wu, P.; Liu, G.; Zhuang, D.; Jiang, H.; Chen, X.; He, Y.; et al. Advances in 3D bioprinting technology for cardiac tissue engineering and regeneration. *Bioact Mater* **2021**, *6* (5), 1388-1401. DOI: 10.1016/j.bioactmat.2020.10.021.

(37) Hauser, P. V.; Chang, H. M.; Nishikawa, M.; Kimura, H.; Yanagawa, N.; Hamon, M. Bioprinting Scaffolds for Vascular Tissues and Tissue Vascularization. *Bioengineering (Basel)* **2021**, *8* (11). DOI: 10.3390/bioengineering8110178.

(38) Wu, Y.; Kennedy, P.; Bonazza, N.; Yu, Y.; Dhawan, A.; Ozbolat, I. Three-Dimensional Bioprinting of Articular Cartilage: A Systematic Review. *Cartilage* **2021**, *12* (1), 76-92. DOI: 10.1177/1947603518809410.

(39) Bahraminasab, M. Challenges on optimization of 3D-printed bone scaffolds. *Biomed Eng Online* **2020**, *19* (1), 69. DOI: 10.1186/s12938-020-00810-2.

(40) Paxton, N.; Smolan, W.; Bock, T.; Melchels, F.; Groll, J.; Jungst, T. Proposal to assess printability of bioinks for extrusion-based bioprinting and evaluation of rheological properties governing bioprintability. *Biofabrication* **2017**, *9* (4), 044107. DOI: 10.1088/1758-5090/aa8dd8.

(41) Holzl, K.; Lin, S. M.; Tytgat, L.; Van Vlierberghe, S.; Gu, L. X.; Ovsianikov, A. Bioink properties before, during and after 3D bioprinting. *Biofabrication* **2016**, *8* (3), 032002. DOI: 10.1088/1758-5090/8/3/032002.

(42) Jungst, T.; Smolan, W.; Schacht, K.; Scheibel, T.; Groll, J. Strategies and Molecular Design Criteria for 3D Printable Hydrogels. *Chem Rev* **2016**, *116* (3), 1496-1539. DOI: 10.1021/acs.chemrev.5b00303.

(43) Blaeser, A.; Campos, D. F. D.; Puster, U.; Richtering, W.; Stevens, M. M.; Fischer, H. Controlling Shear Stress in 3D Bioprinting is a Key Factor to Balance Printing Resolution and Stem Cell Integrity. *Advanced Healthcare Materials* **2016**, *5* (3), 326-333. DOI: 10.1002/adhm.201500677.

(44) Lee, S. C.; Gillispie, G.; Prim, P.; Lee, S. J. Physical and Chemical Factors Influencing the Printability of Hydrogel-based Extrusion Bioinks. *Chem Rev* **2020**, *120* (19), 10834-10886. DOI: 10.1021/acs.chemrev.0c00015.

(45) Townsend, J. M.; Beck, E. C.; Gehrke, S. H.; Berkland, C. J.; Detamore, M. S. Flow Behavior Prior to Crosslinking: The Need for Precursor Rheology for Placement of Hydrogels in Medical Applications and for 3D Bioprinting. *Prog Polym Sci* **2019**, *91*, 126-140. DOI: 10.1016/j.progpolymsci.2019.01.003.

(46) Mouser, V. H.; Melchels, F. P.; Visser, J.; Dhert, W. J.; Gawlitta, D.; Malda, J. Yield stress determines bioprintability of hydrogels based on gelatin-methacryloyl and gellan gum for cartilage bioprinting. *Biofabrication* **2016**, *8* (3), 035003. DOI: 10.1088/1758-5090/8/3/035003.

(47) Schwab, A.; Levato, R.; D'Este, M.; Piluso, S.; Eglin, D.; Malda, J. Printability and Shape Fidelity of Bioinks in 3D Bioprinting. *Chemical Reviews* **2020**, *120* (19), 10850-10877. DOI: 10.1021/acs.chemrev.0c00084.

(48) Cooke, M. E.; Rosenzweig, D. H. The rheology of direct and suspended extrusion bioprinting. *APL Bioeng* **2021**, *5* (1), 011502. DOI: 10.1063/5.0031475.

(49) Knowlton, S.; Yenilmez, B.; Anand, S.; Tasoglu, S. Photocrosslinking-Based Bioprinting: Examining Crosslinking Schemes. *Bioprinting* **2017**, *5*. DOI: 10.1016/j.bprint.2017.03.001.

(50) Nichol, J. W.; Koshy, S. T.; Bae, H.; Hwang, C. M.; Yamanlar, S.; Khademhosseini, A. Cell-laden microengineered gelatin methacrylate hydrogels. *Biomaterials* **2010**, *31* (21), 5536-5544. DOI: 10.1016/j.biomaterials.2010.03.064.

(51) Gaudet, I. D.; Shreiber, D. I. Characterization of Methacrylated Type-I Collagen as a Dynamic, Photoactive Hydrogel. *Biointerphases* **2012**, *7* (1-4), 25. DOI: 10.1007/s13758-012-0025-y.

(52) Burdick, J. A.; Chung, C.; Jia, X.; Randolph, M. A.; Langer, R. Controlled degradation and mechanical behavior of photopolymerized hyaluronic acid networks. *Biomacromolecules* **2005**, *6* (1), 386-391. DOI: 10.1021/bm049508a.

(53) Gockler, T.; Haase, S.; Kempter, X.; Pfister, R.; Maciel, B. R.; Grimm, A.; Molitor, T.; Willenbacher, N.; Schepers, U. Tuning Superfast Curing Thiol-Norbornene-Functionalized Gelatin Hydrogels for 3D Bioprinting. *Advanced Healthcare Materials* **2021**, *10* (14), e2100206. DOI: 10.1002/adhm.202100206.

(54) Gramlich, W. M.; Kim, I. L.; Burdick, J. A. Synthesis and orthogonal photopatterning of hyaluronic acid hydrogels with thiol-norbornene chemistry. *Biomaterials* **2013**, *34* (38), 9803-9811. DOI: 10.1016/j.biomaterials.2013.08.089.

(55) Aimetti, A. A.; Machen, A. J.; Anseth, K. S. Poly(ethylene glycol) hydrogels formed by thiol-ene photopolymerization for enzyme-responsive protein delivery. *Biomaterials* **2009**, *30* (30), 6048-6054. DOI: 10.1016/j.biomaterials.2009.07.043.

(56) Van Vlierberghe, S.; Schacht, E.; Dubruel, P. Reversible gelatin-based hydrogels: Finetuning of material properties. *European Polymer Journal* **2011**, *47* (5), 1039-1047. DOI: 10.1016/j.eurpolymj.2011.02.015.

(57) Gyarmati, B.; Némethy, A.; Szilágyi, A. Reversible disulphide formation in polymer networks: A versatile functional group from synthesis to applications. *European Polymer Journal* **2013**, *49* (6), 1268-1286. DOI: 10.1016/j.eurpolymj.2013.03.001.

(58) Yue, K.; Trujillo-de Santiago, G.; Alvarez, M. M.; Tamayol, A.; Annabi, N.; Khademhosseini, A. Synthesis, properties, and biomedical applications of gelatin methacryloyl (GelMA) hydrogels. *Biomaterials* **2015**, *73*, 254-271. DOI: 10.1016/j.biomaterials.2015.08.045.

(59) Falcone, G.; Mazzei, P.; Piccolo, A.; Esposito, T.; Mencherini, T.; Aquino, R. P.; Del Gaudio, P.; Russo, P. Advanced printable hydrogels from pre-crosslinked alginate as a new tool in semi solid extrusion 3D printing process. *Carbohydrate Polymers* **2022**, *276*, 118746. DOI: 10.1016/j.carbpol.2021.118746.

(60) GhavamiNejad, A.; Ashammakhi, N.; Wu, X. Y.; Khademhosseini, A. Crosslinking Strategies for 3D Bioprinting of Polymeric Hydrogels. *Small* **2020**, *16* (35). DOI: ARTN 2002931

10.1002/smll.202002931.

(61) Monfared, M.; Mawad, D.; Rnjak-Kovacina, J.; Stenzel, M. H. 3D bioprinting of dual-crosslinked nanocellulose hydrogels for tissue engineering applications. *J Mater Chem B* **2021**, *9* (31), 6163-6175. DOI: 10.1039/d1tb00624j.

(62) Wang, X.; Wang, Q.; Xu, C. Nanocellulose-Based Inks for 3D Bioprinting: Key Aspects in Research Development and Challenging Perspectives in Applications-A Mini Review. *Bioengineering (Basel)* **2020**, *7* (2). DOI: 10.3390/bioengineering7020040.

(63) Cernencu, A. I.; Lungu, A.; Dragusin, D. M.; Stancu, I. C.; Dinescu, S.; Balahura, L. R.; Mereuta, P.; Costache, M.; Iovu, H. 3D Bioprinting of Biosynthetic Nanocellulose-Filled GelMA Inks Highly Reliable for Soft Tissue-Oriented Constructs. *Materials* **2021**, *14* (17). DOI: 10.3390/ma14174891.

(64) Muller, M.; Ozturk, E.; Arlov, O.; Gatenholm, P.; Zenobi-Wong, M. Alginate Sulfate-Nanocellulose Bioinks for Cartilage Bioprinting Applications. *Annals of Biomedical Engineering* **2017**, *45* (1), 210-223. DOI: 10.1007/s10439-016-1704-5.

(65) Guo, Z.; Dong, L.; Xia, J.; Mi, S.; Sun, W. 3D Printing Unique Nanoclay-Incorporated Double-Network Hydrogels for Construction of Complex Tissue Engineering Scaffolds. *Adv Healthc Mater* **2021**, *10* (11), e2100036. DOI: 10.1002/adhm.202100036.

(66) Gao, Q.; Niu, X.; Shao, L.; Zhou, L.; Lin, Z.; Sun, A.; Fu, J.; Chen, Z.; Hu, J.; Liu, Y.; et al. 3D printing of complex GelMA-based scaffolds with nanoclay. *Biofabrication* **2019**, *11* (3), 035006. DOI: 10.1088/1758-5090/ab0cf6.

(67) Hu, C.; Hahn, L.; Yang, M. S.; Altmann, A.; Stahlhut, P.; Groll, J.; Luxenhofer, R. Improving printability of a thermoresponsive hydrogel biomaterial ink by nanoclay addition. *J Mater Sci* **2021**, *56* (1), 691-705. DOI: 10.1007/s10853-020-05190-5.

(68) Ouyang, L.; Yao, R.; Zhao, Y.; Sun, W. Effect of bioink properties on printability and cell viability for 3D bioplotting of embryonic stem cells. *Biofabrication* **2016**, *8* (3), 035020. DOI: 10.1088/1758-5090/8/3/035020.

(69) Zhao, Y.; Li, Y.; Mao, S.; Sun, W.; Yao, R. The influence of printing parameters on cell survival rate and printability in microextrusion-based 3D cell printing technology. *Biofabrication* **2015**, *7* (4), 045002. DOI: 10.1088/1758-5090/7/4/045002.

(70) Endes, C.; Camarero-Espinosa, S.; Mueller, S.; Foster, E. J.; Petri-Fink, A.; Rothen-Rutishauser, B.; Weder, C.; Clift, M. J. D. A critical review of the current knowledge regarding the biological impact of nanocellulose. *J Nanobiotechnol* **2016**, *14* (1), 78. DOI: 10.1186/s12951-016-0230-9.

(71) Harper, B. J.; Clendaniel, A.; Sinche, F.; Way, D.; Hughes, M.; Schardt, J.; Simonsen, J.; Stefaniak, A. B.; Harper, S. L. Impacts of chemical modification on the toxicity of diverse nanocellulose materials to developing zebrafish. *Cellulose (Lond)* **2016**, *23* (3), 1763-1775. DOI: 10.1007/s10570-016-0947-5.

(72) Brandelli, A. Toxicity and Safety Evaluation of Nanoclays. In *Nanomaterials: Ecotoxicity, Safety, and Public Perception*, Rai, M., Biswas, J. K. Eds.; Springer International Publishing, 2018; pp 57-76.

(73) Zhang, Y. S.; Khademhosseini, A. Advances in engineering hydrogels. *Science* **2017**, *356* (6337). DOI: 10.1126/science.aaf3627.

(74) Ashammakhi, N.; Ahadian, S.; Xu, C.; Montazerian, H.; Ko, H.; Nasiri, R.; Barros, N.; Khademhosseini, A. Bioinks and bioprinting technologies to make heterogeneous and biomimetic tissue constructs. *Mater Today Bio* **2019**, *1*. DOI: ARTN 100008

10.1016/j.mtbio.2019.100008.

(75) Cui, X.; Li, J.; Hartanto, Y.; Durham, M.; Tang, J.; Zhang, H.; Hooper, G.; Lim, K.; Woodfield, T. Advances in Extrusion 3D Bioprinting: A Focus on Multicomponent Hydrogel-Based Bioinks. *Adv Healthc Mater* **2020**, *9* (15), e1901648. DOI: 10.1002/adhm.201901648.

(76) Tanaka, M.; Nakahata, M.; Linke, P.; Kaufmann, S. Stimuli-responsive hydrogels as a model of the dynamic cellular microenvironment. *Polym J* **2020**, *52* (8), 861-870. DOI: 10.1038/s41428-020-0353-6.

(77) Hunt, J. N.; Feldman, K. E.; Lynd, N. A.; Deek, J.; Campos, L. M.; Spruell, J. M.; Hernandez, B. M.; Kramer, E. J.; Hawker, C. J. Tunable, high modulus hydrogels driven by ionic coacervation. *Adv Mater* **2011**, *23* (20), 2327-2331. DOI: 10.1002/adma.201004230.

(78) Srivastava, S.; Andreev, M.; Levi, A. E.; Goldfeld, D. J.; Mao, J.; Heller, W. T.; Prabhu, V. M.; de Pablo, J. J.; Tirrell, M. V. Gel phase formation in dilute triblock copolyelectrolyte complexes. *Nature Communications* **2017**, *8*. DOI: ARTN 14131

10.1038/ncomms14131.

(79) Srivastava, S.; Levi, A. E.; Goldfeld, D. J.; Tirrell, M. V. Structure, Morphology, and Rheology of Polyelectrolyte Complex Hydrogels Formed by Self-Assembly of Oppositely Charged Triblock Polyelectrolytes. *Macromolecules* **2020**, *53* (14), 5763-5774. DOI: 10.1021/acs.macromol.0c00847.

(80) Li, D.; Gockler, T.; Schepers, U.; Srivastava, S. Polyelectrolyte Complex-Covalent Interpenetrating Polymer Network Hydrogels. *ChemRxiv* **2022**, Pre-print.

(81) Kim, J. M.; Heo, T. Y.; Choi, S. H. Structure and Relaxation Dynamics for Complex Coacervate Hydrogels Formed by ABA Triblock Copolymers. *Macromolecules* **2020**, *53* (21), 9234-9243. DOI: 10.1021/acs.macromol.0c01600.

(82) Bertassoni, L. E.; Cardoso, J. C.; Manoharan, V.; Cristino, A. L.; Bhise, N. S.; Araujo, W. A.; Zorlutuna, P.; Vrana, N. E.; Ghaemmaghami, A. M.; Dokmeci, M. R.; et al. Direct-write bioprinting of cell-laden methacrylated gelatin hydrogels. *Biofabrication* **2014**, *6* (2), 024105. DOI: Artn 024105

10.1088/1758-5082/6/2/024105.

(83) Xie, M.; Yu, K.; Sun, Y.; Shao, L.; Nie, J.; Gao, Q.; Qiu, J.; Fu, J.; Chen, Z.; He, Y. Protocols of 3D Bioprinting of Gelatin Methacryloyl Hydrogel Based Bioinks. *JoVE* **2019**, (154), e60545. DOI: doi:10.3791/60545.

(84) Chen, M. H.; Wang, L. L.; Chung, J. J.; Kim, Y. H.; Atluri, P.; Burdick, J. A. Methods To Assess Shear-Thinning Hydrogels for Application As Injectable Biomaterials. *Acs Biomater Sci Eng* **2017**, *3* (12), 3146-3160. DOI: 10.1021/acsbiomaterials.7b00734.

(85) Rad, M. A.; Mahmodi, H.; Filipe, E. C.; Cox, T. R.; Kabakova, I.; Tipper, J. L. Micromechanical characterisation of 3D bioprinted neural cell models using Brillouin microspectroscopy. *Bioprinting* **2022**, *25*, e00179. DOI: https://doi.org/10.1016/j.bprint.2021.e00179.

(86) Guvendiren, M.; Lu, H. D.; Burdick, J. A. Shear-thinning hydrogels for biomedical applications. *Soft Matter* **2012**, *8* (2), 260-272. DOI: 10.1039/c1sm06513k.

(87) Zhao, H.; Xu, K.; Zhu, P.; Wang, C. L.; Chi, Q. J. Smart hydrogels with high tunability of stiffness as a biomimetic cell carrier. *Cell Biol Int* **2019**, *43* (2), 84-97. DOI: 10.1002/cbin.11091.

(88) Levental, I.; Georges, P. C.; Janmey, P. A. Soft biological materials and their impact on cell function. *Soft Matter* **2007**, *3* (3), 299-306. DOI: 10.1039/b610522j.

(89) Neitzel, A. E.; de Hoe, G. X.; Tirrell, M. V. Expanding the structural diversity of polyelectrolyte complexes and polyzwitterions. *Curr Opin Solid St M* **2021**, *25* (2). DOI: ARTN 100897

10.1016/j.cossms.2020.100897.

(90) Kammerer, S.; Küpper, J.-H. Human hepatocyte systems for in vitro toxicology analysis. *Journal of Cellular Biotechnology* **2018**, *3* (2), 85-93. DOI: 10.3233/JCB-179012.

(91) Serras, A. S.; Rodrigues, J. S.; Cipriano, M.; Rodrigues, A. V.; Oliveira, N. G.; Miranda, J. P. A Critical Perspective on 3D Liver Models for Drug Metabolism and Toxicology Studies. *Front Cell Dev Biol* **2021**, *9*, 626805. DOI: 10.3389/fcell.2021.626805.

(92) Trabulo, S.; Cardoso, A. L.; Mano, M.; De Lima, M. C. Cell-Penetrating Peptides-Mechanisms of Cellular Uptake and Generation of Delivery Systems. *Pharmaceuticals (Basel)* **2010**, *3* (4), 961-993. DOI: 10.3390/ph3040961.

(93) Madani, F.; Lindberg, S.; Langel, U.; Futaki, S.; Graslund, A. Mechanisms of cellular uptake of cell-penetrating peptides. *J Biophys* **2011**, *2011*, 414729. DOI: 10.1155/2011/414729.

(94) Verbeek, S. F.; Awasthi, N.; Teiwes, N. K.; Mey, I.; Hub, J. S.; Janshoff, A. How arginine derivatives alter the stability of lipid membranes: dissecting the roles of side chains, backbone and termini. *Eur Biophys J Biophy* **2021**, *50* (2), 127-142. DOI: 10.1007/s00249-021-01503-x.

(95) Krogstad, D. V.; Lynd, N. A.; Miyajima, D.; Gopez, J.; Hawker, C. J.; Kramer, E. J.; Tirrell, M. V. Structural Evolution of Polyelectrolyte Complex Core Micelles and Ordered-Phase Bulk Materials. *Macromolecules* **2014**, *47* (22), 8026-8032. DOI: 10.1021/ma5017852.

Chapter 6

Coupling Between Microstructures and Relaxation Dynamics in Polyelectrolyte Complex Hydrogels

Abstract

The relaxation dynamics of hydrogels have been known to not only correlate with bulk shear properties, swelling characteristics, and microstructures but also influence hydrogel functioning, such as affecting cell behaviors. Hydrogels typically possess a fairly understood fast relaxation dynamic, but there exists an additional slow relaxation dynamic behavior of some hydrogels, which is poorly understood. In recent years, the dynamics of hydrogels with ordered microstructures started to attract research attention but it still requires much effort to understand the relationship between dynamics and microstructures. Here, we investigated the relationship between microstructures and relaxation dynamics of ABA triblock polyelectrolytes complex (PEC) hydrogels, wherein block B comprised neutral poly(ethylene glycol) (PEO) and block A functionalized with either ammonium or sulfonate moieties. Upon mixing, the oppositely charged blocks of polyelectrolytes form PEC domains, serving as physical cross-links, and the bridging PEO chains connected the PEC domains to construct 3-D polymer networks. X-ray photon correlation spectroscopy (XPCS) was employed to investigate structural relaxation dynamics, and small-angle X-ray scattering (SAXS) was applied to acquire nanoscale microstructural information on PEC domain arrangement. Interestingly, we found a coupling relationship between the

structural relaxation modes and microstructures, which has not been reported previously. Single-mode structural relaxation, only containing the fast dynamics, was found to be correlated with a disordered sphere. Double-mode structural relaxation, containing both fast and slow dynamics, was discovered to be coupled with lamellar structure. Besides, stress relaxation time scales, investigated by the linear viscoelastic response via rheology, were found to be smaller than the structural relaxation times measured by XPCS. Our findings regarding the coupling relationship between microstructure and structural relaxation modes expanded the research scope of slow dynamics and provided a new route for future investigation.

6.1 Introduction

Hydrogels are covalently or physically crosslinked three-dimensional (3-D) hydrophilic polymer networks, which can be swellable but not dissolved in water.[1-11] Due to high water content,[2-4, 7, 11] mechanical tunability,[7] and biocompatibility,[5, 11, 12] hydrogels have been demonstrated as promising materials for biomedical applications, such as cell scaffolds for tissue engineering,[13-15] bioadhesives,[16-18] cartilage regeneration engineering,[19-23] and drug delivery[8, 24-26]. The feature of the 3-D polymer network structure, similar to extracellular matrix (ECM),[12] provides structural and mechanical support for cell proliferation, growth, and differentiation.[27, 28] Mechanical stimuli have been acknowledged as an important factor to influence cellular behaviors.[28-30] Thus, the development of hydrogels, that can mimic the dynamics of natural ECM, is highly anticipated. In recent years, reversible and dynamic physical interactions are harnessed to acquire stimuli-responsive and self-healing hydrogels, such as polyelectrolyte complex (PEC) hydrogels. PEC hydrogels are formed by mixing oppositely charged block polyelectrolytes, carrying either cationic or anionic moieties. In most hydrogels, dynamics at the molecular level exhibit a closed relationship with microscopic structure, bulk mechanical properties[31], and swelling properties [31].[32, 33] An understanding of dynamics is crucial to clarifying the relationship and designing biomaterials that tailored mechanical and functional properties. Yet, the dynamics of PEC hydrogels remain poorly understood, especially the relationship between dynamics and microstructures.

Dynamic light scattering (DLS) is a powerful technique for characterization of hydrogel structural dynamics, such as dynamics of DNA in a charged hydrogel,[34] the influence of surfactant on hydrogels,[35], polymer diffusion in gels,[11] diffusion coefficient,[36] and the relationship between elasticity and dynamics[36]. Structural dynamics, influenced by a local environment of polymer

networks, are closely related to bulk mechanical properties and performance of hydrogels.[11, 31] Microscopic dynamics have received increasing research attention because dynamics can influence cellular behaviors by applying mechanical stimuli, which can be converted to biochemical signals by cells. [27, 28, 37] With a similar hydrogel stiffness, hydrogels with a faster relaxing behavior ($t_{1/2} \approx 50$ s) had demonstrated the ability to stimulate cell activity and accelerate bone regeneration. [28] Besides, reversible dynamic bonds were employed to dissipate energy during hydrogel deformation and thus improve fracture toughness, which has been repeatedly observed in double network hydrogels[38-43] and polymer/silica hydrogel systems[44]. Previous research work by DLS has shown that hydrogels typically possess a fast dynamic behavior but some of them can feature additional slower dynamics.[45] Fast dynamics, observed repeatedly in gel systems, are believed to be caused by diffusion or cooperative diffusion of polymer chains. However, slow dynamics were poorly understood but had been repeatedly observed in semi-dilute or concentrated polymer systems by DLS. [45, 46] There are several suggested origins of slow dynamics, such as restricted motion of interacting polymer chains,[45] relaxations of a transient network,[45] diffusion of large polymer aggregates,[45] long-distance concentration fluctuations,[47] aggregations of charged polymers,[46] and even diffusion of dust particles[45]. Yet, the concepts and mechanisms of slow dynamics have not been fully established.

X-ray photon correlation spectroscopy (XPCS) has emerged as an effective technique that applies coherent X-ray synchrotron beams to acquire structural dynamics of soft materials by tracking scattering intensity fluctuations and time correlation.[48-52] The shorter wavelength nature of XPCS allows it to easily access motions of materials on a smaller length scale (~1 nm), measure cloudy and opaque materials and avoid the influence caused by dust, which is difficult to be achieved by

DLS. XPCS has been employed to investigate dynamics behaviours of polymer melts,[48, 53] colloids,[50] Newtonian nanoparticle fluids,[54] particles in elastomers,[55] polymer film,[56], and gels[29]. In recent years, XPCS and rheology have been combined and harnessed to investigate structural relaxation dynamics and stress relaxation dynamics in various polymer systems, respectively. For instance, Patel *et al* studied polystyrene-*block*-polyisoprene copolymer with hexagonally closed packed cylinder (HEX) microstructure and found that the structural relaxation time by XPCS was 1-2 order magnitude larger than the terminal stress relaxation by bulk rheology, indicating the structural dynamics was slower than stress dynamics. They reported that the structural relaxation time was primarily caused by micelles diffusion and the stress relaxation was contributed by disordered concentration fluctuations. In addition, they suggested that stress relaxation comprised multiple relaxation processes across various time and length scales, resulting in a smaller stress relaxation time.[49] In a different polymer system, Quah et al observed a different phenomenon in commercial PEO-PPO-PEO triblock copolymer F-127, the structural relaxation time scales measured by XPCS did not show the corresponding crossover frequency by conventional rheology. They estimated a crossover frequency by extrapolating G'' to a lower frequency outside the measurable range and found a smaller stress relaxation time. They suggested that structural dynamic was more rapid at small length scales compared to stress dynamics at the macroscale.[29] In recent years, dynamic behaviors during a disorder-order transition of block polymers have attracted increasing attention, especially block polymers with ordered microstructures (e.g., body-center cubic (BCC), hexagonally closed packed cylinders (HEX), and lamellae (LAM)). Lewis III *et al* used XPCS to investigate the diblock polymer melt with BCC microstructure, and they observed speed distribution within a sample. They believed the speed distribution was caused by

BCC grain boundary migration.[53] Sanz et al discovered that a better-defined LAM microstructure could result in a slower diffusive motion owing to interfacial diffusion of chain segments.[57] With a similar LAM microstructure, Oparaji *et al* observed a hyperdiffusive motion in the diblock polymers doped with different lithium salt concentrations and at different temperatures. They attributed this behaviour to cooperative dynamics, more specifically grain rotation. Overall, despite the development of recent progress, it would require much effort to gain insights into the interplay relationship between dynamics and microstructures of hydrogels.

In this work, polyelectrolyte complexes (PEC) hydrogels, which were prepared by mixing oppositely charged *ABA* triblock polyelectrolytes, were exploited to investigate the relationship between microstructures and relaxation dynamics owing to their tunable microstructures. Block *A* was functionalized with either ammonium or sulfonate moieties via thiol-ene click reactions, and block *B* consists of neutral poly (ethylene glycol) (PEO) block. The oppositely charged blocks *A* rapidly attract each other by electrostatic interaction and form polyelectrolyte complex domains upon mixing, serving as physical cross-links of three-dimensional polymer networks. We systematically acquired the information on microstructures and structural relaxation dynamics with varying polymer concentrations, salt concentrations, and charged block length by SAXS and XPCS. Besides, rheology was applied to characterize stress relaxation behaviours, wherein the stress relaxation time scales were similar to or smaller than those measured by XPCS. We discovered a coupling relationship between relaxation dynamics and LAM microstructure, in which the lamellar structures coexisted with the double-mode relaxation behaviours. These findings provide a deeper understanding of how polymer concentration and salt content affect the microstructures of PEC domains and structural relaxation dynamics at the same time.

6.2 Material and Method

Triblock Polyelectrolytes Synthesis*:* The synthesis method of polyelectrolytes was based on previous studies.[58, 59] First, 20 grams of dried poly(ethylene oxide) (PEO, MW 20,000) was dissolved in around 60 mL anhydrous tetrahydrofuran (THF) at 45 °C in a glove box with low huminity and Argon gas. The PEO solution in a 250 mL round bottom flask was titrated with potassium naphthalenide until the solution color became light green. Then, anhydrous allyl glycyl ether (AGE) was added to the PEG-dialkoxide macroinitiator solution to make poly(allyl glycidyl ether)$_m$-polyethylene glycol$_{455}$- poly(allyl glycidyl ether)$_m$ (PAGE$_m$-PEO$_{455}$-PAGE$_m$) via anionic polymerization. The polymerization was allowed to run for two days and then terminated by degassed methanol. The PAGE$_m$-PEO$_{455}$-PAGE$_m$ was precipitated in hexane solvent, filtered, and dried in vacuum.

Ammonium or sulfonate-funcitonalized PAGE$_m$-PEO$_{455}$-PAGE$_m$ was synthesized by thiol-ene click reactions. 2 grams of PAGE$_m$-PEO$_{455}$-PAGE$_m$, an appropriate amount (5 Equiv. per alkene) of functional thiol reactants, photoinitiator 2,2-dimethoxy-2 phenylacetophenone (0.05 equiv. per alkene) were dissolved in a mixture of water and Dimethylformamide (DMF) with volume ratio of 1 : 1. The mixture solution was degassed by nitrogen gas for 30 minutes. Cysteamine hydrochloride and sodium 3-mercapto-1-propanesulfonate were used as thiol reactants for ammonium and sulfonate functionalization, respectively. The solutions were exposed under ultraviolet (UV) light (365 nm, 8 watt) for at least 6 hours to complete thiol-ene click reactions. The ammonium or sulfonate functionalized PAGE$_m$-PEO$_{455}$-PAGE$_m$ product solution was first dialyzed against deionized water for 14 cycles and then lyophilized. The final products were characterized by ^{1}H NMR (**Figures 6-S1 and 6-S2**).

X-ray Photon Correlation Spectroscopy (XPCS)

XPCS experimental results were collected at the Sector 8-ID of the Advanced Photon Source (APS), Argonne National Laboratory. The PEC hydrogels were loaded into the 3 mm diameter holes of the aluminum strip with both sides sealed with Kapton tapes to avoid water evaporation. The distance between samples and detector was set to 3.9 m to obtain the wave vector q. The coherent 11 keV X-ray with a beam size of 15 x 15 um^2 was shined into samples. The X-ray scatterings were collected with a large area Medipix based detector array (LAMBDA, 516 × 1556 pixels, each pixel size is 55 um). The time autocorrelation function g_2 was analyzed at the principal peak q^* to acquire clear and reliable data information. The g_2 experimental data, outside the vicinity of q^*, were not represented and discussed in this article due to weak scattering and noised data.

Rheology Characterization

Rheological information was collected by Anton Paar (MCR 302) with a cone plate (diameter 25mm, cone angle 2°) at room temperature (25 °C). A solvent trap was used to reduce water evaporation during measurement. Oscillatory Amplitude sweep tests were performed at ω=1 rad/s to determine the linear viscoelastic regime. Oscillatory frequency sweeps (0.01-100 Hz) were measured within the strain in the linear viscosity region.

6.3 Results and Discussion

Previous studies have suggested that relaxation dynamics exhibit a close relationship with mechanical properties and structure of complex coacervate materials,[32, 33] but the relationship remains poorly understood owing to little knowing their microstructures. In order to systematically

clarify this relationship, the PEC hydrogels with varied polymer concentration and salt concentration were characterized by XPCS and SAXS to acquire information on structural relaxation dynamics and microstructures, respectively. The PEC hydrogels were prepared by mixing ammonium and sulfonate-functionalized $PAGE_m$-PEO_{455}-$PAGE_m$ with a molar charge ratio of 1:1, where m represents the repeating unit of the PAGE block. Both cationic and anionic polyelectrolytes were derived from the same parent polymer ($PAGE_m$-PEO_{455}-$PAGE_m$) via thiol-ene reactions. This feature not only eliminated the uncertainty of mismatched polymer chain length and stoichiometry issues but also ensured similar inter-domain distance and predictability of PEC domain properties.[58] Due to the highly-dense polymer chains inside the PEC domains and the high electron number of nitrogen and sulfonate atoms, their sizes, microstructures, and dynamics were capable to be measured by synchrotron X-ray techniques, SAXS, and XPCS.[59]

A high brightness coherent X-ray source (APS) provided the possibility to probe dynamics of soft matter by recording the speckles fluctuations on the detectors in an XPCS experiment. The pixel positions on the detector were typically arranged in the cartesian coordinates. Here, the pixels were positioned in the polar coordinates, wherein the center of the polar coordinate was the incident beam position ($q = r = 0$). Thus, the pixel location was expressed by radial distance r and azimuthal angle φ. Therefore, $g_2(q, t)$ could be expressed as

$$g_2(q,t) = \frac{\langle I_{r\phi}(q(r,\phi),t_1) I_{r\phi}(q(r,\phi),t+t_1)\rangle_{t_1,\phi}}{\langle I_{r\phi}(q(r,\phi),t_1)\rangle_{t_1,\phi}\langle I_{r\phi}(q(r,\phi),t+t_1)\rangle_{t_1,\phi}} \qquad (1)$$

Equation 1 was typically used to compute g_2 by azimuthally averaging isotropic scattering patterns. However, the ordering of PEC domains produced anisotropic 2-D scattering patterns in company

with Bragg reflection peaks, which caused Equation 1 to be invalid. Therefore, Equation 1 was modified as a function of *r*, *φ*, and *t*, as shown in Equation 2.

$$g_2(q,t) = \frac{\langle I_{r\phi}(q(r),\phi,t_1) I_{r\phi}(q(r),\phi,t+t_1)\rangle_{t_1,\phi}}{\langle I_{r\phi}(q(r),\phi,t_1)\rangle_{t_1,\phi}\langle I_{r\phi}(q(r),\phi,t+t_1)\rangle_{t_1,\phi}} \qquad (2)$$

The normalized $g_2(q(r), \varphi, t)$ exhibited an independence of the azimuthal anisotropy feature of intensity $I(q, \varphi)$. Therefore, the ordering of the PEC domain had little influence on the local thermal fluctuations and resulted in the decorrelation of $I(q, \varphi)$. The φ-independent isotropic feature of $g_2(q(r), \varphi, t)$ permits the possibility to integrate and an average of all $g_2(q(r), \varphi, t)$ functions to a single function, $g_2(q, t)$.

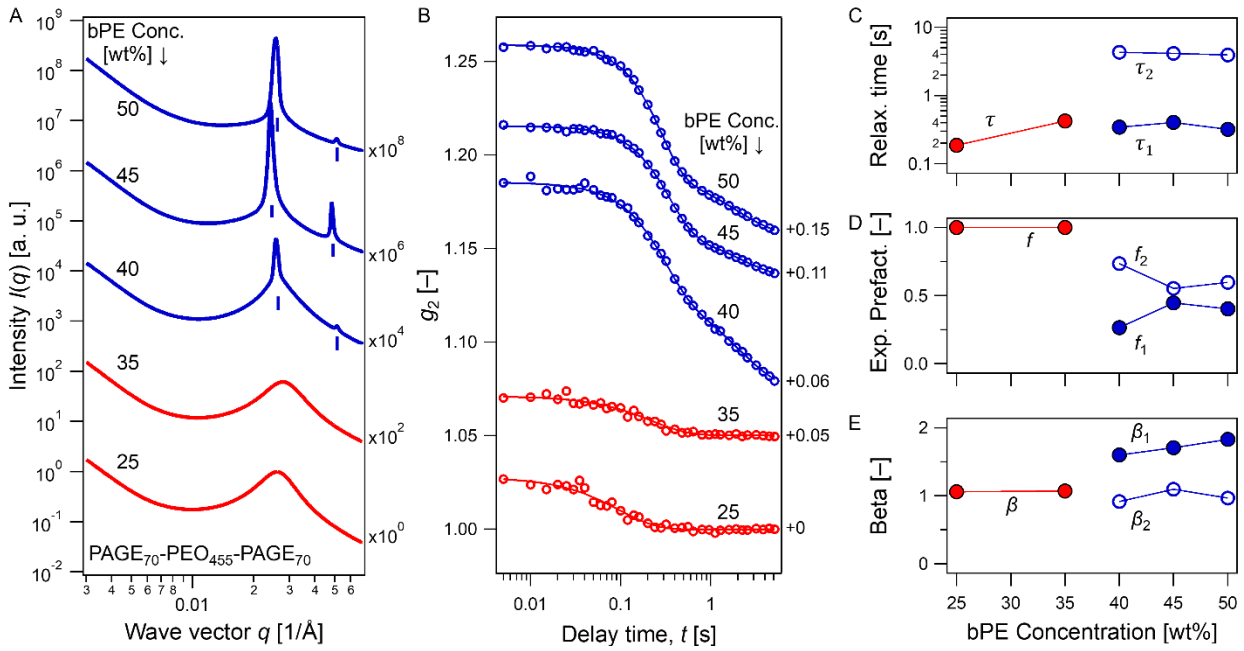

Figure 6-1. Microstructure and relaxation of $PAGE_{70}$-PEO_{455}-$PAGE_{70}$ hydrogels. (A) One-dimensional small-angle X-ray scattering intensity $I(q)$ versus wave factor q of the PEC hydrogels at C_{bPE} from 25 wt% to 50 wt%. $I(q)$ were scaled vertically for clarity based on the scale factors labelled on the right axis. (B) Intensity-intensity time autocorrelation function, $g_2(q^*,t)$ and corresponding fitting function $g_{2,fit}(q^*,t)$ versus delay time t of C_{bPE} from 25 wt% to 50 wt%. Both $g_2(q^*,t)$ and $g_{2,fit}(q^*,t)$ were shifted vertically for clarity according to the values labeled on the right axis. The fitting parameters, (C) Relaxation time (τ), (D) Exponential pre-factors f_1 and f_2, and (E) Stretching exponential (β) were plotted against polyelectrolyte concentration.

6.3.1 Coupling Relationship between Microstructure and Dynamic Mode

An examination of the static scattering profiles from the $PAGE_{70}$-PEO_{455}-$PAGE_{70}$ PEC hydrogels with increasing C_{bPE} revealed a morphological and ordering transition of the PEC domains from disordered spheres to parallelly arranged lamellae. As shown in **Figure 6-1A**, $I(q)$ from the PEC hydrogels with C_{bPE} = 25 wt% and 35 wt% had a broad peak near $q = 0.028$ Å^{-1}, indicating the presence of the PEC domains in the three-dimensional network and revealing their spherical shape and disordered arrangements in the network, as quantified by fitting the $I(q)$ spectra with a sphere form factor $P(q)$ and hard sphere structure factor $S(q)$ (see Supplementary Information for details). When C_{bPE} was increased to 40 wt% and above, the primary peak sharpened prominently and a secondary peak appeared in the q range of 0.05-0.06 Å^{-1}. These peaks are indicated by short vertical bars in **Figure 6-1A**, and their sharpening and appearance indicate an ordering transition leading to emergence of the Bragg scattering. Moreover, the secondary peaks in the 40 wt% $\leq C_{bPE} \leq$ 50 wt% $I(q)$ spectra appeared at exactly twice the location of the primary peak (q^*), indicating the presence of parallelly arranged lamellar PEC domains in these hydrogels. Similar morphological and ordering transition have been previously reported in the PEC hydrogels,[59] induced by variations in block polyelectrolyte length and concentrations, salt concentration and pH, and the presence of (interacting or inert) additives in the hydrogels.

The scattering intensity autocorrelation functions, revealing the relaxation dynamics in PEC hydrogels, exhibited an intriguing correlation with the static scattering from the PEC hydrogels. **Figure 6-1B** shows the normalized autocorrelation functions, g_2, obtained at $q = q^*$ of each hydrogel, for $PAGE_{70}$-PEO_{455}-$PAGE_{70}$ hydrogels with increasing C_{bPE}. For the $C_{bPE} \leq$ 35 wt% hydrogels that comprise disordered arrangements of spherical PEC domains (red curves in **Figure**

6-1A), the g_2 curves featured a single step decay in the vicinity of 0.05 – 0.5 s (red curves in **Figure 6-1B**). For the $C_{bPE} \geq 40$ wt% hydrogels that featured parallelly stacked lamellar PEC domains (blue symbols in **Figure 6-1A**), however, the g_2 curves exhibited a two-step decay, with a fast decay in the vicinity of 0.05 – 0.5 s followed by a slow decay in the vicinity of 0.5 – 5 s (blue symbols in **Figure 6-1B**).

The correlation between the PEC domain microstructure and their relaxation behaviors was further explored by quantitative analysis of the g_2 curves to obtain the intermediate scattering function F as

$$g_2(q^*, t) = a + kF^2(q^*, t) \qquad (3)$$

where a and k are the baseline and Siegert factor, respectively. F was further described as a single stretched exponential decay or a linear combination of two stretched exponential decays (Eq. 4 and Eq. (5), respectively) as:

$$F(q^*, t) = f \exp - \left(\frac{t}{\tau(q^*)}\right)^{\beta(q^*)} \qquad (4)$$

$$F(q^*, t) = f_1 \exp - \left(\frac{t}{\tau_1(q^*)}\right)^{\beta_1(q^*)} + f_2 \exp - \left(\frac{t}{\tau_2(q^*)}\right)^{\beta_2(q^*)} \qquad (5)$$

Here τ, τ_1, and τ_2 are the characteristic relaxation times, β, β_1, and β_2 are the stretching exponents, and f, f_1, and f_2 are the exponential pre-factors such that $f = 1$ and $f_1 + f_2 = 1$.[32, 60, 61] f_1 and f_2 thus represent the fraction of fast dynamics and slow decay, respectively. The values of the characteristic relaxation times, stretching exponents and the exponential pre-factors, as

obtained from fits to the data shown in **Figure 6-1B** with Eq. 3 combined with either Eq. 4 or Eq.5, are summarized in **Figures 6-1C-E**.

The characteristic relaxation time τ for the g_2 exhibiting single step relaxation were found to be in the range of 0.2 - 0.5 s. These τ values were similar to the faster characteristic relaxation time τ_1 for the g_2 exhibiting two-step relaxation. Thus, it can be surmised that the fast relaxation processes occurred in both disordered and ordered PEC hydrogels. Moreover, the relaxation time increased with C_{bPE} from 25 wt% to 35wt%, as expected with increasing density of the PEC domains, but then became nearly independent of C_{bPE}. The slower characteristic relaxation time τ_2 for the g_2 exhibiting two-step relaxation were found in the range of 5 s, approximately one order of magnitude slower than τ and τ_1.

The faster and slower relaxation processes both contributed substantially to the overall relaxation in the ordered hydrogels. Rather counterintuitively, the slower relaxation processes contributed most significantly upon the emergence of the two-step relaxation processes, as indicated by f_2 being the highest for the 40 wt% hydrogels (**Figure 6-1D**). At higher C_{bPE}, f_1 and f_2 approached each other, indicating nearly equal contributions from the fast and slow relaxation processes. Surprisingly, we also observed the stretching exponents transition from $\beta \sim 1$ for the single step relaxation to $\beta_1 \sim 1.5$ accompanied with a $\beta_2 \sim 1$ for the faster and the slower relaxation steps, respectively, in the two-step relaxations. These observations were in agreement with previous studies, where $\beta > 1$ was a common feature reported in the jammed polymer system.[62]

A similar transition of g_2 from a one-step to two-step relaxation was observed upon the ordering transition in PEC hydrogels composed of oppositely charged triblock polyelectrolytes based on $PAGE_{40}$-PEO_{455}-$PAGE_{40}$ (**Figure 6-S3**), which possessed a shorter charged block length.

Expectedly, as the charged blocks were shorter, the PEC domain size and interdomain distances were smaller as well, resulting in the primary $S(q)$ peak and the primary Bragg peak being located at a slightly higher q. Nevertheless, similar trends as those observed for the $PAGE_{70}$-PEO_{455}-$PAGE_{70}$ hydrogels were noted in these systems, with (i) the faster relaxation timescale τ_1 in the two-step relaxation processes being similar to the relaxation timescale for the single step relaxation τ, (ii) the slower relaxation timescale τ_2 approximately 10 times larger than the τ_1 regardless of charged block length and polymer concentration, and (iii) coupling relationship between the lamellar microstructure and double-mode relaxation.

The PEC domains contain high concentration of the polyelectrolyte endblocks comprising high atomic number elements, such as sulfur, nitrogen and oxygen. Therefore, the information acquired by SAXS and XPCS largely reflect the physical properties and relaxation dynamics of the PEC domains. Moreover, the relaxation dynamics reported here were obtained at a length scale ~26 nm and ~22 nm for the $PAGE_{70}$-PEO_{455}-$PAGE_{70}$ hydrogels and the $PAGE_{40}$-PEO_{455}-$PAGE_{40}$ hydrogels, respectively, as estimated by $2\pi/q^*$ which corresponded to the average inter-domain distances in the hydrogels. It is expected that the interconnected nature of PEC domains in the networks limit their displacement larger than inter-domain distance, in the absence of an external force. Therefore, the relaxation dynamics in the disordered hydrogels were attributed to the thermally induced relaxation of PEC the domains around their mean positions.

The fast dynamics always occurred regardless of polymer concentration and PEC domain microstructure, while the slow dynamics only emerged in the ordered hydrogels. The similarity of the timescales of the fast relaxation in the disordered and ordered hydrogels also pointed towards a similar relaxation mechanism at play in these systems. At the same time, in the ordered hydrogels,

we also expect the PEC lamellae to form microcrystalline domains (or grains), and the relaxation of these microcrystalline grains is hypothesized to occur through slow rearrangements contributed by motion along the grain boundaries. Therefore, we hypothesize that the two step relaxation observed in the ordered hydrogels emerges from a combination of fast relaxing disordered spherical PEC domains and slow relaxing microcrystalline grains of PEC lamella, both of which coexist in the $PAGE_{70}$-PEO_{455}-$PAGE_{70}$ hydrogels with $C_{bPE} \geq 40$ wt%.

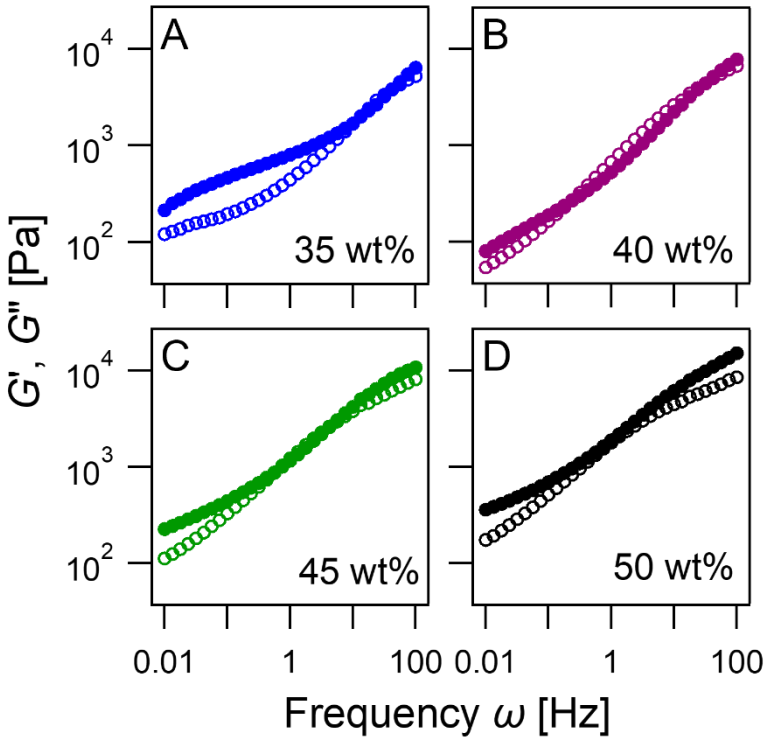

Figure 6-2. Frequency sweeps for $PAGE_{70}$-PEO_{455}-$PAGE_{70}$ hydrogels with varying polymer concentrations, C_{bPE} = 25 and 45wt%, in the linear viscoelastic regime. The open and closed symbol denoted the storage (G') and loss moduli (G"), respectively.

Coexisting PEC domain morphologies have been previously reported in PEC hydrogels and have been attributed to a combination of thermodynamic and kinetic origins. The coexisting morphologies can exist in metastable equilibrium and can also result from heterogenous local hydrogel compositions. While the former is expected to be prominent in hydrogels with composition near the morphology transitions, the latter is more prevalent in hydrogels with high polymer concentrations wherein uniform mixing becomes increasingly cumbersome. In this context, the unusual variation of f_1 and f_2 with C_{bPE} for the $PAGE_{70}$-PEO_{455}-$PAGE_{70}$ hydrogels can also be rationalized. It can be expected that with increasing C_{bPE}, the fraction of ordered domains in the hydrogels increases and result in a greater contribution from the slow relaxation to the overall relaxation dynamics. Thus, f_2 can be expected to grow with C_{bPE}, at the expense of f_1. However, we find that f_2 decreases significantly upon C_{bPE} increasing from 40 wt% to 45 wt% before increasing slightly upon increasing C_{bPE} to 50 wt%. We hypothesize that the competition between increasing C_{bPE} leading to a higher fraction of ordered domains and increasing difficulty in achieving homogenously mixed hydrogels result in the unusual behaviors of f_1 and f_2. The similar unusual phenomena were also observed in $PAGE_{40}$-PEO_{455}-$PAGE_{40}$ hydrogels, in which f_2 decreased slightly upon increasing C_{bPE} from 45 wt% to 50 wt%.

These transitions in the relaxation behavior of the PEC hydrogels upon the ordering transition also manifest in their distinct response to oscillatory strain. **Figure 6-2 and Figure 6-S4** shows the frequency (ω) response of $PAGE_{70}$-PEO_{455}-$PAGE_{70}$ hydrogels before and after the ordering transition, at C_{bPE} = 25 and 30 wt%, and at 40, 45, and 50 wt%, respectively. For hydrogels with disordered spherical PEC domains, the storage and the loss moduli, G' and G'', appear to be similar to each other in the high- ω region before settling onto a plateau in the low-ω region. These

observations point towards distinct fast relaxation processes coupled with very slow relaxations that are not captured in the ω window in the disordered hydrogels. Although there was no frequency crossover for 25 wt% $PAGE_{70}$-PEO_{455}-$PAGE_{70}$ hydrogel and 25 wt%, 35 wt% $PAGE_{40}$-PEO_{455}-$PAGE_{40}$ hydrogels (**Figure 6-S5**) within the measured frequency range, it is reasonable to expect a fast stress relaxation behavior in each of these systems, which has been well-known and repeatedly observed in dilute polymer solutions and gel systems. Therefore, a fast stress relaxation, whose crossover frequency was higher than 100 Hz, was expected. In contrast, hydrogels that exhibit an ordered lamellar morphology of the PEC domains have moduli that continually increase with ω and overlap over a large range of ω. Thus, it can be argued that in the ordered hydrogels, there is a continuous spectra of relaxation times associated with stress relaxation processes, possibly arising from the presence of both disordered spherical PEC domains and microcrystals (of varying sizes) of lamellar PEC domains, with a possibility of the fraction of either or the sizes of the latter evolving in response to the external stresses applied on the hydrogels.

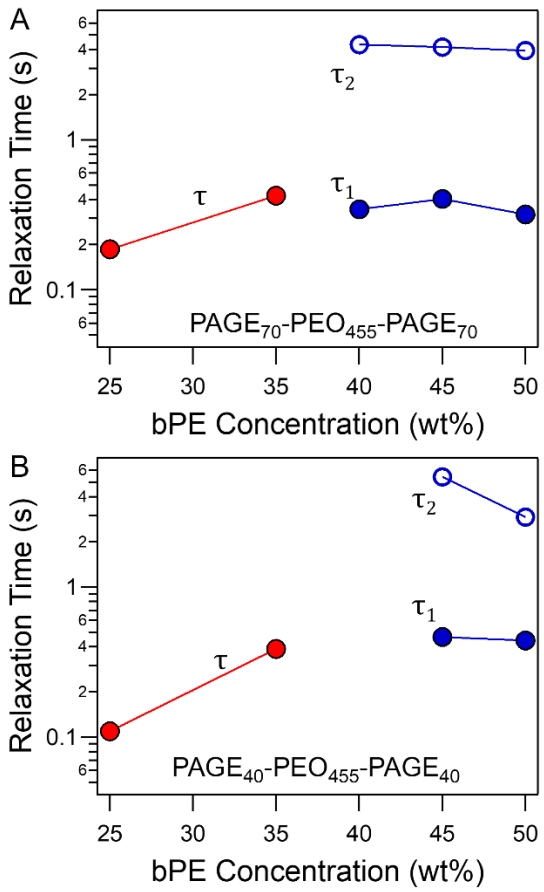

Figure 6-3. Comparison of relaxation times measured by XPCS and rheology for (A) $PAGE_{70}$-PEO_{455}-$PAGE_{70}$ hydrogels and (B) $PAGE_{40}$-PEO_{455}-$PAGE_{40}$ hydrogels.

A characteristic stress relaxation time τ_s for a material can be determined by the frequency of the oscillatory strain, ω_c at which storage modulus (G') and loss modulus (G'') cross over as $\tau_s = 1/\omega_c$. In the case of ordered hydrogels, since we observe a range of ω over which the moduli overlap spanning from ω_2 to ω_1, we define a window of stress relaxation times in these hydrogels spanning from $\tau_{s1} = 1/\omega_{s1}$ to $\tau_{s2} = 1/\omega_{s2}$. As shown in **Figure 6-3**, the stress relaxation window coincides closely with the structural relaxation times for both $PAGE_{70}$-PEO_{455}-$PAGE_{70}$ and $PAGE_{40}$-PEO_{455}-$PAGE_{40}$ ordered hydrogels, indicating that the stress relaxation phenomena in these hydrogels manifest from the nanoscale structural relaxation processes, which in turn comprise the thermal relaxation of the spherical PEC domains in the disordered hydrogels and a combination of thermal motion of the spherical PEC domains and a slow relaxation arising from the rearrangements of the lamellar PEC microcrystals in the ordered hydrogels. These observations are in agreement with previous studies wherein similarity of relaxation timescales from stress relaxation measured by rheology and structural dynamics measured by the XPCS were demonstrated.[49]

6.3.2 Structure and Dynamics of PEC Hydrogels Influenced by NaCl

Addition of salt is an effective approach to control the microstructure, chain relaxation dynamics, and rheology of PEC materials.[63] Salt ions screen the electrostatic interactions among the oppositely charged bPE chains and diminish the entropy gains from the release of counterions bounded in the bPE chains into the surrounding aqueous environment.[64] Consequently, salt ions suppress the complexation and phase separation of bPE chains, hinder the formation of PEC domains, increase the water content in the PEC domains, and induce morphological transition to

lower ordered systems.[64, 65] Moreover, with enhanced screening and weakened interactions between the intrinsic ionic pairs, acceleration of chain relaxation is expected.[66]

The microstructure, dynamics, and rheology of PEC hydrogels were examined by varying salt (NaCl) concentration C_{salt} from 0 mM to 1000 mM in $PAGE_{70}$-PEO_{455}-$PAGE_{70}$ hydrogels with a fixed C_{bPE}. As shown in **Figure 6-4A**, parallelly aligned lamellar PEC domains persisted in PEC hydrogels with C_{bPE}= 45 wt% up till a C_{salt} = 600 mM, but the static scattering from hydrogels with $C_{salt} \geq$ 800 mM indicated an absence of Bragg peaks, indicating disordered spherical PEC domains comprising the three-dimensional network in these hydrogels. Correspondingly, the g_2 curves transitioned from a two-step decay behavior to a single-step decay upon increasing the C_{salt} > 600 mM (**Figure 6-4B**), denoting vanishment of double-mode relaxation.

In both double- and single-mode relaxations, the fast structural dynamics were observed across C_{salt} ranging from 0 mM to 1000 mM (**Figure 6-4C**). However, the slow structural dynamics disappeared upon transition from ordered to disordered PEC domains when C_{salt} was increased from 600 mM to 800 mM. Interestingly, we observed that both τ_1 and τ_2 remained stable values at 0 mM $\leq C_{salt} \leq$ 600 mM where the double-mode relaxation existed (**Figure 6-4B**). In a saline environment, the time scale of τ_2 was around one magnitude larger than that of τ_1, which was

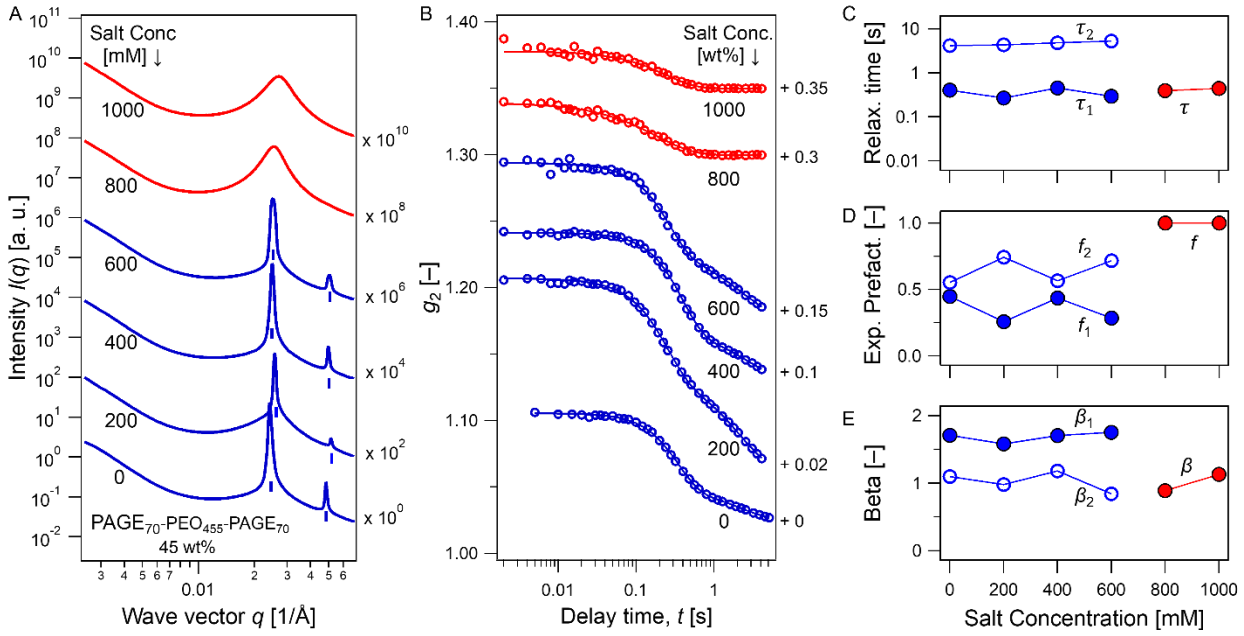

Figure 6-4. Microstructures and dynamics of 45 wt% PEC hydrogels with C_{salt} from 0 mM to 1000 mM. (A) $I(q)$ versus q. (B) $g_2(q^*,t)$ and corresponding $g_{2,fit}(q^*,t)$ versus delay time t. (C) Relaxation time (τ), (D) Exponential pre-factors f_1 and f_2, and (E) Stretching exponential(β) were the fitting parameters obtained for the $g_{2,fit}(q^*,t)$. The $I(q)$, $g_2(q^*,t)$, and $g_{2,fit}(q^*,t)$ were scaled vertically for clarity based on the factors labeled on the right axis.

similar in a salt-free environment. At $C_{salt} \geq$ 800 mM,τ_2 disappeared owing to vanishment of double-mode relaxation, and τ_1 remained the similar values. This indicated that although addition of salt could accelerate chain dynamics, it had limited influence on the relaxation behaviors of PEC domains and crystalline grains. Upon increasing C_{salt} from 0 mM to 600 mM, f_1 and f_2 varied slightly but remained relatively stable (**Figure 6-4D**). Similar phenomena were also observed in β_1 and β_2 (**Figure 6-4E**). The relative stability of (1) f_1 and f_2 or (2) β_1 and β_2 also reflected that increasing salt loading had a limited impact on the relaxation behaviors and fractions of PEC domains and crystalline grains.

The frequency response of the salt-doped PEC hydrogels followed a similar evolution with C_{salt} as was observed with decreasing C_{bPE}. Broad regions of G' and G'' overlap were observed in the frequency sweeps for PEC hydrogels with $C_{salt} \leq$ 400 mM, while a liquid-like response with a small characteristic relaxation time was observed for the gels with $C_{salt} \geq$ 600 mM (**Figure S6**). The stress relaxation time window for the PEC hydrogels with $C_{salt} \leq$ 400 mM coincided closely with τ_1 and τ_2 from XPCS. The behavior of the PEC hydrogel with C_{salt} = 600 mM was intriguing, as it exhibited an ordered microstructure and a two-step relaxation in g_2, but a liquid-like response in oscillatory rheology experiments. We attribute this behavior to two reasons: (i) C_{salt} = 600 mM was closed to the critical salt concentration separating the ordered and disordered microstructure and the single- or two-mode relaxation behavior, and (ii) the external force applied during rheology measurements may accelerate the relaxation dynamics of the PEC domains but also their morphological rearrangements. Therefore, the two-mode relaxation in the quiescent state in the C_{salt} = 600 mM hydrogels transitions into a single mode relaxation under stress. Overall, the relaxation time scales and relaxation modes by rheology were in agreement with the ones acquired

by XPCS. Both experiments reflected the coupling relationship between the microstructure and relaxation modes in a saline environment.

6.4 Conclusion

In this contribution, XPCS and SAXS were employed to investigate structural relaxation and microstructures, respectively. We found a strong correlation between the occurrence of the disordered spheres microstructure and the single-mode relaxation, while the two-mode relaxation coupled strongly with the presence of lamellar PEC domains. The relaxation timescale in the single-mode relaxation was comparable to the fast structural relaxation in the two-mode relaxation, indicating this type of fast dynamics existed regardless of microstructures. The fast dynamic behavior was mostly attributed to the thermally induced motion of the PEC domains. In comparison, the slow dynamics is hypothesized to emerge from the slow motion of the lamellar microcrystalline grains along the grain boundaries. The coupling between the relaxation processes and microstructures was observed either with varying polymer concentrations or salt content in the hydrogels. Moreover, the stress relaxation time scales were comparable to or smaller than those structural relaxation measured by XPCS, corroborating the hypothesis that the overall relaxation in PEC hydrogels comprises a combination of fast thermal motion of the PEC domains, slow rearrangements of the ordered PEC microcrystals, and very slow chain exchange between the PEC domains.

6.5 Supplementary Information

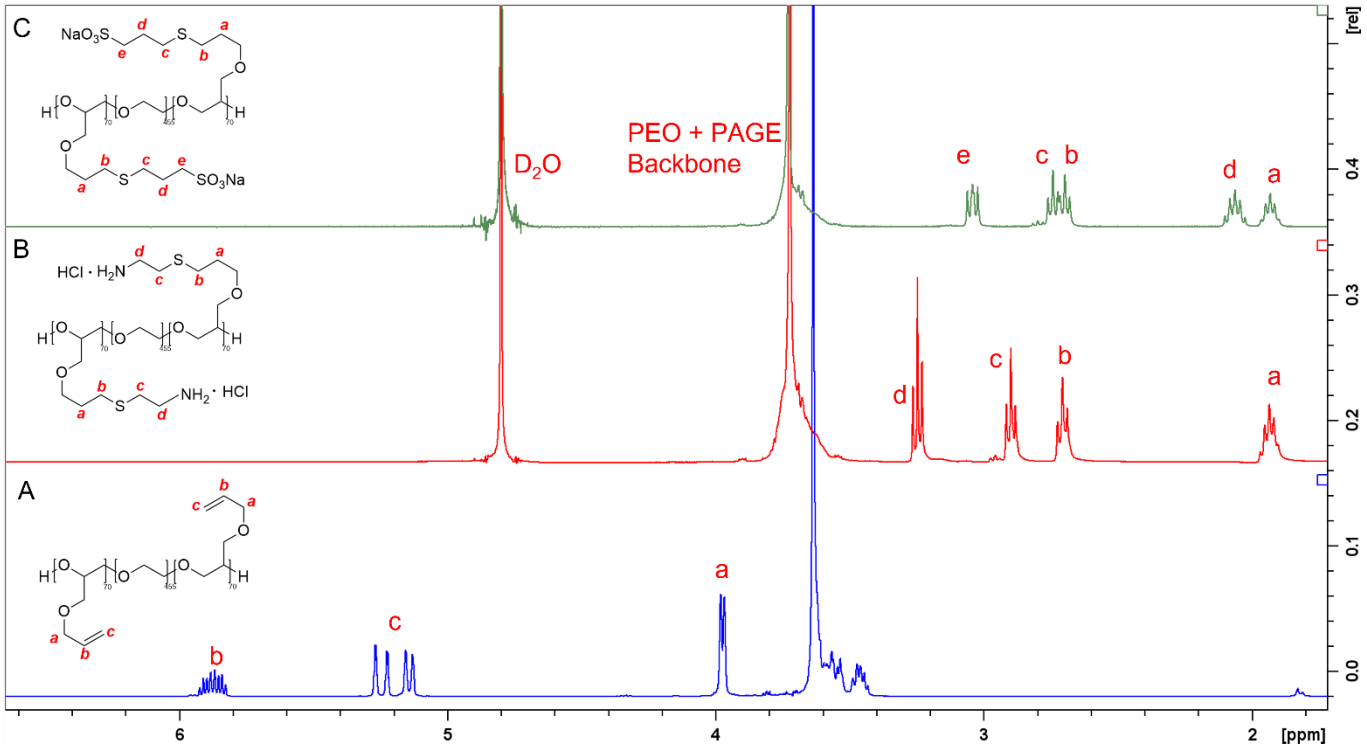

Figure 6-S1. ^{1}H NMR spectroscopy of **(A)** $PEGA_{70}$-PEO_{455}-$PAGE_{70}$ triblock polymer and its **(B)** ammonium and **(C)** sulfonate functionalized derivatives.

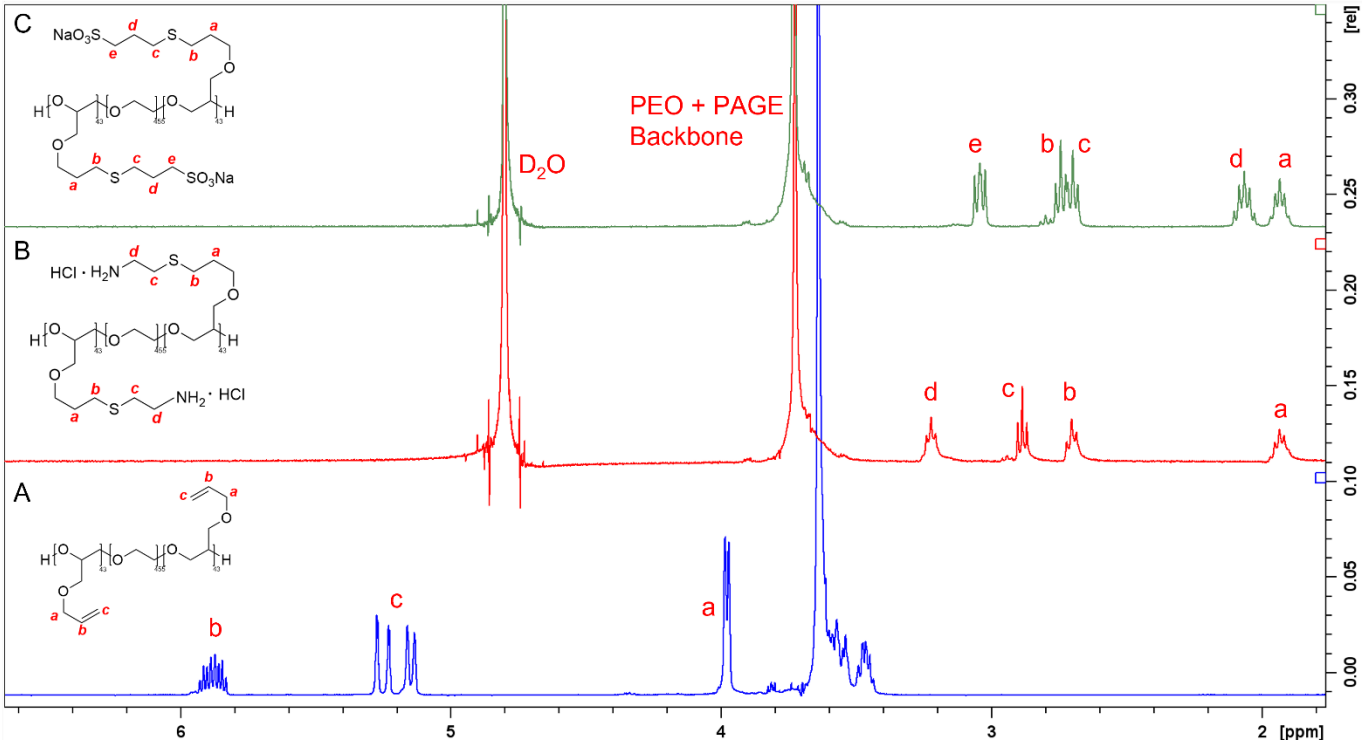

Figure 6-S2. ^{1}H NMR spectroscopy of **(A)** $PEGA_{43}$-PEO_{455}-$PAGE_{43}$ triblock polymer and its **(B)** ammonium and **(C)** sulfonate functionalized derivatives.

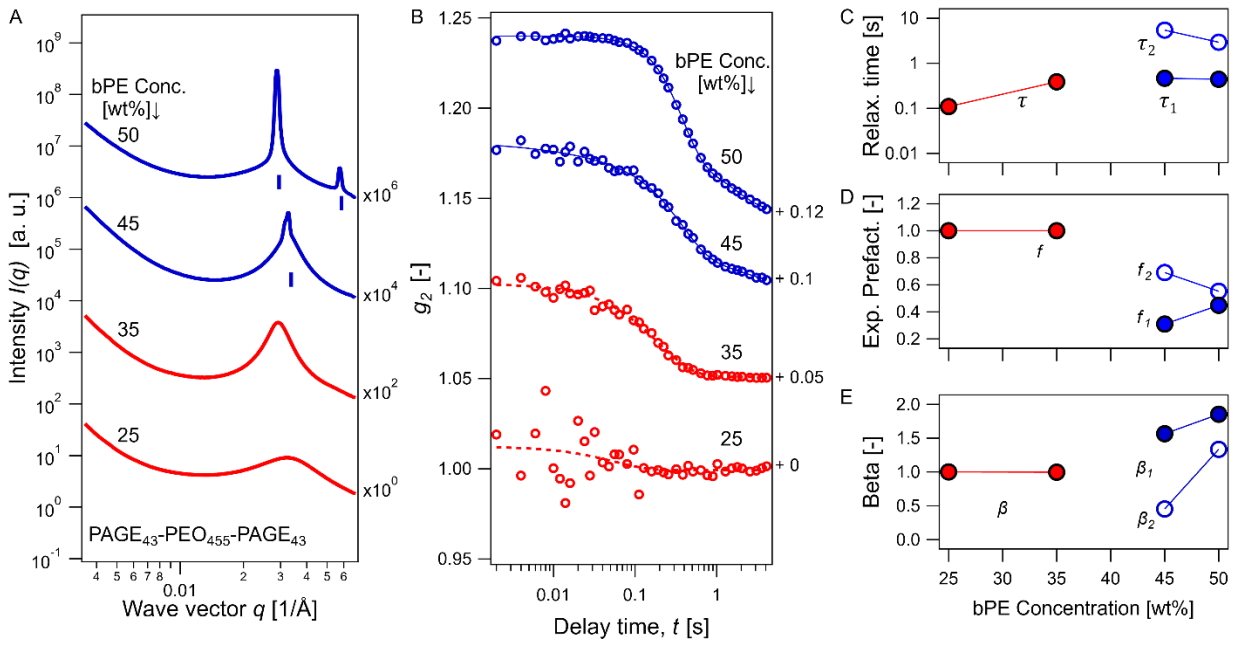

Figure 6-S3. Microstructure and relaxation of PEGA$_{43}$-PEO$_{455}$-PAGE$_{43}$ PEC hydrogels with C_{bPE} varied from 25 wt% to 50 wt%. (A) One-dimensional small-angle X-ray scattering intensity $I(q)$ versus wave factor q. (note: the 45 wt% PEGA$_{43}$-PEO$_{455}$-PAGE$_{43}$ should have a secondary peak 2q* but it was slightly outside the q range. This has been further confirmed by another SAXS scattering in Figure S7.) (B) Intensity-intensity time autocorrelation function, $g_2(q^*,t)$ and corresponding fitting function $g_{2,fit}(q^*,t)$ versus delay time t. The fitting parameters, (C) Relaxation time (τ), (D) Exponential pre-factors f_1 and f_2, and (E) Stretching exponential(β) were plotted against polyelectrolyte concentration. $I(q)$, $g_2(q^*,t)$, and $g_{2,fit}(q^*,t)$ were shifted vertically for clarity based on the scale factors labeled on the right axis.

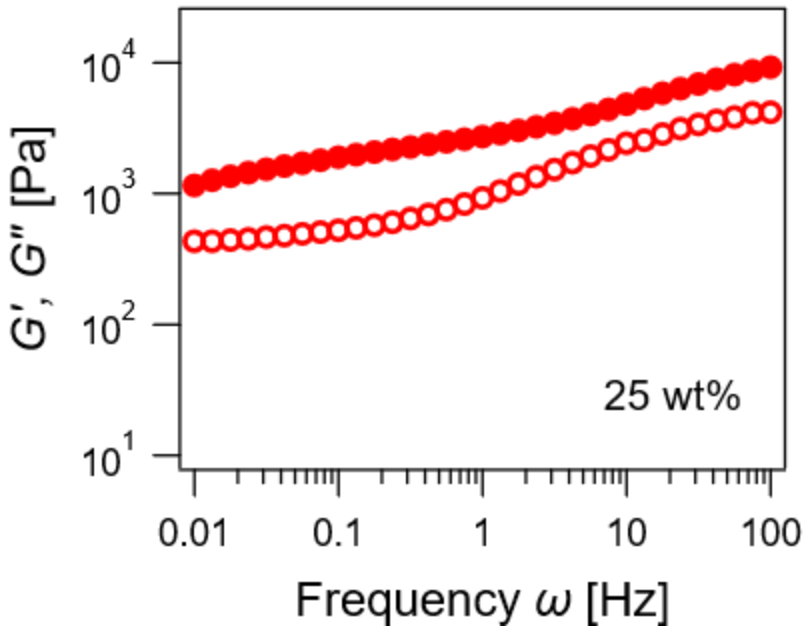

Figure 6-S4. Frequency sweeps for $PAGE_{70}$-PEO_{455}-$PAGE_{70}$ hydrogels with varying polymer concentrations, C_{bPE} = 25 wt%, in the linear viscoelastic regime . The open and closed symbol denoted the storage (G') and loss moduli (G''), respectively.

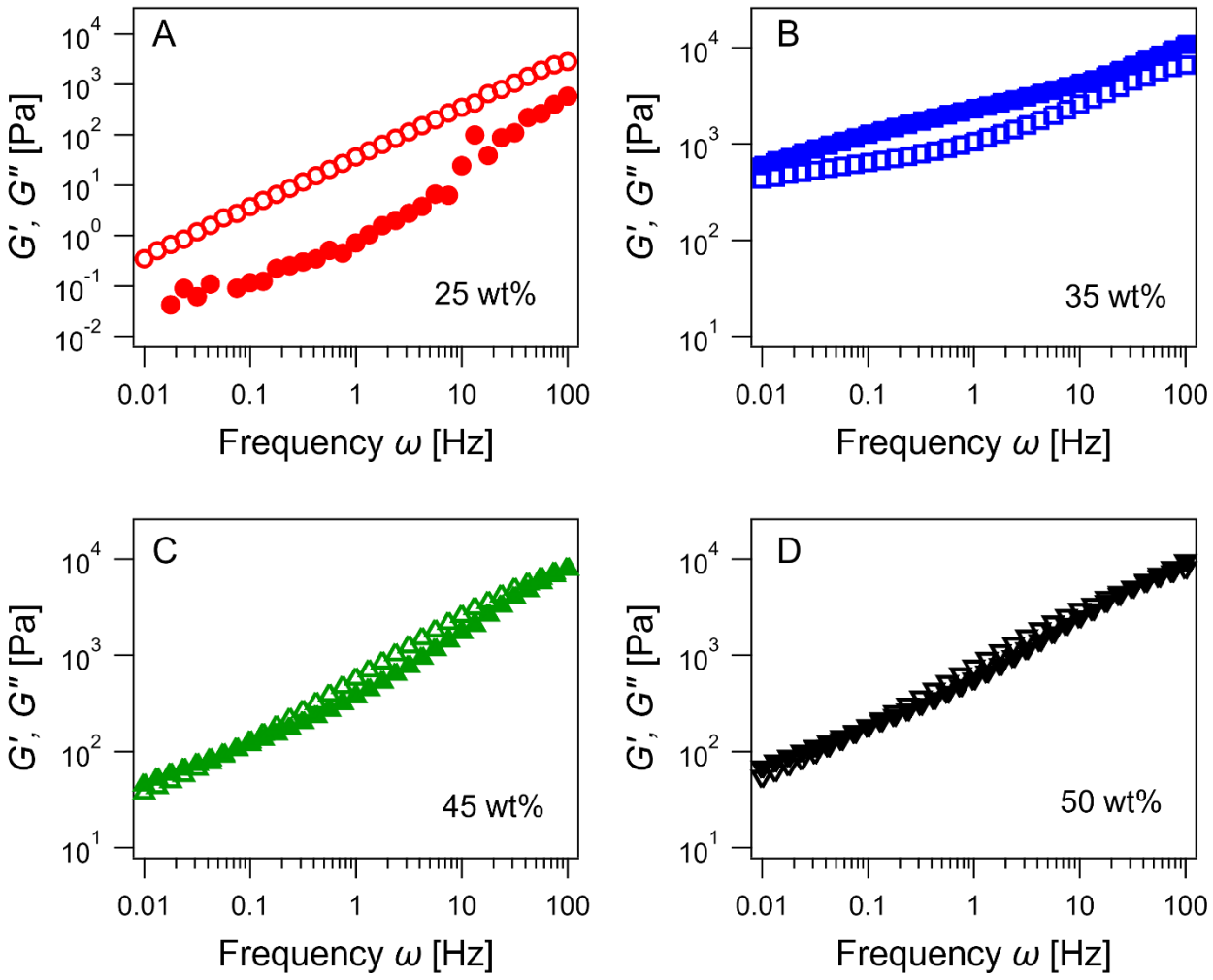

Figure 6-S5. Frequency sweeps of $PAGE_{43}$-PEO_{455}-$PAGE_{43}$ hydrogels in different polymer concentrations , (A) 25 wt%, (B) 35 wt%, (C) 45 wt%, and (D) 50 wt%.

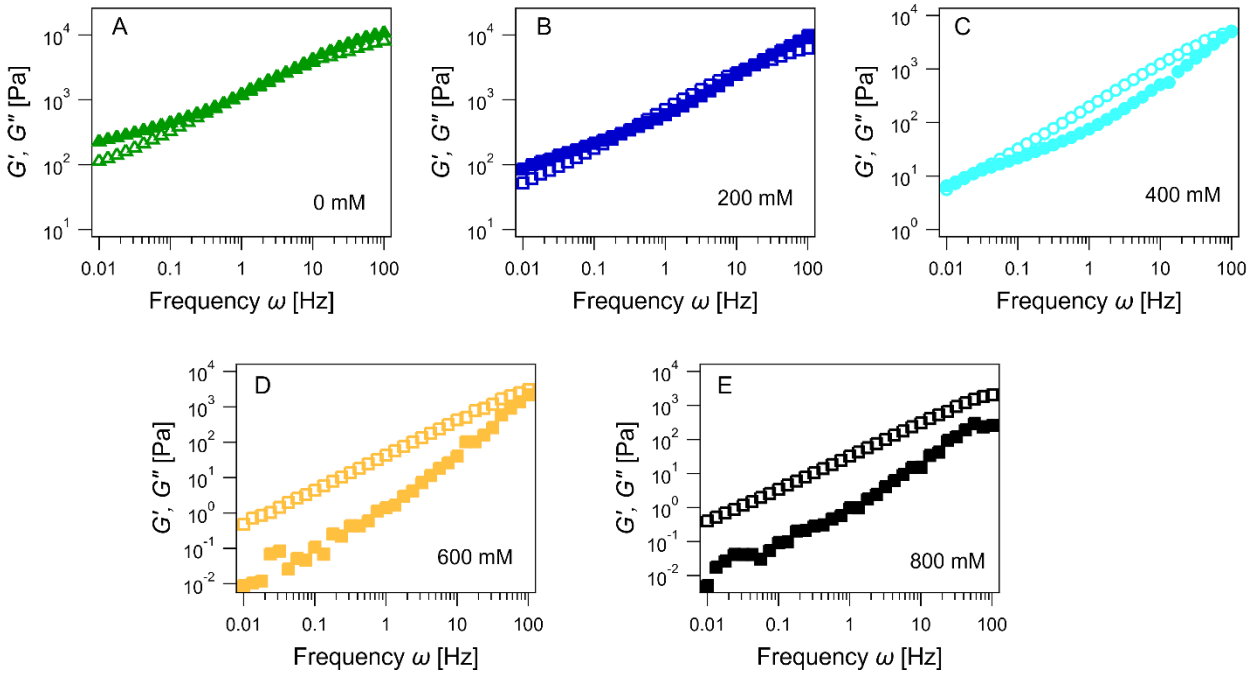

Figure 6-S6. Frequency sweeps for 45 wt% $PAGE_{70}$-PEO_{455}-$PAGE_{70}$ hydrogels with varied salt concentrations, C_{salt} = 0, 200, 400, 600, and 800 mM. The open and closed symbol denotes the storage (G') and loss moduli (G"), respectively.

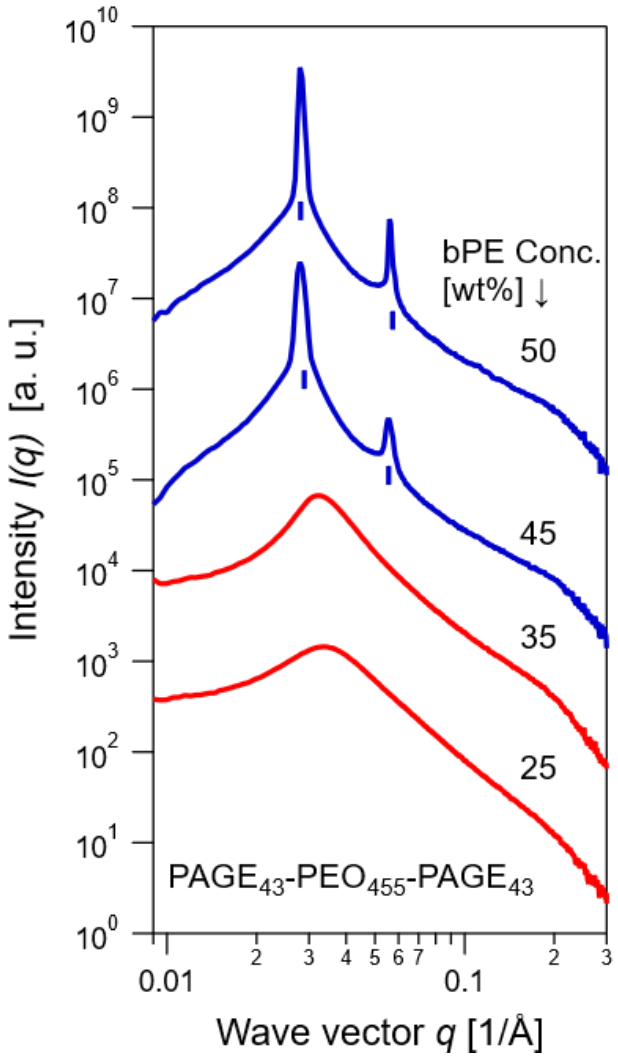

Figure 6-S7. One-dimensional small-angle X-ray scattering intensity $I(q)$ versus wave factor q for $PAGE_{43}$-PEO_{455}-$PAGE_{43}$ hydrogels. This SAXS experiment was performed in 12-ID, Argonne national laboratory.

6.6 Reference

(1) Zhang, Y. S.; Khademhosseini, A. Advances in Engineering Hydrogels. *Science* **2017**, *356* (6337), eaaf3627. DOI: 10.1126/science.aaf3627.

(2) Caló, E.; Khutoryanskiy, V. V. Biomedical Applications of Hydrogels: A Review of Patents and Commercial Products. *European Polymer Journal* **2015**, *65*, 252-267. DOI: 10.1016/j.eurpolymj.2014.11.024.

(3) Ullah, F.; Othman, M. B. H.; Javed, F.; Ahmad, Z.; Akil, H. M. Classification, Processing and Application of Hydrogels: A Review. *Materials Science and Engineering: C* **2015**, *57*, 414-433. DOI: 10.1016/j.msec.2015.07.053.

(4) Kamata, H.; Li, X.; Chung, U.-i.; Sakai, T. Design of Hydrogels for Biomedical Applications. *Advanced Healthcare Materials* **2015**, *4* (16), 2360-2374. DOI: 10.1002/adhm.201500076.

(5) Hoffman, A. S. Hydrogels for Biomedical Applications. *Advanced Drug Delivery Reviews* **2012**, *64*, 18-23. DOI: 10.1016/j.addr.2012.09.010.

(6) Chai, Q.; Jiao, Y.; Yu, X. Hydrogels for biomedical applications: their characteristics and the mechanisms behind them. *Gels* **2017**, *3* (1), 6.

(7) Buwalda, S. J.; Boere, K. W. M.; Dijkstra, P. J.; Feijen, J.; Vermonden, T.; Hennink, W. E. Hydrogels in a Historical Perspective: From Simple Networks to Smart Materials. *Journal of Controlled Release* **2014**, *190*, 254-273. DOI: 10.1016/j.jconrel.2014.03.052.

(8) Dimatteo, R.; Darling, N. J.; Segura, T. In situ Forming Injectable Hydrogels for Drug Delivery and Wound Repair. *Advanced Drug Delivery Reviews* **2018**, *127*, 167-184. DOI: 10.1016/j.addr.2018.03.007.

(9) Burdick, J. A.; Murphy, W. L. Moving from Static to Dynamic Complexity in Hydrogel Design. *Nature Communications* **2012**, *3* (1), 1-8. DOI: 10.1038/ncomms2271.

(10) Koetting, M. C.; Peters, J. T.; Steichen, S. D.; Peppas, N. A. Stimulus-responsive hydrogels: Theory, modern advances, and applications. *Materials Science and Engineering: R: Reports* **2015**, *93*, 1-49.

(11) Rahalkar, A.; Muthukumar, M. Diffusion of Polyelectrolytes in Polyelectrolyte Gels. *Macromolecules* **2017**, *50* (20), 8158-8168. DOI: 10.1021/acs.macromol.7b01310.

(12) Wang, Y.; Zhang, S.; Wang, J. Photo-crosslinkable hydrogel and its biological applications. *Chinese Chemical Letters* **2021**, *32* (5), 1603-1614. DOI: 10.1016/j.cclet.2020.11.073.

(13) Tan, H.; Marra, K. G. Injectable, biodegradable hydrogels for tissue engineering applications. *Materials* **2010**, *3* (3), 1746-1767. DOI: 10.3390/ma3031746.

(14) Klotz, B. J.; Gawlitta, D.; Rosenberg, A. J.; Malda, J.; Melchels, F. P. Gelatin-methacryloyl hydrogels: towards biofabrication-based tissue repair. *Trends in Biotechnology* **2016**, *34* (5), 394-407. DOI: 10.1016/j.tibtech.2016.01.002.

(15) Lee, K. Y.; Mooney, D. J. Hydrogels for Tissue Engineering. *Chemical Reviews* **2001**, *101* (7), 1869-1880. DOI: 10.1021/cr000108x.

(16) Annabi, N.; Yue, K.; Tamayol, A.; Khademhosseini, A. Elastic sealants for surgical applications. *European Journal of Pharmaceutics and Biopharmaceutics* **2015**, *95* (Pt A), 27-39. DOI: 10.1016/j.ejpb.2015.05.022.

(17) Jayakumar, R.; Prabaharan, M.; Sudheesh Kumar, P. T.; Nair, S. V.; Tamura, H. Biomaterials based on chitin and chitosan in wound dressing applications. *Biotechnology Advances* **2011**, *29* (3), 322-337. DOI: 10.1016/j.biotechadv.2011.01.005.

(18) Mehdizadeh, M.; Yang, J. Design Strategies and Applications of Tissue Bioadhesives. *Macromolecular Bioscience* **2013**, *13* (3), 271-288. DOI: 10.1002/mabi.201200332.

(19) Mei, Q.; Rao, J.; Bei, H. P.; Liu, Y.; Zhao, X. 3D bioprinting photo-crosslinkable hydrogels for bone and cartilage repair. *International Journal of Bioprinting* **2021**, *7* (3), 367. DOI: 10.18063/ijb.v7i3.367.

(20) Galarraga, J. H.; Kwon, M. Y.; Burdick, J. A. 3D Bioprinting via an in situ Crosslinking Technique towards Engineering Cartilage Tissue. *Scientific Reports* **2019**, *9* (1), 1-12. DOI: 10.1038/s41598-019-56117-3.

(21) Roberts, J. J.; Bryant, S. J. Comparison of photopolymerizable thiol-ene PEG and acrylate-based PEG hydrogels for cartilage development. *Biomaterials* **2013**, *34* (38), 9969-9979.

(22) Qi, C.; Liu, J.; Jin, Y.; Xu, L.; Wang, G.; Wang, Z.; Wang, L. Photo-crosslinkable, injectable sericin hydrogel as 3D biomimetic extracellular matrix for minimally invasive repairing cartilage. *Biomaterials* **2018**, *163*, 89-104. DOI: 10.1016/j.biomaterials.2018.02.016.

(23) Wang, Y.; Koole, L. H.; Gao, C.; Yang, D.; Yang, L.; Zhang, C.; Li, H. The potential utility of hybrid photo-crosslinked hydrogels with non-immunogenic component for cartilage repair. *NPJ Regenerative Medicine* **2021**, *6* (1), 1-14. DOI: 10.1038/s41536-021-00166-8.

(24) Aubert, S.; Bezagu, M.; Spivey, A. C.; Arseniyadis, S. Spatial and temporal control of chemical processes. *Nature Reviews Chemistry* **2019**, *3* (12), 706-722. DOI: 10.1038/s41570-019-0139-6.

(25) Kesharwani, P.; Bisht, A.; Alexander, A.; Dave, V.; Sharma, S. Biomedical Applications of Hydrogels in Drug Delivery System: An Update. *Journal of Drug Delivery Science and Technology* **2021**, *66*, 102914. DOI: 10.1016/j.jddst.2021.102914.

(26) Li, J.; Mooney, D. J. Designing Hydrogels for Controlled Drug Delivery. *Nature Reviews Materials* **2016**, *1* (12), 1-17. DOI: 10.1038/natrevmats.2016.71.

(27) Chaudhuri, O.; Gu, L.; Klumpers, D.; Darnell, M.; Bencherif, S. A.; Weaver, J. C.; Huebsch, N.; Lee, H.-p.; Lippens, E.; Duda, G. N. Hydrogels with tunable stress relaxation regulate stem cell fate and activity. *Nature materials* **2016**, *15* (3), 326-334.

(28) Darnell, M.; Young, S.; Gu, L.; Shah, N.; Lippens, E.; Weaver, J.; Duda, G.; Mooney, D. Substrate stress‐relaxation regulates scaffold remodeling and bone formation in vivo. *Advanced healthcare materials* **2017**, *6* (1), 1601185.

(29) Quah, S. P.; Zhang, Y.; Fluerasu, A.; Yu, X.; Zheng, B.; Yin, X.; Liu, W.; Bhatia, S. R. Techniques to characterize dynamics in biomaterials microenvironments: XPCS and microrheology of alginate/PEO–PPO–PEO hydrogels. *Soft Matter* **2021**.

(30) Dey, K.; Agnelli, S.; Sartore, L. Dynamic freedom: substrate stress relaxation stimulates cell responses. *Biomaterials science* **2019**, *7* (3), 836-842.

(31) Raia, N. R.; Jia, D.; Ghezzi, C. E.; Muthukumar, M.; Kaplan, D. L. Characterization of silk-hyaluronic acid composite hydrogels towards vitreous humor substitutes. *Biomaterials* **2020**, *233*, 119729. DOI: https://doi.org/10.1016/j.biomaterials.2019.119729.

(32) Spruijt, E.; Leermakers, F. A. M.; Fokkink, R.; Schweins, R.; van Well, A. A.; Cohen Stuart, M. A.; van der Gucht, J. Structure and Dynamics of Polyelectrolyte Complex Coacervates Studied by Scattering of Neutrons, X-rays, and Light. *Macromolecules* **2013**, *46* (11), 4596-4605. DOI: 10.1021/ma400132s.

(33) Spruijt, E.; Sprakel, J.; Lemmers, M.; Stuart, M. A. C.; van der Gucht, J. Relaxation Dynamics at Different Time Scales in Electrostatic Complexes: Time-Salt Superposition. *Physical Review Letters* **2010**, *105* (20), 208301. DOI: 10.1103/PhysRevLett.105.208301.

(34) Jia, D.; Muthukumar, M. Topologically frustrated dynamics of crowded charged macromolecules in charged hydrogels. *Nature communications* **2018**, *9* (1), 1-12.

(35) Wang, W.; Sande, S. A. A dynamic light scattering study of hydrogels with the addition of surfactant: a discussion of mesh size and correlation length. *Polymer Journal* **2015**, *47* (4), 302-310.

(36) Jia, D.; Muthukumar, M. Theory of Charged Gels: Swelling, Elasticity, and Dynamics. *Gels* **2021**, *7* (2), 49.

(37) Vogel, V.; Sheetz, M. Local force and geometry sensing regulate cell functions. *Nature reviews Molecular cell biology* **2006**, *7* (4), 265-275.

(38) Nonoyama, T.; Gong, J. P. Double-network Hydrogel and its Potential Biomedical Application: A Review. *Proceedings of the Institution of Mechanical Engineers, Part H: Journal of Engineering in Medicine* **2015**, *229* (12), 853-863. DOI: 10.1177/0954411915606935.

(39) Haque, M. A.; Kurokawa, T.; Gong, J. P. Super tough double network hydrogels and their application as biomaterials. *Polymer* **2012**, *53* (9), 1805-1822. DOI: https://doi.org/10.1016/j.polymer.2012.03.013.

(40) Nakajima, T.; Fukuda, Y.; Kurokawa, T.; Sakai, T.; Chung, U.-i.; Gong, J. P. Synthesis and fracture process analysis of double network hydrogels with a well-defined first network. *ACS Macro Letters* **2013**, *2* (6), 518-521.

(41) Nakajima, T.; Ozaki, Y.; Namba, R.; Ota, K.; Maida, Y.; Matsuda, T.; Kurokawa, T.; Gong, J. P. Tough Double-Network Gels and Elastomers from the Nonprestretched First Network. *ACS Macro Letters* **2019**, *8* (11), 1407-1412.

(42) Nakajima, T.; Sato, H.; Zhao, Y.; Kawahara, S.; Kurokawa, T.; Sugahara, K.; Gong, J. P. A universal molecular stent method to toughen any hydrogels based on double network concept. *Advanced Functional Materials* **2012**, *22* (21), 4426-4432.

(43) Matsuda, T.; Nakajima, T.; Fukuda, Y.; Hong, W.; Sakai, T.; Kurokawa, T.; Chung, U.-i.; Gong, J. P. Yielding criteria of double network hydrogels. *Macromolecules* **2016**, *49* (5), 1865-1872.

(44) Rose, S.; Marcellan, A.; Hourdet, D.; Creton, C.; Narita, T. Dynamics of Hybrid Polyacrylamide Hydrogels Containing Silica Nanoparticles Studied by Dynamic Light Scattering. *Macromolecules* **2013**, *46* (11), 4567-4574. DOI: 10.1021/ma4004874.

(45) Li, J.; Ngai, T.; Wu, C. The slow relaxation mode: from solutions to gel networks. *Polymer journal* **2010**, *42* (8), 609-625.

(46) Muthukumar, M. Ordinary–extraordinary transition in dynamics of solutions of charged macromolecules. *Proceedings of the National Academy of Sciences* **2016**, *113* (45), 12627-12632.

(47) Förster, S.; Schmidt, M.; Antonietti, M. Static and dynamic light scattering by aqueous polyelectrolyte solutions: effect of molecular weight, charge density and added salt. *Polymer* **1990**, *31* (5), 781-792.

(48) Lewis III, R. M.; Beech, H. K.; Jackson, G. L.; Maher, M. J.; Kim, K.; Narayanan, S.; Lodge, T. P.; Mahanthappa, M. K.; Bates, F. S. Dynamics of a Supercooled Disordered Sphere-Forming

Diblock Copolymer as Determined by X-Ray Photon Correlation and Dynamic Mechanical Spectroscopies. *ACS Macro Letters* **2018**, *7* (12), 1486-1491.

(49) Patel, A. J.; Narayanan, S.; Sandy, A.; Mochrie, S. G.; Garetz, B. A.; Watanabe, H.; Balsara, N. P. Relationship between structural and stress relaxation in a block-copolymer melt. *Physical review letters* **2006**, *96* (25), 257801.

(50) Srivastava, S.; Archer, L. A.; Narayanan, S. Structure and transport anomalies in soft colloids. *Physical review letters* **2013**, *110* (14), 148302.

(51) Gutt, C.; Ghaderi, T.; Chamard, V.; Madsen, A.; Seydel, T.; Tolan, M.; Sprung, M.; Grübel, G.; Sinha, S. Observation of heterodyne mixing in surface x-ray photon correlation spectroscopy experiments. *Physical review letters* **2003**, *91* (7), 076104.

(52) Oparaji, O.; Narayanan, S.; Sandy, A.; Ramakrishnan, S.; Hallinan, D. Structural Dynamics of Strongly Segregated Block Copolymer Electrolytes. *Macromolecules* **2018**, *51* (7), 2591-2603. DOI: 10.1021/acs.macromol.7b01803.

(53) Lewis III, R. M.; Jackson, G. L.; Maher, M. J.; Kim, K.; Narayanan, S.; Lodge, T. P.; Mahanthappa, M. K.; Bates, F. S. Grain growth and coarsening dynamics in a compositionally asymmetric block copolymer revealed by X-ray photon correlation spectroscopy. *Macromolecules* **2020**, *53* (19), 8233-8243.

(54) Srivastava, S.; Agarwal, P.; Mangal, R.; Koch, D. L.; Narayanan, S.; Archer, L. A. Hyperdiffusive dynamics in Newtonian nanoparticle fluids. *ACS Macro Letters* **2015**, *4* (10), 1149-1153.

(55) Ehrburger-Dolle, F. o.; Morfin, I.; Bley, F. o.; Livet, F. d. r.; Heinrich, G.; Richter, S.; Piché, L.; Sutton, M. XPCS investigation of the dynamics of filler particles in stretched filled elastomers. *Macromolecules* **2012**, *45* (21), 8691-8701.

(56) Kim, H.; Rühm, A.; Lurio, L.; Basu, J.; Lal, J.; Mochrie, S.; Sinha, S. Polymer film dynamics using X-ray photon correlation spectroscopy. *Materials Science and Engineering: C* **2004**, *24* (1-2), 11-14.

(57) Sanz, A.; Ezquerra, T. A.; Hernández, R.; Sprung, M.; Nogales, A. Relaxation processes in a lower disorder order transition diblock copolymer. *The Journal of Chemical Physics* **2015**, *142* (6), 064904.

(58) Hunt, J. N.; Feldman, K. E.; Lynd, N. A.; Deek, J.; Campos, L. M.; Spruell, J. M.; Hernandez, B. M.; Kramer, E. J.; Hawker, C. J. Tunable, High Modulus Hydrogels Driven by Ionic Coacervation. *Advanced Materials* **2011**, *23* (20), 2327-2331. DOI: 10.1002/adma.201004230.

(59) Srivastava, S.; Levi, A. E.; Goldfeld, D. J.; Tirrell, M. V. Structure, Morphology, and Rheology of Polyelectrolyte Complex Hydrogels Formed by Self-Assembly of Oppositely Charged Triblock Polyelectrolytes. *Macromolecules* **2020**, *53* (14), 5763-5774. DOI: 10.1021/acs.macromol.0c00847.

(60) Zhou, Y.; Schroeder, C. M. Dynamically Heterogeneous Relaxation of Entangled Polymer Chains. *Physical Review Letters* **2018**, *120* (26), 267801. DOI: 10.1103/PhysRevLett.120.267801.

(61) Kandar, A.; Srivastava, S.; Basu, J.; Mukhopadhyay, M.; Seifert, S.; Narayanan, S. Unusual dynamical arrest in polymer grafted nanoparticles. *The Journal of chemical physics* **2009**, *130* (12), 121102.

(62) Caronna, C.; Chushkin, Y.; Madsen, A.; Cupane, A. Dynamics of Nanoparticles in a Supercooled Liquid. *Physical Review Letters* **2008**, *100* (5), 055702. DOI: 10.1103/PhysRevLett.100.055702.

(63) Syed, V. M. S.; Srivastava, S. Time–Ionic Strength Superposition: A Unified Description of Chain Relaxation Dynamics in Polyelectrolyte Complexes. *ACS Macro Letters* **2020**, *9* (7), 1067-1073. DOI: 10.1021/acsmacrolett.0c00252.

(64) Li, L.; Srivastava, S.; Andreev, M.; Marciel, A. B.; de Pablo, J. J.; Tirrell, M. V. Phase behavior and salt partitioning in polyelectrolyte complex coacervates. *Macromolecules* **2018**, *51* (8), 2988-2995.

(65) Shah, S.; Leon, L. Structural Dynamics, Phase behavior, and Applications of Polyelectrolyte Complex Micelles. *Current Opinion in Colloid & Interface Science* **2021**, *53*, 101424. DOI: 10.1016/j.cocis.2021.101424.

(66) Zhang, Y.; Batys, P.; O'Neal, J. T.; Li, F.; Sammalkorpi, M.; Lutkenhaus, J. L. Molecular origin of the glass transition in polyelectrolyte assemblies. *ACS central science* **2018**, *4* (5), 638-644.

Chapter 7

Conclusions and Future Work

In summary, we first reported the innovative PEC IPN hydrogels, which consisted of interpenetrated electrostatic networks formed by triblock polyelectrolytes and covalent networks. The physical and mechanical properties of PEC IPN have been investigated systematically, and PEC IPN hydrogels have demonstrated promising properties for extrusion-based 3D bioprinting and wet bioadhesives applications. The PEC IPN hydrogels integrate the advantages of two kinds of networks and meanwhile mitigate their drawbacks. PEC IPN hydrogels exhibited synergistic effects in shear moduli and tensile properties, which are inaccessible by either PEC or covalent networks. Furthermore, the PEC network platform has demonstrated high compatibility with different photocrosslinkable polymers or monomers, such as 4-arm PEGA, PEGDA, AAm, and GelMA. All these four polymers or monomers have different molecular structures, polymer origin, crosslinking mechanisms, and molecular weight. Besides, the PEC network platform also exhibited synergistic effects with covalent networks with varying mesh sizes, which were formed by PEGDA with different molecular weights ranging from 0.7 kg/mol to 20 kg/mol. Overall, our one-pot solution strategy was adequate to address some significant drawbacks of photocrosslinkable hydrogels with a simple one-pot solution method, thus enhancing their applications, such as wet bioadhesives and extrusion-based 3D bioprinting.

PEC networks retained self-assembly properties regardless of the perturbance of polymer additives or covalent networks. Self-assembly of PEC domains is essential because PEC domains serve as electrostatic network joints, which contribute to PEC network formation and mechanical strength. Polymer additives with a large molecular weight, such as GelMA, occupied space and caused

macromolecular crowding, which hindered self-assembly of PEC domains and thus reduced connectivity of PEC networks. The arrangement of PEC domains enriched the microstructural complexity of PEC hydrogels and resultant PEC IPN hydrogels. Hierarchical structures of contemporary hydrogels are highly pursued in tissue engineering applications because structural complexity of human tissues has been discovered to play a vital role in multi-functions, such as responsiveness to mechanical and chemical cues.[1] Contemporary hydrogels not only consider similar mechanical properties of hydrogels to human tissues but also take into account nanoscopic structures. The tunable and anisotropic structure of PEC domains provides a feasible platform to create PEC IPN hydrogels with a similar structure to mimic human tissues. PEC IPN hydrogels have tunable shear and tensile properties and meanwhile controllable swelling characteristics. One interesting work in the future is to design PEC IPN hydrogels with the microstructures and mechanical properties similar to human tissues to systematically investigate the relationship between microstructures and multifunctional functions of human tissues. Besides, electrostatic interactions of PEC domains render the ability to encapsulate the charged therapeutic agents (e.g., nucleic acid, drug, and protein), improving drug delivery application of PEC IPN hydrogels. The electrostatic interaction also contributes to pH- and salt- responsiveness properties of PEC IPN hydrogels, which can be applied to encapsulate or release therapeutic agents. We first reported PEC IPN hydrogels but we lacked the chance to investigate the drug delivery applications. One interesting direction is to use PEC IPN hydrogels to encapsulate charged therapeutic agents for drug delivery applications. To the best of our knowledge, no research work has been reported for the drug delivery applications of PEC IPN hydrogels.

Interpenetration between PEC and covalent networks contributes to synergistic effects in shear moduli and tensile properties. Owing to physical interaction, the PEC hydrogels typically feature

shear moduli less than 20 kPa, negligible tensile strength, and uncontrollable swelling in an aqueous environment, which restrict their biomedical applications. In comparison, photocrosslinkable precursors feature low viscosity and negligible mechanical strength, which limit wet bioadhesives application owing to concentration dilution and material loss in an aqueous environment and restrict 3D bioprinting application because of undesirable secondary flow from a target site. After photocrosslinking, covalent hydrogels have limited toughness, lack microstructural complexity, and possess poor ability to encapsulate and deliver charged therapeutic drugs. A combination of PEC networks and photocrosslinkable materials can combine the advantages of the two networks and meanwhile minimize their disadvantages. Introduction of PEC networks can bring in microstructural diversity in the resulting hydrogels. Before light irradiation, PEC networks serve as protective scaffolds to enhance the viscosity of precursors and prevent precursors from concentration dilution in an aqueous environment. After photocrosslinking, the polymer entanglement between interpenetrated PEC and covalent networks contributes to remarkable improvements and synergistic effects in both shear moduli and tensile properties, which are inaccessible by either single network. Besides, the electrostatically crosslinked PEC networks act as an energy-dissipative structure to enhance reversibility and toughness of PEC IPN hydrogels. Interpenetration between PEC and covalent networks overcame the original drawbacks of each network and demonstrated the promising properties for wet bioadhesives and extrusion-based 3D bioprinting applications. PEC IPN hydrogels have demonstrated promising properties for 3D bioprinting because PEC networks could serve as scaffolds to enhance viscosity and mechanical properties for photocrosslinkable GelMA bioink (e.g., GelMA). Thus, the PEC+GelMA bioink at 37 C° could achieve a similar printing resolution as the GelMA bioink below 22 C°. The 3D extrusion-based applications can be further expanded

in two directions. The first direction is to apply PEC networks to other bioinks (e.g., PEGDA) in extrusion-based bioprinting applications. The second direction is to develop new polyelectrolytes, which not only can achieve similar effects as the polyelectrolytes used in this dissertation but also have less cell toxicity, high biocompatibility, and biodegradability. In addition, PEC IPN hydrogels also have demonstrated promising properties for wet bioadhesives applications. The PEC networks can serve as scaffolds to protect adhesive ingredient precursors from dilution in a wet environment, which are typically seen in biomedical applications owing to blood and biological fluid. Besides, our preliminary work has demonstrated that adhesive ingredient precursors were able to crosslink and form hydrogels underwater with the presence of PEC networks. Thus, future work can be expanded to combine PEC networks with different types of adhesive materials to enhance their functionality in a wet environment.

Polymer dynamics have gradually attracted more attention in recent years. Nanoscale polymer dynamics not only influence bulk mechanical properties but also affect their biomedical applications. For instance, a proper range of dynamics could influence cells' behaviors and stimulate growth. Despite importance of dynamics, it remains poorly understood about polymer dynamics and their influences, especially slow dynamics. Slow dynamics was first observed by dynamic light scattering (DLS) around 40 years ago, but researchers still doubted its existence. Due to the long wavelength (~ 300-700 nm) of DLS, dust particles can even cause another mode of dynamics. By using XPCS, we can avoid the influence of dust particles because the X-ray wavelength of XPCS is around 1.13 Å. In our projects, we observed the appearance of slow dynamics in PEC hydrogels with a high concentration, further confirming the existence of slow dynamics. Besides, we used and averaged the high-intensity regions of 2D scattering at four angles to process and generate autocorrection function g_2. Our results showed that the anisotropic analysis

of scattering patterns provided an alternative and feasible method to process the XPCS scattering data. XPCS collected the information on microstructures and dynamics at the same time and length scale, providing a chance to investigate their relationship. By varying polyelectrolyte concentrations, the PEC hydrogels underwent a microstructural transition from disordered spheres to lamellar structures. The PEC hydrogels with disordered spheres and lamellar structure have single dynamics mode and double dynamics mode, respectively. The coupling relationship between PEC microstructure and dynamics modes was observed in both saline and salt-free environments. Besides, the structural dynamics by XPCS were in agreement with stress dynamics by rheology. We believe that the discovered coupling relationship between microstructure and dynamics will provide a new direction and reference for future structure-dynamics research of hydrogels in the future. Furthermore, another future work is to investigate how the dynamics and microstructures of hydrogels influence cell behaviors, which still remains poorly understood in tissue engineering.

Reference

(1) Yue, Y.; Gong, J. P. Structure and unique functions of anisotropic hydrogels comprising uniaxially aligned lamellar bilayers. *Bulletin of the Chemical Society of Japan* **2021**.